TESTING GRAVITY WITH COSMOLOGY: EFFICIENT SIMULATIONS, NOVEL STATISTICS AND ANALYTICAL APPROACHES

A Dissertation

Presented to the Faculty of the Graduate School

of Cornell University

in Partial Fulfillment of the Requirements for the Degree of

Doctor of Philosophy

by

Georgios Valogiannis

August 2020

TESTING GRAVITY WITH COSMOLOGY: EFFICIENT SIMULATIONS, NOVEL STATISTICS AND ANALYTICAL APPROACHES

Georgios Valogiannis, Ph.D.

Cornell University 2020

In the era of precision cosmology, a wide range of cosmological surveys, such as the LSST, DESI, Euclid and WFIRST will precisely probe the large-scale structure of the universe, shedding light on the nature of the dark sectors. Given how sensitively the growth of structure depends on the nature of the underlying gravitational field, this will be a unique opportunity to constrain the so-called Modified Gravity models (MG), that are theoretical alternatives to dark energy, which attempt to explain cosmic acceleration through a large-scale modification to General Relativity. In order to fully utilize the wealth of incoming data, however, theoretical predictions of structure formation in such alternative scenarios are necessary. Due to the existence of an additional degree of freedom that these models introduce, N-body simulations prove to be highly computationally expensive. In the first chapter of this thesis, we discuss how we can overcome this issue by using Lagrangian hybrid techniques, which can lead to a speed-up by 2 orders of magnitude, compared to the conventional tools, while still achieving % level of accuracy. Then, in chapter 2 we proceed to introduce novel statistics that can help us more confidently detect MG signals hidden in cosmic density fields, by up-weighting the significance of cosmic voids, where the MG-ΛCDM degeneracy is broken. In the scales where structure formation is analytically tractable, finally, we show that we can make accurate analytical predictions for the two-point statistics of halos in MG, using Lagrangian per-

turbation theory and the Gaussian Streaming Model, simultaneously capturing, for the first time in modified gravity, the effects of both halo-bias (in chapter 3) and redshift space distortions (in chapter 4), effects crucial for the interpretation of photometric and spectroscopic observations. Our results demonstrate that a series of analytical, semi-analytical and simulation-based tools can be utilized in order to dramatically improve our understanding of the nature of cosmic acceleration and gravity at cosmic scales.

BIOGRAPHICAL SKETCH

Georgios Valogiannis was born and raised in Trikala, Greece, where he graduated from high school in June 2009. Early in his high school career, he got actively involved in the national Astronomy high school competition and was awarded an honorable mention in the student's International Olympiad on Astronomy and Astrophysics (IOAA) in Bandung, Indonesia, in 2008. He won the first prize in the national competition the following year and also participated in the 2009 IOAA in Tehran, Iran, before joining the Aristotle University of Thessaloniki, Greece in the fall of 2009. As an undergraduate student, he continued his active participation in various Astronomical activities at a national level and got particularly interested in a variety of topics in theoretical astrophysics, general relativity and cosmology. He graduated first of his class in the year of 2014, with a major in Physics and a specialization in Astronomy, before moving to the US to begin his graduate studies in Astronomy at Cornell University, in the fall of 2014. While at Cornell, he obtained a M.Sc. in Astronomy in 2017 and then pursued a PhD in theoretical cosmology, with an emphasis on cosmological tests of dark energy and modified gravity theories, under the supervision of Professor Rachel Bean. He is an active member of the LSST DESC, DESI, Euclid and WFIRST collaborations, and since February 2020 he is the leader of the topical beyond wCDM models team within the LSST DESC. After the completion of his PhD studies at Cornell University, he is expected to join the Physics Department of Harvard University as a postdoctoral researcher in the fall of 2020.

To my parents, Athanasia and Thanasis

ACKNOWLEDGEMENTS

Conducting a PhD has been one of the most challenging and rewarding experiences in my life, which shaped my personality in ways I could never imagine and taught me that the journey is equally, if not more, important than the destination. It also gave me the opportunity to meet and collaborate with many amazing people, without the help of whom I could have never reached this point.

I am indebted to my PhD supervisor, Professor Rachel Bean, for giving me the opportunity to conduct this PhD, for her invaluable guidance and support and for providing me with the freedom to explore and develop my research interests. Your contributions have been crucial in allowing me to overcome every obstacle along the way and gain confidence in myself, for which I am extremely grateful!

I would also like to thank the rest of my special committee, Professors David Chernoff, Saul Teukolsky and Dominik Riechers, for carefully monitoring my progress over the course of my graduate path, as well as all the members of the Cornell Astronomy community. Being a member of the Department of Astronomy has truly been an amazing experience, that gave me the opportunity to interact and become friends with many brilliant people, that come from a variety of cultural and educational backgrounds.

Being a member of many international collaborations and participating in meetings and conferences all around the world has been another exciting component of my graduate career. To that end, I would like to thank all of my colleagues within LSST DESC, DESI and Euclid for the numerous fascinating discussions and Mustapha Ishak, in particular, for trusting me with the leadership of the beyond wCDM topical team within DESC. I would also like to sincerely

thank Baojiu Li, for continuously providing valuable insights and simulation resources over the course of this PhD, as well as Alejandro Aviles, for his valuable contributions as a co-author in my latest paper.

Taking the leap to pursue graduate studies in the US would not have been possible without the guidance of my mentors from Aristotle University, Nikolaos Stergioulas and John Hugh Seiradakis, which was pivotal in encouraging me to move forward with this decision in the fall of 2013. I am also very grateful to Vasileios Charmandaris, Manolis Papastergis and Ioannis Contopoulos, for their useful advice on the graduate school decision and on relocating to Ithaca and joining Cornell.

Last but not least, a special thanks goes to my family and friends for their unconditional love and support. To my mom, Athanasia, and my dad, Thanasis, for always supporting my childhood dream of studying the universe, no matter how unconventional it would sound, for emphasizing the importance of not forgetting my goals and dreams and for always reminding me the importance of patience along each step of the academic ladder. To my sister, Konstantina, for helping me avoid the pitfalls of the academic journey, for always being willing to listen to my crazy stories about constellations and for reminding me to also remain down-to-earth. To all my friends, in Greece, the US and all over the world, who proved to me that no matter which part of the world you are in, your friends will always be there for you. Thank you all!

Georgios Valogiannis

Ithaca, April 2020

TABLE OF CONTENTS

Biographical Sketch . . . iii
Dedication . . . iv
Acknowledgements . . . v
Table of Contents . . . vii

1 Introduction **1**
1.1 The problem of cosmic acceleration . . . 1
1.2 The motivation for modifying gravity . . . 3

2 Efficient simulations of large scale structure in modified gravity cosmologies with COLA **9**
2.1 Introduction . . . 9
2.2 Formalism . . . 11
2.2.1 Modified gravity and screening models . . . 11
2.2.2 Simulating non-linear clustering . . . 17
2.3 Analysis/Results . . . 25
2.3.1 Modified gravity results . . . 25
2.4 Conclusions . . . 33
2.5 Acknowledgments . . . 37

3 Beyond δ: tailoring marked statistics to reveal modified gravity. **41**
3.1 Introduction . . . 41
3.2 Formalism . . . 42
3.2.1 Modified gravity models . . . 42
3.2.2 Density transformations . . . 45
3.3 Results . . . 49
3.4 Conclusions . . . 57
3.5 Acknowledgments . . . 59

4 Convolution Lagrangian perturbation theory for biased tracers beyond general relativity **65**
4.1 Introduction . . . 65
4.2 Formalism . . . 68
4.2.1 Modified gravity models . . . 68
4.2.2 Convolution Lagrangian Perturbation Theory for biased tracers in MG . . . 73
4.3 Results . . . 88
4.3.1 Lagrangian Perturbation Theory for Biased Tracers in MG 88
4.3.2 Comparison with simulations . . . 107
4.4 Conclusions . . . 119
4.5 Acknowledgments . . . 122

5 An accurate perturbative approach to redshift space clustering of biased tracers in modified gravity 124
5.1 Introduction . . . 124
5.2 Modified Gravity Scenarios and Simulation Tools . . . 127
5.2.1 Modified Gravity Scenarios . . . 127
5.2.2 N-body Simulations . . . 129
5.3 Redshift-Space Correlation Function For Biased Tracers In Modified Gravity . . . 131
5.3.1 Lagrangian Perturbation Theory For Dark Matter In Modified Gravity . . . 132
5.3.2 Lagrangian Biased Tracers In Modified Gravity . . . 135
5.3.3 Direct Lagrangian Approach to RSD in Modified Gravity . 139
5.3.4 The Gaussian Streaming Model In Modified Gravity . . . 141
5.3.5 Velocity Moments in Modified Gravity . . . 143
5.4 Results . . . 147
5.4.1 Halo Pairwise Velocity Statistics . . . 148
5.4.2 Halo Redshift-Space 2-point Correlation Function . . . 156
5.5 Conclusions . . . 166
5.6 Acknowledgments . . . 170

6 Conclusions 171

A Lagrangian perturbation theory in Modified Gravity 177

B One loop corrections for biased statistics in MG 180
B.1 Polyspectra and k-functions in MG . . . 181
B.2 Lagrangian correlators and q-functions in MG . . . 188
B.3 SPT and LRT Power spectra . . . 192

C PBS biases in MG 194

D GSM functions in MG 198
D.1 LPT kernels . . . 198
D.2 k functions . . . 201
D.3 q functions . . . 204
D.4 Tidal bias . . . 207

E Direct Lagrangian approach in MG 208

Bibliography 210

CHAPTER 1

INTRODUCTION

1.1 The problem of cosmic acceleration

The accelerated expansion of the universe, as precisely measured by Type 1a supernovae [138, 147], baryon acoustic oscillations (BAO) in galaxy clustering [63, 136, 137, 89], and the Cosmic Microwave Background (CMB) radiation [173, 7, 6], represents one of the greatest, open questions in modern cosmology and physics. This is due to the fact that such a feature directly contradicts the common expectation, prior to this discovery, of a decelerating universe, due to the mutual gravitational attraction of cosmic matter described by Einstein's General Relativity (GR). In order to illustrate this argument, let us describe the dynamics of an evolving universe containing matter and energy that abide by the principles of GR. Following the Lagrangian description of field theory, the GR action, S, is expressed as follows:

$$S = \int d^4x \sqrt{-g} \left[\frac{R}{16\pi G} + \mathcal{L}_m(g_{\mu\nu}, \psi_m) \right], \tag{1.1}$$

with $\mathcal{L}_m$ denoting the Lagrangian of matter fields ψ_m, that follow the geodesics of the metric tensor $g_{\mu\nu}$, the determinant of which is g and G the gravitational constant. Finally, R is the Ricci scalar, the definition of which will be presented shortly. From the variational principle, taking $\frac{\delta S}{\delta R} = 0$ gives the Einstein equations of GR:

$$G_{\mu\nu} = R_{\mu\nu} - \frac{1}{2} g_{\mu\nu} R = 8\pi G T_{\mu\nu}. \tag{1.2}$$

In (1.2), which employs the Einstein notation and assumes $c = \hbar = 1$, $R_{\mu\nu}$ is the Ricci tensor (which is given by derivatives of the metric tensor) and $R = R_{\mu\nu} g^{\mu\nu}$

the Ricci scalar. On the right hand side of (1.2), $T_{\mu\nu}$ is the energy-momentum tensor.

Physical cosmology amins to identify the solutions of (1.2) (or any alternative theory of gravity) that are consistent with the Large-Scale Structure (LSS) of the universe. At 0^{th} perturbative order, an expanding homogeneous and isotropic spacetime is described by the Friedmann - Robertson - Walker (FRW) metric:

$$ds^2 = g_{\mu\nu}dx^\mu dx^\nu = -dt^2 + a^2(t)\delta_{ij}dx^i dx^j, \tag{1.3}$$

where $a(t)$ is the scale factor in an expanding universe and δ_{ij} the Kronecker delta. For a perfect isotropic fluid, the energy momentum tensor takes the matrix form:

$$T^\mu_\nu = \begin{bmatrix} -\rho & 0 & 0 & 0 \\ 0 & P & 0 & 0 \\ 0 & 0 & P & 0 \\ 0 & 0 & 0 & P \end{bmatrix} \tag{1.4}$$

where ρ and P are the density and pressure, respectively. Now solving eq. (1.2) with (1.3) and (1.4), at the 0^{th} level of perturbations we get the two Friedmann equations

$$H^2(a) = \left(\frac{\dot{a}}{a}\right)^2 = \frac{8\pi G}{3}\rho - \frac{k}{a^2}, \tag{1.5}$$

and

$$\dot{H} + H^2 = \frac{\ddot{a}}{a} = -\frac{4\pi G}{3}(\rho + 3P) = -\frac{4\pi G}{3}\rho(1 + 3w), \tag{1.6}$$

where k is the curvature parameter, which is equal to $\{1, 0, -1\}$, depending on whether the geometry of the universe is closed, flat (i.e. Euclidean) or open, $w = \frac{P}{\rho}$ is the equation of state and dots indicate derivatives with respect to time. A wide range of observations suggests that the dominant form of matter at cosmic scales is Cold Dark Matter (CDM), which behaves as a pressure-less fluid

(w=0) and interacts merely gravitationally. However, one immediately notices that eq. (1.6) for $w = 0$ predicts a continuous phase of cosmic deceleration, $(\ddot{a}) < 0$, in stark contrast to the overwhelming amount of observational evidence supporting a recent phase of accelerated expansion [138, 147, 63, 136, 137, 89]! Eq. (1.6) implies that, assuming GR, acceleration can be generated only by a source of energy with equation of state $w < -\frac{1}{3}$. Within the set of principles laid out so far, this condition can be minimally satisfied by the existence of a positive cosmological constant Λ, that plays the role of *constant* vacuum energy density and causes the expansion of the universe to accelerate. Indeed, the energy-momentum conservation condition $\nabla_\mu T^{\mu\nu} = 0$ gives the continuity equation

$$\dot{\rho} + 3H\rho(1 + w) = 0, \tag{1.7}$$

which shows that a constant energy density (i.e. $\dot{\rho} = 0$) implies a negative equation of state, equal to $w = -1$, which is consistent with the acceleration condition $w < -\frac{1}{3}$ from (1.6). This scenario, the Λ-Cold Dark Matter (ΛCDM) model of the universe, can successfully account for all observations up to date and has been rightfully called the standard model of cosmology.

1.2 The motivation for modifying gravity

Despite the notable observational success of ΛCDM, the model unfortunately suffers from an undesirable property: the value of the vacuum energy predicted by quantum field theory is orders of magnitude larger than the best-fit one that is necessary to explain cosmic acceleration, so Λ needs to be fine-tuned; the infamous cosmological constant problem [201]. Such an unfortunate mismatch, together with the need to fully explore the space of all theoretical alternatives,

has generated growing interest in considering beyond-ΛCDM scenarios. Introducing a minimally coupled scalar field with a negative equation of state called "dark energy" or quintessence [202, 143, 52] could also match the observed expansion history of ΛCDM, but suffers from fine-tuning obstacles of a very similar nature.

All the proposals we considered so far attempt to tackle the problem of cosmic acceleration by introducing a new energy source term, that is, modifying the right hand side of (1.2). In light of the theoretical challenges these scenarios face, an alternative proposal considers looking into the left hand side of (1.2), and states that what we observe might be the signal of a fundamental misunderstanding of the behavior of gravity at large scales, the so-called Modified Gravity (MG) models [97, 84]. Such scenarios broadly attribute cosmic acceleration to a new scalar field ϕ, in the presence of which the gravitational action becomes

$$S = \int d^4x \sqrt{-g} \left[\frac{R}{16\pi G} + \mathcal{L}(\phi, \partial_\mu \phi, \partial_\mu \partial^\mu \phi) + \mathcal{L}_m(e^{2\beta(\phi)\phi/M_{pl}} g_{\mu\nu}, \psi_m) \right]. \tag{1.8}$$

Modifying the Einstein-Hilbert action as in (1.8), however, introduces in principle an additional degree of freedom that is conformally coupled to matter (as one can see in the third term of the Lagrangian) and can produce significant deviations from the predictions of GR, which have passed a wide array of precise observational tests, especially in the Solar System [206]. Furthermore, the recent simultaneous detection of gravitational waves and EM counterparts by the LIGO/Virgo collaboration [3, 68, 155, 1, 2], has placed additional constraints [150, 65, 54, 19] into the form of the most general expression of a scalar-tensor theory that produces second order equations of motion, described by the Horndeski action [80, 58].

In order to be able to confront such tight constraints successfully, while at the same time provide a stable self-accelerative cosmic mechanism, viable MG candidates contain a restoring property, called "screening" [90, 91], which is a dynamical mechanism that weakens the additional fifth forces in high-density environments through the corresponding scalar field self-interactions, encoded in the second Lagrangian term in (1.8). In the Vainshtein mechanism [187, 18], GR is recovered thanks to the second derivative terms in the scalar field Lagrangian, that become large in high density environments and effectively weaken the coupling to the matter sources. The Vainshtein mechanism is very efficient in the vicinity of a massive source and contains a rich phenomenology, which makes it particularly attractive. Another popular class of screening consists of the chameleons [92, 93], where in regions of high potential the scalar fields become massive and cannot propagate, resulting thus in suppression of the fifth forces. Despite the fact that chameleons cannot produce self-acceleration [197], their very interesting phenomenology makes them serve as ideal testbeds for gravity and considerable efforts have been put into their study in the past decade [45]. Other screening classes include the symmetrons [77, 130], that employ spontaneous symmetry breaking and share qualitative similarities with the chameleons and the K-Mouflage [61, 18], in which deviations are suppressed when scalar field gradients exceed a certain value.

The observed inhomogeneous LSS of the Universe, is the outcome of the subsequent nonlinear gravitational evolution of the primordial density fluctuations, partially modulated by the late-time acceleration. As a result, it provides us with an observational window into the fundamental physics that shaped this process, including sensitive tests of the underlying large-scale gravitational law, making it particularly valuable for constraining the various MG models. In-

deed, if we consider linear perturbations around the smooth expanding FRW spacetime, the metric (in the conformal-Newtonian gauge) will take the form

$$ds^2 = -(1 + 2\Phi)dt^2 + a^2(t)(1 + 2\Psi)\delta_{ij}dx^i dx^j, \tag{1.9}$$

where the perturbation Φ corresponds to the Newtonian potential and Ψ is the perturbation to the spatial curvature. In the context of pure GR considerations, solving (1.9) with (1.2) gives us the known form of the Poisson equation

$$\nabla^2\Phi = 4\pi G\delta\rho_m, \tag{1.10}$$

which describes how the matter density perturbations $\delta\rho_m$ are the source of the gravitational potential and force. In MG scenarios, however, as we shall see in the following chapters, we generally find that

$$\nabla^2\Phi = 4\pi G_{eff}\delta\rho_m, \tag{1.11}$$

where $G_{eff} \neq G$ is a complicated function of both space and time that will give rise to non-trivial deviations from GR in cosmic scales, impacting structure formation in an observable manner. As we are entering the era of "precision cosmology", multiple spectroscopic and photometric surveys of the LSS, both already operating, such as the DES [4] and also about to be commissioned in the next decade, like DESI [106], Euclid [105], the LSST [5] and WFIRST [172], will provide us with particularly precise maps of the LSS that will shed light on the mysterious nature of the dark sector. Taking full advantage of this wealth of cosmological information poses a great challenge for experiment and theory alike.

On the theoretical side, fully utilizing upcoming observations requires a precise modeling of the distinct LSS signals both from ΛCDM and also its alternatives. These predictions should extend down to the smaller scales, where the

non-linear nature of the gravitational equations renders the problem analytically intractable and makes full N-body simulations of structure formation inevitable. In the case of MG scenarios, the necessary simulations are notoriously computationally expensive, due to the need to account for the MG screening mechanism, which is highly nonlinear and adds a new layer of complexity to the whole process. In Chapter 2, we will discuss how to speed up such simulations for MG by two orders of magnitude, by employing the efficient hybrid COLA scheme, that combines Lagrangian perturbation theory (LPT) with a pure N-body component and represents an ideal trade-off between accuracy and computational cost.

The MG screening mechanism, that suppresses deviations from GR by means of a novel scalar field interplay, might restore the phenomenological viability of such candidates, but at the same time suppresses these signals so much, to the extent that their detection becomes very challenging, even for the future ambitious surveys of the LSS. In Chapter 3, we will demonstrate that a set of very simple density transformations, that up-weight the lower density, unscreened regions, can help us more confidently expose modifications to gravity that can be hidden in the cosmic web.

If our focus is restricted on detecting signals of MG on relatively larger scales, where the problem of structure formation is analytically tractable, useful insights can be gained by employing perturbative approaches, that require only a very small fraction of the computational cost a full N-body simulation would require. Even in that case, however, if we want our predictions to realistically confront the upcoming observations, for the variety of competing scenarios, we need to account for the fact that the observed galaxies do not perfectly trace the

underlying dark matter density field (the evolution of which is straightforward to predict), but are *biased tracers* of it. In Chapter 4, we will obtain accurate predictions for statistics of biased tracers in theories of MG, combining the halo model with the framework of Lagrangian perturbation theory.

A significant portion of the upcoming observations, such as the ones that will be obtained by DESI [106], Euclid [105] and WFIRST [172], will be spectroscopic ones, that will determine the positions of galaxies in redshift space. The peculiar velocities of galaxies about the Hubble flow, contribute a spectroscopic component that introduces thus an anisotropy in the observed clustering pattern, the Redshift Space Distortions (RSD). In Chapter 5, finally, we will show how the analytical framework developed in Chapter 4 can be expanded to incorporate the RSD effects for biased tracers, for the first time in MG, by means of the scale-dependent Gaussian streaming approach.

CHAPTER 2

EFFICIENT SIMULATIONS OF LARGE SCALE STRUCTURE IN MODIFIED GRAVITY COSMOLOGIES WITH COLA

2.1 Introduction

In this chapter, we will implement an adaptation of the COLA approach, a hybrid scheme that combines Lagrangian perturbation theory with an N-body approach, to model non-linear collapse in chameleon and symmetron modified gravity models. Gravitational screening, a key feature of such models, as we shall see, will be modeled effectively through the attachment of a suppression factor to the linearized Klein-Gordon equations. The adapted COLA approach will then be benchmarked, with respect to an N-body code both for the ΛCDM scenario and for the modified gravity theories. This work has been published in [189].

A variety of analytical, semi-analytical and numerical approaches have been used to study ΛCDM and dark energy scenarios in the non-linear regime of the large-scale structure of the Universe. Lagrangian perturbative techniques up to first [212, 135] or second order [38], have been shown to produce accurate results for ΛCDM in the linear and mildly non-linear scales without having to perform a complete numerical treatment of structure formation. They fail to achieve the desired accuracy, however, at smaller, non-linear scales for which a full N-body simulation is required. In light of the computational resources necessary for N-body simulations, and given the successes of Lagrangian Perturbation Theory (LPT), hybrid schemes have been proposed, with the aim of combining the strengths of both approaches. In this chapter, we focus on the Comoving

Lagrangian Acceleration (COLA) hybridization scheme [182]. By evolving the large scales analytically using LPT and the small scales exactly with a full N-body treatment, the COLA method manages to produce accurate results deep in the mildly non-linear regime with only a few number of time steps, making it possible to produce fast results in exchange for some accuracy.

In modified gravity simulations, the need to accurately capture the effects of the fifth forces and the screening mechanism adds a new layer of complexity. For an exact description, one needs to solve the full Klein-Gordon equation, whose non-linearities render the procedure both challenging and computationally expensive. It is natural consequently to investigate whether an inexpensive, approximate scheme can be used instead. A linear treatment of the perturbation equations, together with the linearized Klein-Gordon equation it produces may seem efficient at first, but a more careful examination shows [39, 40] that it fails to incorporate the non-linear screening effects and gives poor results. Effective approaches [207] have managed to implement screening successfully, however, following a phenomenological path. An ineffective but computationally fast linearized scheme, can be combined with the attachment of a screening factor for a spherically symmetric configuration, to speed up MG simulations without the sacrifice of much accuracy.

Given the success of Lagrangian approaches in ΛCDM simulations and the need to develop effecient, but representative, realizations of the LSS in different cosmological scenarios, it is natural to see alternative routes in MG models. The benefits of LPT have already been discussed in the context of generating initial conditions, appropriate for coupled scalar field cosmologies [108] or MG models [188] . In this chapter, we study the effectiveness of the COLA hybrid scheme,

in which the linear scales are evolved exactly using LPT and the non-linear ones using N-body simulations, for MG scenarios. As far as the N-body component is concerned, the fifth force calculation lies in the solution of the linearized KG equation and an approximate screening implementation through the thin shell factor for a dense sphere, similar to [207]. In chameleon-type (and symmetron) models, a scalar field acquires a very large mass within a massive object and consequently decouples due to the Yukawa suppression, so essentially only a fraction of the total mass (thin shell) contributes to the fifth force.

The layout of the rest of the chapter is as follows: in Sec. 2.2 we first review the MG models studied and the non-linear approaches used in the analysis. In Sec. 2.3 we present our results, assessing the performance for the scheme to predict a number of LSS observables, including the matter power spectrum, the redshift space distortions, and halo mass function, before summarizing the findings and discussing implications in Sec. 2.4.

2.2 Formalism

2.2.1 Modified gravity and screening models

A wide class of viable scalar-tensor theories have been shown to be described by a Horndeski Lagrangian [80, 58]. Using a general single scalar field Lagrangian, in the Einstein frame, written in terms of a scalar field ϕ and its derivatives,

$$\mathcal{L} = \frac{M_{Pl}^2}{2}R + \mathcal{L}(\phi, \partial_\mu\phi, \partial_\mu\partial^\mu\phi) + \mathcal{L}_m(e^{2\beta(\phi)\phi/M_{pl}}g_{\mu\nu}, \psi_m), \tag{2.1}$$

where R is the Ricci scalar, ϕ the scalar field, M_{Pl} the reduced planck mass $M_{Pl} = \frac{m_{Pl}}{\sqrt{8\pi G}}$ and $\mathcal{L}_m$ is the Lagrangian for the matter sector, in which the matter fields ψ_m are non-minimally coupled to the scalar field with a dimensionless coupling constant $\beta(\phi)$. In the chameleon and symmetron models, the properties of the single scalar field can be described by a simple, scalar field Lagrangian

$$\mathcal{L} = -\frac{1}{2}(\nabla\phi)^2 - V(\phi) \tag{2.2}$$

where $V(\phi)$ is the self-interacting potential. Varying the action gives us the equations of motion for the scalar field, the Klein-Gordon equation

$$\Box\phi = V_{eff,\phi} \tag{2.3}$$

where the effective potential combining the self-interaction potential and coupling term is given by

$$V_{eff} = V(\phi) + \frac{e^{\beta\phi/M_{pl}}\rho_m}{M_{Pl}} \tag{2.4}$$

The chameleon screening mechanism lies in the fact that the effective mass of the scalar field calculated at the minimum, m, which is given by

$$m^2 = \frac{d^2V_{eff}}{d\phi^2}, \tag{2.5}$$

has to be positive. For the chameleon theories, this requirement is guaranteed through the interplay between a monotonically decreasing potential $V(\phi)$ and an increasing coupling. In the symmetron model, on the other hand, the viability is restored using a "Mexican hat" symmetry breaking potential [77], the behavior of which still gives rise to a positive density-dependent mass.

The observational consequences of such models can be demonstrated by extracting the scalar field profile, $\phi(r)$, produced by the density profile

$$\rho(r) = \begin{cases} \rho_c & \text{if } r < \mathcal{R}_c \\ \rho_\infty & \text{if } r > \mathcal{R}_c \end{cases} \tag{2.6}$$

where r is the radial distance from the center of a compact spherically symmetric configuration of density ρ_c and radius $\mathcal{R}_c$ (not to be confused with the Ricci scalar R), that is isolated on a uniform density background ρ_∞. Under spherical symmetry, (2.3) becomes

$$\frac{1}{r^2}\frac{d}{dr}\left(r^2\frac{d\phi}{dr}\right) = \left(\frac{\partial V}{\partial \phi} + \frac{\beta(\phi)\rho_c(r)}{M_{Pl}}\right). \tag{2.7}$$

Even though (2.7) does not have, in principle, an analytical solution, accurate approximations can be performed for two different configurations, that correspond to opposite regimes with respect to screening [93, 92]. The first case is that of a large, strongly perturbing object of very large density ρ_c, for which the interior field is forced to acquire the value that corresponds to the minimum of the effective potential, ϕ_c and the scalar field profile outside the object is given by

$$\phi(r) = \phi_\infty + \frac{(\phi_c - \phi_\infty)\,\mathcal{R}_c}{r} e^{-m_\infty r}, r > \mathcal{R}_c. \tag{2.8}$$

The corresponding fifth-force experienced by a unit mass particle outside the object is

$$F_\phi(r) \;=\; 2\beta_\infty^2\left(\frac{\Delta\mathcal{R}_c}{\mathcal{R}_c}\right)\frac{GM}{r^2}\,(1 + m_\infty r)\,e^{-m_\infty r}, \tag{2.9}$$

where m_∞, β_∞ are respectively the background values of the mass and coupling and M the mass of the object. Given the characteristic large values of the Compton wavelength $\lambda_c \equiv m_\infty^{-1}$, the scalar field is essentially free within our scales of interest and the Yukawa suppression can be neglected in (2.9),

$$F_\phi(r) \;\approx\; 2\beta_\infty^2\left(\frac{\Delta\mathcal{R}_c}{\mathcal{R}_c}\right)\frac{GM}{r^2}, \qquad m_\infty r \ll 1. \tag{2.10}$$

The above approximation is valid when the "screening factor" is

$$\frac{\Delta\mathcal{R}_c}{\mathcal{R}_c} = \frac{|\phi_\infty - \phi_c|}{2\beta_\infty M_{Pl}\Phi_N} \ll 1, \tag{2.11}$$

which also defines the criterion for the existence of a thin shell [77, 91], whose mass is the fraction of the total that actually contributes to the fifth force, due to the strong Yukawa suppression deep inside dense objects. The Newtonian gravitational potential is denoted by Φ_N in (2.11). On the other hand, when linear perturbation theory is valid, which is the case when $\frac{\Delta\mathcal{R}_c}{\mathcal{R}_c} > 1$, the linearized form of (2.7) gives

$$F_\phi(r) \approx 2\beta_\infty^2 \frac{GM}{r^2}, \qquad m_\infty r \ll 1 \tag{2.12}$$

for the fifth force. Based on (2.10)-(2.12), we see that in the linear regime the fifth force is the same as the Newtonian force with a coupling $2\beta_\infty^2$ and deep in the non-linear (screened) regime, it is suppressed by the thin shell factor (2.11).

Furthermore, it should be also noted that, as shown in [41], one can derive a pair of functions $\beta(a), m(a)$, for the characterization of a model within the above framework. Unlike models with constant couplings, symmetrons exhibit an additional form of screening [77, 130] due to the fact that in dense environments symmetry is restored and the coupling $\beta(\phi)$ vanishes.

Adopting this formulation, linear perturbation theory gives [113, 41] for the growth of CDM density perturbations in the quasi-static limit and for sub-horizon scales

$$\ddot{\delta}_m + 2H\dot{\delta}_m = \frac{3}{2}\Omega_m(a)H^2\delta_m \frac{G_{eff}(k,a)}{G} \tag{2.13}$$

with

$$\frac{G_{eff}(k,a)}{G} = 1 + \frac{2\beta^2(a)k^2}{k^2 + a^2m^2(a)} \tag{2.14}$$

where a is scale factor, with $a = 1$ today, and k is the comoving wavenumber.

The effects of gravity modifications at the linear approximation are incorporated in the second term. For very large scales and/or early times (GR regime),

$am(a)/k \gg 1$ and (2.13) reduces to the standard GR expression in the weak gravity regime, where the Newtonian gravitational potential is given by the Poisson equation,

$$\nabla^2 \Phi_N = \frac{3}{2}\Omega_{m0}\frac{H_0^2}{a}\delta_m. \tag{2.15}$$

When $am(a)/k \leq 1$ however (scalar-tensor regime), the second term becomes significant and gives the linearized Klein-Gordon equation for the fifth potential ϕ

$$\phi(k,a) = -\frac{\beta(a)}{k^2 + a^2 m^2(a)}\frac{\bar{\rho}_m a^2}{M_{pl}}\delta_m. \tag{2.16}$$

with the real space expression being

$$\nabla^2\phi = a^2 m^2(a)\phi + \frac{\beta(a) a^2 \bar{\rho}_m}{M_{pl}}\delta_m. \tag{2.17}$$

The $f(R)$ model

$f(R)$ theories [48] are widely-studied modified gravity scenarios, that give rise to acceleration on cosmic scales and can be incorporated [43] into the chameleon formalism with a constant coupling $\beta = 1/\sqrt{6}$. The first model we tested thus, was the Hu-Sawicky $f(R)$ model [81] with a scalar field mass

$$m(a) = \left(\frac{1}{3(n+1)}\frac{\bar{R}}{|\bar{f}_{R_0}|}\left(\frac{\bar{R}}{\bar{R}_0}\right)^{n+1}\right)^{\frac{1}{2}} \tag{2.18}$$

where

$$\bar{R} = -3(H_0^2\Omega_{m0})^2\left(a^{-3} + 4\frac{\Omega_{\Lambda 0}}{\Omega_{m0}}\right) \tag{2.19}$$

where H_0 is the Hubble Constant and $\Omega_{\Lambda 0}$ and Ω_{m0} are, respectively, the dark energy and dark matter fractional energy densities today. The mass takes the form

$$m(a) = \frac{1}{2997}\left(\frac{1}{2|\bar{f}_{R_0}|}\right)^{\frac{1}{2}}\frac{\left(\Omega_{m0}a^{-3} + 4\Omega_{\Lambda 0}\right)^{1+\frac{n}{2}}}{\left(\Omega_{m0} + 4\Omega_{\Lambda 0}\right)^{\frac{n+1}{2}}}[Mpc/h]. \tag{2.20}$$

Furthermore, the screening factor is given by

$$\frac{\Delta\mathcal{R}_c}{\mathcal{R}_c} = \frac{3}{2}\left|\frac{\bar{f}_{R_0}}{\Phi_N}\right|\left(\frac{\Omega_{m0}+4\Omega_{\Lambda 0}}{\Omega_{m0}a^{-3}+4\Omega_{\Lambda 0}}\right)^{n+1}. \tag{2.21}$$

$\bar{f}_{R_0} = \frac{df(R)}{dR}\Big|_{z=0}$ and n are the model's free parameters. In this chapter, we consider the model for $n = 1$ and $\left|\bar{f}_{R_0}\right| = \{10^{-4}, 10^{-5}, 10^{-6}\}$. These describe cosmologically viable scenarios whose non-linear properties have been simulated using the full Klein-Gordon equation [213, 207] with which our results can be compared.

The symmetron model

The general framework laid previously, can also incorporate the symmetron model, with a "Mexican hat" symmetry breaking potential [77], for which scalar fields couple to matter after $a > a_{ssb}$, with

$$\begin{aligned} m(a) &= \frac{1}{\lambda_{\phi 0}}\sqrt{1-\left(\frac{a_{ssb}}{a}\right)^3} \\ \beta(a) &= \beta_0\sqrt{1-\left(\frac{a_{ssb}}{a}\right)^3} \end{aligned} \tag{2.22}$$

and the coupling vanishes for $a < a_{ssb}$, when symmetry is restored. The screening factor for this model becomes [55, 207]

$$\frac{\Delta\mathcal{R}_c}{\mathcal{R}_c} = \frac{\Omega_{m0}}{3.0a_{ssb}^3}\left(\frac{\lambda_{\phi 0}}{Mpc/h}\right)^2\left|\frac{10^{-6}}{\Phi_N}\right| \tag{2.23}$$

We consider this model with values $a_{ssb} = 0.5, \beta_0 = 1$ and $\lambda_{\phi 0} = 1 Mpc/h$ which again have been shown [55] to predict deviations consistent with experimental constraints. It should be also pointed out that, as explained previously, models of this type exhibit field dependent couplings which cause additional screening due to the coupling suppression in dense environments, where symmetry is again restored. This effect is not taken into account in our approximate scheme.

2.2.2 Simulating non-linear clustering

The N-body method

The COLA code has been loosely based on A. Klypin's PM code [95], and this motivates the latter's use as a comparison for our approximate scheme's effectiveness. It is also a simple and representative implementation of a Particle-Mesh (PM) N-body code. N-body simulations for MG using the PM code have been performed previously [176, 104, 94]. For each scenario, we consider 10 simulated realizations, initialized at an initial redshift $z_i = 49$, at which density perturbations on the scales we study are linear. After providing a linear power spectrum from the cosmological code CAMB [107] for the desired ΛCDM cosmology at the time z_i, $N_p = 256^3$ particles are placed in our simulation box with side L=200 Mpc/h, in a mesh of 512^3, using 1st order Lagrangian Perturbation Theory (Zel'dovich approximation) [212]. The parameters that define our background ΛCDM cosmology are $\Omega_{m0} = 0.25$, $\Omega_{\Lambda 0} = 0.75$, $h = 0.7$, $n_s = 1.0$ and $\sigma_8 = 0.8$. The particle positions are updated, using 500 time steps, through the displacement equation:

$$\ddot{\mathbf{x}} + 2H\dot{\mathbf{x}} = -\frac{1}{a^2}\nabla_{\mathbf{x}}\Phi_N. \tag{2.24}$$

In Fig. 2.1, it is shown that the choice of 500 iterations, which corresponds to steps of $\Delta a = 0.00196$ in the scale factor, guarantees convergence at the 0.08% level.

In MG cosmologies, the modified geodesic equation gives, in the weak gravity regime, the modified version of (2.24),

$$\ddot{\mathbf{x}} + \left(2H + \frac{\beta}{M_{Pl}}\dot{\phi}\right)\dot{\mathbf{x}} = -\frac{1}{a^2}\left(\nabla_{\mathbf{x}}\Phi_N + \frac{\beta}{M_{Pl}}\nabla_{\mathbf{x}}\phi\right), \tag{2.25}$$

where the term $\left|\frac{\beta}{M_{Pl}}\dot{\phi}\right|$ is negligible given observational constraints from variations of constants [207]. Equation (2.25), which also holds for the full non-linear KG description, forms a closed system of equations with (2.15) and (2.17) that are solved in the Fourier space for the potentials Φ_N and ϕ.

The linearized form of KG equation, (2.17), does not incorporate the screening effects. To account for the screening effect, we adopt an effective parameterization similar to the one proposed in [207]. In section Sec. 2.2.1, we showed that the linear solution for the fifth force, (2.10), is suppressed by the screening factor deep in the non-linear regime. As a result, we incorporate the screening effects by explicitly attaching the screening factor to the fifth force in accordance with (2.10)-(2.12) and (2.25),

$$\ddot{\mathbf{x}} + 2H\dot{\mathbf{x}} = -\frac{1}{a^2}\left(\nabla_{\mathbf{x}}\Phi_N + \frac{\Delta\mathcal{R}_c}{\mathcal{R}_c}\frac{\beta}{M_{Pl}}\nabla_{\mathbf{x}}\phi\right). \tag{2.26}$$

To interpolate properly between the screened and the unscreened regime we set

$$\frac{\Delta\mathcal{R}_c}{\mathcal{R}_c} = \begin{cases} \frac{\phi(a)}{2\beta(a)M_{Pl}|\Phi_N|} & \text{if } \frac{\phi(a)}{2\beta(a)M_{Pl}|\Phi_N|} < 1 \\ 1 & \text{if } \frac{\phi(a)}{2\beta(a)M_{Pl}|\Phi_N|} > 1. \end{cases} \tag{2.27}$$

Within our approximate scheme, the functions $|\phi_\infty - \phi_c|$ and β_∞ have been set equal to the background ones $|\phi(a)|$ and $\beta(a)$ correspondingly, which has been shown to be a good approximation in [207].

The COLA method

The fact that N-body codes manage to simulate the Large Scale Structure accurately but at a significant computational cost, has motivated the development of several analytical perturbative techniques to avoid a full blown N-body simulation. Lagrangian Perturbation Theory (LPT) [212, 38] works perturbatively

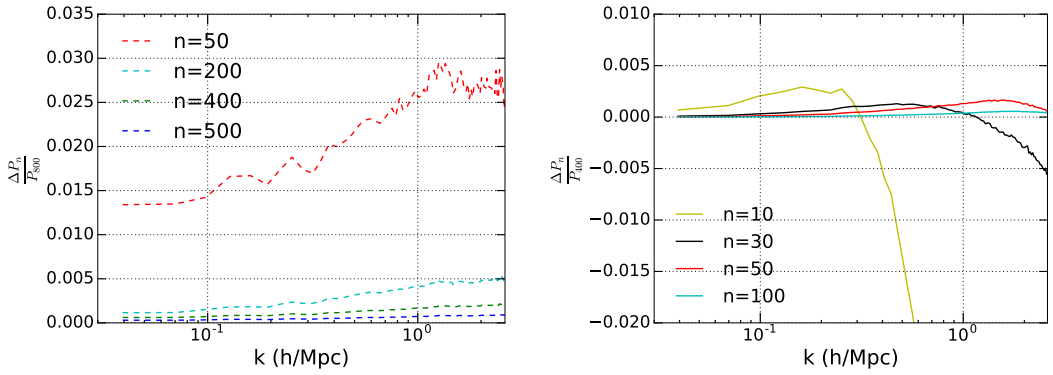

Figure 2.1: The fractional difference between the ΛCDM power spectrum, P_n, for one realization as obtained using different choices of time steps, n, and the high resolution results, P_{800} for PM (left) , and P_{400} for COLA (right), respectively.

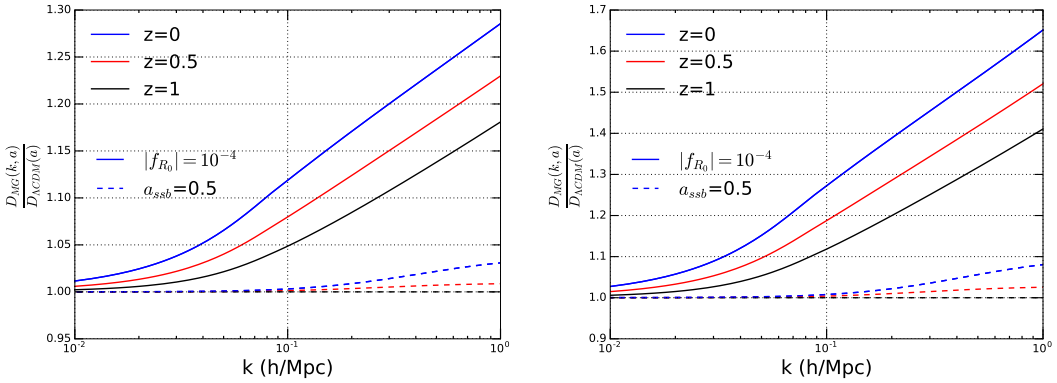

Figure 2.2: The ratio of the 1^{st} (left) and 2^{nd} (right) order growth factors, D_1 and D_2 respective, relative to the ΛCDM growth factor in each case, for the $|f_{R_0}| = 10^{-4}$ model (solid lines) and the symmetron scenario (dashed lines) described in section 3.2.1.

in a Lagrangian displacement field and manages to give accurate results in the Linear and the Mildly Non-Linear regime. However, it quickly fails to capture the non-linearities associated with the smaller scales and consequently it underestimates significantly the power at large k. Given that we have to choose between accurate, but expensive N-body simulations and fast but approximate

perturbative techniques, it is reasonable to ask whether one can efficiently combine the benefits of both approaches. Such a hybrid method, named COmoving Lagrangian Acceleration (COLA) was proposed in [182]. Here we outline the basic framework and its modifications for MG, while details can be found at [182]. The particle comoving positions are decomposed as a sum of two pieces, in the "manifestly" exact form

$$\mathbf{x} = \mathbf{x}_{res} + \mathbf{x}_{LPT} \tag{2.28}$$

By defining a new time variable $d\theta \equiv H_0 \frac{dt}{a^2} = \frac{H_0}{a} d\eta$, where η is conformal time, (2.24) can be cast in the simpler form

$$T^2(\mathbf{x}) = -\frac{a^2}{H_0^2} \nabla_{\mathbf{x}} \Phi_N, \tag{2.29}$$

with $T \equiv \frac{d}{d\theta} = \frac{a}{H_0} \partial_\eta = Q(a) \partial_a$, and $Q(a) = a^3 \frac{H(a)}{H_0}$. In the Lagrangian description $\mathbf{x} = \mathbf{q} + \mathbf{s}(\mathbf{q}, a)$, with $\mathbf{q}$ the initial Eulerian position and $\mathbf{s}$ the Lagrangian displacement and

$$T^2(\mathbf{s}) = -\frac{a^2}{H_0^2} \nabla_{\mathbf{x}} \Phi_N. \tag{2.30}$$

One can now solve for the residual displacement in ΛCDM

$$T^2(\mathbf{s}_{res}) = -\frac{a^2}{H_0^2} \nabla_{\mathbf{x}} \Phi_N - T^2[D_1(a)]\mathbf{s}_1 - T^2[D_2(a)]\mathbf{s}_2, \tag{2.31}$$

where $D_1(a)$ and $D_2(a)$ are the first and second order growth factors, respectively, and $\mathbf{s}_1$, $\mathbf{s}_2$ are the Zel'dovich and second order LPT displacements. The fact that the LPT piece is evolved analytically and we only solve numerically for $\mathbf{s}_{res}$, can be interpreted as working on a frame that is co-moving with observers that follow LPT trajectories.

T can be discretized using a Leapfrog scheme [142] to get the core COLA equations for each particle's position and velocity change between the times

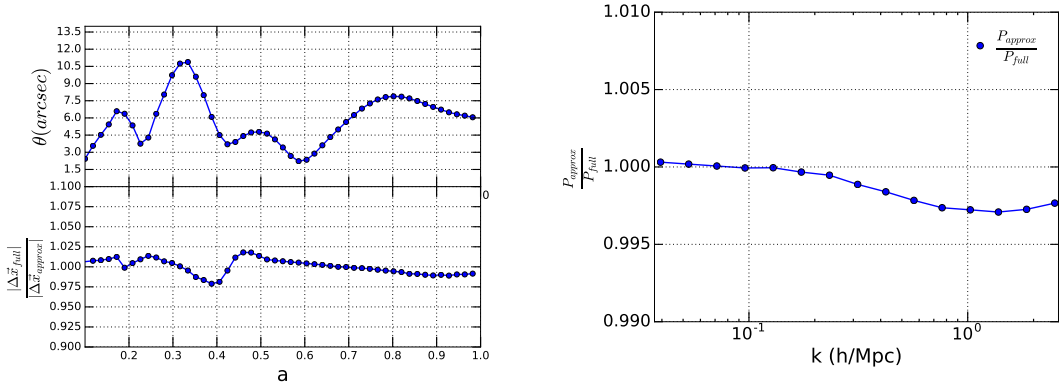

Figure 2.3: Left: Tracking a particle's position throughout the simulation for the exact and approximate hybrid in the $|f_{R_0}| = 10^{-4}$ model. Right: Ratio of the power spectra obtained from the approximate and the exact method for the $|f_{R_0}| = 10^{-4}$ model today.

a_i, a_f

$$
\begin{aligned}
\mathbf{x}(a_f) &= \mathbf{x}(a_i) + \upsilon(a_c)\int_{a_i}^{a_f}\frac{da}{Q(a)} + \\
&+ \Big(\mathbf{s}_1(\mathbf{q},a_f) - \mathbf{s}_1(\mathbf{q},a_i)\Big) + \\
&+ \Big(\mathbf{s}_2(\mathbf{q},a_f) - \mathbf{s}_2(\mathbf{q},a_i)\Big) \\
\upsilon(a_f) &= \upsilon(a_i) - \left(\int_{a_i}^{a_f}\frac{a}{a_c Q(a)}da\right)\times \\
&\left[-1.5\Omega_{m0}a_c\left(\nabla_{\mathbf{x}}\tilde{\Phi}_N(\mathbf{x}) + \frac{\Delta\mathcal{R}_c}{\mathcal{R}_c}\frac{\beta}{M_{Pl}}\nabla_{\mathbf{x}}\tilde{\phi}(\mathbf{x})\right) - \right. \\
&\left. -T^2[\mathbf{s}_1](a_c) - T^2[\mathbf{s}_2](a_c)\right],
\end{aligned}
\tag{2.32}
$$

where a tilde denotes a quantity in units of $1.5\Omega_{m0}H_0^2/a$.

Initial conditions are produced using the 2LPT initial conditions code (2LPTic) [158] which does so by performing LPT up to second order. In a ΛCDM cosmology, growth functions $D_1(a)$ and $D_2(a)$ are scale independent [212, 38] and one only needs to produce an LPT snapshot for $z = 0$ for both generating initial conditions and obtaining the LPT terms at the different timesteps.

In such a case, the LPT displacements are given by $\mathbf{s}_1(\mathbf{q}, a) = D_1(a)\mathbf{s}_1(\mathbf{q}, a_0)$, $\mathbf{s}_2(\mathbf{q}, a) = D_2(a)\mathbf{s}_2(\mathbf{q}, a_0)$ and (2.32) reduces to the standard COLA ΛCDM scheme (with the fifth force term omitted). Initial conditions and background cosmology are produced, for 10 realizations, for the same cosmological parameters as used in the PM code, at the initial redshift z=9.0 which has been shown [182] to work well for COLA in ΛCDM. The simulation box size, number of particles and mesh size are the same as used in the PM code. It should be noted though that we don't perform a comparison of the codes by initiating both with identically seeded initial conditions, but instead, we compare the statistical consistency of the means of the 10 runs for each of the two techniques with the respective sets each using different random generated seeds. In its initial formulation, COLA was used with 10 time steps, which enables accurate predictions down to $k \sim 0.5$ h/Mpc, which can be also seen in Fig. 2.1, where the ΛCDM power spectrum by COLA is presented for various choices of time steps. By increasing the number of steps to 50, still significantly fewer than the typical number of iterations performed in a standard N-body code, we can provide accuracy down to smaller scales, $k \sim 2$ h/Mpc. The ΛCDM COLA run-time in this set up is ~10 times shorter than that of the PM code. COLA's accuracy as a function of the number of time steps used, is further discussed in section 2.3.1.

When gravity is modified, the core equations need to be changed appropriately to account for the additional fifth forces and the screening effects. As in the N-body code, one can use an approximate framework to model the modified gravity effects both on the growth rate and screening: solving the linearized KG equation (2.16) and attaching the screening factor (2.27) to fifth force term in (2.32). For the LPT component of COLA, one must consider that, in MG theories, the growth factors D_1 and D_2 become scale dependent.

In Figure 2.2, we summarize the first and second order growth factors for a chameleon and symmetron scenario. In each case as we approach late times, $z < 2$ for the chameleon model, and $z < 0.5$ for the symmetron, we find significant scale dependent deviations from ΛCDM at the level of 10% for D_1 and 25% for D_2 at k=0.1 h/Mpc today, which means that not all Fourier modes evolve the same way with time [188]. This causes the LPT trajectories of a given particle to bend, in principle. As a consequence one has to be very cautious about how to obtain the LPT terms at the different times. We briefly outline the application of LPT to scale dependent growth functions in MG in Appendix A.

Unlike the ΛCDM case, here the growth factors' scale dependent nature does not allow one to evolve the Zel'dovich and 2^{nd} order displacements with a single scale independent function for all scales. To account for that, we have considered two alternative modifications to COLA. In the first approach, we create an MG version of COLA that calculates the LPT displacements numerically at each time step using an MG version of 2LPTic. The relevant LPT terms in (2.32) are calculated after Fourier transforming (A.13) and (A.14). Besides the modified N-body component, the fact that we have to solve numerically for the Lagrangian terms at every discrete time step increases the computational cost significantly. In a second approach, we utilize the fact that the LPT part of the scheme serves to evolve the linear scales, for which the MG deviations with respect to ΛCDM are known to be small for most times and adopt an approximate scheme in which only the N-body part is modified and the ΛCDM solutions are used for the Lagrangian displacements. The resulting scheme has the same N-body component as in (2.32) and the known ΛCDM LPT terms, in which the Lagrangian

displacements are evolved with $D_{1,\Lambda}(a)$ and $D_{2,\Lambda}(a)$.

$$\begin{aligned}
\mathbf{x}(a_f) &= \mathbf{x}(a_i) + \upsilon(a_c)\int_{a_i}^{a_f}\frac{da}{Q(a)} + \\
&+ \Big(D_{1,\Lambda}(a_f) - D_{1,\Lambda}(a_i)\Big)\mathbf{s}_1(\mathbf{q}, a_0) + \\
&+ \Big(D_{2,\Lambda}(a_f) - D_{2,\Lambda}(a_i)\Big)\mathbf{s}_2(\mathbf{q}, a_0) \\
\upsilon(a_f) &= \upsilon(a_i) - \left(\int_{a_i}^{a_f}\frac{a}{a_c Q(a)}da\right)\times \\
&\left[-1.5\Omega_{m0}a_c\left(\nabla_{\mathbf{x}}\tilde{\Phi}_N(\mathbf{x}) + \frac{\Delta\mathcal{R}_c}{\mathcal{R}_c}\frac{\beta}{M_{Pl}}\nabla_{\mathbf{x}}\tilde{\phi}(\mathbf{x})\right) - \right. \\
&\left. -T^2[D_{1,\Lambda}](a_c)\mathbf{s}_1(\mathbf{q}, a_0) - T^2[D_{2,\Lambda}](a_c)\mathbf{s}_2(\mathbf{q}, a_0)\right].
\end{aligned} \tag{2.33}$$

A comparison of the two approaches for the $f(R)$ model with $\left|f_{R_0}\right| = 10^{-4}$, for which we expect the largest modifications, is shown in Fig. 2.3. One comparison tracks a given particle inside our volume during the simulation and we also compare the resulting power spectra using both schemes. We find excellent agreement between the approximate and fully modified schemes, in both the linear and mildly non-linear regimes. We also find very small differences for the position and displacement vectors (magnitude & direction) with differences in angular orientation of at most 11 arcseconds, and differences in the magnitude of steps less than $2,5\%$, which result in power spectra that have a fractional difference no larger than 0.3% today. The approximate scheme takes under half the run time of the full implementation. In light of these results, we adopt the approximate scheme in the COLA simulations used in this analysis. This has the great advantage of not having to solve numerically for the LPT displacements at every time step, without sacrificing much accuracy.

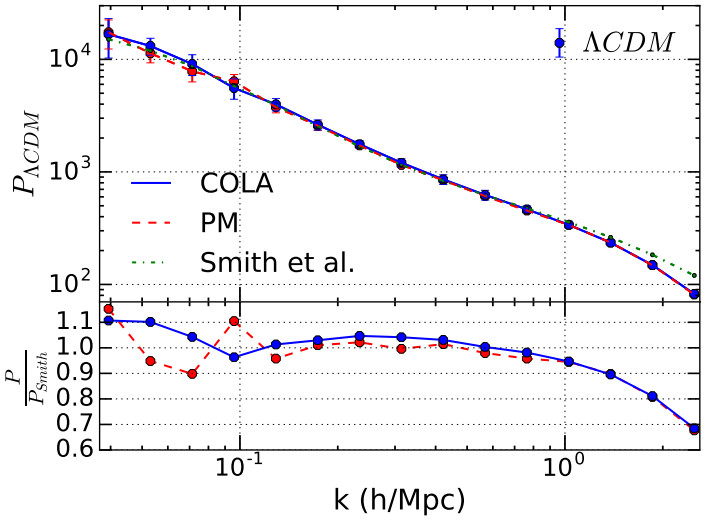

Figure 2.4: [Top] Power spectra benchmarking for ΛCDM with the PM N-body code [red dashed line] and COLA method [blue full line]. The nonlinear power spectrum fit developed by Smith et al. [green dotted line] is also shown for comparison. [Bottom] Ratio between both the COLA and PM code ΛCDM results above to the fit by Smith et al. The number of time steps used for COLA and PM is 50 and 500, respectively.

2.3 Analysis/Results

2.3.1 Modified gravity results

In this section we present the results of the assessment of COLA's performance with respect to the predicted power spectra, redshift space distortions (RSD) and dark matter halos for the modified gravity scenarios and ΛCDM. For every given model and choice of parameters, simulations have been performed using both COLA and the PM code.

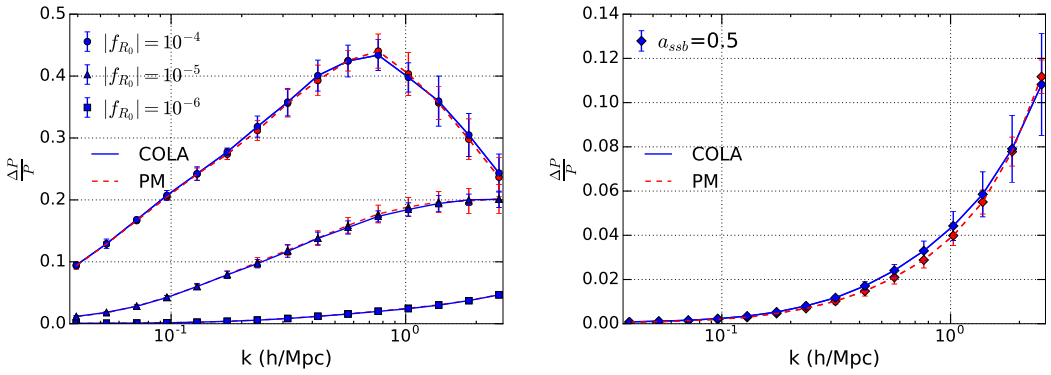

Figure 2.5: Fractional difference in the CDM power spectra for the MG scenario relative to the ΛCDM model, $\frac{\Delta P}{P_{\Lambda CDM}}$, at $a = 1$, for the same initial conditions for [left] the $f(R)$ scenario, for $f_{R_0} = 10^{-4}, 10^{-5}$ and 10^{-6}, and [right] the symmetron model with $a_{ssb} = 0.5$. The averaged results, and standard deviations, from the simulations with the PM code [red dashed line] and the COLA code [blue full] are presented in each case. The number of time steps used for COLA and PM is 50 and 500, respectively.

Power spectra

To appropriately benchmark the COLA performance for modified gravity, we first compare the performance of COLA for ΛCDM. In Fig. 2.4, we show the ΛCDM power spectra as obtained by both codes, together in comparison with the fit by [171]. The two results agree well within a standard deviation of each other for all scales, but start to, underestimate power, consistently with one another, by $k \sim 2$ h/Mpc, relative to higher resolution simulations. For that reason, we choose to compare performance down to a scales with $k = 2.5$ h/Mpc, while the Nyquist wavenumber, for our simulation, is $k \sim 4$ h/Mpc.

In Fig. 2.5, the fractional difference in the power spectra is plotted for all our models and both codes are found to agree with each other well within one standard deviation, with the differences being smaller than 1%. Our results

demonstrate the consistency between COLA and the N-body approach using the approximate scheme. In turn this connects with previous work that has shown, in general, the good degree of consistency of this approximate scheme with N-body simulations using the full Klein Gordon for the same models in the literature [213, 55, 39, 207]. In particular the results for the $\left|f_{R_0}\right| = 10^{-5}$ & $\left|f_{R_0}\right| = 10^{-6}$ models are in excellent agreement with the literature for all scales. Our results confirm findings in [207], in studying the effectiveness of the linearized screening schema: for the lowest screening $f(R)$ model, with $\left|f_{R_0}\right| = 10^{-4}$, and the symmetron model the effective screening parameterization, respectively, under and overestimates the power, relative to the full KG simulation, at the non-linear scales.

Fig. 2.6 shows our COLA scheme's accuracy in predicting the fractional difference in the power spectra for the highest deviation model, $\left|f_{R_0}\right| = 10^{-4}$, as a function of the number of time steps used, for one realization. We find that using 50 time steps provides excellent convergence, at the level of 0.9%, to the scales we want to consider, $k \sim 2$ Mpc/h. Using 30 time steps provides convergence at the level of 8% at $k \sim 2$ Mpc/h.

Redshift space distortions

A great amount of observational effort is being invested in studying the three-dimensional Large Scale Structure (LSS) through spectroscopic galaxy surveys that measure precise redshifts. Among various challenges faced by such measurements, the observed clustering structures appear distorted in redshift space.

Density perturbations give rise to peculiar velocities with respect to the Hub-

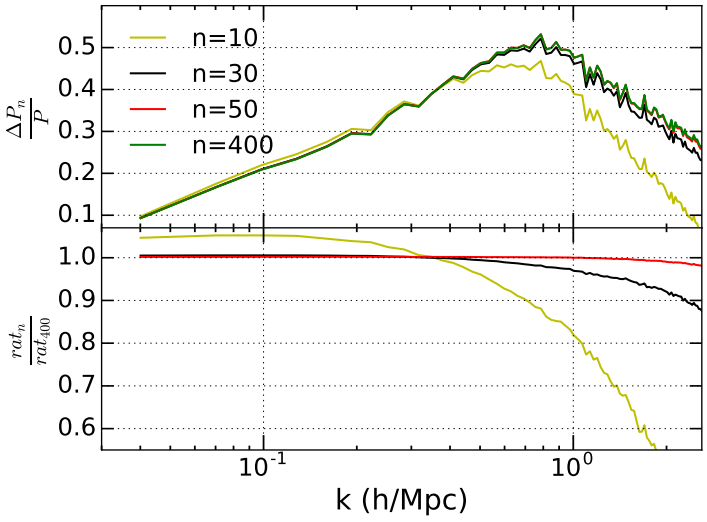

Figure 2.6: [Top] Fractional difference in the CDM power spectra for the $|f_{R_0}| = 10^{-4}$ scenario relative to ΛCDM for one realization, as obtained by COLA using various choices of time steps. [Bottom] Ratio of the fractional difference $rat_n = \left(\frac{\Delta P}{P}\right)_n$ for each choice to the high resolution result using 400 steps, rat_{400} .

ble flow, which result in the redshift space position $\mathbf{r}_s$, being different than the real space position $\mathbf{r}_r$, with the relationship between them taking the form

$$\mathbf{r}_s = \mathbf{r}_r + \frac{\mathbf{v}\cdot\hat{\mathbf{n}}}{H_0}\hat{\mathbf{n}}. \tag{2.34}$$

By $\mathbf{v}$ we denote the peculiar velocity and by $\hat{\mathbf{n}}$ the unit vector along the line of sight. At linear scales, coherent motions of galaxies that tend to collapse within an overdense region, cause it to appear squashed in redshift space. As shown by [87], in the distant observer approximation, such an overdensity will be distorted in the redshift space:

$$\delta_s(\mathbf{k}, a) = \left(1 + f\mu^2\right)\delta_r(\mathbf{k}, a), \tag{2.35}$$

where μ is the angle between the peculiar velocity and the line of sight in k

space, $\hat{\mathbf{k}}$, and f the linear growth rate,

$$f_g(a) = \frac{d \ln D_1(a)}{d \ln a}, \tag{2.36}$$

with subscript 'g' to differentiate it from the $f(R)$ function. Such an effect gives rise to, based on (2.35), an overestimation of the power spectrum measured in the redshift space:

$$P_s(k, \mu, a) = \left(1 + \beta_g \mu^2\right)^2 P_r(k, a), \tag{2.37}$$

where we introduced the factor $\beta_g = f_g/b$ (not to be confused with the coupling β) to account for the galaxy bias b, with $b = 1$ for cold dark matter. Averaging (2.37) over all directions, gives the 0^{th} order piece

$$P_s(k, a) = \left(1 + \frac{2}{3}\beta_g + \frac{1}{5}\beta_g^2\right) P_r(k, a). \tag{2.38}$$

At smaller, non-linear, scales the random incoherent velocities of galaxies within virialized structures cause overdense regions to appear elongated along the line of sight ("Fingers of God"), causing suppression of power. An exact quantitative treatment of the phenomenon is hard, due to the complicated nature of the small-scale velocity correlations and as a result phenomenological approaches have been proposed. Such models [134] treat the line-of-sight distortion as a radial convolution of the correlation function ξ_r (including the Kaiser boost) with an incoherent velocity distribution $f(v)$

$$\xi_s(r_\perp, r_\parallel) = \int_{-\infty}^{\infty} \xi_r(r_\perp, r) f(r_\parallel - r) dr, \tag{2.39}$$

where $r_\perp$ and $r_\parallel$ are the perpendicular and parallel components. Assuming a Gaussian velocity distribution [134], the Fourier space expression would then be

$$P_s(k, \mu, a) = P_r(k, a)\left(1 + \beta_g \mu^2\right)^2 \exp(-k^2 \mu^2 \sigma_{com}^2) \tag{2.40}$$

with σ_{com} being the comoving distance dispersion that is related [200] to the velocity dispersion σ_p through

$$\sigma_p = aH(a)\sigma_{com} \tag{2.41}$$

Even though the exponential term in (2.40) is reasonable as a damping term for capturing the non-linear power suppressions, it has been noted [56] that an exponential pairwise velocity distribution

$$f(v) = \frac{1}{\sqrt{2}\sigma_p} \exp(-\sqrt{2}|v|/\sigma_p) \tag{2.42}$$

is a better fit. This gives rise to the dispersion model [132]

$$P_s(k,\mu,a) = \left(1+\beta_g\mu^2\right)^2 P_r(k,a) \left(\frac{1}{1+\frac{1}{2}k^2\mu^2\sigma_{com}^2}\right), \tag{2.43}$$

in which the damping effects are incorporated through a Lorentzian term and σ_{com} (or σ_p) is considered a free parameter to be fitted to the data. It should be noted that σ_p is actually scale and bias dependent, which is one of the limitations the dispersion model faces [159]. The above description can still prove to be a very useful tool for obtaining an effective non-linear velocity dispersion parameter and thus quantifying the non-linear FoG effect. Integrating (2.43) over all directions gives the monopole piece, which can be fitted over the results to obtain σ_p. This is slightly different than other approaches: [10] proposed attaching a simple factor $\frac{1}{1+k^2\sigma^2}$ to the Kaiser boost with σ being a free parameter, loosely related to σ_p, while [100] suggested attaching a free function $F(k,\mu) = \frac{A}{1+Bk^2\mu^2} + Ck^2\mu^2$ and marginalized over the parameters A, B and C for to account for the uncertainties in constraining the effects of modified gravity on the RSD power spectrum.

Through the mapping (2.34), we obtained redshift space power spectra for all of the simulated models, with the results presented in Fig.2.7. We compared

Scenario	Analytic prediction			$\sigma_p(km/s)$
	P_{rsd}/P_{real}	f_g	γ_{eff}	
ΛCDM	1.35	0.462	0.556	567
$f(R), \left\|f_{R_0}\right\| = 10^{-6}$	1.35	0.463	0.555	605
$f(R), \left\|f_{R_0}\right\| = 10^{-5}$	1.38	0.491	0.512	714
$f(R), \left\|f_{R_0}\right\| = 10^{-4}$	1.42	0.541	0.443	834
Symmetron	1.35	0.464	0.554	611

Table 2.1: Analytic predictions for the RSD to real space power spectrum ratios, P_{rsd}/P_{real}, CDM growth rates, $f_g \equiv dlnD_1(a)/dlna$, and the equivalent growth exponent, $\gamma_{eff} = dlnf_g/dln\Omega_m(a)$, are evaluated at $k = 0.05h/Mpc$. The effective velocity dispersion values, σ_p are obtained by fitting the average power spectrum results to the monopole of the RSD suppression function in (2.43).

the large scale results to analytic predictions arising from the linear growth rate, and also used the monopole model in (2.43) to obtain an effective velocity dispersion damping factor for the FoG effect. The results are summarized in Fig. 2.7 and Table 4.1.

We first benchmarked COLA's performance for ΛCDM. We see that the PM and COLA codes' RSD predictions for ΛCDM do not differ by more than 0.5% at all the scales of interest and agree remarkably well with the analytical prediction, with expected values of $f_g(a = 1)$=0.467 and $\frac{P_s(k)}{P_r(k)}$=1.354, assuming $f_g = \Omega_m(a)^\gamma$, with $\gamma = 0.55$. At smaller scales , the "Fingers of God" effect quickly dominates, and causes power suppression and find this suppression is well modeled by (2.43) with $\sigma_p = 567\ km/sec$.

For the MG models, the additional fifth forces cause the redshift space power spectra to have, in principle, different shapes. In large scales, the enhanced clustering results in higher coherent velocities of collapse into overdense regions which translates to a higher boost in the RSD power spectra with respect to GR,

translating into higher values for the growth rate and a lower γ. For lower magnitude modifications, the suppression of the fifth forces gives results that tend to the ΛCDM prediction. At smaller scales, the fifth forces cause higher random velocity dispersions inside virialized structures, making the damping effects stronger in MG.

These combined effects cause the redshift space distortions to be more pronounced in MG compared to GR. This can be clearly seen in the upper left panel in Fig.(2.7). As expected, the redshift space distortions vary from the most pronounced, in the lowest screening model, to very small deviations from GR in the strong screening regime. For the same models, the redshift space power spectra from the PM code agree with COLA well within a standard deviation. The results using the approximate schema are in good agreement with full non-linear MG N-body simulations for redshift space distortions in $f(R)$ gravity performed by [85]. For all the models, COLA predicts deviations that are 0.5% more pronounced (higher in large scales, smaller in small scales) than the PM code.

Halo Mass Function

To determine the halo mass function we identify halos in the simulations using the Rockstar halo finder [25] for all models. In Fig. 2.8 we show the comparison of the halo mass function predicted by COLA and the PM code, together with a high accuracy result by [126]. COLA and PM are found to be in a better than 2.5% agreement in the lower and intermediate mass range, while in the highest mass bins there is a maximum difference of 10%.

In Fig. 2.9, we plot the fractional difference in the halo mass function with

respect to ΛCDM, for all of our models. The COLA and PM code results agree in general, well within the standard deviation from the averaged suite of simulations. In particular, In the $|f_{R_0}| = 10^{-4}$ and $|f_{R_0}| = 10^{-5}$ models, the PM code predicts a fractional boost in the halo mass function that is higher than COLA's by < 2% and 2.5%, for the lower and intermediate bins, while in the highest bin COLA gives a boost larger by 5% and 3% correspondingly. For the $|f_{R_0}| = 10^{-6}$ and symmetron models, the differences are 1% and smaller, with the PM code giving greater number counts for the two mass bins below $10^{14} M_{\odot}/h$ and COLA being higher for the bin over $10^{14} M_{\odot}/h$. The differences between the predictions in each case and especially in the high mass bin, are within, and likely largely resulting from, the differences observed in the ΛCDM benchmarking of the mass functions.

While we do not perform a simulation with the full non-linear Klein-Gordon equation, we note that compared to other full KG treatments in the literature [207, 213], our method performs well and only slightly underestimates the mass function for the $|f_{R_0}| = 10^{-4}$ & $|f_{R_0}| = 10^{-5}$ models, in accordance with the general features noticed in the power spectra discussion. In agreement with [207], we observe an underestimation of halos in the lower end of our mass range (around M $\sim 10^{13} M_{\odot}/h$) for the $|f_{R_0}| = 10^{-6}$ model, indicating too much screening, and an overestimation of the mass function for the symmetron model.

2.4 Conclusions

In this chapter, we have implemented a hybrid scheme, that combines Lagrangian Perturbation Theory and N-body approaches, to numerically charac-

terize the evolution of large scale structure in chameleon and symmetron, modified gravity theories which exhibit gravitational screening in the non-linear regime. LPT is used to evolve linear scales analytically in combination with a full N-body approach that is used for the non-linear scales to reduce computational costs. An effective screening scheme is implemented in place of a solution to the full Klein-Gordon equation for the fifth potential, in which an effective suppression factor is attached to the real-space linearized perturbations.

We demonstrate that while in MG spatial modes evolve differently in LPT (and can have deviations from the nominal GR geodesic paths), the scheme can be further simplified, for the models we studied, by using a displacement coordinate system based on scale-independent ΛCDM growing modes combined with a modified, screened Poisson equation. We note that, while this approximate scheme works well for the chameleon and symmetron models we consider, it should always be tested against the exact LPT solution for a new modified gravity model.

Our method was applied on the $f(R)$ and symmetron models and it was tested against power spectra, redshift space distortions and dark matter halo mass functions, using a fiducial number of 50 time steps. At the same time, we assessed our hybrid's performance against simulations from a pure N-body code with the same screening implementation for the same models, using 500 iterations.

With regards to power spectra, we found COLA to be in better than 1% agreement with the N-body code at all scales for all the models studied. Note that the effective screening scheme we use has previously been shown to be in good agreement with results using the full non-linear Klein Gordon in an

N-body implementation [207]. We find, as was discussed in [207], that the effective screening approach does underestimate power, relative to that found in solving the full Klein-Gordon [213], as one moves into the fully non-linear regime ($k >\sim 2Mpc/h$), however this is also beyond the regime of applicability of COLA's scheme.

COLA and the N-body code are in better than 0.5% agreement with respect to redshift space distortions for all the scales and models of interest. The distortions were modeled by attaching the linear Kaiser factor for the enhancement at large scales and a Lorentzian dispersion factor for the small scale suppression due to incoherent motions within virialized structures. We find that the monopole is a well fit using an effective pairwise velocity dispersion as a fitting parameter to quantify the suppressions at non-linear scales. The additional fifth forces present in the chameleon and symmetron models, cause the redshift space distortions to be more pronounced with respect to ΛCDM. This can be seen by the larger boosts in linear scales due to the higher coherent velocities, and by the stronger suppressions in the non-linear scales because of the higher values of the velocity dispersion. The adapted COLA scheme gives reasonable results for the predicted fractional boost in the halo mass function relative to ΛCDM, with the differences between the N-body and COLA results in the halo mass function estimation most likely being due to the difference between the two codes in ΛCDM.

In this chapter, we have focused on chameleon and symmetron-type scalar-tensor theories, but it would be very interesting to see how well this scheme performs for the simulation of other screening mechanisms as well such as the Vainshtein mechanism [187], as well as other dark energy models, such as those

with non-minimal couplings between dark matter and a quintessence scalar field [108]. Given the level of consistency between COLA and the N-body predictions for the monopole of the redshift power spectrum, it would also be interesting to investigate the COLA scheme's ability to capture higher order moments of the angular power spectrum to, for example, calculate the ratio of the quadrupole to monopole moments to estimate β_g in a way that is robust to systematic effects from incomplete modeling of the nonlinear distortions [103, 85].

Many theories being considered as explanations for cosmic acceleration have tantalizing predictions in the non-linear regime but also present computational challenges in modeling them. With a suite of next-generation large scale structure surveys, including LSST, DESI, Euclid and WFIRST, starting in next few years, there is an unprecedented opportunity to measure the properties of large scale structure clustering as it transitions from linear to mildly and then strongly non-linear scales, and using multiple tracers. The results presented here demonstrate that COLA, proposed to enable accurate and efficient, non-linear predictions for ΛCDM, is a viable approach to study non-linear collapse for a broader portfolio of cosmological scenarios. For example, in a paper that has followed our work in [208], the effectiveness of the COLA approach has also been studied in the $f(R)$ and nDGP models, and was shown to perform very well in predicting the fractional deviations with respect to the ΛCDM power spectra and halo mass functions, using a small number of time steps.

2.5 Acknowledgments

We want to thank Hans Winther and Pedro Ferreira for useful comments on this line of work and also Risa Wechsler for helpful discussions on halo mass function performance with the COLA algorithm. We would also like to thank an anonymous referee, whose valuable comments helped improve improve the quality of this work during the peer review process.

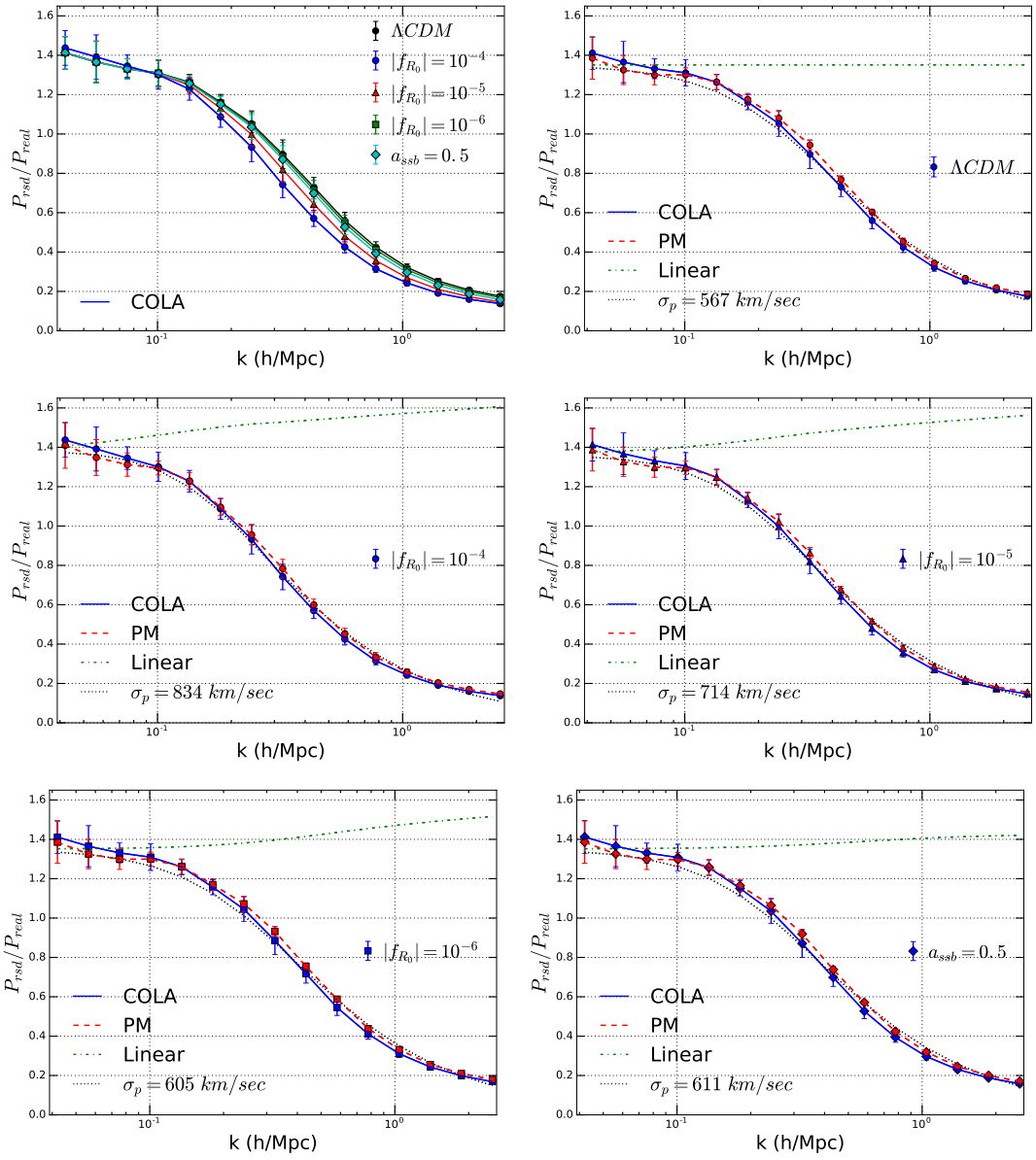

Figure 2.7: The ratio of the redshift space power spectrum, P_{rsd}, to the real space equivalent, P_{real}, for the different models. [Top left] A side-by-side comparison of the suppression of the redshift space clustering by non-linear velocity correlations for the COLA model for ΛCDM [black], $f(R)$ models with $f_{R_0} = 10^{-4}, 10^{-5}$ and 10^{-6} [blue circle, red triangle and green square, respectively], and the symmetron model with $a_{ssb} = 0.5$ [cyan diamonds]. The remaining plots show the comparison of PM [red dashed line] and COLA code [blue full] predictions for the RSD to real space power spectrum ratio for each model in turn: [top right] ΛCDM, [middle left] $f_{R_0} = 10^{-4}$, [middle right] $f_{R_0} = 10^{-5}$, [bottom left] $f_{R_0} = 10^{-6}$, [bottom right] symmetron.

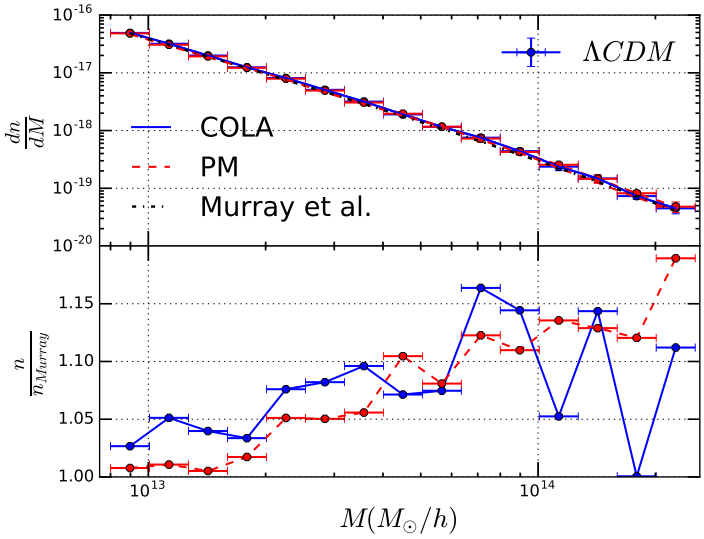

Figure 2.8: Halo mass function benchmarking for Λ*CDM* with the PM N-body code [red dashed line] and COLA method [blue solid line]. The halo mass function fit developed by Murray et al. [black dotted line] is also shown for comparison. The number of time steps used for COLA and PM is 50 and 500, respectively.

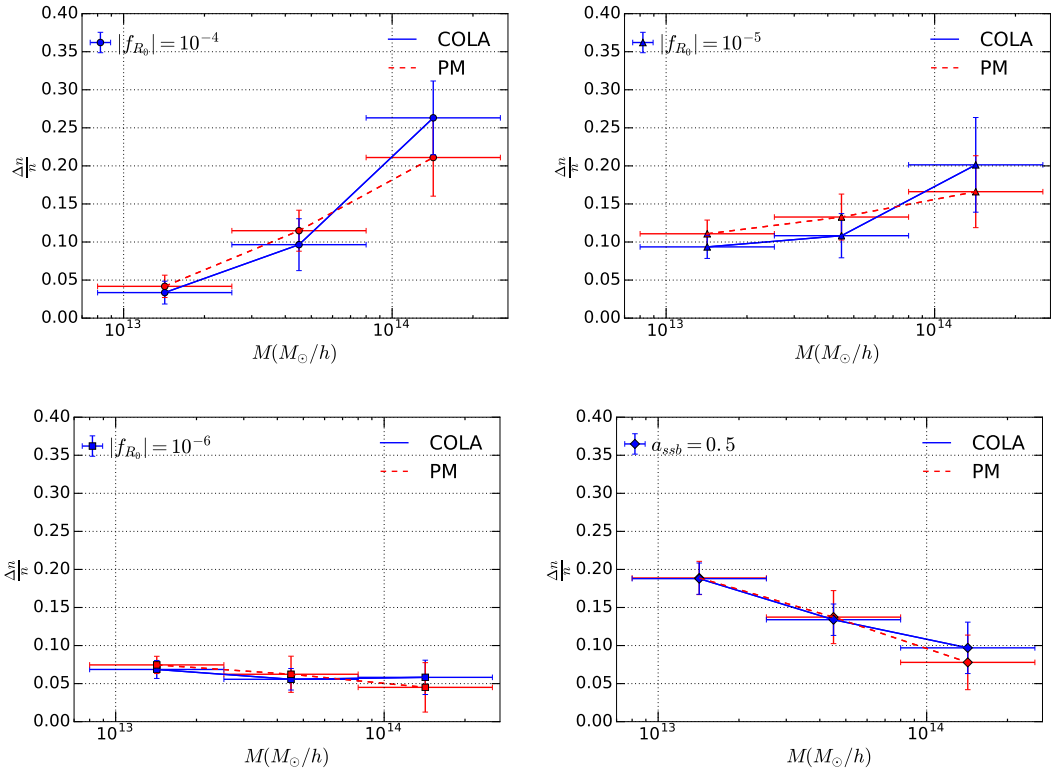

Figure 2.9: Fractional difference in the CDM halo mass function, $n(M)$, for halos of mass M, at $a = 1$, for each MG scenario relative to the ΛCDM model, for the same initial conditions: [left] the $f(R)$ scenario, for $f_{R_0} = 10^{-4}, 10^{-5}$ and 10^{-6}, and [right] the symmetron model with $a_{ssb} = 0.5$. The averaged results, and standard deviations, from the simulations with the PM code [red dashed line] and the COLA code [blue solid line] are presented in each case. The number of time steps used for COLA and PM is 50 and 500, respectively.

CHAPTER 3

BEYOND δ: TAILORING MARKED STATISTICS TO REVEAL MODIFIED GRAVITY.

3.1 Introduction

As we have already seen in the previous chapter, models that seek to explain cosmic acceleration through modifications to General Relativity (GR) evade stringent Solar System constraints through a restoring, screening mechanism. Screening, while essential for a mechanism's viability, also greatly suppresses the modified gravity signals in the high density regions, which dominate the power spectrum signal, making their detection particularly challenging even for the ambitious future surveys of the LSS. This has motivated the consideration of density transformations that up-weight the lower density regime in favor of the higher, screened densities, so as to enhance MG signals in a density-dependent way. Penalizing the higher densities to increase the amount of information encoded in the 2-point statistics of cosmological density fields has been a valuable strategy even in the context of ΛCDM considerations. A logarithmic transform of the density field [128, 199, 49], makes the field more Gaussian allowing the recovery of more information from the 2-point function. Clipping the very high densities [168, 169] has also been found to produce similar beneficial effects. In the context of MG, clipping the screened densities [116] allows better discrimination between MG and GR, while in [114] a new generalized restricted logarithmic transform was found to boost signals.

In this work, we investigate the performance of a new density transformation that up-weights the significance of lower densities and was first proposed

in [204], both as a simple density transformation and as a marked correlation function. We find such a function to provide discriminatory power between MG and GR and to increase the Fisher information significantly. Furthermore, we perform a systematic comparison of the performance of these various transformations and discuss our approach in the context of related work in the literature. The line of work discussed below has been published in [190].

The organization of this chapter is as follows: in Sec. 3.2 we first review the MG models studied, the simulation data used and the different density transformations considered. In Sec. 3.3 we present our results, assessing the performance of the different functions, before concluding and discussing future work in Sec. 3.4.

3.2 Formalism

3.2.1 Modified gravity models

The most general form of a Lagrangian that describes ghost-free scalar-tensor extensions to GR is of the known Horndeski form [80, 58]. If by M_{Pl} we denote the reduced planck mass $M_{Pl} = \frac{m_{Pl}}{\sqrt{8\pi G}}$, by R the Ricci scalar, and by $\mathcal{L}_m$ the matter sector component with fields ψ_m that possess non-minimal coupling to the scalar field ϕ, the Einstein frame form of such a Lagrangian is

$$\mathcal{L} = \frac{M_{Pl}^2}{2} R + \mathcal{L}(\phi, \partial_\mu \phi, \partial_\mu \partial^\mu \phi) + \mathcal{L}_m(e^{2\beta(\phi)\phi/M_{Pl}} g_{\mu\nu}, \psi_m). \tag{3.1}$$

The particular subclass that contains the screening mechanisms considered here, the chameleons and the phenomenologically similar symmetrons, corresponds

to a scalar field Lagrangian of the form

$$\mathcal{L} = -\frac{1}{2}(\nabla\phi)^2 - V(\phi). \tag{3.2}$$

The conformal coupling to matter, expressed through the dimensionless coupling constant $\beta(\phi)$, gives rise to an effective potential

$$V_{eff} = V(\phi) + \frac{e^{\beta\phi/M_{pl}}\rho_m}{M_{Pl}}, \tag{3.3}$$

which consists of the self-interaction potential $V(\phi)$ and a matter dependent component. The qualitative features of the particular screening mechanism are incorporated into the interplay between these two components. In the chameleon screening, $V(\phi)$ is of runaway form and in high densities the field settles down to a minimum of V_{eff}, becomes very massive and decouples. In the symmetron model, on the other hand, the interaction potential is of the "Mexican hat" symmetry breaking form [77], which additionally generates a density-dependent coupling. In low-density regions, spontaneous symmetry breaking allows coupling to matter, while in high-density environments the symmetry is restored, the coupling to matter vanishes and GR is recovered.

The $f(R)$ model

Adding a non-linear function of the Ricci scalar R to the String-frame expression of the Einstein-Hilbert action, has been shown to produce cosmic acceleration, making the so-called $f(R)$ theories [48] widely-studied modified gravity models. Here we consider the Hu-Sawicky $f(R)$ model [81], which can be incorporated [43] into the chameleon screening formalism with $\beta = 1/\sqrt{6}$ and is usually parametrized as

$$f(R) = -m^2\frac{c_1\left(R/m^2\right)^n}{c_2\left(R/m^2\right)^n + 1}, \tag{3.4}$$

where $m = H_0\sqrt{\Omega_{m0}}$, is a characteristic mass scale determined by the the Hubble Constant H_0, and Ω_{m0}, the matter fractional energy density today. The additional requirement of matching the ΛCDM background expansion dictates that $\frac{c_1}{c_2} = 6\frac{\Omega_{\Lambda 0}}{\Omega_{m0}}$ and the two final free parameters of the model are $\bar{f}_{R_0} = \frac{df(R)}{dR}\Big|_{z=0}$ and n, with

$$\bar{f}_{R_0} = -n\frac{c_1}{c_2^2}\left(\frac{\Omega_{m0}}{3(\Omega_{m0}+\Omega_{\Lambda 0})}\right)^{n+1}. \tag{3.5}$$

By $\Omega_{\Lambda 0}$ above we denote the dark energy fractional energy density today. Finally, within this formulation the characteristic model-dependent mass takes the form

$$m(a) = \frac{1}{2997}\left(\frac{1}{2|\bar{f}_{R_0}|}\right)^{\frac{1}{2}}\frac{\left(\Omega_{m0}a^{-3}+4\Omega_{\Lambda 0}\right)^{1+\frac{n}{2}}}{\left(\Omega_{m0}+4\Omega_{\Lambda 0}\right)^{\frac{n+1}{2}}}[Mpc/h]. \tag{3.6}$$

In this work, we will consider models that correspond to $n = 1$ and $\left|\bar{f}_{R_0}\right| = \{10^{-6}, 10^{-4}\}$, that correspond to representative choices of a weak and a strong modification choice respectively.

The symmetron model

The free parameters of the symmetron model presented previously, are the scale factor at which symmetry breaking occurs, a_{ssb}, the force length range $\lambda_{\phi 0}$ and the coupling parameter β_0. The characteristic coupling and mass take the form

$$\begin{aligned}\beta(a) &= \beta_0\sqrt{1-\left(\frac{a_{ssb}}{a}\right)^3}\\ m(a) &= \frac{1}{\lambda_{\phi 0}}\sqrt{1-\left(\frac{a_{ssb}}{a}\right)^3}\end{aligned} \tag{3.7}$$

We study the model with the choice of values $a_{ssb} = 0.5$, $\lambda_{\phi 0} = 1Mpc/h$ and $\beta_0 = 1$ for the free parameters, which represents a viable, realistic candidate based on the current experimental constraints.

N-body Simulations

In order to produce accurate realizations of the LSS for a wide range of scales, analytical considerations are inadequate due to the non-linear nature of the collapsed structures and as a result we have to resort to full blown N-body simulations. In the case of MG scenarios, the situation is further complicated by the need to accurately capture the screening effects, which are fundamentally incorporated in the non-linearities. In this chapter, we use $z = 0$ density snapshots that have been produced in CDM N-body simulations presented in [189]. The simulations were performed using a suitably modified version of A. Klypin's PM code [95], in which the MG screening was captured effectively through the attachment of a phenomenological thin shell factor to the fifth force term [207]. The simulations were initialized at an initial redshift of $z_i = 49$, for 40 random initial seeds, for a background ΛCDM cosmology that corresponds to $\Omega_{\Lambda 0} = 0.75$, $\Omega_{m0} = 0.25$, $\sigma_8 = 0.8$, $n_s = 1.0$ and $h = 0.7$. The simulation box side L and number of particles used N_p were L=200 Mpc/h and $N_p = 256^3$ respectively, while the density was resolved in a 512^3 grid using the Cloud-In-Cell (CIC) assignment scheme. More details on the specifics of the simulations and the screening implementation can be found at [189].

3.2.2 Density transformations

The fundamental quantity of interest in our analysis, is the fractional cold dark matter over-density $\delta(\mathbf{x}, a)$, which is defined as

$$\delta(\mathbf{x}, a) = \frac{\rho_m(\mathbf{x}, a)}{\bar{\rho}_m} - 1, \tag{3.8}$$

with a the scale factor, $\rho_m(\mathbf{x}, a)$ the matter density in each grid cell and $\bar{\rho}_m$ the mean density at the cosmological time considered (which is $a = 1$ for our analysis).

Using the CIC interpolation scheme, the density field, δ, from each snapshot is reconstructed on a 256^3 resolution Cartesian grid and is then projected onto three orthogonal 2D planes that correspond to the 3 independent Cartesian axes. Through this process, the 40 random seeds initially produced for each model, generate 120 independent realizations. We find that 2D projections are significantly better for considering the transformations than the 3D density fields, sampled in the initial 256^3 snapshots, because the 3D cells, when up- and down- weighted with the transformation, are more sensitive to the sparse sampling and shot noise. The 3D cell size, which is an arbitrary choice, that corresponds to this choice of parameters, is equal to $0.5 \left(\frac{Mpc}{h}\right)^3$. This choice of cell volume was found to provide the best combination of low shot noise and high resolution.

Through a specific transformation, a new field $\delta' = f(\delta)$ can be constructed, with the aim of enhancing the amount of information that can be extracted. In the following section, we briefly introduce the various density transformations investigated in this chapter and focus on the key aspects that will be relevant to our analysis.

Logarithmic transformation

The non-linearities in the dark matter power spectrum have been shown [128, 199, 49] to become significantly smaller, and the amount of carried in-

formation significantly greater, in terms of signal-to-noise, when the fractional matter over-density undergoes a transformation

$$\delta' = \ln(\delta + 1)\,. \tag{3.9}$$

Besides restoring the linear character of the power spectrum, down-weighting screened regions through a logarithmic mapping [116, 114] can serve to enhance the predicted power of MG signals.

After such a mapping is performed, a large-scale multiplicative bias, b_{log}, develops [146] between the power spectra of the original and transformed fields, as given by

$$P_{\ln(1+\delta)}(k) = \frac{\sigma^2_{\ln(1+\delta)}}{\sigma^2_{\delta}} P_{\delta}(k) = b^2_{log} P_{\delta}(k), \tag{3.10}$$

with (3.10) being valid as $k \to 0$ and where σ^2 denotes the variances of the density fields, as calculated by integrating over the corresponding power spectra. Predicting the developed multiplicative bias, as has been also performed through other expressions proposed in [128, 209], will be particularly useful in interpreting the large-scale behavior of ratios of transformed fields in section 3.3, when compared to the ratios of standard power spectra. Measuring ratios of transformed-density power spectra could, however, be performed directly, without requiring knowledge of the ordinary power spectrum or biases with respect to it. It should be noted here, that we calculate $\sigma^2_{\ln(1+\delta)}$ through a direct integration of the logarithmic power spectrum over a top-hat filter, rather than making use of the phenomenological formula proposed in [146].

Clipped transformation

Another transformation that reduces the contribution of higher over-densities, for the sake of maximizing the extraction of cosmological information from the up-weighted, less dense regions, is clipping [168, 169, 116]. In this procedure, all densities higher than a desired threshold δ_0 are truncated to form a new distribution:

$$\delta' = \delta_c = \begin{cases} \delta & \text{if } \delta < \delta_0 \\ \delta_0 & \text{if } \delta > \delta_0. \end{cases} \tag{3.11}$$

After (3.10) is applied, the new density field is "renormalized" using the new mean density of the distribution, in order to ensure that $\langle \delta' \rangle = 0$, which was proposed in [168] to get results that are rather insensitive to the choice of the threshold. In our analysis we found such a prescription to perform slightly better in terms of the Fisher information, compared to when the density field is not "renormalized", and so this is the one adopted. Just like the logarithmic transform, clipping enhances the extracted signals not only in ΛCDM, but also in MG, by emphasizing on regions not subject to screening.

Similar to the result of (3.10), the response of the density power spectrum to clipping on linear scales can be calculated [169] by

$$P_c(k) = \frac{\sigma_c^2}{\sigma_{\delta_c}^2} P_\delta(k), \tag{3.12}$$

where $P_c(k)$ is the power spectrum of a clipped field δ_c, and the variances are again given by integrating the power spectra. The validity of (3.12) can, if desired, be extended into the mildly non-linear regime after the introduction of perturbative one-loop contributions [169].

Given that the value of δ_0 itself is dependent on the details of each simula-

tion, the fraction of cells clipped is a more easily transferable descriptor and so this is the one we will report.

Marked transformation

The use of density-dependent marks has been explored in the context of breaking degeneracies in halo occupation distributions [205], and as a probe of identifying MG signatures in the LSS [204].

In this work, we consider an analytical function as a means of re-weighting the density field,

$$\delta' = m(\delta) = \left(\frac{\rho_* + 1}{\rho_* + \rho_m}\right)^p = \left(\frac{\rho_* + 1}{\rho_* + \bar{\rho}_m(\delta + 1)}\right)^p . \tag{3.13}$$

where ρ_* and p are free parameters and ρ_m the grid cell density field, in units of the mean density $\bar{\rho}_m$.

3.3 Results

In Figure 3.1, we present the ratios between the MG and ΛCDM matter power spectra, $\frac{P_{MG}}{P_{\Lambda CDM}}$, for all transformations considered. For the transformed fields, the ratios are found to have, in principle, different values than in the case of the standard δ, on both the large and the small scales. The large scales are characterized by signal suppression with respect to the standard ratios, which, for the logarithmic and clipped transformations, is consistent with the low-k analytical predictions from equations (3.10) and (3.12). For the logarithmic case, in particular, applying (3.10) twice on the individual MG and GR power spectra and

dividing by parts, gives

$$\frac{P_{\ln(1+\delta)}(MG)}{P_{\ln(1+\delta)}(GR)} = \frac{b_{MG}^2}{b_{GR}^2}\frac{P_\delta(MG)}{P_\delta(GR)}. \tag{3.14}$$

When $b_{MG} < b_{GR}$, which we found to be the case for all MG models, the different values of the multiplicative bias produced, as seen through (3.14), result in the transformed ratio being smaller at the lowest k bins. As shown in the left column of Figure 3.1 for all 3 gravity models, when applied on our simulations, (3.14) performs well in predicting the offset between the two ratios at the smallest k modes. We note that in some previous analyses, e.g. [116], the power spectrum ratios were normalized applying arbitrary multiplicative factors to align the transformed ratios with unity at the lowest k bins, however this is not necessary, since there is a clear analytic reason, in (3.14), for an inequality between the two ratios. We find that the clipped statistic has a lower standard error, in particular at small k, than the logarithmic and marked cases. This can be attributed to the fact that the clipped mapping only alters a small fraction (∼1%) of the highest density regions, while the logarithmic and marked cases affect the whole volume, and upweight the most sparse regions associated with larger shot noise, as found in [169].

On small scales, the signal is enhanced for the symmetron and the $|f_{R_0}| = 10^{-6}$ models for all transformations by roughly 1 %, and also for the $|f_{R_0}| = 10^{-4}$ model in the marked transformation.

We calculate the covariances for P_{MG}/P_Λ, in Figure 3.1, directly by considering the ratios of the statistics from the MG and ΛCDM simulations with matching initial conditions. The errors could, alternatively, be calculated from the covariances of the individual simulations, as was proposed in [114], however, for simulations like ours in which the MG and ΛCDM simulations have the same

initial conditions, one needs to factor in the cross-correlation between the two [64]:

$$Var\left(\frac{P_{MG}}{P_{\Lambda CDM}}\right) = \left(\frac{\bar{P}_{MG}}{\bar{P}_{\Lambda CDM}}\right)^2 \times \left[\frac{Var(P_{MG})}{\bar{P}^2_{MG}} - 2\frac{Cov(P_{MG}, P_{\Lambda CDM})}{\bar{P}_{MG}\bar{P}_{\Lambda CDM}} + \frac{Var(P_{\Lambda CDM})}{\bar{P}^2_{\Lambda CDM}}\right]. \tag{3.15}$$

In order to assess each transformation's efficiency in enhancing the information carried in MG signals, we calculate the matter power spectra of the 2D projected density fields, and density transformations, as described in sec. 3.2.2 for each of the 120 independent realizations. In addition to the fractional boosts in the calculated power, expressed through the ratio $\frac{P_{MG}}{P_{\Lambda CDM}}$, the fundamental quantity of interest for statistically distinguishing MG models is the Fisher information about parameters α, β [184] :

$$F_{\alpha\beta} = -\left\langle \frac{\partial^2 \ln \mathcal{L}\,(data|\alpha, \beta, priors)}{\partial\alpha\partial\beta} \right\rangle. \tag{3.16}$$

Given a set of data with dependence on the parameters α, β, $\mathcal{L}$ is defined as the likelihood function of the parameters from the data, and in the case of a single parameter α, the above reduces to the Fisher information about a parameter α:

$$I_\alpha = -\left\langle \frac{\partial^2 \ln \mathcal{L}\,(data|\alpha)}{\partial^2\alpha} \right\rangle. \tag{3.17}$$

When restricting our focus on information encoded in the power spectra, as relevant for our analysis, (3.17) takes the form

$$I_\alpha = -\left\langle \frac{\partial P(k_i)}{\partial\alpha} \frac{\partial^2 \ln \mathcal{L}}{\partial P(k_i)\partial P(k_j)} \frac{\partial P(k_j)}{\partial\alpha} \right\rangle, \tag{3.18}$$

in which the expectation value of the middle derivative term , basically the power-spectra Fisher matrix, can be well approximated [148, 149, 129] by the inverse covariance C^{-1}_{ij}, with

$$C_{ij} = \frac{1}{N_{seed} - 1} \sum_r^{N_{seed}} \Big(P_r(k_i) - \bar{P}(k_i)\Big)\Big(P_r(k_j) - \bar{P}(k_j)\Big), \tag{3.19}$$

for the $N_{seed} = 120$ realizations. It should be noted at this point that the precision in the covariance matrix calculation could be improved by applying a set of sinusoidal weightings that depend on combinations of the fundamental modes [72], as e.g. performed in [128], but we do not apply such an improvement in this chapter. Under these assumptions, the Fisher information about a parameter α takes the common form:

$$I_\alpha = \sum_{i,j}^{N_{bins}} \frac{\partial P(k_i)}{\partial \alpha} C_{ij}^{-1} \frac{\partial P(k_j)}{\partial \alpha}. \tag{3.20}$$

In this parametrization, changes in the gravitational model are reflected upon the different values taken by the single parameter α (not to be confused with the scale factor a), which for the f(R) models is set equal to the respective values of $|f_{R_0}|$, for the symmetron equal to $z_{ssb} = 1$, and equal to 0 for ΛCDM, as the limit of both parameters that recovers GR. The numerator in the derivative terms is of course given by the difference between the corresponding MG and ΛCDM power spectra. In the general and realistic treatment involving multiple cosmological parameters, the inverse Fisher matrix is associated with the marginalized errors in the parameter estimates, while, in our single-parameter case, the unmarginalized error in the parameter estimation is predicted to be [184], $\sigma_\alpha = I_\alpha^{-1/2}$.

To express the additional Fisher information encoded in each density mapping, we define the "Fisher boost", given by the ratio of $\sqrt{I_\alpha}$ calculated for a given mapping to the $\sqrt{I_\alpha}$ by the standard density for the same cosmological model:

$$\text{Fisher boost} = \sqrt{\frac{I_\alpha(\delta')}{I_\alpha(\delta)}}. \tag{3.21}$$

While the Fisher information provides a way to quantify the sensitivity of an estimator to changes in cosmological model parameters, the "signal-to-noise"

ratio (SNR), :

$$SNR = \sqrt{\sum_{i,j}^{N_{bins}} \bar{P}(k_i) C_{ij}^{-1} \bar{P}(k_j)}, \tag{3.22}$$

is another method used in the literature to compare the performance of different statistics for the same cosmological model [177, 128]. As a comparison we consider how the SNR is affected by the choice of density transformation for the ΛCDM model. In the same vein as in (3.21), we consider the change in the ΛCDM SNR created by each transformation, as the "SNR boost":

$$\text{SNR boost} = \frac{\text{SNR}(\delta')}{\text{SNR}(\delta)}. \tag{3.23}$$

For the clipped density transformation, the threshold, δ_0, relating the fraction of the volume which is clipped, is a free parameter. In Figure 3.2 we show the sensitivity of the Fisher boost as α varies from 0 to $|f_{R_0}| = 10^{-6}$, as well as for the SNR boost, for ΛCDM, to the choice of δ_0. We find that a threshold value that corresponds to clipping the 1.1% most dense cells of the simulated volume maximizes both quantities. We note that our choice of using the same clipping threshold (the same value of δ_0) for both MG and ΛCDM models is different than in Ref. [116], in which *different* clipping thresholds were chosen for ΛCDM and MG. The choice in [116] was made to match the MG to ΛCDM power spectra ratios of the transformed field to those for the normal density field at the lowest k bins. As we discussed for the logarithmic case, however, the ratios of the normal and clipped density fields, in general, will not be equal on large scales but instead are determined by the variances of the original and remapped fields, through (3.12).

For the marked function, varying the values of the two free parameters, p and ρ_*, is found to have, qualitatively, little effect on the shape and form of

the transformed ratio, but a significant impact on the magnitude of the Fisher and SNR boosts, as shown in Figure 3.3. By fixing p and varying ρ_* and vice versa, we found the pair of values $p = 10, \rho_* = 4$ to be the optimal choice that maximizes the Fisher information as α goes from 0 to $|f_{R_0}| = 10^{-6}$, and the SNR boost in our GR simulations.

As was shown in Figure 3.1, the difference between the signal amplitudes and covariances, for the transformed statistics, relative to the normal density field is scale, as well as model, dependent. In Figure 3.4, the variation of the square root of the Fisher information in the power spectrum from ΛCDM to $|f_{R_0}| = 10^{-6}$ is plotted as a function of the maximum wavenumber k_{max}, demonstrating a monotonically increasing behavior for all 4 transforms. Out of all the MG models considered, $|f_{R_0}| = 10^{-6}$ represents the most viable, smallest perturbation around ΛCDM, which motivates its use as the representative example for the behavior of the Fisher information in Figures 3.2, 3.3 and 3.4. When focusing our analysis on wave-modes larger than 0.4 h/Mpc, all transformations comfortably predict boosts in the Fisher information, with the marked and logarithmic mappings performing better than the clipped transformation for all scales. Even though the mark predicts a higher Fisher boost than the logarithmic transformation, the predicted difference is smaller than respective error bars, making it thus hard to differentiate confidently between these two mappings with the current number of realizations. The error bars have been calculated using the Jackknife method.

In Figure 3.5, and in a similar manner as in Figure 3.4, we plot the variation in the cumulative SNR for all transformations, recovering the same qualitative behavior as in the Fisher information case. The marked and logarithmic trans-

	Fisher Boost								
k_{max}	1.0 h/Mpc			1.9 h/Mpc			3.5 h/Mpc		
Transformation	$\ln(1+\delta)$	δ_c	$m(\delta)$	$\ln(1+\delta)$	δ_c	$m(\delta)$	$\ln(1+\delta)$	δ_c	$m(\delta)$
Symmmetron	1.6	1.3	1.5	2.2	1.6	2.4	2.4	2.3	2.5
$f(R): \lvert f_{R_0}\rvert = 10^{-6}$	2.3	1.7	2.4	2.8	1.9	3.3	2.8	2.5	3.2
$f(R): \lvert f_{R_0}\rvert = 10^{-4}$	2.1	1.6	2.2	2.7	1.9	3.2	2.9	2.2	3.8

Table 3.1: A summary of the boost in the Fisher information when using the power spectra of the transformed, logarithmic, clipped and marked, density statistics relative to that of the standard density field for ΛCDM and the three modified gravity, symmetron and $f(R)$, models. The sensitivity of the Fisher boost to the maximum wavenumber considered is shown through the comparison of results with three different values of k_{max}.

formations perform comfortably better, in terms of the SNR boost, than the clipping case, with the difference from each other being once again smaller than the error bars. As in the Fisher case, the error bars were obtained by the Jackknife approach.

The Fisher boosts for each of the transformations, and each modified gravity model, when calculated to three different maximum wavenumbers, 1, 1.9 and 3.5 h/Mpc, are summarized in Table 4.1.

Just like in the $|f_{R_0}| = 10^{-6}$ model, the behavior of which has been shown in detail in Figure 3.4, the marked and logarithmic transformations produce the highest increase in the Fisher information for the rest two gravity models under consideration, and for all 3 wavenumbers reported, with the differences between the two mappings being smaller than the corresponding uncertainties. Furthermore, again in a similar manner with the $|f_{R_0}| = 10^{-6}$ case, the Fisher boosts achieved by the optimal clipping transformation are lower than the ones produced by the other two transformations, demonstrating an overall consistent behavior for all 3 MG models. Our results also reconfirm that clipping high-density screened regions results in unscreening and enhancement of

MG deviations [116] and quantifies the boost on the Fisher information, to our knowledge, for the first time.

Our results are also consistent with other studies [114], that have shown, within the context of MG, that logarithmic mappings improve the total SNR, as they also do for ΛCDM [128], and demonstrate that such transformations can be valuable in providing additional discriminatory power for difficult to detect MG models. It should be noted here that the "restricted" logarithmic function proposed in [114], which is essentially the the "sliced correlation function" at fixed δ proposed in [127], is found to produce Fisher and SNR boosts of 1.1 and 5.7 in the case of the $|f_{R_0}| = 10^{-6}$ and ΛCDM models, respectively, as opposed to corresponding boosts of 3.2 and 3.8 produced by the marked transformation, for $k > 3.5h/Mpc$.

In addition to the Fourier space statistics investigated above, we have also assessed the potential for discriminating between GR and MG models, using a real-space marked correlation function. Marked correlation functions have been proposed [27, 26, 69, 167, 163, 170] as an extension to the standard, autocorrelation function $\xi(r)$. We consider the marked correlation function $\mathcal{M}(r)$ of the form [204],

$$\mathcal{M}(r) = \frac{1 + W(r)}{1 + \xi(r)}, \tag{3.24}$$

where $W(r)$ is the correlation function weighted by the mark in (3.13). In Figure 3.6 we show, for one realization, the variation in $\mathcal{M}(r)$, between GR and MG models for varying values of p and ρ_*. This demonstrates that using a marked correlation function of this form can serve as another quantity that breaks the degeneracy between MG models and the standard ΛCDM cosmological scenario. In Figure 3.7, we plot the marked correlation function $\mathcal{M}(r)$ with $p = 10$

and $\rho_* = 0.4$, for ΛCDM and the $|f_{R_0}| = 10^{-4}$ model, averaged over 10 random realizations. For this analysis, we used the initial 10, out of the total of 30, realizations of the 3D density snapshots resolved in the 256^3 mesh, rather than the projected ones, while the 3D real space autocorrelation functions were calculated using the Super W of Theta (SWOT) code [53]. We note that, given the functional form of (3.24), the observed difference between the MG and ΛCDM models is smaller than that for the standard power spectra. At $r = 1.81 Mpc/h$, the fractional difference is maximal, $\mathcal{M}_{\Lambda CDM}/\mathcal{M}_{MG} = 1.37$, while at $r = 4 Mpc/h$, $\mathcal{M}_{\Lambda CDM}/\mathcal{M}_{MG} = 1.13$. The SNR boost between W and the standard ξ is equal to ~ 3 for ΛCDM.

3.4 Conclusions

Re-weighting cosmological density fields in order to suppress the contribution of dense, screened regions in favor of the low-density, unscreened regime, has been proposed as a recipe to improve the detectability of potential MG signatures. In this chapter, we assess the performance of a new analytical function, first proposed in [204], both as a density re-mapping and as a real space marked correlation function and also perform a systematic comparison with the logarithmic and clipping transformations. Besides the fractional deviation in the dark matter power spectra, $\frac{P_{MG}}{P_{\Lambda CDM}}$, each transformation is assessed through the boost, with respect to the standard density field, in the Fisher information in the power spectra for all MG models, as well as through the boost in the total signal-to-noise ratio for ΛCDM.

By exploring the parameter space of the "marked" density transformation,

we found the parameter choice of $p = 10$, $\rho_* = 4$, to be the one that produces the maximum boost in the Fisher information for the $|f_{R_0}| = 10^{-6}$ model, as well as the highest increase in the signal-to-noise in ΛCDM. The logarithmic mapping was found to perform roughly equally well, within the levels of accuracy, in maximizing these quantities, while both transformations were found to be superior to clipping of density peaks. These results, that also hold for the rest of the gravity models considered, demonstrate that the marked tracer could serve as a useful tool with which to discriminate between MG models and the standard cosmological scenario.

The value of the clipping threshold that truncates the densest 1.1% of each snapshot, was found to be the optimal one that simultaneously produces the maximum boosts in the Fisher information and the total signal-to-noise ratio, for all models considered. By studying the performance as a function of the maximum Fourier mode, k_{max}, included, we found clipping to predict smaller boosts compared to the other two transformations at all scales, while still performing considerably better than the standard density field.

Finally, we assessed the discriminatory potential of a real-space, marked correlation function of the form (3.24), which, tested on the $|f_{R_0}| = 10^{-4}$ model, was found to provide a maximum difference relative to ΛCDM of 37% at $r = 1.81 Mpc/h$ and a ΛCDM SNR boost of ∼3, comparing W to ξ, clearly demonstrating the power of such a real space statistic.

In this work, we have focused on the application of the statistics using the dark matter particle distribution from the N-body simulations. We recognize that in reality surveys sample astrophysical, biased, baryonic tracers of the dark matter distribution, and the next natural step, that we will undertake in future

work, will be to investigate the utility of these statistics on mock galaxy catalogs that more accurately represent what we will observe with upcoming surveys. Other lines of improvement could be incorporating the effects of redshift-space distortions to the current analysis.

Models that aim to explain cosmic acceleration through modifications to GR, evade strict solar system constraints through characteristic screening mechanisms which suppress deviations in high-density environments. In our work we demonstrate how one can, through a series of simple density transformations, differentiate more confidently between ΛCDM and alternative scenarios. Such density-dependent suppressions make the detection of potential MG signatures challenging, even for future ambitious surveys of the LSS, like the LSST, Euclid and DESI.

3.5 Acknowledgments

We would like to thank Baojiu Li for providing helpful comments on this line of work. We also wish to thank an anonymous referee for their careful reading and useful comments on the above results during the peer review process.

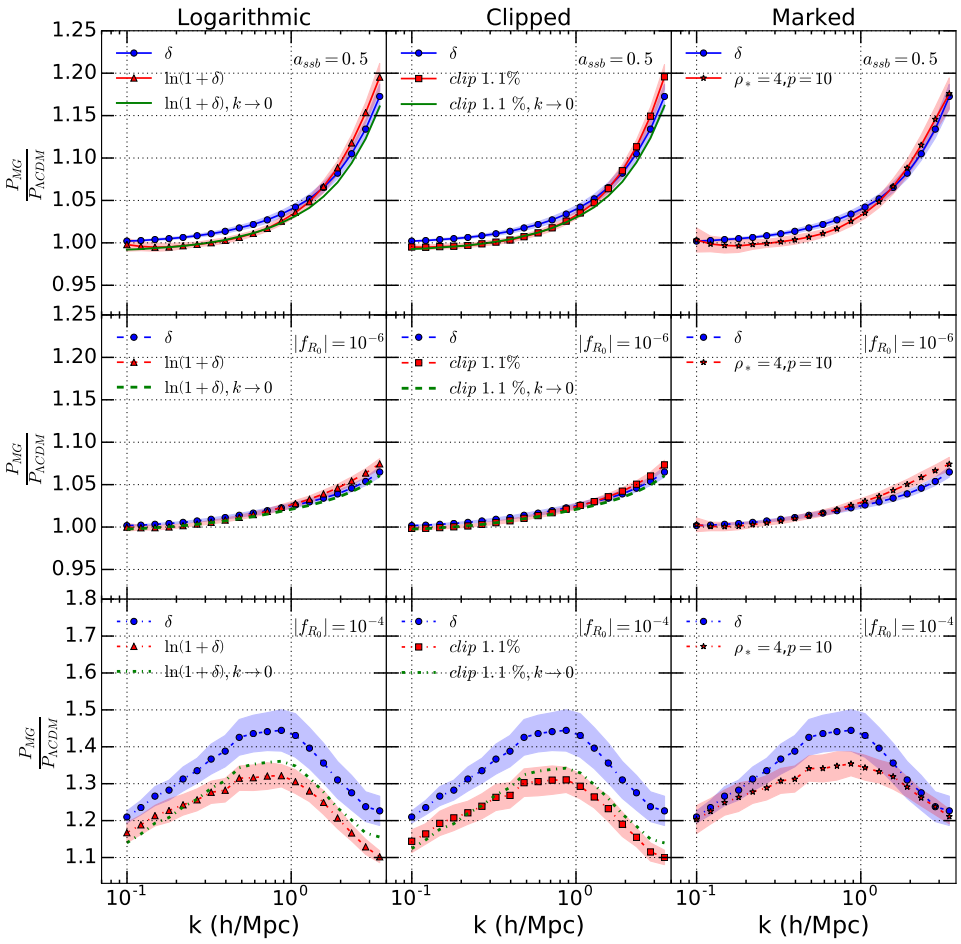

Figure 3.1: A side-by-side comparison of the ratios of the MG matter power spectra, P_{MG}, for the symmetron [top row], $|f_{R_0}| = 10^{-6}$ [middle row] and $|f_{R_0}| = 10^{-4}$ [bottom row] modified gravity models relative to ΛCDM, $P_{\Lambda CDM}$. For each model, the ratio is shown for the three density transformations: logarithmic transformation [left column, red triangle], the clipped density field when 1.1% of the volume is clipped [center column, red square] and the "marked" transform, $m(\delta)$ [right column, red star], with $\rho_* = 4$ and $p = 10$, compared to the standard density field, δ [all panels, blue circle]. The green lines in the left and middle columns show the variance-dependent, analytic predictions for the power spectrum ratios for the large scale regime, as $k \to 0$, for the logarithmic and the clipped transformation, from equations (10) and (12) respectively. The error bands correspond to the standard deviations over the 120 realizations.

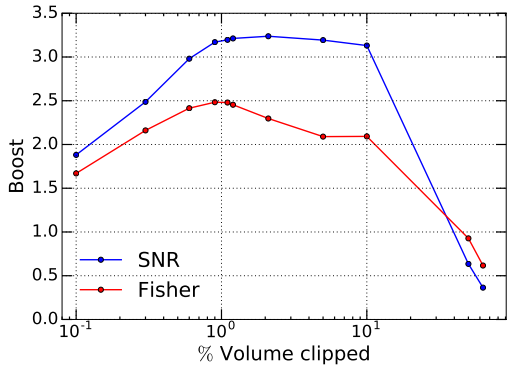

Figure 3.2: The variation of the Fisher and SNR boosts, defined in (3.21) and (3.23), for the clipped density transformation relative to the normal density distribution, as a function of the clipping threshold, shown as the % of the simulation volume that is clipped (i.e. has $\delta > \delta_0$). The Fisher boost is shown for an $|f_{R_0}| = 10^{-6}$ cosmology, while the SNR for the ΛCDM scenario.

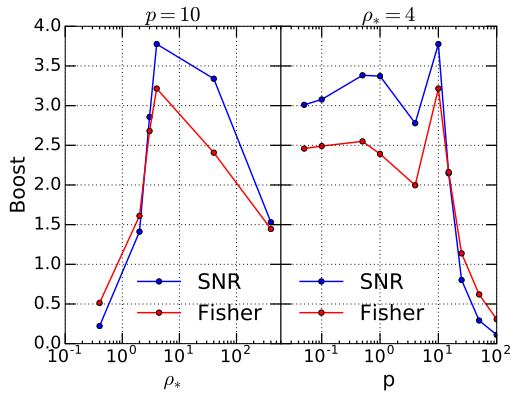

Figure 3.3: The variation of the Fisher and SNR boosts, defined in (3.21) and (3.23), for the marked transformation in an $|f_{R_0}| = 10^{-6}$ and ΛCDM scenario, correspondingly, as a function of [left] ρ_*, with fixed $p = 10$, and [right] p, with fixed $\rho_* = 4$.

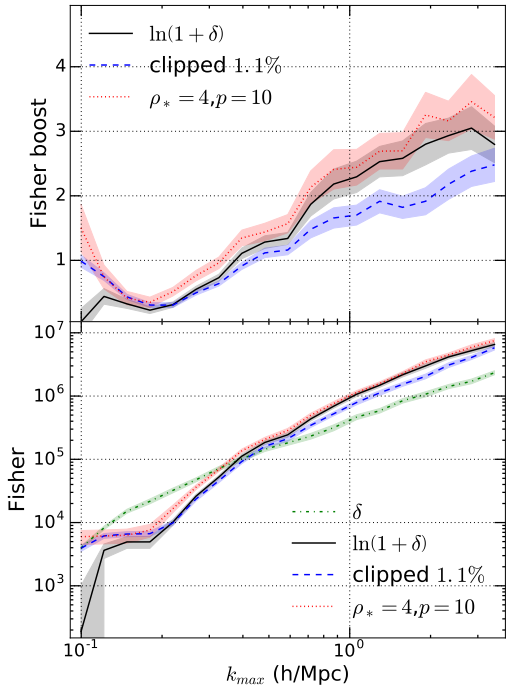

Figure 3.4: [Top] The variation of the Fisher boost for the logarithmic [black, full], clipped [blue, dashed] and marked [red,dotted] transformation as a function of k_{max} for the $|f_{R_0}| = 10^{-6}$ case. [Bottom] The variation of the square root of the Fisher information for the standard [green, dashdot], logarithmic [black, full], clipped [blue, dashed] and marked [red,dotted] density transformation as a function of k_{max} for the $|f_{R_0}| = 10^{-6}$ model. The error bars have been obtained using the Jackknife approach.

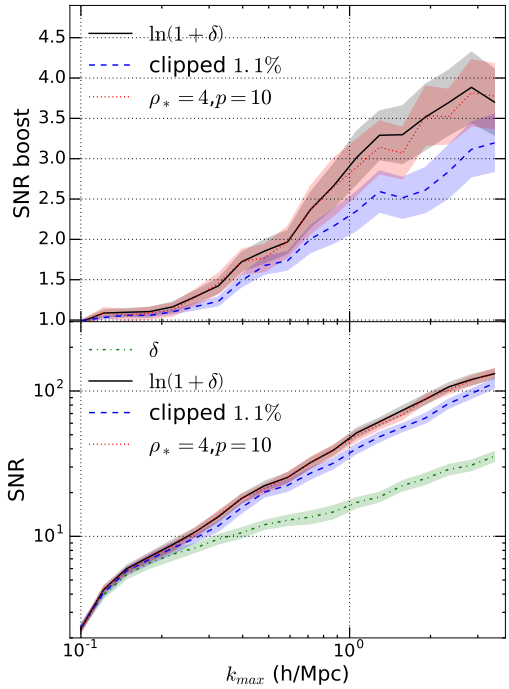

Figure 3.5: [Top] The variation of the signal-to-noise ratio (SNR) boost for the logarithmic [black, full], clipped [blue, dashed] and marked [red,dotted] transformation as a function of k_{max} for the ΛCDM case. [Bottom] The variation of the signal-to-noise ratio (SNR) for the standard [green, dashdot], logarithmic [black, full], clipped [blue, dashed] and marked [red,dotted] density transformation as a function of k_{max} for ΛCDM. The error bars have been obtained using the Jackknife approach.

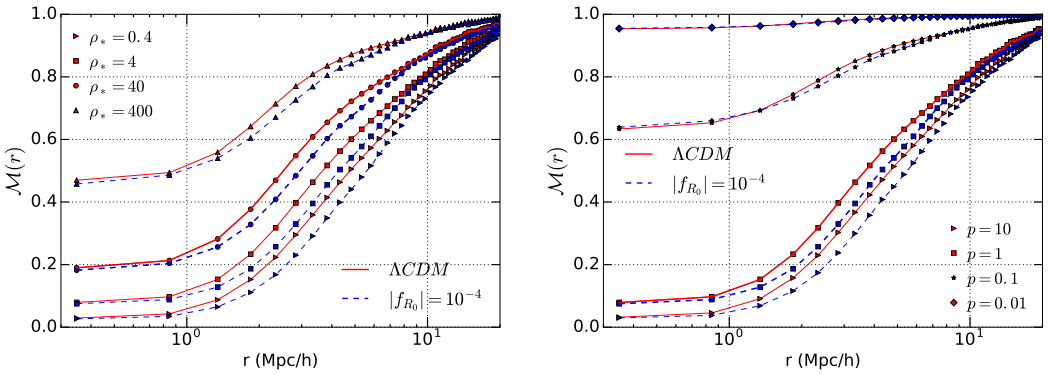

Figure 3.6: The variation of the marked correlation function, $\mathcal{M}(r)$ for one realization, as a function of comoving length scale, r, for the ΛCDM [red, full line] and $|f_{R_0}| = 10^{-4}$ [blue, dashed line] scenario, as a function of [left] ρ_*, with fixed $p = 10$, and [right] p, with fixed $\rho_* = 0.4$.

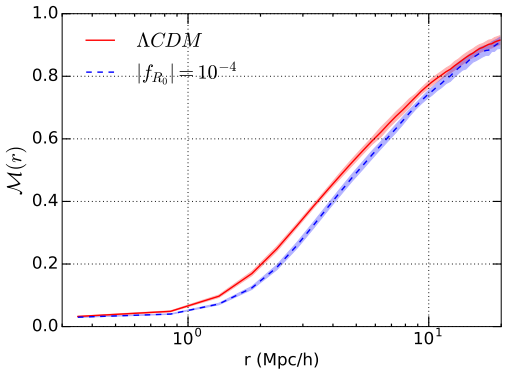

Figure 3.7: The marked correlation functions, $\mathcal{M}$, for ΛCDM [red, full line] and the $|f_{R_0}| = 10^{-4}$ [blue, dashed line] model, for $\rho_* = 0.4$ and $p = 10$, showing the average and variance over 10 realizations.

CHAPTER 4

CONVOLUTION LAGRANGIAN PERTURBATION THEORY FOR BIASED TRACERS BEYOND GENERAL RELATIVITY

4.1 Introduction

In this chapter, we will compare analytic predictions for real and Fourier space two-point statistics for biased tracers from a variety of Lagrangian Perturbation Theory approaches against those from state of the art N-body simulations in $f(R)$ Hu-Sawicki and the nDGP braneworld modified gravity theories.

From a theoretical standpoint, models of structure formation rely upon accurately tracing the nonlinear evolution of dark matter perturbations. In the linear regime and when gravity is governed by GR, different modes evolve independently, with the time evolution encapsulated in the scale-independent growth factor. At nonlinear scales, however, the dynamics of the self-gravitating dark matter system can only be tracked accurately by full-blown N-body simulations, which are highly computationally expensive . Additional complexity arises in accounting for the fact that the observed galaxies do not perfectly trace the underlying dark matter density field, but are biased tracers of it [86]. While this effect can be easily captured by introducing a multiplicative bias factor in the large scales [62], in the regime of nonlinear dynamics, empirical modeling needs to be combined with sophisticated simulations in order to predict the spatial distribution of galaxies inside gravitationally collapsed dark matter halos [29, 99, 214]. Furthermore, when MG configurations are considered, the fifth forces introduce an additional layer of complexity, scale-dependent growth is generally present even at the linear level and in the nonlinear scales, one needs to solve the scalar

field Klein-Gordon (KG) equation that is highly nonlinear and adds to the computational costs significantly. The intermediate, quasi-linear, scales can fortunately be analytically accessed by higher order Perturbation Theory (PT) [30, 47] approaches or hybrid methods [182, 189].

The Lagrangian Perturbation Theory approach [212, 44, 38, 78, 183, 120, 119, 46, 122, 59] to structure formation is one the oldest and most popular analytical frameworks in the literature, that has been been particularly successful at describing the Baryon Acoustic Oscillation (BAO) peak [63], observed at a comoving scale of ~110 Mpc/h, and the power-law correlation function, on comoving scales ~20-90 Mpc/h, in ΛCDM [194]. Combined with a model for halo bias [86, 124, 166, 123, 157, 119], it can be used to predict the 2-point statistics for halos in the real and redshift space [46, 119, 193], which serves as a crucial step to the theoretical description of galaxy clustering. Additional contributions from small-scale physics can also be included using techniques inspired by effective field theory theory [196, 193]. In the context of MG cosmologies, extensive studies have been performed in the framework of Eulerian Standard Perturbation Theory (SPT) [98, 179, 42, 180, 28, 66, 35, 36]. LPT was first found to work very well within the COLA hybrid framework for chameleon and Vainshtein MG cosmologies [189], while third order LPT for dark matter was recently developed in the case of scalar-tensor theories in [15].

In this work, we perform a comprehensive study of how LPT can be used to make predictions for biased tracers in modified gravity theories, and how well the predictions compare with full numerical simulations for a variety of modified gravity models. We study chameleon and Vainsthein MG theories, focusing on the $f(R)$ Hu-Sawicki [81] and nDGP braneworld models [60] as popular, rep-

resentative examples for each category. The underlying dark matter clustering is described using the formalism in [15]. We then consider the Convolution Lagrangian Perturbation Theory (CLPT) [46] for biased tracers, as well as the variants, using the particular resummation scheme in [196, 193]. We extend the peak-background split formalism (PBS) [86, 20, 157] in which the Lagrangian bias factors are calculated as responses, to account for modifications to the halo mass function in modified gravity theories and the environmental dependence of screening effects. We show how this formalism should be extended in the case of each screening mechanism. Finally, we cross-check and validate our results in terms of the 2-point statistics against state-of-the-art cosmological N-body simulations that allow us to assess the LPT predictions in the nonlinear, quasi non-linear and baryon acoustic oscillation peak regimes. Comparison with simulations is required to ensure that the predictions will be sufficiently robust for upcoming surveys such as DESI, Euclid, LSST and WFIRST. The work presented below, has been published in [191].

This chapter is structured as follows: in Section 4.2.1, we present the MG models we studied and the details of the N-body simulations employed to test our LPT implementation. We summarize the formalism for developing biased tracer statistics for GR in Section 4.2.2. In Section 4.3.1, we discuss the modifications required to the perturbative schemes to predict the real and Fourier space 2-point statistics and the associated bias parameters for tracers of different masses for models beyond GR. The LPT predictions are compared to statistics derived from simulations in Section 4.3.2. Finally, we conclude, and discuss implications for future work, in Section 4.4.

4.2 Formalism

4.2.1 Modified gravity models

The $f(R)$ model

Despite the latest surge in the field of MG, deformations to GR, together with associated experimental tests, have been around for almost as long as GR itself [206]. One of the oldest attempts consisted of adding a nonlinear function $f(R)$ of the Ricci scalar R to the standard Einstein-Hilbert action, the so-called $f(R)$ theories [57], with a resulting action S of the form:

$$S = \int d^4x \sqrt{-g} \left[\frac{R + f(R)}{16\pi G} + \mathcal{L}_m \right], \tag{4.1}$$

with $\mathcal{L}_m$ denoting the matter sector Lagrangian and G the gravitational constant. Since such an action frees up an additional degree of freedom, the latest interest in this class of theories comes from the idea that a modification of this type is responsible for cosmic acceleration, rather than dark energy [48].

Such a model is the Hu-Sawicki $f(R)$ model [81], which we study in this chapter and the functional form of which is given by:

$$f(R) = -m^2 \frac{c_1 \left(R/m^2\right)^n}{c_2 \left(R/m^2\right)^n + 1}. \tag{4.2}$$

In equation (5.2), Ω_{m0} denotes the matter fractional energy density and H_0 the Hubble Constant, both evaluated today, $m = H_0 \sqrt{\Omega_{m0}}$, which has dimensions of mass and n, c_1 and c_2 are free parameters.

In order to match the ΛCDM expansion history and for sufficiently small

values of $|f_{R_0}|$, the background value of the Ricci scalar, $\bar{R}$, becomes equal to:

$$\bar{R} = 3\Omega_m H_0^2 \left(1 + 4\frac{\Omega_{\Lambda 0}}{\Omega_{m0}}\right). \tag{4.3}$$

where $\Omega_{\Lambda 0}$ is the dark energy fractional density evaluated at the present time.

The derivative $f_R = \frac{df(R)}{dR}$ becomes a functional of the cosmological parameters when evaluated today, through the relationship

$$\bar{f_{R_0}} = -n\frac{c_1}{c_2^2}\left(\frac{\Omega_{m0}}{3(\Omega_{m0} + \Omega_{\Lambda 0})}\right)^{n+1}. \tag{4.4}$$

The above mapping allows us to reduce the number of free parameters and the Hu-Sawicki model is commonly parametrized by quoting the values chosen for n and $|f_{R_0}|$, with the latter being the background value of the fifth potential evaluated today.

The reason the Hu-Sawicki model is so popular is that it can be cast into the form of a scalar-tensor theory that realizes the chameleon screening mechanism [92, 93], through a conformal transformation [43], with the quantity f_R identified as the scalar field that is coupled to matter. Through the interplay between matter and the self-interaction potential, the scalar chameleon field becomes massive near high over-densities and the associated fifth forces get exponentially suppressed due to the Yukawa effect. A stronger screening effect is manifested in lower values of the parameter $|f_{R_0}|$, with the limit of $|f_{R_0}| \to 0$ exactly recovering GR. Following the literature and also because of the available simulations (as we will discuss below in 4.2.1), we choose $n = 1$ and consider three different $f(R)$ models with $\left|\bar{f_{R_0}}\right| = \{10^{-6}, 10^{-5}, 10^{-4}\}$, which we shall refer to, from now on, as F6, F5 and F4.

When considering perturbations around a homogeneous and isotropic FRW metric in the conformal Newtonian gauge, the resulting system of the Poisson

and KG equations becomes [81]:

$$\begin{aligned} \nabla^2\Phi_N &= 4\pi G a^2 \delta\rho_m - \frac{1}{2}\nabla^2 f_R, \\ \nabla^2 f_R &= -\frac{a^2}{3}\delta R - \frac{8\pi G a^2}{3}\delta\rho_m, \end{aligned} \tag{4.5}$$

where Φ_N is the Newtonian potential and $\delta\rho_m$ the matter density perturbation. δR, the perturbation to the Ricci scalar, can be written as a function of the scalar field f_R, which will play a central role in our screening implementation in Section 4.2.2.

The nDGP model

The second MG model under consideration comes from the realm of higher-dimensional braneworld cosmology. The simplest example of such a configuration is the so-called Dvali-Gabadadze-Porrati (DGP) model [60], which is described by an action of the following form:

$$S = \int d^4x\sqrt{-g}\left[\frac{R}{16\pi G} + \mathcal{L}_m\right] + \int d^5x\sqrt{-g_5}\left(\frac{R_5}{16\pi G r_c}\right). \tag{4.6}$$

In this model, the spacetime consists of 5 dimensions, rather than the usual 4, but the standard model fields are restricted to a 4-dimensional (4D) brane and the free parameter, r_c, denotes the length-scale below which gravity becomes 4D. R_5 and g_5 denote the corresponding 5D versions of the Ricci scalar and metric tensor determinant, respectively. The resulting Friedman equation from (5.4) is:

$$\epsilon\frac{H}{r_c} = H^2 - \frac{\rho_m}{24\pi G}, \tag{4.7}$$

where $\epsilon = \pm 1$. Each of the two values of ϵ represents a particular branch of the model, with $\epsilon = +1$ producing the self-accelerating solution, which, however, suffers from undesirable "ghost" instabilities [96] and is thus an unphys-

ical model to consider. The value of $\epsilon = -1$ corresponds to the so-called normal branch, hereafter called nDGP, which is well behaved, but does not self-accelerate and can match a ΛCDM expansion history only in the presence of dark energy.

When focusing on the normal branch and in the quasi-static limit for sub-horizon scales, the perturbations in the conformal Newtonian gauge give the modified Poisson system of equations [98]:

$$\begin{aligned} \nabla^2\Phi_N &= 4\pi G a^2 \delta\rho_m + \frac{1}{2}\nabla^2\varphi, \\ \nabla^2\varphi &= \frac{8\pi G a^2}{3\beta}\delta\rho_m - \frac{r_c^2}{3\beta a^2}\Big[(\nabla^2\varphi)^2 - (\nabla_i\nabla_j\varphi)^2\Big], \end{aligned} \tag{4.8}$$

with the coupling β given by

$$\beta(a) = 1 + 2H(a)r_c\left(1 + \frac{\dot{H(a)}}{3H(a)^2}\right). \tag{4.9}$$

The nDGP model is a typical example of a scalar-tensor theory that realizes the Vainshtein screening mechanism [187, 18], in which the modifications to gravity are suppressed in the existence of large second derivatives of the scalar field. In the second equation of (4.8), in particular, it can be seen how, once the second derivatives of the scalar field become large in high densities, the second term on the right hand side (r.h.s.) becomes significant and effectively weakens the source strength, resulting in strong screening of the fifth forces.

We consider the nDGP model for two choices of the free parameter r_c, corresponding to $n \equiv H_0 r_c = 1$ and $n = 5$, which we shall call, from now on, N1 and N5, respectively.

N-body Simulations

Accurate realizations of structure formation in the nonlinear regime can only be achieved by performing N-body simulations. In this chapter, we test our results against two groups of state-of-the-art N-body simulations, that serve complementary purposes to each other, as explained below.

The first group of simulations, to which we shall refer as Group I from now on, are the ELEPHANT simulations, presented in [50]. These span the parameter space of both MG models we study: the F4, F5 and F6 $f(R)$ models and N1 and N5 nDGP models. The $f(R)$ simulations were performed using the ECOSMOG code [112, 37], while the nDGP ones [73] using the ECOSMOG-V version [111, 21], both of which were based on the GR code RAMSES [185] and where suitably extended to integrate the scalar field KG equation for the corresponding models using adaptive-mesh-refinement techniques. The parameters describing the background ΛCDM cosmology are the best-fit ones given by the 9-year WMAP release [76] and have the following values: $\Omega_b = 0.046$, $\Omega_{cdm} = 0.235$, $\Omega_m = 0.281$, $\Omega_L = 0.719$, $h = 0.7$, $n_s = 0.971$ and $\sigma_8 = 0.82$. $N_p = 1024^3$ equal mass particles were placed in a simulation box with a side $L_{box} = 1024$ Mpc/h and the density field was resolved in a 1024^3 resolution grid. Furthermore, the simulations were initialized at redshift $z_i = 49$ using the Zel'dovich approximation [212] and evolved through $z_f = 0$.

Gravitationally bound dark matter halos were identified using the ROCKSTAR halo finder [25]. Finally, so as to get an estimate of the variance, each model was simulated for 5 random realizations, corresponding to different random phases in the initial density field.

The 1024^3 $(Mpc/h)^3$ volume simulations' results in Group I become noisy at scales $r > 100$ Mpc/h. To probe the BAO scales, where LPT has been previously found to perform very well for GR [194], we also test our results against the largest volume $f(R)$ simulations performed to date for the modified gravity lightcone simulation project [13]. In these simulations, which we will call Group II from now on, the box side is $L_{box} = 1536$ Mpc/h with 2048^3 equal mass particles used, for GR and the $|\bar{f}_{R_0}|=10^{-5}$ model. The parameters describing the background ΛCDM cosmology are the best-fit ones given by the Planck collaboration [139] and have the following values: $\Omega_b = 0.0486$, $\Omega_m = 0.3089$, $\Omega_L = 0.6911$, $h = 0.6774$, $n_s = 0.9667$ and $\sigma_8 = 0.8159$. The simulations were performed using the MG code MG-GADGET [141], which is a MG extension to the code P-GADGET3, an improved version of the code GADGET-2 [174], created for GR simulations. Dark matter halo catalogues were produced using the SUBFIND algorithm [175]. Each model has been simulated for one random realization.

For more detailed discussions on the N-body implementations, we refer interested readers to the corresponding publications.

4.2.2 Convolution Lagrangian Perturbation Theory for biased tracers in MG

LPT for dark matter

The Lagrangian Perturbation Theory approach to structure formation has been extensively studied [212, 44, 38, 78, 183, 120, 119, 46, 122, 59] in the context of

ΛCDM scenarios. Opposite to the Eulerian picture, in which one monitors the evolution of the desired quantities at a given, fixed, position, in LPT one instead tracks down the evolution of a given fluid element over time. Starting from an initial, Eulerian, comoving position $\mathbf{q}$ at a desired early time t_0, each mass element is mapped to its comoving Lagrangian position $\mathbf{x}(\mathbf{q}, t)$ at time t, through the relationship

$$\mathbf{x}(\mathbf{q}, t) = \mathbf{q} + \mathbf{\Psi}(\mathbf{q}, t). \tag{4.10}$$

The Lagrangian displacement $\mathbf{\Psi}(\mathbf{q}, t)$, taken to be 0 at the initial time t_0, is the fundamental quantity of interest in LPT. Furthermore, enforcing mass conservation, through the continuity equation, between the initial and final infinitesimal volume elements centered around $\mathbf{q}$ and $\mathbf{x}$, respectively, gives $\rho_m(\mathbf{x}, t)d^3x = \rho_m(\mathbf{q}, t_0)d^3q$. Assuming t_0 refers to an epoch early enough that the density perturbations around the background density $\bar{\rho}$ are negligible, meaning $\rho_m(\mathbf{q}, t_0) = \bar{\rho}_m$, allows us to obtain the dark matter fractional overdensity, δ_m, in the Lagrangian picture:

$$1 + \delta_m(\mathbf{x}, t) = \int d^3q \delta_D \left[\mathbf{x} - \mathbf{q} - \mathbf{\Psi}(\mathbf{q}, t)\right] = \frac{1}{J(\mathbf{q}, t)}, \tag{4.11}$$

with δ_D being the Dirac delta function and $J(\mathbf{q}, t)$ the determinant of the deformation matrix

$$J_{ij} = \frac{\partial x^i}{\partial q^j} = \delta_{ij} + \frac{\partial \Psi^i}{\partial q^j}. \tag{4.12}$$

For an irrotational flow, which is a good approximation for cold dark matter and assuming that the gravitational evolution is governed by GR, perturbations around a flat FRW metric give the geodesic and Poisson equations, in the quasi-static approximation and for sub-horizon scales, as:

$$\begin{aligned} \ddot{\mathbf{x}} + 2H\dot{\mathbf{x}} &= -\frac{1}{a^2}\nabla_{\mathbf{x}}\psi(\mathbf{x}, t), \\ \frac{1}{a^2}\nabla^2_{\mathbf{x}}\psi(\mathbf{x}, t) &= 4\pi G\bar{\rho}_m\delta(\mathbf{x}, t). \end{aligned} \tag{4.13}$$

We should point out that in (5.11) $\psi(\mathbf{x}, t)$ denotes the metric perturbation, which should not be confused with the Lagrangian displacement field $\mathbf{\Psi}(\mathbf{q}, t)$.
In the LPT picture, we perturbatively expand $\mathbf{\Psi}$ as

$$\mathbf{\Psi}(\mathbf{q}, t) = \sum_{n=1}^{\infty} \mathbf{\Psi}^{(n)}(\mathbf{q}, t) = \mathbf{\Psi}^{(1)}(\mathbf{q}, t) + \mathbf{\Psi}^{(2)}(\mathbf{q}, t) + \mathbf{\Psi}^{(3)}(\mathbf{q}, t)... \tag{4.14}$$

and equations (5.7)-(5.10) form a closed system, that is recursively solved for the various orders of $\mathbf{\Psi}$. The first order solution is the so-called Zel'dovich approximation [212].

In MG theories, as also explained in Section 4.2.1, an additional degree of freedom is present, that directly couples to matter and causes particles to deviate from the nominal geodesics of GR. Consequently, equations (5.11) are, in principle, modified for a scalar-tensor theory and so is the LPT framework presented above. In [189], the LPT approach was expanded for chameleons and symmetrons, including the first order contribution to the Klein-Gordon equation and was shown to perform very well in the context of the COLA hybrid framework. The LPT approach for scalar-tensor theories up to third order was presented in [15], the main results of which we summarize in this section.

In [28], which developed an SPT framework for studying MG theories with a screening mechanism in the nonlinear regime, based on the closure theory approximation in [178], the scalar field KG equation for a Brans-Dicke-like (BD) theory with interactions of a scalar field, ϕ, was written as:

$$(3 + 2\omega_{BD})\frac{1}{a^2}k_x^2\phi(\mathbf{k}_x, t) = 8\pi G\bar{\rho}_m\delta(\mathbf{k}_x, t) - \mathcal{I}(\phi), \tag{4.15}$$

where $\mathcal{I}(\phi)$ denotes the perturbative form of the field self-interaction term:

$$\begin{aligned}\mathcal{I}(\phi) &= M_1(\mathbf{k},t)\phi \\ &+\frac{1}{2}\int \frac{d^3k_1 d^3k_2}{(2\pi)^3}\delta_D(\mathbf{k}-\mathbf{k}_{12})M_2(\mathbf{k}_1,\mathbf{k}_2)\phi(\mathbf{k}_1)\phi(\mathbf{k}_2) \\ &+\frac{1}{6}\int \frac{d^3k_1 d^3k_2 d^3k_3}{(2\pi)^6}\delta_D(\mathbf{k}-\mathbf{k}_{123}) \\ &\quad \times M_3(\mathbf{k}_1,\mathbf{k}_2,\mathbf{k}_3)\phi(\mathbf{k}_1)\phi(\mathbf{k}_2)\phi(\mathbf{k}_3), \end{aligned} \tag{4.16}$$

where we adopted the standard notation $\mathbf{k}_{ijk} = \mathbf{k}_i + \mathbf{k}_j + \mathbf{k}_k$ and $M_1(\mathbf{k},t)$, $M_2(\mathbf{k}_1,\mathbf{k}_2)$ and $M_3(\mathbf{k}_1,\mathbf{k}_2,\mathbf{k}_3)$ are mass terms. The higher order piece in the Fourier space representation of the interaction term in equation (5.16), incorporates the screening effect, up to third order, that is responsible for recovering GR at small scales. The mapping between a given scalar-tensor theory and the BD form above can be easily performed through assigning appropriate values to the mass terms and the BD coupling ω_{BD} above, as we will later show for our two models of study.

The perturbed modified Einstein equations have the form [15]

$$\begin{aligned}\nabla_{\mathbf{x}}\hat{\mathcal{T}}\boldsymbol{\Psi} &= -\frac{1}{a^2}\nabla^2_{\mathbf{x}}\psi(\mathbf{x},t), \\ \frac{1}{a^2}\nabla^2_{\mathbf{x}}\psi(\mathbf{x},t) &= 4\pi G\bar{\rho}_m\delta(\mathbf{x},t) - \frac{1}{2a^2}\nabla^2\phi - \frac{1}{2a^2}\left(\nabla^2_{\mathbf{x}}\phi - \nabla^2\phi\right),\end{aligned} \tag{4.17}$$

where we use (5.7) and introduce the time derivative operator $\hat{\mathcal{T}} = \frac{d^2}{dt^2} + 2H\frac{d}{dt}$, as in [120]. The last term in the second line of (5.14), called *frame-lagging* in [15], is a geometrical term that occurs due to the fact that, in LPT, the KG equation should be expressed in Lagrangian $\left(\nabla^2\right)$, rather than Eulerian coordinates $\left(\nabla^2_{\mathbf{x}}\right)$. Taking this into account, equations (5.15)-(5.14) are combined to give

$$\begin{aligned}\left(J^{-1}\right)_{ij}\hat{\mathcal{T}}\Psi_{i,j}(\mathbf{k}) &= -A(k)\delta(\mathbf{k}) + \frac{k^2}{a^2 3\Pi(k)}\delta\mathcal{I}(\mathbf{k}) \\ &+ \frac{M_1(k)}{3\Pi(k)}\frac{1}{2a^2}\left(\nabla^2_{\mathbf{x}}\phi - \nabla^2\phi\right)(\mathbf{k}),\end{aligned} \tag{4.18}$$

where, following the definitions in [28], we have

$$A(k) = 4\pi G\bar{\rho}_m\left(1 + \frac{k^2}{a^2 3\Pi(k)}\right),$$
$$\Pi(k) = \frac{1}{3a^2}\left[(3 + 2\omega_{BD})\,k^2 + M_1 a^2\right] \tag{4.19}$$

and all the quantities are Fourier transforms in the Lagrangian **q**-space. The inverse Jacobean in (4.18) reflects the derivative transformation to the **q**-space, where the Einstein notation is adopted. Furthermore, $\delta(\mathbf{k})$, $\delta\mathcal{I}(\mathbf{k})$ and $\left(\nabla^2_{\mathbf{x}}\phi - \nabla^2\phi\right)(\mathbf{k})$ are the Lagragian Fourier transformations of the Lagrangian-transformed overdensity (5.8), the higher order interaction Kernels in (5.16) and the frame-lagging Kernel, correspondingly. The expression for the latter is given in [15]. Equation (4.18) forms a closed system with (5.8), (5.9), (5.15) and (5.16) that is solved, perturbatively, to obtain the MG solution up to various orders in $\mathbf{\Psi}$, as in (5.10).

Solving for the first order solution, one gets [189]:

$$\mathbf{k}\cdot\mathbf{\Psi}^{(1)} = iD^{(1)}(k,t)\delta^{(1)}(\mathbf{k}, t=0), \tag{4.20}$$

which can be easily solved for the displacement field, as:

$$\Psi^j(k,t) = \frac{ik^j}{k^2}D^{(1)}(k,t)\delta^{(1)}(\mathbf{k}, t=0). \tag{4.21}$$

We see that the r.h.s of (4.21) can be conveniently decomposed into a product of the first order density mode at very early times, $\delta^{(1)}(\mathbf{k}, t=0)$, early enough to be gaussian and a space-time dependent growth factor $D^{(1)}(k,t)$, given by:

$$\hat{\mathcal{T}}D^{(1)}(k,t) = A(k)D^{(1)}(k,t). \tag{4.22}$$

In the GR limit, $A(k) = A(k=0) = 4\pi G\bar{\rho}_m$, $D^{(1)}$ becomes scale independent and is nothing else than the first order growing mode for GR; the Zel'dovich approximation.

Moving on to the second order piece, we have:

$$\mathbf{k}\cdot\mathbf{\Psi}^{(2)} = \frac{i}{2}\int \frac{d^3k_1 d^3k_2}{(2\pi)^3}\delta_D(\mathbf{k}-\mathbf{k}_{12})D^{(2)}(\mathbf{k}_1,\mathbf{k}_2)\delta_1^{(1)}\delta_2^{(1)}, \tag{4.23}$$

where, for compactness, we adopted the notation $\delta_1^{(1)} = (\mathbf{k}_1, 0)$ and the second order growth factor, $D^{(2)}(\mathbf{k}_1,\mathbf{k}_2)$, is given by [15]:

$$\begin{aligned} D^{(2)}(\mathbf{k}_1,\mathbf{k}_2) &= D_a^{(2)}(\mathbf{k}_1,\mathbf{k}_2) - D_b^{(2)}(\mathbf{k}_1,\mathbf{k}_2)\frac{\mathbf{k}_1\cdot\mathbf{k}_2}{k_1^2k_1^2} \\ &\quad + D_{FL}^{(2)}(\mathbf{k}_1,\mathbf{k}_2) - D_{\delta I}^{(2)}(\mathbf{k}_1,\mathbf{k}_2). \end{aligned} \tag{4.24}$$

The four individual components are given by:

$$\begin{aligned} \left(\hat{\mathcal{T}} - A(k)\right) D_a^{(2)}(\mathbf{k}_1,\mathbf{k}_2) &= A(k)D^{(1)}(k_1)D^{(1)}(k_2), \\ \left(\hat{\mathcal{T}} - A(k)\right) D_b^{(2)}(\mathbf{k}_1,\mathbf{k}_2) &= \left(A(k_1) + A(k_2) - A(k)\right) D^{(1)}(k_1)D^{(1)}(k_2), \\ \left(\hat{\mathcal{T}} - A(k)\right) D_{\delta I}^{(2)}(\mathbf{k}_1,\mathbf{k}_2) &= \left(\frac{2A_0}{3}\right)^2 \frac{k^2}{a^2}\frac{M_2(\mathbf{k}_1,\mathbf{k}_2)D^{(1)}(k_1)D^{(1)}(k_2)}{6\Pi(k)\Pi(k_1)\Pi(k_2)}, \\ \left(\hat{\mathcal{T}} - A(k)\right) D_{FL}^{(2)}(\mathbf{k}_1,\mathbf{k}_2) &= \left(\frac{M_1}{3\Pi(k)}\right) K_{FL}^{(2)}(\mathbf{k}_1,\mathbf{k}_2)D^{(1)}(k_1)D^{(1)}(k_2). \end{aligned} \tag{4.25}$$

The two last terms represent the second order contributions to the growth factor, given by the screening and frame-lagging effects, correspondingly, while the expression for $K_{FL}^{(2)}$ is given in [15]. Despite its lengthier expression, when taking the GR limit we get $D_{FL}^{(2)} = D_{\delta I}^{(2)} = 0$ and $D_a^{(2)} = D_b^{(2)}$, allowing $D^{(2)}$ to become scale-independent, reducing to the known GR result, which can be well approximated by $D^{(2)}(t) = -\frac{3}{7}\left(D^{(1)}(t)\right)^2$ for ΛCDM cosmologies [38].

Solving for the third order piece in (4.18) results in a lengthy differential equation for the third order MG growth factor, $D^{(3)}(\mathbf{k}_1,\mathbf{k}_2,\mathbf{k}_3)$, that also needs to be symmetrized. The result is given by equation (B.5) in the appendix B.1. It should be also noted that equations (4.22), (4.25) and f(B.5) can be either solved by inverting the linear operator $\left(\hat{\mathcal{T}} - A(k)\right)$ using its Green function, as done in [122, 15], or by numerically solving the corresponding differential equations.

Even though both methods give results that agree with each other well, we chose to proceed with the latter because it is computationally faster. The differential equations were solved using a 5^{th} order Runge-Kutta scheme, implemented in *Mathematica* [83].

We finish this section by showing the particular expressions for the mass terms in (5.16) and the sources in (5.18) for the $f(R)$ and nDGP models we study. For the $f(R)$ Hu-Sawicki model, the Brans-Dicke scalar is simply $\omega_{BD} = 0$, while the mass terms are given by the expansion [98]:

$$M_n = \frac{d^n \bar{R}(f_{R_0})}{df_{R_0}^n}, \tag{4.26}$$

which, using (5.2), gives [15]:

$$\begin{aligned} M_1(a) &= \frac{3H_0^2}{2|f_{R_0}|}\frac{\left(\Omega_m a^{-3} + 4\Omega_\Lambda\right)^3}{\left(\Omega_m + 4\Omega_\Lambda\right)^2}, \\ M_2(a) &= \frac{9H_0^2}{4|f_{R_0}|}\frac{\left(\Omega_m a^{-3} + 4\Omega_\Lambda\right)^5}{\left(\Omega_m + 4\Omega_\Lambda\right)^4}, \\ M_3(a) &= \frac{45H_0^2}{8|f_{R_0}|}\frac{\left(\Omega_m a^{-3} + 4\Omega_\Lambda\right)^7}{\left(\Omega_m + 4\Omega_\Lambda\right)^6}. \end{aligned} \tag{4.27}$$

In the case of the nDGP braneworld model, a similar procedure, informed by (4.8), gives the relevant expressions [98, 17]:

$$\begin{aligned} &M_1(a) = 0, \\ &M_2(\mathbf{k}_1, \mathbf{k}_2, a) = 2\frac{n^2}{H_0^2 a^4}\left(k_1^2 k_2^2 - (\mathbf{k_1}\cdot\mathbf{k_2})^2\right), \\ &M_3(\mathbf{k}_1, \mathbf{k}_2, \mathbf{k}_3, a) = 18\frac{n^2\beta(a)}{H_0^2 a^6 4\pi G\bar{\rho}_m}\Big((\mathbf{k_1}\cdot\mathbf{k_2})k_1^2 k_3^2 + 2(\mathbf{k_1}\cdot\mathbf{k_2})^2 k_3^2 \\ &- 2(\mathbf{k_1}\cdot\mathbf{k_2})(\mathbf{k_1}\cdot\mathbf{k_3})(\mathbf{k_2}\cdot\mathbf{k_3}) - (\mathbf{k_1}\cdot\mathbf{k_2})(\mathbf{k_1}\cdot\mathbf{k_3})^2\Big), \end{aligned} \tag{4.28}$$

with β defined in (4.9). It is interesting to notice that, even though the interaction term in (4.8) contains only second order derivatives, in (4.28) a 3^{rd} order

mass contribution is now present, that arises when transforming the Eulerian derivatives to the Lagrangian space through (5.9).

2-point statistics for biased tracers in GR

The perturbative theory of galaxy clustering [59], which aims to describe the statistics of biased tracers in the quasi-linear regime, consists of a perturbative description for the evolution of the underlying dark matter density field, combined with an analytical description for the bias parameters at each given order. In the case of cold dark matter, the calculation of the 2-point statistics, even in LPT, is a more straightforward process, since one just needs to plug the **q**-space Lagrangian overdensity, mapped to the Eulerian frame through (5.8), into the common expressions for the autocorrelation function:

$$\xi(r) = \langle \delta_m(\mathbf{x}) \delta_m(\mathbf{x} + \mathbf{r}) \rangle \tag{4.29}$$

and its Fourier space counterpart, the matter power spectrum

$$(2\pi)^3 \, \delta_D(\mathbf{k} + \mathbf{k}') P(k) = \langle \tilde{\delta}_m(\mathbf{k}) \tilde{\delta}_m(\mathbf{k}') \rangle. \tag{4.30}$$

When studying biased tracers, like for example dark matter halos, we need an analytical model to describe their statistical prevalance with respect to the underlying density field. Following [119, 46], we employ a model of a local in matter density Lagrangian bias in which the positions of biased tracers are purely specified by a distribution of the underlying CDM density field $\delta(\mathbf{q}, t = 0) \equiv \delta(\mathbf{q})$, encoded through a function $F\left[\delta_R(\mathbf{q})\right]$, as

$$\rho_X(\mathbf{q}) = \bar{\rho}_X F\left[\delta_R(\mathbf{q})\right], \tag{4.31}$$

where, consistent with the literature, we use the subscript X to indicate biased tracers. $\delta_R(\mathbf{q})$ denotes the primordial density field smoothed over some scale R, while $\bar{\rho}_X$ is the mean density of tracers. Density conservation provides the equivalent of equation (5.8) for tracers,

$$\delta_X(\mathbf{x}, t) = \int d^3q F\left[\delta_R(\mathbf{q})\right] \delta_D\left[\mathbf{x} - \mathbf{q} - \mathbf{\Psi}(\mathbf{q}, t)\right] - 1. \tag{4.32}$$

This model of local Lagrangian bias, which corresponds to a non-local bias in the Eulerian space, can be extended to include a biasing scheme that is non-local in the Lagrangian space [121]. Combining (5.22) and (5.23) and after some transformations one gets the general expression for the 2-point correlation function for biased tracers in LPT,

$$1 + \xi_X(r) = \int d^3q \int \frac{d^3k}{(2\pi)^3} e^{i\mathbf{k}\cdot(\mathbf{q}-\mathbf{r})} \int \frac{d\lambda_1}{(2\pi)} \frac{d\lambda_2}{(2\pi)} L(\mathbf{q}, \mathbf{k}, \lambda_1, \lambda_2), \tag{4.33}$$

with

$$L(\mathbf{q}, \mathbf{k}, \lambda_1, \lambda_2) = \tilde{F}_1 \tilde{F}_2 \underbrace{\langle e^{i\left[\lambda_1\delta_1 + \lambda_2\delta_2 + \mathbf{k}\cdot(\mathbf{\Delta})\right]} \rangle}_{K(\mathbf{q}, \mathbf{k}, \lambda_1, \lambda_2)}, \tag{4.34}$$

where $\tilde{F}_1$, $\tilde{F}_2$ are the Fourier space representations of F, with corresponding wavemodes λ_1 and λ_2 and $\mathbf{\Delta} = \mathbf{\Psi}_2 - \mathbf{\Psi}_1$. The notation $\delta(\mathbf{q}_1) \equiv \delta_1$ has been adopted for all quantities. The ensemble average K in (4.34) can be cast into an exponent of a power series in cumulants, through the cumulant expansion theorem, $\langle e^{iX} \rangle = \exp\left[\sum_{N=1}^{\infty} \frac{i^N}{N!} \langle X^N \rangle_c\right]$, which, combined with a multinomial expansion, gives:

$$K(\mathbf{q}, \mathbf{k}, \lambda_1, \lambda_2) = \exp\left[\sum \frac{i^{n+m+r}}{m!n!r!} \lambda_1^m \lambda_2^n k_{i_1} .. k_{i_r} \langle \delta_1^m \delta_1^n \Delta_{i_1} .. \Delta_{i_r} \rangle_c\right], \tag{4.35}$$

in terms of a series of correlators

$$\begin{aligned}
\sigma_R^2 &= \langle \delta^2 \rangle_c \\
\xi_L(\vec{q}) &= \langle \delta_1 \delta_2 \rangle_c, \\
A_{ij}^{mn}(\vec{q}) &= \langle \delta_i^m \delta_j^n \Delta_i \Delta_j \rangle_c, \\
W_{ijk}^{mn}(\vec{q}) &= \langle \delta_i^m \delta_j^n \Delta_i \Delta_j \Delta_k \rangle_c, \\
U_i^{mn}(\vec{q}) &= \langle \delta_1^m \delta_2^n \Delta_i \rangle_c,
\end{aligned} \tag{4.36}$$

where we adopted the commonly used notation for the Lagrangian cumulants in (5.26).

Keeping all terms in (4.35) that contain cumulants up to third order, which is the equivalent of the one-loop correction to the linear power spectrum, results in a highly oscillatory integrand that presents challenges when ensuring the integral is fully converged. [120] proposed expanding all contributions to the exponent but the scale-independent "zero-lag" piece of A_{ij}^{00}, which results in a non-perturbative resummation scheme that is simpler to handle analytically. Building upon this result, [46] proposed keeping all the terms of A_{ij}^{00} in the exponent, in their Convolution Lagrangian Perturbation Theory (CLPT) scheme. Keeping only the linear component of A_{ij}^{00} exponentiated, as done in [196, 193], and performing the λ and k integrations in (4.33) gives a CLPT expression for the 2-point real space correlation function,

$$\begin{aligned}
1 + \xi_X(r) \quad = \quad & \int d^3q \frac{e^{-\frac{1}{2}(q_i - r_i)(A_L^{-1})_{ij}(q_j - r_j)}}{(2\pi)^{3/2} |A_L|^{1/2}} \times \Bigg(1 - \frac{1}{2} G_{ij} A_{ij}^{loop} \\
& + \frac{1}{6} \Gamma_{ijk} W_{ijk} - b_1 \left(2 U_i g_i + A_{ij}^{10} G_{ij} \right) \\
& - b_2 \left(U_i^{(1)} U_j^{(1)} G_{ij} + U_i^{20} g_i \right) \\
& + b_1^2 \left(\xi_L - U_i^{(1)} U_j^{(1)} G_{ij} - U_i^{11} g_i \right) \\
& + \frac{1}{2} b_2^2 \xi_L^2 - 2 b_1 b_2 \xi_L U_i^{(1)} g_i \Bigg),
\end{aligned} \tag{4.37}$$

with

$$\begin{aligned} g_i &\equiv (A_L^{-1})_{ij}(q_j - r_j), \\ G_{ij} &\equiv (A_L^{-1})_{ij} - g_i g_j, \\ \Gamma_{ijk} &\equiv (A_L^{-1})_{ij} g_k + (A_L^{-1})_{ki} g_j + (A_L^{-1})_{jk} g_i - g_i g_j g_k. \end{aligned} \tag{4.38}$$

Furthermore, in (5.24) we define $U_i^{10} \equiv U_i$, $W_{ijk}^{000} \equiv W_{ijk}$ and use superscript numbers in brackets to indicate the various orders of contribution. The 1^{st} and 2^{nd} order Lagrangian bias factors, b_1 and b_2, are the expectation values of the 1^{st} and 2^{nd} order derivatives of the Lagrangian bias function F, respectively, through the identity [119, 121],

$$b_n \equiv \int \frac{d\lambda}{2\pi} \tilde{F}(\lambda) e^{-\frac{1}{2}\lambda^2\sigma_R^2} (i\lambda)^n = \left\langle \frac{d^n F}{d\delta^n} \right\rangle. \tag{4.39}$$

In the case of dark matter, we have $F = 1$ and $\tilde{F}(\lambda) = 2\pi\delta_D(\lambda)$ [46], and we recover $b_1 = b_2 = 0$ for the unbiased, dark matter distribution.

The Fourier transform gives the CLPT power spectrum for biased tracers [196, 193]:

$$\begin{aligned} P_X(k) &= \int d^3q e^{i\mathbf{k}\cdot\mathbf{q}} e^{-\frac{1}{2}k_i k_j A_{ij}^L} \times \Bigg(1 - \frac{1}{2} k_i k_j A_{ij}^{loop} - \frac{i}{6} k_i k_j k_k W_{ijk} \\ &\quad + b_1 \left(2ik_i U_i - k_i k_j A_{ij}^{10} \right) + b_2 \left(ik_i U_i^{20} - k_i k_j U_i^{(1)} U_j^{(1)} \right) \\ &\quad + b_1^2 \left(\xi_L + ik_i U_i^{11} - k_i k_j U_i^{(1)} U_j^{(1)} \right) \\ &\quad + \frac{1}{2} b_2^2 \xi_L^2 + 2 b_1 b_2 \xi_L i k_i U_i^{(1)} \Bigg). \end{aligned} \tag{4.40}$$

In addition to the one-loop expressions for the two-point statistics, we also calculate the Zel'dovich (1^{st} order LPT) approximation [203] for biased tracers in the configuration and Fourier space, which can be identified as the subset of terms in (5.24) and (4.40) that are linear in $P_L(k)$. These are the terms that depend on combinations of ξ_L, $U^{(1)}$ and A_{ij}^L.

While, for GR, CLPT does a very good job at modeling the configuration space $\xi(r)$, it is known to perform less well in reconstructing clustering in the Fourier space [194]. Expanding the resummed exponent in (4.40) and performing the resulting integrals gives the Eulerian one-loop Standard Perturbation Theory (SPT) power spectrum for biased tracers in GR [119],

$$\begin{aligned} P_X^{SPT}(k) &= \left(1-k^2\sigma_L^2\right)(1+b_1)^2\,P_L(k)+\frac{9}{98}Q_1(k)+\frac{3}{7}Q_2(k) \\ &\quad +\frac{1}{2}Q_3(k)+b_1\left(\frac{6}{7}Q_5(k)+2Q_7(k)\right)+b_2\left(\frac{3}{7}Q_8(k)+Q_9(k)\right) \\ &\quad +b_1^2\left(Q_9(k)+Q_{11}(k)\right)+2b_1b_2Q_{12}(k)+\frac{1}{2}b_2^2Q_{13}(k) \\ &\quad +\frac{6}{7}(1+b_1)^2\left[R_1(k)+R_2(k)\right]-\frac{8}{21}(1+b_1)R_1(k), \end{aligned} \tag{4.41}$$

where

$$\sigma_L^2=\frac{1}{6\pi^2}\int_0^\infty dk P_L(k), \tag{4.42}$$

is the 1D variance of the Lagrangian displacement and the functions Q_n and R_n were defined in [119] for GR. The SPT power spectrum has been shown to follow the power spectrum much better than the CLPT prediction in GR [194].

The correlation function obtained from Fourier transforming (4.41) is, unfortunately, known to be ill-behaved [120]. However, if one performs an alternative resummation proposed in [120, 119], known as Lagrangian Resummation Theory (LRT), the resulting power spectrum,

$$\begin{aligned} P_X^{LRT}(k) &= e^{-k^2\sigma_L^2}\Bigg[(1+b_1)^2\,P_L(k)+\frac{9}{98}Q_1(k)+\frac{3}{7}Q_2(k)+\frac{1}{2}Q_3(k) \\ &\quad +b_1\left(\frac{6}{7}Q_5(k)+2Q_7(k)\right)+b_2\left(\frac{3}{7}Q_8(k)+Q_9(k)\right) \\ &\quad +b_1^2\left(Q_9(k)+Q_{11}(k)\right)+2b_1b_2Q_{12}(k) \\ &\quad +\frac{1}{2}b_2^2Q_{13}(k)+\frac{6}{7}(1+b_1)^2\left[R_1(k)+R_2(k)\right] \\ &\quad -\frac{8}{21}(1+b_1)R_1(k)\Bigg], \end{aligned} \tag{4.43}$$

which differs from (4.41) only by the exponential prefactor, can be Fourier transformed to the configuration space and is found to characterize the BAO scales well for both dark matter [120, 194] and biased tracers [119, 46]. It decays sharply for large values of k however.

Calculation of bias parameters in GR

In this section, we present an analytical model for the calculation of the bias parameters (5.27) in GR, which will be extended to include MG in section 4.3.1. It should be noted though, that even in the complete absence of an analytical model, one or both of the bias parameters in CLPT can be treated as free parameters, to be fitted over simulations, as for example done in [46, 145]. With regards to analytical models for bias, arguably the most popular one is the halo approach [125, 124, 164, 166, 117, 133, 161, 51], that is based on the extended Press-Schechter (PS) formalism [140, 33], in combination with the Peak-Background Split (PBS) approach [86]. A discussion of the accuracy of such approaches can be found in [118, 79]. In what follows, we briefly summarize the main ingredients of this prescription in GR.

Let M_0 be the mass of a collapsed region at a redshift of interest z, that is enclosed in a Lagrangian region of radius R_0, which, given the mean matter density ρ_{m0}, will be given by

$$R_0 = \left(\frac{3M_0}{4\pi\rho_{m0}}\right)^{\frac{1}{3}}. \tag{4.44}$$

The variance of matter density fluctuations in this region is,

$$\sigma^2(M_0) = \int \frac{dkk^2}{2\pi^2} W^2\left(kR_0\right) P_L(k, z=0), \tag{4.45}$$

with $P_L(k, z = 0)$ the linear matter power spectrum evaluated today and $W(kR_0)$ the top-hat smoothing Kernel,

$$W(kR_0) = \frac{3\left[\sin(kR_0) - kR_0\cos(kR_0)\right]}{(kR_0)^3}. \tag{4.46}$$

For GR, density perturbations are evolved in time, relative to present time using the GR linear growth factor $D(z)$.

Based on the PS theory and its variants [140, 33], the comoving mean number density of halos per logarithmic mass bin $d\ln M$, $\bar{n}_h$, can be analytically modeled as:

$$\bar{n}_h(M) = \frac{\partial^2 \bar{N}_h}{\partial V \partial \ln M} = \frac{\bar{\rho}_m}{M}\nu_c(M) f\left[\nu_c(M)\right] \frac{d\ln \nu_c(M)}{dM}, \tag{4.47}$$

where $\bar{N}_h$ is the mean number of halos with mass M, in a bin of width dM, enclosed in a comoving volume V.

The quantity $\nu_c(M)$, the peak significance, is given by

$$\nu_c(M) = \frac{\delta_{cr}}{\sigma(M, z)} = \frac{\delta_{cr}}{D(z)\sigma(M)}. \tag{4.48}$$

where $D(z)$ is the linear growth factor at the time of collapse z, normalized so that $D(z = 0) = 1$. In (4.48), $\sigma(M, z) = D(z)\sigma(M)$ is the variance at redshift z, with $\sigma(M)$ the variance (4.45) evaluated today and δ_{cr} is the critical overdensity for collapse at redshift z. For an Einstein De-Sitter (EDS) cosmology, the latter is always $\delta_{cr} = 1.686$, which turns out to be a very good approximation for ΛCDM cosmologies and will be adopted here.

$f\left[\nu_c(M)\right]$ is the multiplicity function, that in the original PS theory is given by:

$$\nu_c f\left[\nu_c\right] = \sqrt{\frac{2}{\pi}}\nu_c e^{\frac{-\nu_c^2}{2}}. \tag{4.49}$$

The prescription (4.47), often referred to as the universal mass function, is exact in an EDS universe with a power law power spectrum. While (4.49) has been

used to describe the halo mass function for a broad range of cosmologies, it lacks the necessary accuracy for precision predictions. For this reason, Sheth and Tormen (ST) [166], introduced an alternative function:

$$\nu_c f\left[\nu_c\right] = \sqrt{\frac{2}{\pi}} A(p) \left[1 + \frac{1}{(q\nu_c^2)^p}\right] \sqrt{q}\nu_c e^{\frac{-q\nu_c^2}{2}}, \tag{4.50}$$

where $A(p) = \left[1 + \pi^{-\frac{1}{2}} 2^{-p} \Gamma(0.5 - p)\right]^{-1}$ and q, p are free parameters that can be fitted over N-body simulations. The best fit pair was initially proposed to be $(q, p) = (0.707, 0.3)$ which was later updated to $(q, p) = (0.75, 0.3)$. These are considered to be the "standard" ST parameters [166, 165]. For the PS function, $q = 1, p = 0$.

Based on the PBS argument [86], a large-wavelength density perturbation Δ (that is effectively constant on small scales) has the same effect on the formation of biased tracers as a modification to the mean background density by this offset. If by $\bar{n}_h(M, \Delta)$ we denote the halo mass function's response to such a perturbation, also sometimes called the conditional mass function, then the fractional overdensity of halos will be given by [125, 124, 164]:

$$1 + \delta_h(M) = \frac{\bar{n}_h(M, \Delta)}{\bar{n}_h(M, 0)}, \tag{4.51}$$

where $\bar{n}_h(M, 0) = \bar{n}_h(M)$, is the standard, unconditional halo mass function. It also worth noticing that equation (4.51) also defines $F\left[\delta_R(\mathbf{q})\right]$, through (5.21). The Lagrangian bias of order n, is then given by

$$b_n^L(M) = \frac{1}{\bar{n}_h(M, 0)} \frac{d^n \bar{n}_h(M, \Delta)}{d\Delta^n}\bigg|_{\Delta=0}, \tag{4.52}$$

where the time argument in the above is assumed and omitted for simplicity. Equation (5.28) is the rigorous definition of the bias parameters, that is exact even in the absence of an analytical description for the halo mass function and

can be calculated numerically, for example employing separate universe simulations [157]. In the presence of a universal mass function, the conditional mass function is given by the same expression (4.47), but with the modified peak significance $\nu_c'(M) = \frac{\delta_{cr}-\Delta}{D(z)\sigma(M)}$, in which case the the bias factors are easily calculated [164] by (4.51), as:

$$b_n^L(M) = \frac{(-1)^n}{\left(D(z)\sigma(M)\right)^n} \frac{1}{\nu_c f\left[\nu_c\right]} \frac{d^n\left(\nu_c f\left[\nu_c\right]\right)}{d\nu_c^n}, \tag{4.53}$$

which are the so-called PBS Lagrangian biases. Applied on the ST function (4.50), the PBS biases are:

$$\begin{aligned} b_1^L(M) &= \frac{-1}{\delta_{cr}}\left[q\nu_c^2 - 1 + \frac{2p}{1+\left(q\nu_c^2\right)^p}\right], \\ b_2^L(M) &= \frac{1}{\delta_{cr}^2}\left[q^2\nu_c^4 - 3q\nu_c^2 + \frac{2p\left(2q\nu_c^2 + 2p - 1\right)}{1+\left(q\nu_c^2\right)^p}\right]. \end{aligned} \tag{4.54}$$

These PBS biases are identical to the Lagrangian bias factors defined within the context of CLPT through (5.27) [119, 121].

4.3 Results

4.3.1 Lagrangian Perturbation Theory for Biased Tracers in MG

2-point statistics for Biased Tracers in MG

In section 4.2.2, we showed the expressions for the calculation of 2-point statistics in CLPT and its variants, under the assumption that gravitational evolution is governed by GR. Here we explain how each of these relationships have to be

modified in the case of MG theories. We note that these results are consistent with those recently presented in [17].

The two-point statistics for biased tracers in MG are given, as in GR, by the definitions 5.23 and 4.30, in the configuration and Fourier space, respectively. Considering biased tracers in the Lagrangian space, through (5.21), the overdensity of biased tracers in LPT is given by

$$\delta_X(\mathbf{x},t) = \int d^3q F\left[\delta_R(\mathbf{q})\right]\delta_D\left[\mathbf{x}-\mathbf{q}-\mathbf{\Psi}(\mathbf{q},t)\right] - 1, \tag{4.55}$$

where we used density conservation. The above equation is similar to (5.22) for GR, but differs in that the Lagrangian field $\mathbf{\Psi}(\mathbf{q})$ follows the MG evolution presented in Section 4.2.2. In particular, if we work in terms of the Fourier transform of $\mathbf{\Psi}(\mathbf{q})$, labeled as $\tilde{\mathbf{\Psi}}(\mathbf{p})$, the n^{th} order LPT solutions in MG will be given by,

$$\begin{aligned}\tilde{\Psi}_j^{(n)}(\mathbf{p}) &= \frac{i}{n!}\int \frac{d^3p_1}{(2\pi)^3}..\frac{d^3p_n}{(2\pi)^3}\delta_D^3\left(\sum_{j=1}^{n} p_j - p\right) \\ &\quad \times L_j^{(n)}(\mathbf{p}_1,..,\mathbf{p}_n)\tilde{\delta}_L(\mathbf{p}_1)..\tilde{\delta}_L(\mathbf{p}_n),\end{aligned} \tag{4.56}$$

where $\tilde{\delta}_L(\mathbf{p}_n)$ are the linear-density Fourier transformed fields at the time of evaluation and the Kernels $L_j^{(n)}(\mathbf{p}_1,..,\mathbf{p}_n)$ are given by [15]:

$$\begin{aligned}L_j^{(1)}(\mathbf{p}) &= \frac{p^j}{p^2}, \\ L_j^{(2)}(\mathbf{p}_1,\mathbf{p}_2) &= \frac{p^j}{p^2}\frac{D^{(2)}(\mathbf{p_1},\mathbf{p_2})}{D^{(1)}(p_1)D^{(1)}(p_2)}, \\ (L_j^{(3)})_{sym}(\mathbf{p}_1,\mathbf{p}_2,\mathbf{p}_3) &= i\frac{p^j}{p^2}\frac{D^{(3)}_{sym}(\mathbf{p_1},\mathbf{p_2},\mathbf{p}_3)}{D^{(1)}(p_1)D^{(1)}(p_2)D^{(1)}(p_3)}.\end{aligned} \tag{4.57}$$

The MG growth factors in (4.57), are the ones given by (4.22), (4.24) and (B.5). Plugging the overdensity (4.55) into (5.23) and (4.30) and working as in (4.33)-(5.26), we arrive at equations (5.24) and (4.40), that give the 2-point statistics for

biased tracers in MG and depend on the MG Lagrangian correlators

$$\begin{aligned}
\sigma_R^2 &= \langle \delta^2 \rangle_c \\
\xi_L(\vec{q}) &= \langle \delta_1 \delta_2 \rangle_c, \\
A_{ij}^{mn}(\vec{q}) &= \langle \delta_i^m \delta_j^n \Delta_i \Delta_j \rangle_c, \\
W_{ijk}^{mn}(\vec{q}) &= \langle \delta_i^m \delta_j^n \Delta_i \Delta_j \Delta_k \rangle_c, \\
U_i^{mn}(\vec{q}) &= \langle \delta_1^m \delta_2^n \Delta_i \rangle_c.
\end{aligned} \tag{4.58}$$

For the MG correlators (4.58), we use the same definition and index structure as in GR, but these functions differ from their GR counterparts, because the quantities in the cumulants follow the MG LPT solutions (4.57). In particular,

plugging (4.56) and (4.57) into (4.58), we get the Lagrangian correlators in MG:

$$
\begin{aligned}
V_1^{(112)}(q) &= \frac{1}{2\pi^2}\int \frac{dk}{k}\left(-\frac{3}{7}\right)[R_1(k)]_{MG}\, j_1(kq),\\
V_3^{(112)}(q) &= \frac{1}{2\pi^2}\int \frac{dk}{k}\left(-\frac{3}{7}\right)[Q_1(k)]_{MG}\, j_1(kq),\\
S^{(112)}(q) &= \frac{3}{14\pi^2}\int \frac{dk}{k}\left[2\,[R_1]_{MG}+4R_2+[Q_1]_{MG}+2Q_2\right]\frac{j_2(kq)}{kq},\\
T^{(112)}(q) &= \frac{-3}{14\pi^2}\int \frac{dk}{k}\left[2\,[R_1]_{MG}+4R_2+[Q_1]_{MG}+2Q_2\right] j_3(kq),\\
U^{(1)}(q) &= \frac{1}{2\pi^2}\int dkk\,(-1)\,P_L(k)\,j_1(kq),\\
U^{(3)}(q) &= \frac{1}{2\pi^2}\int dkk\left(-\frac{5}{21}\right)R_1(k)\,j_1(kq),\\
U_{20}^{(2)}(q) &= \frac{1}{2\pi^2}\int dkk\left(-\frac{6}{7}\right)Q_8(k)\,j_1(kq),\\
U_{11}^{(2)}(q) &= \frac{1}{2\pi^2}\int dkk\left(-\frac{6}{7}\right)[R_1(k)+R_2(k)]_{MG}\, j_1(kq),\\
X_{10}^{(12)}(q) &= \frac{1}{2\pi^2}\int dk\frac{1}{14}\Bigg(2\left([R_1]_{MG}-R_2(k)\right)+3\,[R_1]_{MG}\, j_0(kq)\\
&- 3\quad\left[[R_1]_{MG}+2R_2+2\left[R_1(k)+R_2(k)\right]_{MG}+2Q_5\right]\frac{j_1(kq)}{kq}\Bigg),\\
Y_{10}^{(12)}(q) &= \frac{1}{2\pi^2}\int dk\left(-\frac{3}{14}\right)\Bigg([R_1]_{MG}+2R_2\\
&\qquad +2\left[R_1(k)+R_2(k)\right]_{MG}+2Q_5\Bigg)\times\left[j_0(kq)-3\frac{j_1(kq)}{kq}\right],\\
X(q) &= \frac{1}{2\pi^2}\int dk\; a(k)\left[\frac{2}{3}-2\frac{j_1(kq)}{kq}\right],\\
Y(q) &= \frac{1}{2\pi^2}\int dk\; a(k)\left[-2\,j_0(kq)+6\frac{j_1(kq)}{kq}\right],
\end{aligned}
\tag{4.59}
$$

where we additionally performed the decompositions

$$
\begin{aligned}
A_{ij}^{mn}(q) &= X_{mn}(q)\delta_{ij}+Y_{mn}\hat{q}_i\hat{q}_j\\
W_{ijk}(q) &= V_1(q)\hat{q}_i\delta_{jk}+V_2(q)\hat{q}_j\delta_{ki}+V_3(q)\hat{q}_k\delta_{ij}+T(q)\hat{q}_i\hat{q}_j\hat{q}_k
\end{aligned}
\tag{4.60}
$$

and defined $a(k) = P_L(k) + \frac{9}{98}Q_1(k) + \frac{10}{21}R_1(k)$. The functions $Q_n(k)$ and $R_n(k)$ that

appear in the r.h.s of (4.59), are defined, as in GR, to be:

$$\begin{aligned} Q_n(k) &= \frac{k^3}{4\pi^2}\int_0^\infty dr P_L(kr) \\ &\quad \times \int_{-1}^{1} dx P_L(k\sqrt{1+r^2-2rx})\tilde{Q}_n(r,x) \\ R_n(k) &= \frac{k^3}{4\pi^2}P_L(k)\int_0^\infty dr P_L(kr)\int_{-1}^{1} dx \tilde{R}_n(r,x). \end{aligned} \tag{4.61}$$

The scale and redshift dependency of the growth factors alters the evaluation of these expressions relative to GR:

$$\begin{aligned} \tilde{Q}_1 &= r^2\left(\bar{D}_a^{(2)} - \bar{D}_b^{(2)}\frac{x^2+r^2-2rx}{1+r^2-2rx} + \bar{D}_{FL}^{(2)} - \bar{D}_{\delta I}^{(2)}\right)^2 \\ \tilde{Q}_2 &= \frac{rx(1-rx)}{1+r^2-2rx}\left(\bar{D}_a^{(2)} - \bar{D}_b^{(2)}\frac{x^2+r^2-2rx}{1+r^2-2rx} + \bar{D}_{FL}^{(2)} - \bar{D}_{\delta I}^{(2)}\right) \\ \tilde{Q}_3 &= \frac{x^2(1-rx)^2}{(1+r^2-2rx)^2} \\ \tilde{Q}_5 &= rx\left(\bar{D}_a^{(2)} - \bar{D}_b^{(2)}\frac{x^2+r^2-2rx}{1+r^2-2rx} + \bar{D}_{FL}^{(2)} - \bar{D}_{\delta I}^{(2)}\right) \\ \tilde{Q}_7 &= \frac{x^2(1-rx)}{(1+r^2-2rx)} \\ \tilde{Q}_8 &= r^2\left(\bar{D}_a^{(2)} - \bar{D}_b^{(2)}\frac{x^2+r^2-2rx}{1+r^2-2rx} + \bar{D}_{FL}^{(2)} - \bar{D}_{\delta I}^{(2)}\right) \\ \tilde{Q}_9 &= \frac{rx(1-rx)}{1+r^2-2rx} \\ \tilde{Q}_{11} &= x^2 \\ \tilde{Q}_{12} &= rx \\ \tilde{Q}_{13} &= r^2 \\ \left[\tilde{Q}_1\right]_{MG} &= \frac{r^2(1-x^2)}{1+r^2-2rx}\left(\bar{D}_a^{(2)} - \bar{D}_b^{(2)}\frac{x^2+r^2-2rx}{1+r^2-2rx} + \bar{D}_{FL}^{(2)} - \bar{D}_{\delta I}^{(2)}\right). \end{aligned} \tag{4.62}$$

and

$$\begin{aligned}
\tilde{R}_1 &= \frac{21}{10} r^2 \frac{D^{(3)}_{sym}(\mathbf{k}, -\mathbf{p}, \mathbf{p})}{D^{(1)}(\mathbf{k}) \left(D^{(1)}(\mathbf{p})\right)^2} \\
\tilde{R}_2 &= \frac{rx(1-rx)}{1+r^2-2rx} \left(\bar{D}^{(2)}_a - \bar{D}^{(2)}_b x^2 + \bar{D}^{(2)}_{FL} - \bar{D}^{(2)}_{\delta I}\right) \\
\left[\tilde{R}_1(k) + \tilde{R}_2(k)\right]_{MG} &= \frac{r^2(1-rx)}{1+r^2-2rx} \left(\bar{D}^{(2)}_a - \bar{D}^{(2)}_b x^2 + \bar{D}^{(2)}_{FL} - \bar{D}^{(2)}_{\delta I}\right) \\
\left[\tilde{R}_1\right]_{MG} &= \frac{r^2(1-x^2)}{1+r^2-2rx} \left(\bar{D}^{(2)}_a - \bar{D}^{(2)}_b x^2 + \bar{D}^{(2)}_{FL} - \bar{D}^{(2)}_{\delta I}\right).
\end{aligned} \tag{4.63}$$

The functions Q_1-Q_{13} in (4.62) and R_1, R_2 in (4.63) differ from GR as they depend on the MG growth factors (4.22), (4.24) and (B.5). In addition, the functions $[Q_1]_{MG}$, $[R_1]_{MG}$ and $[R_1(k) + R_2(k)]_{MG}$ are new ones that arise in MG. In the GR limit, that corresponds to $\bar{D}^{(2)}_a = \bar{D}^{(2)}_b = 1$ and $\bar{D}^{(2)}_{FL} = \bar{D}^{(2)}_{\delta I} = 0$, $[Q_1]_{MG} = Q_1$, $[R_1]_{MG} = R_1$, $[R_1(k) + R_2(k)]_{MG} = R_1(k) + R_2(k)$ and the functions Q_n and R_n reduce to their GR expressions in [120]. In that limit, furthermore, the correlators (4.59) recover their GR forms presented in [46]. The derivations of the above, along with a more detailed discussion, are presented in Appendices B.1 and B.2.

In Figure 4.1, we show the contributions of the different terms in (5.24) as a function of r for the F4 model (which predicts the largest deviations from GR), evaluated at $z = 0.5$.

As in the GR case, proceeding to expand the resummed exponent in (4.40) and performing the resulting integrals, as shown in Appendix B.3, gives the equivalent of the Eulerian one-loop SPT power spectrum for biased tracers in

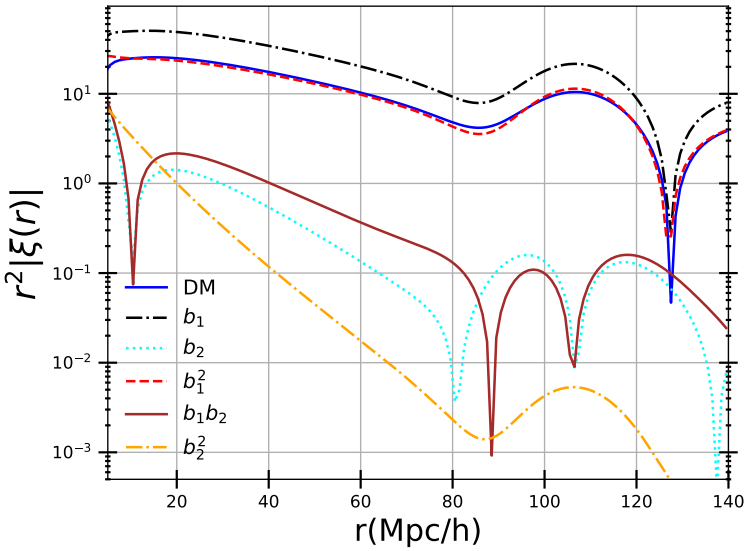

Figure 4.1: Contributions to the CLPT correlation function prediction, ξ, given in (5.24), for the F4 model at z=0.5, by the various terms in the expansion: dark matter (no bias prefactors) [blue solid], b_1 term [black dash-dot], b_2 term [cyan dotted], b_1^2 term [red dash], b_2^2 term [orange dash-dot] and $b_1 b_2$ term [brown solid].

MG:

$$
\begin{aligned}
&P_X^{SPT}(k) = \\
&\left(1 - k^2\sigma_L^2\right)(1+b_1)^2\, P_L(k) + \frac{9}{98}Q_1(k) + \frac{3}{7}Q_2(k) + \frac{1}{2}Q_3(k) \\
&+ b_1\left(\frac{6}{7}Q_5(k) + 2Q_7(k)\right) + b_2\left(\frac{3}{7}Q_8(k) + Q_9(k)\right) \\
&+ b_1^2\left(Q_9(k) + Q_{11}(k)\right) + 2b_1 b_2 Q_{12}(k) \\
&+ \frac{1}{2}b_2^2 Q_1 3(k) + \frac{6}{7}\left(b_1^2 + b_1\right)\left[R_1(k) + R_2(k)\right]_{MG} \\
&+ \frac{6}{7}(1+b_1)\left[R_1(k) + R_2(k)\right] - \frac{8}{21}(1+b_1)\, R_1(k).
\end{aligned}
\tag{4.64}
$$

Equation (4.64), that depends on the functions (4.61), is the MG version of (4.41). Appendix B.1 provides a more thorough discussion. While we refer to this as the "SPT" expression, we note that, unlike in GR, where equation (4.41) has been shown to be identical to the SPT expression, in MG, additional terms

that appear when transforming the Klein-Gordon equation from Eulerian to Lagrangian coordinates need to be considered to show the equivalence [17].

The LRT power spectrum for MG theories is obtained, just like in GR, by keeping the zero-lag term exponentiated:

$$\begin{aligned} P_X^{LRT}(k) &= e^{-k^2\sigma_L^2}\Bigg[(1+b_1)^2 P_L(k) + \frac{9}{98}Q_1(k) + \frac{3}{7}Q_2(k) + \frac{1}{2}Q_3(k) \\ &+b_1\left(\frac{6}{7}Q_5(k) + 2Q_7(k)\right) + b_2\left(\frac{3}{7}Q_8(k) + Q_9(k)\right) \\ &+b_1^2\left(Q_9(k) + Q_{11}(k)\right) + 2b_1b_2Q_{12}(k) \\ &+\frac{1}{2}b_2^2Q_13(k) + \frac{6}{7}\left(b_1^2 + b_1\right)\left[R_1(k) + R_2(k)\right]_{MG} \\ &+\frac{6}{7}\left(1+b_1\right)\left[R_1(k) + R_2(k)\right] - \frac{8}{21}\left(1+b_1\right)R_1(k)\Bigg]. \end{aligned} \tag{4.65}$$

The derivation is discussed in Appendix B.3. The configuration space counterpart, $\xi_X^{LRT}(r)$, is obtained by Fourier transforming (4.65),

$$\begin{aligned} \xi_X^{LRT}(r) &= \int \frac{d^3k}{(2\pi)^3} e^{i\mathbf{k}\cdot\mathbf{r}} P_X^{LRT}(k) \\ &= \int \frac{dk}{2\pi^2} k^2 P_X^{LRT}(k)\, j_0(kr), \end{aligned} \tag{4.66}$$

with $j_0(kr)$ the zeroth-order Bessel function.

To evaluate the expressions (5.24), (4.40), (4.64) and (4.65) we modified a publicly available code released by [193] in [1], that efficiently performs the 2D integrals in (5.24), (4.40) using Haskel transformations, as well those in (4.59) and (4.61). On top of the functions Q_1-Q_{13} and R_1, R_2, the code was extended to evaluate the new functions $[Q_1]_{MG}$, $[R_1]_{MG}$ and $[R_1(k) + R_2(k)]_{MG}$, as well as the modified correlators (4.59). We make this code publicly available in [2]. Our modified version accepts the modified gravity model growth factors, $D_{MG}(k, z)$

[1] https://github.com/martinjameswhite/CLEFT_GSM
[2] https://github.com/CornellCosmology/bias_MG_LPT_products

as input along with the linear power spectrum given by:

$$P^L_{MG}(k,z) = \left(\frac{D^1_{MG}(k,z)}{D^1_{GR}(k,0)}\right)^2 P^L_{GR}(k,0). \tag{4.67}$$

The linear power spectrum for the background ΛCDM cosmology is calculated using the publicly available code CAMB [107].

After calculating the necessary MG growth factors using our *Mathematica* notebook, we feed our modified version of the code with tabulated values of the growth factors for the various values of k, r and x needed at a given cosmological redshift z. The PYTHON module computes the various $Q_n(k)$ and $R_n(k)$ functions through equations (4.62) and (4.63), which are then used to calculate the various components of the CLPT power spectrum $P_X(k)$. The k functions can then be simply combined to give the SPT and LRT power spectra, by equations (4.64) and (4.65), respectively. Finally, the modified C++ counterpart follows a similar procedure to compute the configuration space two-point correlation function given by CLPT, through (5.24). The procedure is explained in more detail in the Appendix B.2.

We finish this section by noting that, even though we restrict our model to the case of a local Lagrangian bias, our framework can be extended to include a curvature bias and/or corrections from EFT, as in [193]. For modified gravity theories with scale-dependent growth, a general expansion bias is not possible in principle, though for some theories, such as the $f(R)$, the effects of the fifth force can be perturbatively absorbed in terms of higher-order derivatives [59, 17].

Calculation of bias parameters in MG

In this section we turn to the final necessary ingredient to describe biased tracers, an analytical model for the calculation of the bias parameters in MG.

Central to the GR derivation in Section 4.2.2, is the assumption that spherical collapse is independent of the exterior spacetime, which, in the case of GR evolution, is given by Birkhoff's theorem. In MG theories, however, the additional degree of freedom violates Birkhoff's theorem, which will have important consequences for the modeling of the halo mass function, as well as on its response to an external density perturbation.

The Press-Schechter formalism (4.47) relies upon the assumption that the linearly evolved critical overdensity, δ_{cr}, is always constant at the time of collapse, for example $\delta_{cr} = 1.686$ for an EDS evolution. This is not the case for MG due to the presence of the additional scalar field that generates the fifth forces. Following [109, 115], if we define $1 + \delta_h = y_h^{-3}$, the evolution of a spherically symmetric halo density perturbation, will be given by:

$$y_h'' - \left(2 - \frac{3}{2}\Omega(a)\right) y_h' + \frac{1}{2}\Omega(a)\frac{G_{eff}}{G}\left(y_h^{-3} - 1\right) y_h = 0, \tag{4.68}$$

where $'$ denotes derivatives with respect to $\ln(a)$ and G_{eff}, the modified Newton's constant, is given by

$$G_{eff} = (1 + E)\, G, \tag{4.69}$$

For the nDGP braneworld model,[156]

$$E = \frac{2}{3\beta(a)} \frac{\sqrt{1 + \chi^3} - 1}{\chi^{-3}}, \tag{4.70}$$

where $\beta(a)$ was defined in (4.28) and

$$\chi^{-3} = \frac{\Omega_m n^2}{1.10894 a^3 \beta^2(a)} \frac{y_h^3 - 1}{y_h^3}, \tag{4.71}$$

with the nDGP parameter, $n = H_0 r_c$. Note that the fifth force modification does not depend on either the mass or the environment, a property of the Vainshtein mechanism, which means that the collapse barrier for this model is redshift and scale independent [156, 22]. Thanks to this property, the halo biases for this model can be easily calculated by the corresponding GR expressions (4.54), with a different value for the *constant* threshold δ_{cr}. For the background cosmology of the Group I simulations, at $z = 0.5$, we integrate equation (4.68) and find δ_{cr} to have values (linearly extrapolated at $z = 0.5$) of $\delta_{cr} = 1.571$ and $\delta_{cr} = 1.657$ for the N1 ($n = 1$) and N5 ($n = 5$) cases, respectively.

For $f(R)$ models, for a collapsing sphere of mass M and radius R_{th}, E is given by

$$E = 2\beta^2 \left[3\frac{\Delta R}{R_{th}} - 3\left(\frac{\Delta R}{R_{th}}\right)^2 + \left(\frac{\Delta R}{R_{th}}\right)^3 \right], \tag{4.72}$$

with $\beta = \frac{1}{\sqrt{6}}$. Finally, $\frac{\Delta R}{R_{th}}$ is given by

$$\begin{aligned} \frac{\Delta R}{R_{th}} &= \frac{|f_{R0}| a^3}{\Omega_m y_h^{-3} H_0^2 R_{th}^2} \\ &\times \left[\left(\frac{1 + 4\frac{\Omega_\Lambda}{\Omega_m}}{(y_{env} a)^{-3} + 4\frac{\Omega_\Lambda}{\Omega_m}} \right)^{n+1} - \left(\frac{1 + 4\frac{\Omega_\Lambda}{\Omega_m}}{(y_h a)^{-3} + 4\frac{\Omega_\Lambda}{\Omega_m}} \right)^{n+1} \right]. \end{aligned} \tag{4.73}$$

Here the overdensity related to y_h is embedded on a longer wavelength environment with over density, $1 + \delta_{env} = y_{env}^{-3}$. In models that realize the chameleon screening mechanism, like the $f(R)$ Hu-Sawicki, only a thin shell of a massive sphere contributes to the fifth force, with a fractional thickness $\frac{\Delta R}{R_{th}}$, that causes an enhancement given by E. It is this factor E that causes the environmental dependence of spherical collapse in MG, through (4.68). When set equal to zero, we recover the standard GR solution, which is the one that describes the evolution of the environment, since on such a long wavelength perturbations $G_{eff} \approx G$

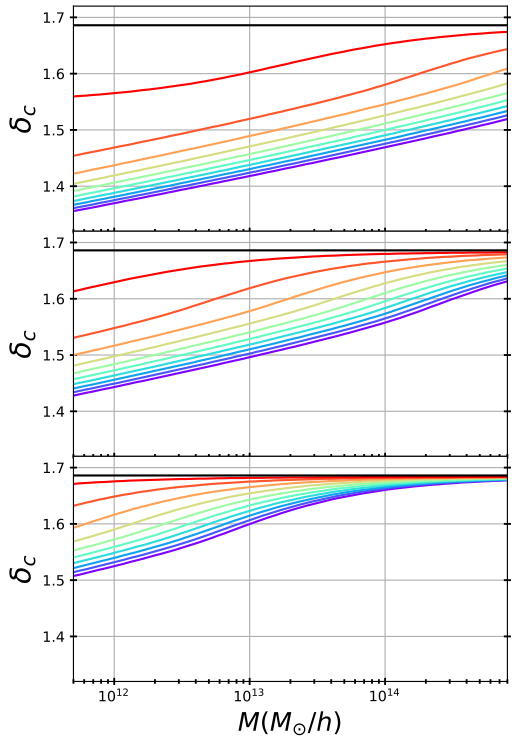

Figure 4.2: Critical overdensity for collapse, δ_{cr}, as a function of halo mass for the F4 [top], the F5 [middle] and the F6 [bottom] MG models at $z = 0.5$ and for various environments. The different color curves correspond to the solutions for the following values of the environment overdensity, $\delta_{env} = [-1(\text{purple}), -0.72, -0.43, -0.15, 0.13, 0.42, 0.7, 0.98, 1.27, 1.55(\text{red})]$. The horizontal black line shows the $\delta_{cr} = 1.686$ value for GR. The background cosmology is that of the Group I simulations.

and we have:

$$y''_{env} - \left(2 - \frac{3}{2}\Omega(a)\right) y'_{env} + \frac{1}{2}\Omega(a)\left(y_{env}^{-3} - 1\right) y_{env} = 0. \tag{4.74}$$

In light of the coupling between a collapsing halo and the background on which it evolves, as seen through (4.68), it is clear that in MG the collapse barrier, δ_{cr}, that is constant in GR, should now be promoted to a function of both the mass M and the environment overdensity δ_{env}. For each choice of M and δ_{env_i},

equations (4.68) and (4.74) form a system of coupled differential equations that we solve simultaneously, as in [109, 115]. The critical overdensity is identified as the smallest value of the boundary condition $\delta_h(a_i)$ at the initial scale factor $a_i = 0.002$, that causes a singularity i.e. signifying the onset of nonlinear collapse, at the scale factor of interest, which is then evolved to that scale factor a through [109, 115]:

$$\delta_h(a) = \frac{D^{(1)}(a)}{D^{(1)}(a_i)}\delta_h(a_i), \tag{4.75}$$

with $D^{(1)}$ the linear GR growth factor

In Figure 4.2, we show the critical density, $\delta_{cr}(z, M, \delta_{env})$ as a function of mass, M, for the three $f(R)$ models at $z = 0.5$, as it was obtained for a variety of environmental densities, δ_{env}. Because the gravitational strength, G_{eff}, is greater in the modified models this allows haloes to form more easily, translating into a lower value of δ_{cr} than the value in ΛCDM. G_{eff} is scale dependent and tends towards the GR value on large scales (which would collapse into large mass haloes). GR is also recovered for highly screened models and high density environments. For this reason the critical threshold tends towards the GR value $\delta_{cr} = 1.686$ for smaller values of f_{R0}, increasing values of M and more positive values of δ_{env} (regions with larger screening) as found in [109, 115]. The deviations from GR become progressively less pronounced as we move from weaker (F4, top panel) to stronger (F6, lower panel) screening, as one would expect.

Having calculated the function $\delta_{cr}(z, M, \delta_{env})$ for the three $f(R)$ models, the MG halo mass function can be again given by the universal prescription (4.47), but now with a modified peak significance

$$\nu_{cMG}(z, M, \delta_{env}) = \frac{\delta_{cr}(z, M, \delta_{env})}{D^{(1)}(z)\sigma(M)}. \tag{4.76}$$

The growth factors in MG are scale-dependent, meaning that in equation (4.76)

one should in principle use $D^{(1)}_{MG}(k,z)$, however, it has been shown [109, 115], that it is sufficient to use the GR growth factor, $D^{(1)}(z)$ to define the ν_c parameters. Modifications beyond this assumption are accounted for later in the free parameters of the halo mass function.

The dependence on the mass and the environment alters, and makes environment dependent, not only the unconditional halo mass function in MG, but also the conditional one. In the presence of a long-wavelength density perturbation, Δ, the conditional halo mass function will be again described by (4.47), but now with a modified ν'_{cMG} given by:

$$\nu'_{cMG}(M,\delta_{env}) = \frac{\delta_{cr}(z,M,\delta_{env}+\Delta)-\Delta}{D^{(1)}(z)\sigma(M)}. \tag{4.77}$$

Application of the bias definition (5.28) in that case, gives the first and second order bias parameters

$$\begin{aligned}
b^1_{MG}(M,\delta_{env}) &= \frac{\frac{d\delta_{cr}(M,\delta_{env})}{d\delta_{env}}-1}{\delta_{cr}(M,\delta_{env})}\left[q\nu^2_{cMG}-1+\frac{2p}{1+\left(q\nu^2_{cMG}\right)^p}\right],\\
b^2_{MG}(M,\delta_{env}) &= \\
&\frac{\left(\frac{d\delta_{cr}(M,\delta_{env})}{d\delta_{env}}-1\right)^2}{\delta^2_{cr}(M,\delta_{env})}\left[q^2\nu^4_{cMG}-3q\nu^2_{cMG}+\frac{2p\left(2q\nu^2_{cMG}+2p-1\right)}{1+\left(q\nu^2_{cMG}\right)^p}\right]\\
&+\frac{d^2\delta_{cr}(M,\delta_{env})}{d\delta^2_{env}}\frac{1}{\delta_{cr}(M,\delta_{env})}\left[q\nu^2_{cMG}-1+\frac{2p}{1+\left(q\nu^2_{cMG}\right)^p}\right].
\end{aligned} \tag{4.78}$$

In the case of a sample of halos in a mass range of width dM around a single value M, the conditional and unconditional mass functions need to be first av-

eraged over the mass range,

$$
\begin{aligned}
&b^1_{MG}(M,\delta_{env}) = \\
&\frac{1}{I_{dM}}\int\left[\frac{\left(\frac{d\delta_{cr}(M,\delta_{env})}{d\delta_{env}}-1\right)}{\delta_{cr}(M,\delta_{env})}\frac{\nu_{cMG}}{M}\frac{\partial f[\nu_{cMG}]}{\partial\nu_{cMG}}\frac{d\ln\nu_{cMG}}{dM}\right]dM, \\
&b^2_{MG}(M,\delta_{env}) = \\
&\frac{1}{I_{dM}}\int\left[\frac{\left(\frac{d\delta_{cr}(M,\delta_{env})}{d\delta_{env}}-1\right)^2}{\delta^2_{cr}(M,\delta_{env})}\frac{\nu^2_{cMG}}{M}\frac{\partial^2 f[\nu_{cMG}]}{\partial\nu^2_{cMG}}\frac{d\ln\nu_{cMG}}{dM}\right]dM \\
&+\frac{1}{I_{dM}}\int\left[\frac{\frac{d^2\delta_{cr}(M,\delta_{env})}{d\delta^2_{env}}}{\delta_{cr}(M,\delta_{env})}\frac{\nu_{cMG}}{M}\frac{\partial f[\nu_{cMG}]}{\partial\nu_{cMG}}\frac{d\ln\nu_{cMG}}{dM}\right]dM,
\end{aligned}
\tag{4.79}
$$

with

$$
I_{dM} = \int\left[\frac{f[\nu_{cMG}]}{M}\frac{d\ln\nu_{cMG}}{dM}\right]dM. \tag{4.80}
$$

The details of the peak-background split derivations, for (4.78), (4.79), are shown in more detail in Appendix C.

We note that another popular method, as an alternative to PBS, for calculating halo biases is the excursion set approach [33]. Here the universal halo mass function is associated with the Brownian-walk, first crossing distribution of a collapse threshold. In the GR case, the redshift and scale independence of the collapse barrier leads to an analytical solution that recovers the common PBS biases. Given the potential scale, environment and redshift dependence that δ_{cr} has in MG models however, there is no analytical solution for the excursion set approach in MG and one would need to perform numerical simulations, rather than analytic prediction available for PBS, to determine the predicted biases [109, 102, 110].

In order to make predictions to compare against simulations, given that the correlation statistics sample a distribution of environments, rather than a spe-

cific value of δ_{env}, we average all environment-dependent quantities over a probability distribution for environments in which halos form and reside, defining these on a fixed scale ζ which we set to 8 Mpch$/h$ [101, 110, 102],

$$p_\zeta(\delta_{env}) = \frac{\beta^{0.5\omega}}{\sqrt{2\pi}}\left[1 + (\omega - 1)\frac{\delta_{env}}{\delta_{cr}}\right]\left(1 - \frac{\delta_{env}}{\delta_{cr}}\right)^{-0.5\omega-1}, \\ \times \exp\left[-\frac{\beta^\omega}{2}\frac{\delta_{env}}{\left(1 - \frac{\delta_{env}}{\delta_{cr}}\right)^\omega}\right], \tag{4.81}$$

where $\beta \equiv \left(\frac{\zeta}{8}\right)^3/(\delta_{cr}\sigma_8^{(2/\omega)})$ with $\omega \equiv \delta_{cr}\frac{n_s+3}{3}$.

The list of environments over which we average the other dependent quantities for the rest of this work, is $\delta_{env} = [-1, -0.72, -0.43, -0.15, 0.13, 0.42, 0.7, 0.98, 1.27, 1.55]$.

In Figure 4.3 we demonstrate the impact of the reduced δ_{cr} values in modified gravity models, separately from modifications to the halo mass function itself, by plotting the environmentally averaged bias parameters b^1_{MG} and b^2_{MG} for GR and three $f(R)$ models we study calculated from relations (4.54) and (4.78), while assuming *the same underlying halo mass model*, with $(q, p) = (0.707, 0.3)$ for *all* models. As described earlier, the increased gravitational strength in modified gravity models, parameterized by G_{eff} in (4.69), allows haloes of a given mass to collapse more readily, yielding a lower critical threshold values for δ_{cr} and a lower bias relative to the background (reduced b_1 relative to GR). The deviations from GR are most pronounced in the models with least screening, like the $F4$ model and are suppressed in the presence of stronger screening.

To accurately predict the biases in the various modified gravity models, we also need to accurately characterize the halo mass function. The values $(q = 0.707, p = 0.3)$ used to characterize the ST halo mass function in GR were fixed by fitting to ΛCDM simulations [166] and would not be expected to predict the mass function for modified gravity theories, given the different physics

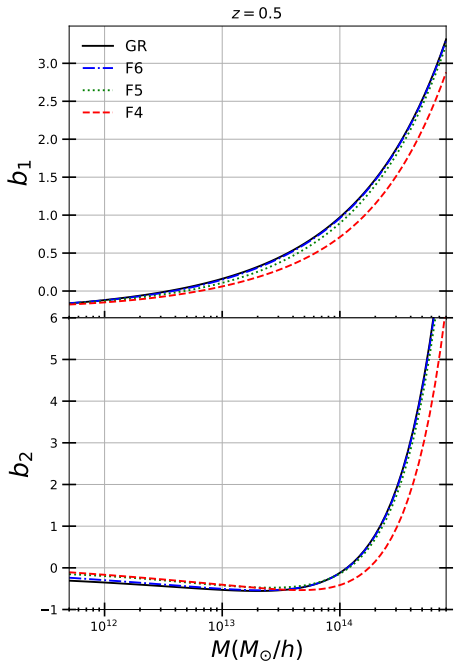

Figure 4.3: First and second order Lagrangian bias factors b_1 [Top] and b_2 [Bottom], as a function of halo mass M, calculated for GR [solid black], F6 [dash-dot blue], F5 [green dotted] and F4 [red dash], through relationships (4.54) and (4.78), using the Sheth-Tormen values $(q, p) = (0.707, 0.3)$ at $z = 0.5$. For the 3 $f(R)$ models, the biases are the environmentally averaged.

involved in the growth rate and collapse of nonlinear structures. Since the form of the halo mass function is critical to evaluating the biases for the LPT correlation function and power spectra predictions, we determine the best fit values for (q, p) from the simulated halo mass functions for each model in the mass ranges considered. These then uniquely determine the predictions for the biased tracer correlation and power spectra. This approach minimizes the errors that would be introduced at the outset of the LPT modeling from an inaccurate halo mass function. To do this, we evaluate the environment averaged Sheth-Tormen halo mass function (4.47) for various pairs values of (q, p), each using the MG prescription (4.76), over the distribution of environments (4.81) and identify the

pair of values that best fits the corresponding halo mass functions from the simulations, through the simple criterion that minimizes the quantity

$$\sum_i \left| \frac{n^{sim}(M_i)}{n^{ST}(M_i, q, p)} - 1 \right|, \tag{4.82}$$

previously used to fit the halo mass function in Galileons [22, 23]. In (4.82), i is the number of mass bins over which the sum is performed, which, can be tuned to model a narrow mass range rather than fitting the whole range with a single set of parameters.

In Figure 4.4, we plot the halo mass functions for the GR and three $f(R)$ MG models we consider at $z = 0.5$, together with the best fit ST halo mass functions obtained through (4.82). In the case of $f(R)$ gravity, we plot both the mean ST halo mass function, as well as the halo mass function for each value of δ_{env}, to give a sense of the variation among various different environments.

In Table 4.1, we show the best fit values of (q, p) for the different models, mass ranges and simulations considered. For Group I simulations, we study predictions at $z = 0.5$ for halos in a mass range $(2 - 3.5) \times 10^{12} M_\odot/h$, for all models. For the Group II simulations we analyze a $z = 1$ snapshot, where we consider halos in three separate mass bins: a lower mass bin of $9 \times 10^{11} - 2 \times 10^{12}\ M_\odot/h$, an intermediate bin of $5 \times 10^{12} - 1 \times 10^{13}\ M_\odot/h$ and a higher mass bin, $1.1 \times 10^{13} - 9 \times 10^{13}\ M_\odot/h$.

In Figure 4.5 we present the predicted correlation function, ξ_{env} for different environments for the F6 model, along with the correlation function for the environment averaged bias values. Changing the environment can have a notable effect on the predicted correlation function, with variations of $\sim 10\%$ for the F6 model presented in the figure. A decrease in the background environmental density corresponds to a reduction in the correlation function because

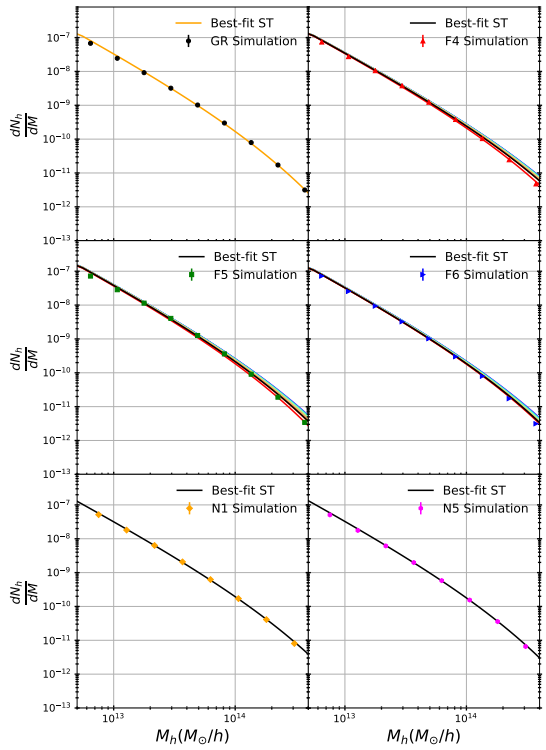

Figure 4.4: Halo mass function, in the form of number of halos dN_h, per mass bin dM, as a function of halo mass M, calculated from the Group I simulations at $z = 0.5$, for GR [black dot] in the upper left panel, F4 [red triangle] in the upper right panel, F5 [green square] in the middle left panel, F6 in the middle right panel and $N1$ and $N5$ nDGP models in the lower left and right panels, respectively . Alongside with the simulations, we show the analytical Sheth-Tormen halo mass functions (4.47), plotted using the best-fit (q, p) values for each model using the criterion (4.82). For the $f(R)$ models, the best-fit values correspond to the environmentally averaged halo mass function, through (4.81), shown with black curves, while we also plot the halo mass functions for individual values for δ_{env} for each $f(R)$ model. The color scheme and distribution of values for δ_{env} is the same as in Figure 4.2.

lower values of δ_{env} give rise to a lower δ_{cr} and consequently a lower value for the linear bias b_1.

	Best-fit ST		Predicted Biases	
Models	q	p	b_1	b_2
Group I : *GR*	0.726	0.345	0.301	-0.501
Group I : *F*4	0.671	0.361	0.120	-0.435
Group I : *F*5	0.765	0.321	0.211	-0.470
Group I : *F*6	0.670	0.362	0.230	-0.449
Group I : *N*1	0.701	0.369	0.224	-0.661
Group I : *N*5	0.702	0.357	0.268	-0.503
Group II : *GR Low*	0.674	0.362	0.345	-0.183
Group II : *GR Mid.*	0.728	0.342	0.925	-0.05
Group II : *GR High*	0.806	0.594	1.720	1.900
Group II : *F5 Low*	0.733	0.314	0.295	-0.170
Group II : *F5 Mid.*	0.788	0.282	0.909	-0.033
Group II : *F5 High*	0.746	0.305	1.491	0.416

Table 4.1: The table presents the values for the best-fit Sheth-Tormen parameters (q, p) for the halo mass function (4.47), with respect to the simulations, through the criterion (4.82), as well as the bias factors b_1 and b_2 evaluated through (4.79) using the best-fit values. All the evaluations for the Group I simulations were performed at redshift $z = 0.5$ and for the Group II simulations at $z = 1$. The labels low, mid. and high indicate reference to the three mass bins, specified in the text. For all $f(R)$ models, the bias values shown are environmentally averaged as described in the text.

4.3.2 Comparison with simulations

In this Section, we compare the performance of the various LPT resummation schemes under consideration, combined with our bias model, against the corresponding results from the Group I and Group II simulations, discussed in Section 4.2.1, with respect to the correlation function and the power spectrum. All correlation functions from the simulations have been calculated employing the publicly available code *CUTE* [9], using 30 linearly spaced bins in the range $0 - 140$ Mpc$/h$. The power spectra, on the other hand, have been extracted using a Cloud-In-Cell (CIC) mass assignment scheme, on a grid with resolution of

$N_{grid} = 1024^3$ and $N_{grid} = 1200^3$ cells, for the Group I and Group II simulations, respectively. The power was binned in 30 linearly spaced points in the k range of $0.008 - 0.3$ h/Mpc.

As discussed in Section 4.3.1, for Group I simulations, we study predictions at $z = 0.5$ for halos in the mass range $(2 - 3.5) \times 10^{12} M_\odot/h$, for all models. For the Group II simulations we analyze a $z = 1$ snapshot, where we consider halos in three separate mass bins: a lower mass bin of $9 \times 10^{11} - 2 \times 10^{12}$ $M_\odot/h$, an intermediate bin of $5 \times 10^{12} - 1 \times 10^{13}$ $M_\odot/h$ and a higher mass bin, $1.1 \times 10^{13} - 9 \times 10^{13}$ $M_\odot/h$.

Correlation function

To assess the accuracy and performance of the LPT predictions, we first utilize the Group II simulations as a comparison dataset. Given that we only have 1 realization available for the F5 and GR models, the correlation functions exhibit noise due to the random initial phase, but still facilitate valuable conclusions about the performance of the methods tested given the appropriate combination of large volume and high resolution. These allow us to evaluate the performance of CLPT and its variations simultaneously across a wide range of scales, including both the BAO scales and the region roughly following a power-law scaling relation, down to $r \sim 5$ Mpc$/h$.

The LPT predictions use the PBS biases evaluated from the best fit halo mass function, when fitted over the specific mass ranges, for each bin as summarized inTable 4.1). Both the LPT and simulation results are compared to the Zel'dovich prediction for the correlation function.

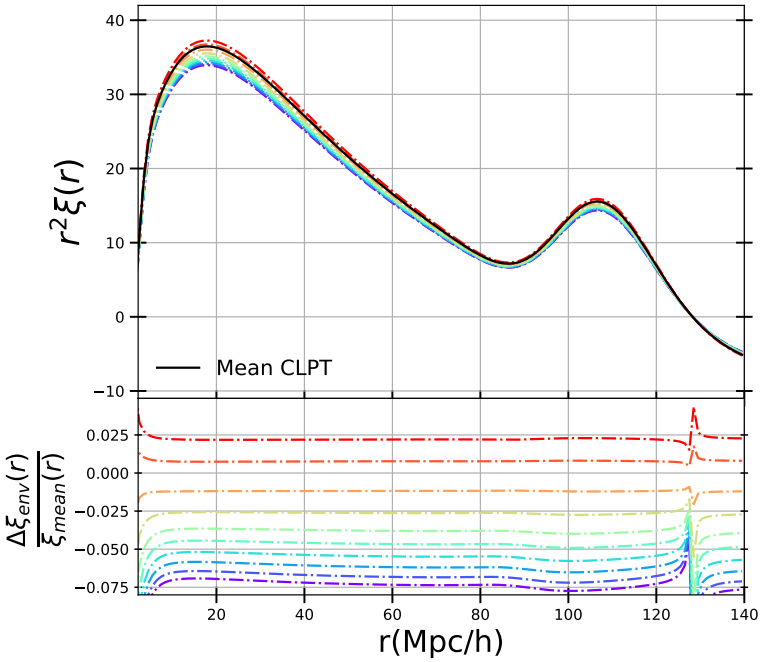

Figure 4.5: [Top] Two-point correlation function prediction form CLPT, through (5.24), for the F6 model at $z = 0.5$ for the various bias values given when $\delta_{env} = [-1(\text{purple}), -0.72, -0.43, -0.15, 0.13, 0.42, 0.7, 0.98, 1.27, 1.55(\text{red})]$ through (4.79) and the result when averaged over environments [black line] using (4.81). [Bottom] Fractional deviation, $\frac{\xi_{env}}{\xi_{mean}} - 1$, for the CLPT result for each environment in the top panel, with respect to the CLPT curve given by the mean b_1 and b_2 values (black curve in the top panel).

To benchmark our findings we consider both the GR simulations as well as those for the modified gravity model. Figure 4.6 shows these comparisons for the three mass bin ranges, and Figure 4.7 shows the fractional variations with respect to the Zel'dovich component of CLPT.

For both the GR and modified gravity cases it is important to carefully understand the form of the halo mass function to get accurate LPT predictions. We find that simply adopting the standard ST pair of values, $(0.75, 0.3)$, gives a poor

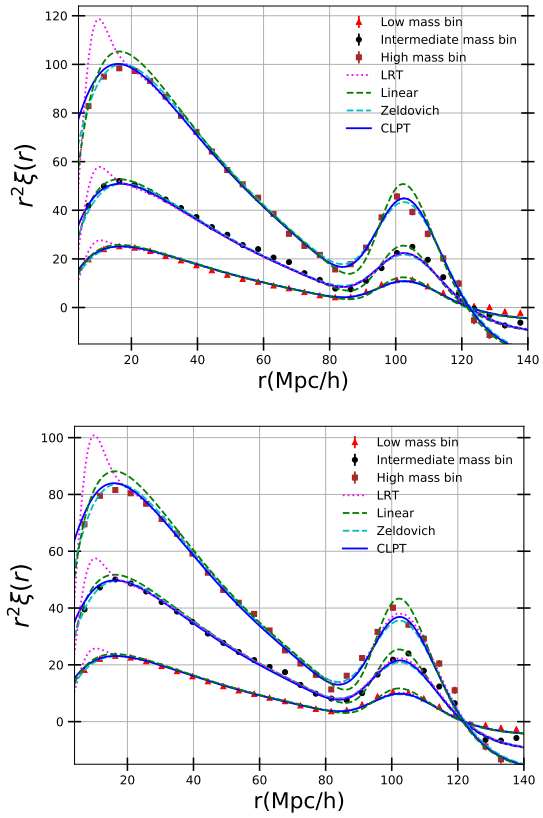

Figure 4.6: Two-point correlation functions for the Group II simulation snapshots at $z = 1$ for GR [top panel] and F5 [lower panel] models. The predictions from CLPT (5.24) [solid blue], the Zel'dovich approximation [dashed cyan], LRT (4.66) [dotted magenta] and the linear theory [dashed green], using the bias values shown in Table 4.1 are compared to the correlation function extracted from simulations, shown with Poisson error bars, for the three mass bins defined in Section 4.3: the low mass [red triangle], intermediate mass [black dot] and high mass [brown square] bins.

approximation to the first order bias b_1 (for the various values of halo mass), consistent with the findings of the simulation creators [13] when they extracted the bias estimate from the simulations and compared it to a standard ST prediction. For the results with the best fit halo mass parameters, we find that the full CLPT results for both the GR and the F5 model, incorporating the bias parame-

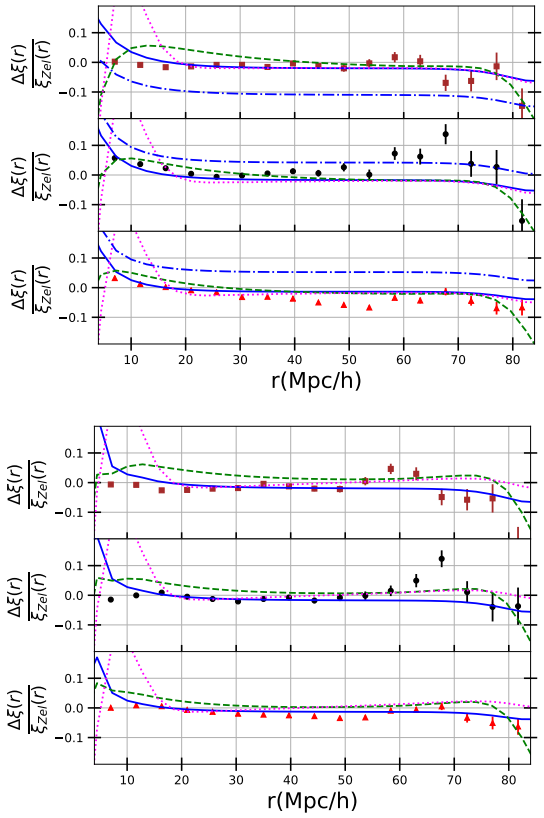

Figure 4.7: Fractional deviations in the power-law regime of the correlation function predictions with respect to the Zel'dovich approximation for the results shown in Figure 4.6. For the GR analysis [top panel], we also plot the ratio of the CLPT prediction using the standard ST values $(q, p) = (0.75, 0.3)$ [dashed-dot blue], rather than the best fit ones in Table 4.1, divided by the Zel'dovich result.

ters evaluated using our PBS model (Table 4.1) and the environment averaging where necessary, does a very good job, in describing the power-law correlation function, 20 – 80 Mpc/h, for all three mass bins and significantly improves upon linear theory at the BAO peak. For all three mass ranges, shown in Figure 4.7, the simulated correlation function falls below the Zel'dovich approximation and we find that the CLPT predictions are reflecting this better than both the linear and LRT predictions. The three approaches, CLPT, LRT and Zel'dovich, all

perform well in characterizing the BAO peak for the low mass and intermediate mass bins, for the largest differences being in the highest mass bin for F5, where the LRT approach performs slightly better. The LRT performs poorly at the smaller scales, under $20Mpc/h$, significantly overshooting the observed correlation function, consistent with the results reported in previous studies performed on ΛCDM cosmologies [194, 119, 46, 145]. The Zel'dovich approximation provides the best agreement at scales below $10Mpch/h$.

It is also interesting to notice that, in Figure 4.6, while the correlation functions have similar values for GR and the F5 model in the lowest mass bins, the F5 result is noticeably lower than the GR one for the highest mass bin. The amplitude of the correlation function depends on the interplay between the dark matter component (which has higher values in MG) and mostly the linear bias factor, b_1, which is lower for MG. In the lower mass bins, the combination of the above two is such that the difference between the GR and the F5 curves is almost neutralized, while in the highest mass bins the linear bias factor b_1 is, relatively, even lower, causing the F5 two-point function to have clearly lower values than in the GR case.

To expand on the results from the large volume simulations, we now look into the comparison with the Group I simulations, that, while spanning a smaller volume, allow us to test our schemes for a wider range of models. For each model, five different random realizations are available and the error bars represent the standard deviations over these realizations. Starting with the $f(R)$ family, which is plotted in Figure 4.8, we see that the picture painted for the $F4$ an $F5$ models here is similar with the one for the $F5$ model (at $z = 1$), with CLPT performing the best at scales $r > 20$ Mpc/h and the Zel'dovich result being su-

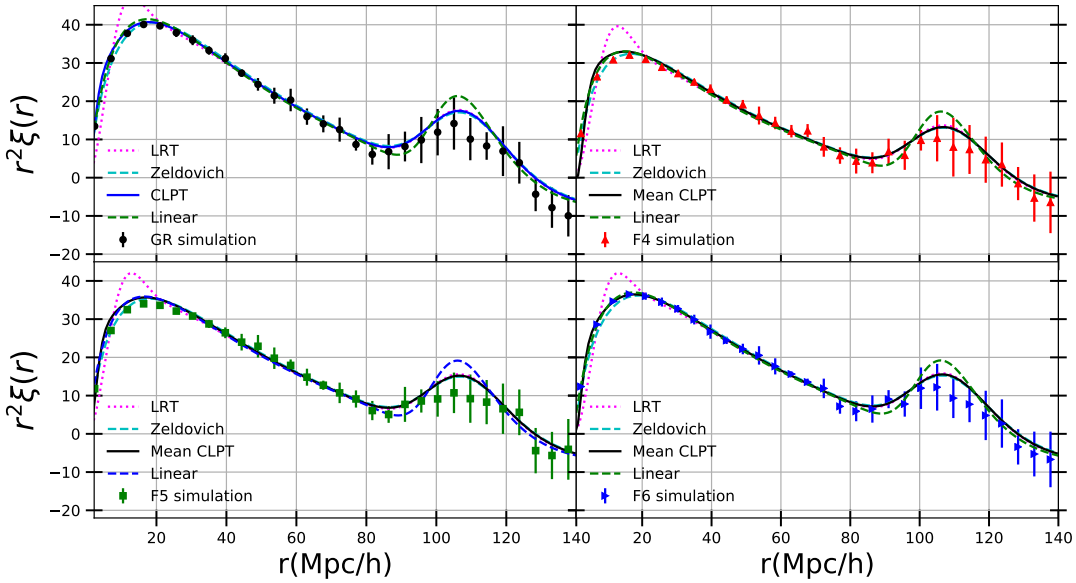

Figure 4.8: Two-point correlation functions from the Group I simulations, calculated at $z = 0.5$, for GR [black dots] in the upper left panel, for F4 [red triangles] in the upper right panel, for F5 [green squares] in the lower left panel and for F6 [blue right triangles] in the lower right panel. The results are the average over the 5 realizations and the error bars shown are standard deviations. Furthermore, for each model we plot the predictions from CLPT (5.24) [solid blue], from the Zel'dovich approximation [dashed cyan], from LRT (4.66) [dotted magenta] and from linear theory [dashed green], using the bias values shown in Table 4.1. The linear theory result for the F5 model is plotted using a blue dashed line instead, for ease of comparison.

perior at capturing the smaller scales, while the trend is more pronounced in the F4 case. For the F6 model however, not only does CLPT perform better at these larger scales, but it seems to trace the simulation results more accurately compared to Zel'dovich down to r~ 7 Mpc/h.

To explore this small scale performance sensitivity to screening in more detail note we consider what makes the linear order LPT and its one-loop extensions perform differently. In [194] (and also in [181]), it was argued, in dark

matter-only studies, that LPT does a poor job at estimating the higher order corrections to the linear displacement dispersion, given by (4.42) and the one-loop correction piece in LPT given by

$$\sigma^2_{1loop} = \frac{1}{6\pi^2}\int_0^\infty dk\left(\frac{9}{98}Q_1(k) + \frac{10}{21}R_1(k)\right). \tag{4.83}$$

Comparison with simulations in [181, 194], found CLPT to overestimate the size of this correction at small scales, through (4.83), with the true value of the total $\sigma^2_L + \sigma^2_{1loop}$ being closer to σ^2_L, which is what the Zel'dovich result uses. Because one-loop CLPT strongly depends on these corrections, through its zero-lag terms (as can be seen in Appendix B.2), it performs worse at the smaller scales compared to its Zel'dovich counterpart. Calculated from our theory prediction for GR at $z = 0.5$, the ratio $\frac{\sigma^2_{1loop}}{\sigma^2_L} = 0.126$, close to the value in Figure 5 of [194]. In comparison, for the $f(R)$ models at $z = 0.5$, the ratio $\frac{\sigma^2_{1loop}}{\sigma^2_L}$ is $(F4, F5, F6) = (0.212, 0.180, 0.152)$. The higher values for F4 and F5 lead to an overestimation in these cases that is responsible for the worse behavior at smaller r. It Is worth noting here that if we do not include screening, the ratio $\frac{\sigma^2_{1loop}}{\sigma^2_L} = 0.17$ in the $F6$ model, as opposed to the full value of 0.152. For the $z = 1$ Group II simulations, the ratios are $(GR, F5) = (0.08, 0.103)$, which explains the lower discrepancy and better performance of CLPT for F5. This also is consistent with considering that this is an earlier reference in which clustering differences between the theories will be less pronounced. From a physical standpoint, the overestimation reflects an inability in LPT (including the Zel'dovich result), to trap dark matter particles within halos [194], which seems to be more apparent in the LPT approach for stronger MG chameleons. Fortunately, as we said earlier, these models are the ones that violate the observational constraints and are thus less interesting from an astrophysical standpoint.

Finally, we test our LPT approaches applied on the nDGP models, that repre-

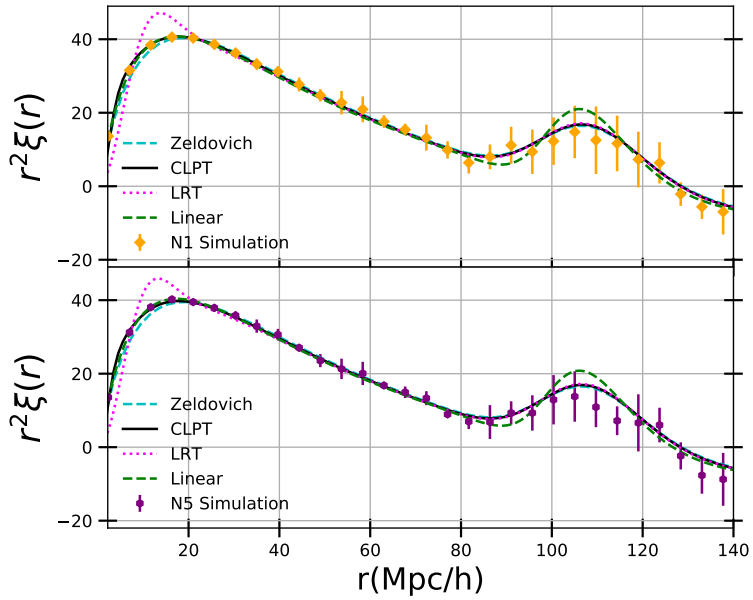

Figure 4.9: Two-point correlation functions from the Group I simulations, calculated at $z = 0.5$, for N1 [orange diamonds] in the upper panel and for N5 [purple hexagons] in the lower panel. The results are the average over the 5 realizations and the error bars shown are standard deviations. Furthermore, for each model we plot the predictions from CLPT (5.24) [solid black], from the Zel'dovich approximation [dashed cyan], from LRT (4.66) [dotted magenta] and from linear theory [dashed green], using the bias values shown in Table 4.1.

sent the Vainshtein screening mechanism, and the correlation functions of which are presented in Figure 4.9, for all LPT schemes and the Group II simulations. Just like in the $f(R)$ models, CLPT does a very good job at describing the correlation function for large scales and beyond that, it even seems to perform at least equally well as the Zel'dovich curve down to scales $r \sim 10$ Mpc/h, similar to the F6 and GR cases in Figure 4.8 discussed earlier. The measurement of the 1-loop statistic discussed in the previous paragraph is consistent with this; for the nDGP models, the ratio $\frac{\sigma^2_{1loop}}{\sigma^2_L} = (0.129, 0.122)$ for (N1, N5) respectively, very consistent with the GR value = 0.126. This is the case even in the weaker screen-

ing case, the N5 model, and is a very promising sign, given that the Vainshtein mechanism is highly efficient at screening modifications to gravity at smaller scales and contains viable candidates that self-accelerate (even though this particular model does not). The relative performance among the different resummation schemes is very similar to the one observed in the GR and $f(R)$ cases, with all LPT models improving the accuracy at the BAO peak upon linear theory, with the LRT scheme giving more power that CLPT and then the Zel'dovich result. The characterization of the BAO peak on scales $r > 100$ Mpc/h is limited in the simulation box with side 1,024 Mpc/h; larger-volume simulations for the nDGP model, comparable to the Group II simulations for F5 or GR, will allow us to more clearly trace the region between 100 – 140 Mpc/h and draw stronger conclusions about how our models perform at the BAO scales.

The fact that CLPT performs well for all modified gravity models considered in the power-law and BAO scales is very encouraging. On the smaller scales, its robustness for highly screened models is also a positive result. If an MG model was ever detected, it would be a highly screened case, given the tight constraints placed on GR; models F4 and F5 are actually ruled out by observations [45], but we include them in our analysis to fully investigate the chameleon phenomenology with LPT.

Power spectrum

Complementary to the correlation function, we also perform tests on its Fourier space counterpart, the halo power spectrum. The mass bins and bias values used in the power spectra calculations are exactly the same as the ones presented in the correlation function case, but with the additional step that all

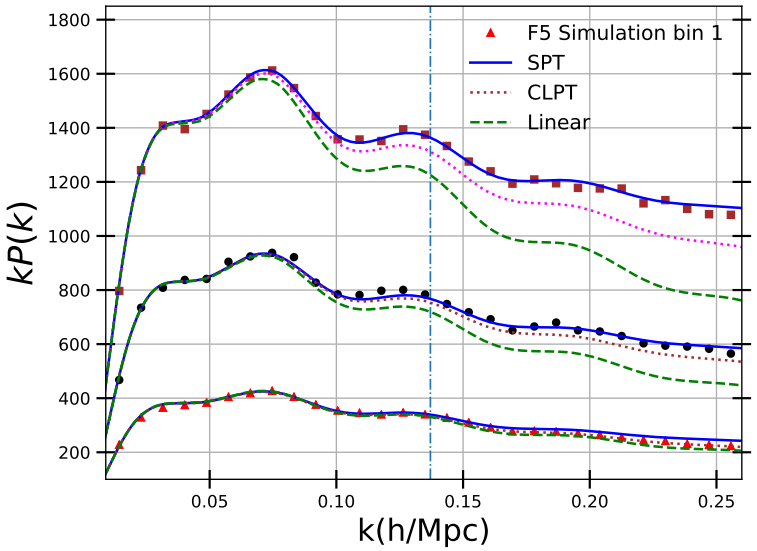

Figure 4.10: Power spectra from the Group II simulations, calculated for F5 at $z = 1$, in the low mass [red triangle], intermediate mass [black dot] and high mass [brown square] bins, that were defined in Section 4.3. The error bars shown are Poisson error bars. Furthermore, for each mass bin we plot the predictions from CLPT (5.24) [dotted magenta], from SPT (4.64) [solid blue] and from linear theory [dashed green], using the bias values shown in Table 4.1.

power spectra are shot noise corrected [162]: $\tilde{P}(k) = P(k) - \frac{1}{n_h}$, where $P(k)$ is the uncorrected power spectrum, and n_h is the number density of halos in each bin. Especially for the higher mass bins that contain less halos, this effect is not negligible, especially at higher k. We also identify the scale at which perturbation theory starts to fail, k_{NL}, with the vertical dashed-dot blue line, using the definition [120], $k_{NL} = (2\sigma_L^2)^{-1}$, with σ_L^2 the linear power spectrum dispersion defined in (4.42).

In Figure 4.10, we present the F5, Group II snapshot at $z = 1$. We find the expanded, SPT power spectrum (4.64) to perform very well at capturing the small k and to follow the power spectrum until $k \sim 0.25h$/Mpc, where it starts to

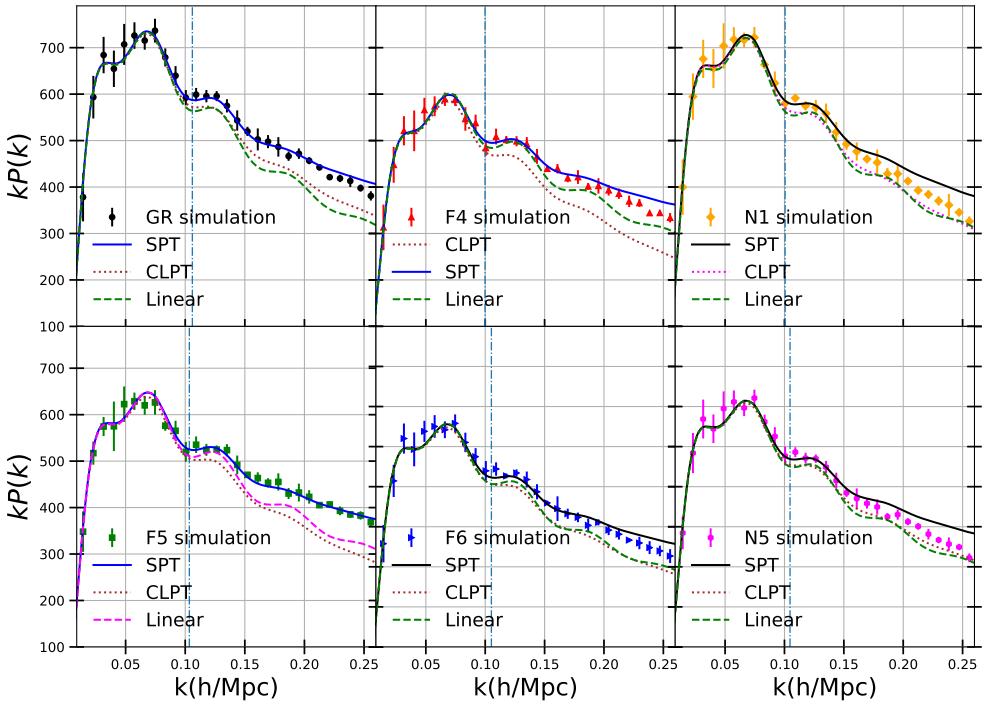

Figure 4.11: Power spectra from the Group I simulations, calculated at $z = 0.5$, for GR [black dots] in the upper left panel, for F4 [red triangles] in the upper middle panel, for F5 [green squares] in the lower left panel, for F6 [blue right triangles] in the lower middle panel, for N1 [orange diamonds] in the upper right panel and for N5 [purple hexagons] in the lower right panel. The results are the average over the 5 realizations and the error bars shown are standard deviations. Furthermore, for each model we plot the predictions from CLPT (5.24) [dotted brown], from SPT (4.64) [solid blue] and from linear theory [dashed green], using the bias values shown in Table 4.1. The linear theory result for the F5 model is plotted using a pink dashed line instead, for ease of comparison.

overestimate power compared to the simulations, for all three mass bins. This behavior is consistent with what was found in the GR case in earlier works on [194, 119] and also for dark matter in MG [15]. The linear theory result is only accurate at very large scales and quickly underestimates the power at $k > 0.05h/\text{Mpc}$. Unlike in the correlation function comparison, where LPT was

found to perform very well at a wide range of scales, here we see that the CLPT power spectrum (4.40) decays quickly and performs considerably worse than the SPT expansion. This is not unexpected, since the power spectrum in LPT has been found to receive, unlike in the configuration space, significant contributions from large, nonlinear k modes, where LPT performs poorly and fails to trap particles inside dark matter halos [194]. Our results show that this to also the case in our MG models. We find that this effect is even more pronounced in the LRT power spectrum (4.65), which decays sharply in k-space, for this reason we do not include the result in our plots.

In Figure 4.11 summarizing the GR and $f(R)$ cases from the Group I simulations, at $z = 0.5$, while the CLPT consistently underestimates the power spectrum for all models, the SPT result tracing the simulation points well for F5 and F6 until $k \sim 0.2h/\text{Mpc}$, at which it starts to overestimate the power spectrum. The performance for the the F4 model is slightly worse on small scales. This earlier deviation is not surprising given that the model has the smallest k_{NL} prediction, resulting from a comparatively higher 1D linear dispersion.

For the two nDGP models, also shown in Figure 4.11, we find that the SPT predictions perform well at scales $k < 0.15$ Mpc/h but overestimate the power on small scales. The CLPT predictions consistently underestimate the power, and are broadly comparable to the linear prediction.

4.4 Conclusions

In this work, we modeled the two-point statistics of biased tracers in modified gravity (MG) up to one-loop order in the linear power spectrum, using the Con-

volution Lagrangian Perturbation Theory (CLPT) framework and its variants. Following standard methods in the literature, the linear piece of the two-point Lagrangian correlator for dark matter is kept exponentiated in the expression for the two-point correlation function, but everything else is expanded, leading to a series of convolution integrals, the expressions of which we derive for scalar-tensor theories.

The evolution of the underlying dark matter density field is described by the LPT framework for dark matter, suitably extended to study scalar-tensor theories, along with an analytical model for the calculation of the first and second order bias parameters in MG. To perform the bias calculations, we employ the Peak-Background split (PBS) approach, in which biases are modeled rigorously as responses of the universal Sheth-Tormen halo mass function in the presence of a long-wavelength density perturbation. This is extended in MG theories, to account for the dependence of the gravitational collapse on the environment and screening. Our PBS implementation, provides a quantitative prediction for the increased production, and the related lower biases, for haloes of a given mass. We apply this scheme to the $f(R)$ Hu-Sawicki and the nDGP braneworld models, that are representatives of the chameleon and Vainshtein screening mechanisms, respectively. We make the code used for the analytic predictions publicly available in [3] and evaluate their performance against state-of-the-art cosmological N-body simulations, for a variety of MG models at $z = 0.5$ and $z = 1$, with respect to the correlation function and the power spectrum in a variety of mass regimes and scales.

The CLPT implementation, in combination with the analytical bias model, gives good agreement with the simulations, with the only free parameters nec-

[3] https://github.com/CornellCosmology/bias_MG_LPT_products

essary being those to best-fit the Sheth-Tormen universal halo mass function at the given mass range. The CLPT predicts the correlation function across scales $20 - 80$ Mpc$/h$, tracing the simulation results at an accuracy of $2 - 3\%$ and better. At the BAO scales, that provide a valuable probe of fundamental physics, CLPT was found to improve significantly upon the linear theory and Zel'dovich predictions for the F5 models, just like in GR. The Lagrangian Resummation Theory (LRT) approach improved the accuracy a little further at BAO scales for the highest mass range considered. At scales of $r < 20$ Mpc$/h$, the CLPT performed well for the highly screened model $F6$ and for the nDGP models, while the Zel'dovich predictions performed better for the weakly screened F5 and F4 models. The reason for this behavior was identified, being an overestimation in these low-screening chameleon models of the one-loop contributions to the zero-lag terms at small scales.

In Fourier space, consistent with findings for GR, the CLPT power spectrum was found to underestimate power quickly, compared to the simulations for all MG models. This is due to the power spectrum receiving significant contributions from large k, where LPT performs poorly. The Standard Perturbation Theory (SPT) approach, though, which is the low-k expanded version of this power spectrum, performs very well and remains consistent with the simulation results down to $k \sim 0.2h$/Mpc for the $f(R)$ models and down to $k \sim 0.15h$/Mpc for the two nDGP models. Beyond these scales, the SPT curve overestimates the power spectrum, as has been found for GR previously.

While we have focused our analysis on LPT predictions for real space, our model can be expanded to capture the redshift-space distortions required for upcoming LSS surveys. Furthermore, even though we focused on a local in

matter density bias scheme in the Lagrangian space, in which the bias is purely a function of the local density, one can extend this to include other factors determining bias into the formalism, such as curvature bias, and model them successfully by this PBS scheme. The same applies for potential extensions to include EFT corrections to our LPT model, as in [193], which could also be used to calculate the components of the Gaussian Streaming Model for MG theories. Finally, our CLPT MG framework can be used to analytically predict marked statistics in MG and assess their ability to boost the MG signals carried in cosmic density fields, as in [204, 190]. We leave these natural extensions to future work.

In the coming decade, a wide array of cosmological surveys will span a large part of the observable universe, searching for hints of new physics beyond ΛCDM. In this work we demonstrate that semi-analytical approaches, extensively employed in the context of standard GR, can serve as invaluable tools to predict structure formation in cosmologies with an extra degree of freedom in the gravitational sector. A next step for these approaches are to confront them in comparison to realistic simulations of galaxies and clusters that will be observed with surveys coming online in the coming year or two and assess survey ability to identify and constrain potential deviations from GR.

4.5 Acknowledgments

We wish to thank Wojciech Hellwing for kindly making available the *n*DGP simulations, on behalf of [73] and Baojiu Li for kindly providing the *ELEPHANT* simulations, on behalf of [50], for numerous discussions and for making us awaref of the Lightcone simulations. We are also grateful to Christian Arnold,

as well as to all the other authors of [13], for kindly providing their Lightcone simulations and for numerous discussions. We also wish to thank Martin White for useful discussions on available simulations of ΛCDM cosmologies.

CHAPTER 5

AN ACCURATE PERTURBATIVE APPROACH TO REDSHIFT SPACE CLUSTERING OF BIASED TRACERS IN MODIFIED GRAVITY

5.1 Introduction

In this chapter, we will extend the scale-dependent Gaussian Streaming Model (GSM) to produce analytical predictions for the anisotropic redshift-space correlation function for biased tracers in modified gravity models. In the hierarchical picture of structure formation, the tiny perturbations in the primordial dark matter density field grow, under the influence of non-linear gravitational collapse, partly opposed by cosmic expansion, to give rise to the rich cosmic pattern observed today. On the large, linear scales and when GR is assumed, dark matter over-densities evolve as a simple function of time, for all scales, whereas on smaller, non-linear scales, computationally expensive N-body simulations are inevitable. This picture is further complicated by the fact that the galaxies observed by surveys of the LSS, do not perfectly trace the underlying dark matter density field, but are biased tracers of it [86] and, are observed in redshift space [88, 62], which introduces redshift-space distortions (RSD) to the observed clustering statistics. In the case of MG models, another layer of complexity is added – one needs to account for the presence of the additional degree of freedom that enhances structure formation and interferes with the evolution of dark matter and biased tracers in a non-linear manner. In the intermediate, quasi-linear scales, higher order Perturbation Theory (PT) [30, 47] approaches or hybrid methods [182, 189], integrating both analytic and numerical simulation approaches, are of great benefit.

RSD effects are induced by the peculiar velocity field of galaxies about the Hubble flow, which breaks the isotropy of the two-point correlation function of galaxies detected through spectroscopic means. At large scales, RSD lead to an enhancement of the amplitude of the correlation function, the "Kaiser boost" [88], that can be modeled analytically, while on the opposite end, the non-linear regime, the Fingers-Of-God (FOG) effect suppresses the correlation function, an effect that is frequently captured through phenomenological "streaming" models [56, 131]. In [145], the Gaussian Streaming Model (GSM) was introduced, to model the RSD correlation function in the quasi-linear scales. It used a non-perturbative resummation of the linear treatment by [67] that convolves the real-space correlation function of biased tracers with a Gaussian pairwise velocity distribution function [160]. The accuracy of the original approach, that used Eulerian Standard PT (SPT) to model the velocity moments, was further improved in [198], using the Lagrangian Perturbation Theory (LPT) approach to structure formation [212, 44, 38, 78, 183, 120, 119, 46, 122] with a resummation scheme called Convolution LPT (CLPT) [46] in which the effects of the bulk flows are not expanded in perturbative order. Further advancements included adding higher order velocity moments [186, 32] or small-scale physics effects through corrections from Effective Field Theory (EFT) [196, 193].

While halo bias and RSD have been studied in tandem for modified gravity in the context of N-body simulations, for example [12, 24, 75], they have only been studied separately, to date, for perturbative approaches to the clustering statistics [98, 179, 42, 180, 28, 66, 35, 34, 36, 17, 16, 191]. In [17, 191], CLPT was extended to predict the two-point statistics for biased tracers in MG, based on the LPT framework for MG developed in [15] and also an analytical model for the prediction of the Lagrangian bias factors in MG [191], extending the Peak-

Background Split formalism (PBS) [86, 20, 157, 124]. Applied on the f(R) Hu-Sawicki [81] and the nDGP [60] models, it was shown to perform very well against results obtained by N-body simulations across a wide variety of screening levels and cosmological redshifts. In the work of [35], the GSM model was employed to model the RSD correlation function in MG models, shown to work very well against data obtained by N-body simulations, but only quantified in the context of pure dark matter considerations and with a local linear bias. Furthermore, [35] used RegPT and also the SPT scheme previously used by [145], for the perturbative representations of the GSM ingredients, but not LPT, which was used in the GSM implementation by [198] and will be the focus of this work.

Building upon the previous work of [17, 191], in this chapter we move forward to expand the scale-dependent GSM, in particular as presented in [198, 193], so as to make analytical predictions for the anisotropic redshift-space correlation function for biased tracers in MG theories. The underlying density field is evolved using the LPT for scalar-tensor theories presented in [15], while the effect of bias is captured through a local Lagrangian bias, up to second order, with the corresponding bias values predicted by the ST model for MG that was presented, and found to work well, in [191]. We apply this framework on two widely-considered MG models, the chameleon f(R) Hu-Sawicki [81] and the Vainshtein-screened nDGP [60] braneworld model and compare our results against state-of-the-art N-body simulations. We first make sure that our CLPT predictions for the remaining GSM ingredients, the pairwise velocity and the scale-dependent velocity dispersion, match the simulations sufficiently well, as already done for the real-space 2-point correlation function inc, before proceeding to cross-check the predictions for the monopole and the quadrupole of the RSD 2-point correlation function against the corresponding ones from the sim-

ulations. This last step is crucial for confirming the robustness of our analytical predictions, as well as the level of their accuracy, as we enter the era of precision cosmology. Our analytical approach is the first one, to the best of our knowledge, that captures both the effects of halo bias and RSD in the context of MG. These results have been published in [192].

This chapter is structured as follows: in Sec. 5.2 we introduce the MG scenarios on which we focus and also introduce the N-body simulations used to cross-validate our analytical results. In Sec. 5.3 we show how the GSM is implemented in scenarios in which gravity deviates from GR. Then, in Sec. 5.4, we discuss the accuracy of our results through the comparison against the N-body simulations, before concluding in Sec. 5.5. The details of the various derivations are laid out in Appendices D and E.

5.2 Modified Gravity Scenarios and Simulation Tools

In this section, we briefly introduce the MG models we consider and also present the N-body simulations we used to cross-check our model's validity.

5.2.1 Modified Gravity Scenarios

One of the oldest ways to depart from GR in the literature, proposes adding a function of the Ricci scalar to the standard form of the Einstein-Hilbert action. In particular, if R is the Ricci scalar, these models, the "f(R)" class of theories

[57], are described by an action S of the form:

$$S = \int d^4x \sqrt{-g} \left[\frac{R + f(R)}{16\pi G} + \mathcal{L}_m \right], \tag{5.1}$$

where in the above expression, modifications to gravity manifest themselves through the nonlinear function $f(R)$. In (5.1) we use $\mathcal{L}_m$ for the matter sector Lagrangian and G for the gravitational constant. The renewed interest in modifications of this type, is motivated by the possibility that such models can be responsible for the observed accelerated expansion of the universe [48]. In what is probably the best-studied candidate of this class, the $f(R)$ Hu-Sawicki model [81], the modifying function is of the form:

$$f(R) = -m^2 \frac{c_1 \left(R/m^2\right)^n}{c_2 \left(R/m^2\right)^n + 1}, \tag{5.2}$$

with $m = H_0 \sqrt{\Omega_{m0}}$, H_0 being the Hubble constant, Ω_{m0} the fractional matter density evaluated today and c_1, c_2 and n the free parameters of the model. The number of free parameters is further reduced by imposing a background expansion that matches the ΛCDM one in the high curvature limit ($R \gg m^2$), which gives:

$$\bar{f}_{R_0} = -n \frac{c_1}{c_2^2} \left(\frac{\Omega_{m0}}{3(\Omega_{m0} + \Omega_{\Lambda 0})} \right)^{n+1}, \tag{5.3}$$

where we defined the scalaron, $f_R = \frac{df(R)}{dR}$, that is evaluated today in equation (5.3). Thanks to this expression, this model is usually parametrized with $|f_{R_0}|$ and n. Its popularity lies in the fact that it realizes the interesting phenomenology of the chameleon screening mechanism [92, 93], as can be shown through a conformal transformation [43]. As $|f_{R_0}| \to 0$ and/or $n \to \infty$, the deviations are suppressed and GR is recovered. In our analysis, we always fix $n = 1$ and consider three variations of $|\bar{f}_{R_0}| = \{10^{-6}, 10^{-5}, 10^{-4}\}$, that will be referred to from now on as F6, F5 and F4, respectively.

In the case of Vainshtein screening, there is a characteristic scale away from a massive source, the Vainshtein radius, below which fifth forces are strongly suppressed, due to the existence of large second derivatives of the gravitational potential. A MG model that exhibits this behavior is the Dvali-Gabadadze-Porrati (DGP) model [60], in which spacetime is actually 5-dimensional (5D), with an action of the form:

$$S = \int d^4x \sqrt{-g}\left[\frac{R}{16\pi G} + \mathcal{L}_m\right] + \int d^5x \sqrt{-g_5}\left(\frac{R_5}{16\pi G r_c}\right), \tag{5.4}$$

where by R_5 and g_5 we label the 5D equivalent versions of the Ricci scalar and the metric determinant. Gravity does become 4-dimensional, however, below a characteristic scale r_c and the usual 4D spacetime corresponds to a brane, on which the Standard Model fields are confined. The DGP model contains a self-accelerating branch (sDGP), which unfortunately has been shown to exhibit undesirable "ghosts" that make it unstable [96]. For this reason, we consider the "normal" branch instead, called the nDGP, that is assumed to co-exist with a dark energy component, so that a ΛCDM homogeneous evolution is matched. We study two instances of the nDGP model, those with $n \equiv H_0 r_c = 1$ and $n = 5$, that we label and, from now on call, N1 and N5, correspondingly.

5.2.2 N-body Simulations

In this section, we briefly introduce the N-body simulations we will use to assess the performance of our analytical model, which is a crucial step for our analysis.

The first set of simulations, that we will refer to from now on as Group I simulations, are the Extended LEnsing PHysics using ANalaytic ray Tracing (ELEPHANT) simulations [50], that were performed with two modified ver-

sions of the GR code (RAMSES): the ECOSMOG module [112, 37] produced snapshots for the F6, F5 and F4 cases at a cosmological redshift of $z = 0.5$, while ECOSMOG-V [111, 21, 73] was used to produce the nDGP N1 and N5 realizations, also at $z = 0.5$. 1024^3 dark matter particles were evolved, in a simulation box with a side $L_{box} = 1024 Mpc/h$ and a cosmology specified by the following parameters:

$$\{\Omega_{m0}, \Omega_{\Lambda 0}, h, n_s, \sigma_8, \Omega_b\} = \{0.281, 0.719, 0.7, 0.971, 0.82, 0.046\}. \tag{5.5}$$

So as to reduce the effects of cosmic variance, each model is run using 5 different random realizations. Finally, the dark matter halos in each snapshot are identified through the `ROCKSTAR` halo finder [25].

The second group of simulations available, that we will call Group II, come from the MG lightcone simulation project [13], that employed the MG code MG-GADGET [141], to simulate GR and F5 cosmologies at a variety of redshifts; in our work we focus on the $z = 1$ snapshot. Using 2048^3 dark matter particles in a cubic box with side $L_{box} = 1536 Mpc/h$, they are the largest-volume MG simulations performed up-to-date, which allows us to explore our GSM predictions at the Baryon Acoustic Oscillation (BAO) scales [63]. The ΛCDM cosmology in these simulations is given by:

$$\{\Omega_{m0}, \Omega_{\Lambda 0}, h, n_s, \sigma_8, \Omega_b\} = \{0.3089, 0.6911, 0.6774, 0.9667, 0.8159, 0.0486\}. \tag{5.6}$$

The halo catalogues are produced making use of the SUBFIND code [175] and each model is simulated for only one random seed.

Finally, to compute the real-space two-point correlation function, the RSD anisotropic correlation function and also the velocity information from the simulations, we utilize the publicly available code `CUTE` [9], using 30 linearly space

bins in the range $0 - 140$ Mpc/h, both in the real and in the redshift space. For the Group I simulations, all error bars are calculated as the standard deviations over the 5 available realizations, whereas in the Group II case, where only 1 realization is available, we use the Jackknife method, splitting the simulation box into 64 sub-volumes.

As was also done in [191], for the Group I simulations, we analyze a $z = 0.5$ snapshot of halos in the mass range $(2 - 3.5) \times 10^{12} M_{\odot}/h$, for all models, using only the main halos identified by ROCKSTAR. For the Group II simulations, on the other hand, we focus our predictions on a redshift of $z = 1$, considering halos in three separate mass bins: a lower mass bin of $9 \times 10^{11} - 2 \times 10^{12}\ M_{\odot}/h$, an intermediate bin of $5 \times 10^{12} - 1 \times 10^{13}\ M_{\odot}/h$ and a higher mass bin, $1.1 \times 10^{13} - 9 \times 10^{13}\ M_{\odot}/h$.

5.3 Redshift-Space Correlation Function For Biased Tracers In Modified Gravity

In this section, we present our analytical framework for the redshift-space correlation function of biased tracers in modified gravity cosmologies. Before the topic of RSD is addressed, we briefly summarize the LPT framework for structure formation in MG cosmologies, as well as the analytical treatment of Lagrangian bias for dark matter halos in such scenarios.

5.3.1 Lagrangian Perturbation Theory For Dark Matter In Modified Gravity

In the Lagrangian Perturbation Theory framework [212, 44, 38, 78, 183, 120, 119, 46, 122], the time-dependent growth of dark matter overdensities is traced in a coordinate system that is comoving with matter particles, as they move along their fluid trajectories. In particular, the fundamental element of LPT is a displacement, vector, field $\mathbf{\Psi}$, which in each moment of interest t, maps a particle from an initial "Lagrangian" position $\mathbf{q}$ to its final, Eulerian position vector $\mathbf{x}(\mathbf{q}, t)$, encoded through the following relationship:

$$\mathbf{x}(\mathbf{q}, t) = \mathbf{q} + \mathbf{\Psi}(\mathbf{q}, t). \tag{5.7}$$

Imposing conservation of matter mass between $\mathbf{q}$ and $\mathbf{x}$, one gets

$$\delta_m(\mathbf{x}, t) = \frac{1 - J(\mathbf{q}, t)}{J(\mathbf{q}, t)}, \tag{5.8}$$

with $\delta_m(\mathbf{x}, t) = \frac{\rho_m}{\bar{\rho}} - 1$ in (5.8) denoting the fractional matter overdensity and $J(\mathbf{q}, t) = det(J_{ij})$, the determinant of the Jacobian of the mapping (5.7), given by

$$J_{ij} = \frac{\partial x^i}{\partial q^j} = \delta_{ij} + \frac{\partial \Psi^i}{\partial q^j}. \tag{5.9}$$

Unlike the Eulerian approach, in LPT the expansion parameter is the displacement $\mathbf{\Psi}$, as

$$\mathbf{\Psi}(\mathbf{q}, t) = \sum_{n=1}^{\infty} \mathbf{\Psi}^{(n)}(\mathbf{q}, t) = \mathbf{\Psi}^{(1)}(\mathbf{q}, t) + \mathbf{\Psi}^{(2)}(\mathbf{q}, t) + \mathbf{\Psi}^{(3)}(\mathbf{q}, t)... \tag{5.10}$$

Equations (5.7)-(5.9) form a closed system that can be solved, order by order, when combined with the coupled pair of the geodesic and Poisson equations

$$\begin{aligned} \ddot{\mathbf{x}} + 2H\dot{\mathbf{x}} &= -\frac{1}{a^2}\nabla_{\mathbf{x}}\psi(\mathbf{x}, t), \\ \frac{1}{a^2}\nabla^2_{\mathbf{x}}\psi(\mathbf{x}, t) &= 4\pi G\bar{\rho}_m\delta(\mathbf{x}, t), \end{aligned} \tag{5.11}$$

with $\psi(\mathbf{x}, t)$ representing the scalar metric perturbation. Equations (5.11) have been derived perturbing about a Friedmann-Robertson-Walker (FRW) background assuming a GR-like evolution. The first order solution to the system (5.7)-(5.11) is the well-known Zel'dovich approximation [212], in which

$$\Psi^j(k, t) = \frac{ik^j}{k^2} D^{(1)}(t)\delta^{(1)}(\mathbf{k}, t = 0), \tag{5.12}$$

where $\delta^{(1)}(\mathbf{k}, t = 0)$ is the linearized overdensity at early times and $D^{(1)}(t)$ the linear growth factor in GR, which is the growing solution of

$$\hat{\mathcal{T}} D^{(1)}(t) = A_0 D^{(1)}(t), \tag{5.13}$$

with $A_0 = 4\pi G\bar{\rho}_m$ and the differential operator $\hat{\mathcal{T}} = \frac{d^2}{dt^2} + 2H\frac{d}{dt}$, defined in [120].

In the presence of a modification to gravity, the above picture is complicated by the action of the additional degree of freedom, the impact of which should be taken into account by the LPT framework. In the work of [189], LPT was studied for the MG chameleons and symmetrons, up to second order, in the context of the COLA hybrid approach, which was found to recover results from full N-body simulations with high accuracy. LPT was first expanded to capture MG theories up to third order by [15] (also see [16, 17, 191]), which is the approach we closely follow and briefly summarize here. For a scalar-tensor theory, equations (5.11) are replaced by the modified version of the perturbed Einstein equations:

$$\begin{aligned} &\nabla_{\mathbf{x}} \hat{\mathcal{T}} \boldsymbol{\Psi} = -\frac{1}{a^2}\nabla^2_{\mathbf{x}}\psi(\mathbf{x}, t), \\ &\frac{1}{a^2}\nabla^2_{\mathbf{x}}\psi(\mathbf{x}, t) = 4\pi G\bar{\rho}_m\delta(\mathbf{x}, t) + \frac{1}{2a^2}\nabla^2_{\mathbf{x}}\phi, \end{aligned} \tag{5.14}$$

combined with the Klein-Gordon (KG) equation

$$(3 + 2\omega_{BD})\frac{1}{a^2}k_x^2\phi(\mathbf{k}_x, t) = 8\pi G\bar{\rho}_m\delta(\mathbf{k}_x, t) - \mathcal{I}(\phi). \tag{5.15}$$

Here, ω_{BD} is a function that depends on the specific theory, and is named in that way because for Brans-Dicke (BD) theories it reduces to the BD parameter. The under-script x is meant to show that the quantities are evaluated in the Eulerian basis. The term $\mathcal{I}(\phi)$ is the perturbative representation of the screening due to the field ϕ self-interactions [98], given by

$$\begin{aligned}\mathcal{I}(\phi) &= M_1(\mathbf{k},t)\phi + \frac{1}{2}\int \frac{d^3k_1 d^3k_2}{(2\pi)^3}\delta_D(\mathbf{k}-\mathbf{k}_{12})M_2(\mathbf{k}_1,\mathbf{k}_2)\phi(\mathbf{k}_1)\phi(\mathbf{k}_2) \\ &+\frac{1}{6}\int \frac{d^3k_1 d^3k_2 d^3k_3}{(2\pi)^6}\delta_D(\mathbf{k}-\mathbf{k}_{123})M_3(\mathbf{k}_1,\mathbf{k}_2,\mathbf{k}_3)\phi(\mathbf{k}_1)\phi(\mathbf{k}_2)\phi(\mathbf{k}_3),\end{aligned}$$

with $M_1(\mathbf{k},t)$, $M_2(\mathbf{k}_1,\mathbf{k}_2)$ and $M_3(\mathbf{k}_1,\mathbf{k}_2,\mathbf{k}_3)$ being mass terms and where we used the convention $\mathbf{k}_{ijk} = \mathbf{k}_i + \mathbf{k}_j + \mathbf{k}_k$. The first order solution in MG is

$$\Psi^j(k,t) = \frac{ik^j}{k^2}D^{(1)}(k,t)\delta^{(1)}(\mathbf{k},t=0), \tag{5.16}$$

where the MG linear growth factor $D^{(1)}(k,t)$ is now obtained through

$$\hat{\mathcal{T}}D^{(1)}(k,t) = A(k)D^{(1)}(k,t), \tag{5.17}$$

with

$$\begin{aligned}A(k) &= 4\pi G\bar{\rho}_m\left(1+\frac{k^2}{a^2 3\Pi(k)}\right), \\ \Pi(k) &= \frac{1}{3a^2}\left[(3+2\omega_{BD})\,k^2 + M_1 a^2\right].\end{aligned} \tag{5.18}$$

A generic feature of many MG models, for which $M_1 \neq 0$, is that, unlike in the GR case (5.13), the linear growth factor is scale-dependent. The 2^{nd} and 3^{rd} order LPT solutions in MG contain two additional contributions, compared to the simpler GR case: a screening term, due to the field self-interactions and a, geometric in nature, Frame-Lagging component that arises when transforming the KG equation from an Eulerian to a Lagrangian basis. The expressions for the 2^{nd} and 3^{rd} order solutions, as well as for the perturbative mass terms $M_1 - M_3$ in the f(R) and nDGP cases can be found in [15] and also [16, 17, 191].

We finally note that a scale dependent linear growth function implies the linear growth rate is also scale dependent,

$$f(k) = \frac{d \ln D^{(1)}(k, a)}{d \ln a}. \tag{5.19}$$

We find it useful to define the large-scale value, f_0, as

$$f_0 = f(k = 0). \tag{5.20}$$

For MG models with $M_1 \neq 0$, f_0 coincides with the standard growth rate in ΛCDM. In models with vanishing mass, such as the nDGP, $f(k) = f_0$ is scale independent, but its value does not coincide with that of ΛCDM.

5.3.2 Lagrangian Biased Tracers In Modified Gravity

Galaxies do not exactly trace the underlying distribution of dark matter, which in principle biases observable quantities [86], like the clustering statistics, extracted from such observations. This effect is taken into account by the perturbative theory of galaxy clustering, which has been greatly explored using a variety of analytical approaches; a comprehensive review of this topic can be found in [59]. Given an analytical model for the nonlinear evolution of the underlying dark matter overdensities (for which we choose LPT), the effects of halo or galaxy formation are captured through a set of bias parameters. Building upon our LPT formalism laid out in the previous section 5.3.1, we employ a local Lagrangian bias to study overdensities of halos, within which the observed galaxies form and reside. Before addressing the biasing scheme in MG scenarios, it is worth mentioning that in the context of GR, approaches in the literature have employed a variety of Lagrangian bias schemes, ranging from

a local-in-matter-density Lagrangian bias [119, 46], to a local Lagrangian bias including curvature and tidal terms [193], all the way to extensions with a non-local Lagrangian bias [121].

The two-point statistics of biased tracers in modified gravity models have recently been expressed using a local-in-matter and curvature Lagrangian bias [17], as well as a local-in-matter density bias [191]. While we will focus on predictions using the latter, we will present the expressions including the curvature bias, which is more general and contains, as we will see below, the local in matter density terms as a limiting case. We make the common assumption that tracers are initially identified in the primordial dark matter density field, at a sufficiently early time t_0, through a local function F. In particular, if by $\delta_R(\mathbf{q}, t_0) \equiv \delta_R(\mathbf{q})$ we denote the dark matter density field, smoothed out over a spatial scale R, then the initial fractional overdensity of tracers (in our case halos), $\delta_X(\mathbf{q}, t_0) \equiv \delta_X(\mathbf{q})$, will be given by [17] [1]:

$$1 + \delta_X(\mathbf{q}) = \frac{\rho_X(\mathbf{q})}{\bar{\rho}_X} = F\left[\delta_R(\mathbf{q}), \nabla^2\delta_R(\mathbf{q})\right]. \tag{5.21}$$

When $F = 1$ in (5.21), we get $\delta_X(\mathbf{q}) = 0$, recovering thus the dark matter case. Having identified the initially biased tracers through (5.21), their subsequent nonlinear evolution is found after applying the continuity equation between $\mathbf{q}$ and $\mathbf{x}$:

$$1 + \delta_X(\mathbf{x}, t) = \int d^3q F\left[\delta_R(\mathbf{q}), \nabla^2\delta_R(\mathbf{q})\right] \delta_D\left[\mathbf{x} - \mathbf{q} - \mathbf{\Psi}(\mathbf{q}, t)\right], \tag{5.22}$$

where in the above equation $\delta_R(\mathbf{q})$ is the extrapolated linear density field evaluated at the observation time. Our goal is to model the two-point correlation

[1] In principle, in MG theories with an additional scalar field ϕ, the bias function F should also depend on the Laplacian, $\nabla^2\phi$, but as noted in [59] and further developed in [17], expanding the KG equation reveals that this dependence is degenerate with $\nabla^2\delta$ for k-modes smaller than the scalar field mass and can thus be absorbed.

function for halos, defined by

$$\xi_X(r) = \langle \delta_X(\mathbf{x}) \delta_X(\mathbf{x}+\mathbf{r}) \rangle, \tag{5.23}$$

where the angle brackets indicate an ensemble averaging. Plugging the result (5.22) into (5.23) and after performing a multinomial expansion and several integrations, one gets the two-point correlation function for biased tracers, up to 1-loop order, as [46, 17, 191]:

$$\begin{aligned} 1+\xi_X(r) \;=\; & \int d^3q \frac{e^{-\frac{1}{2}(q_i-r_i)(A_L^{-1})_{ij}(q_j-r_j)}}{(2\pi)^{3/2}\,|A_L|^{1/2}} \times \Bigg(1 - \frac{1}{2} G_{ij} A_{ij}^{loop} + \frac{1}{6} \Gamma_{ijk} W_{ijk} \\ & - b_1 \left(2 U_i g_i + A_{ij}^{10} G_{ij} \right) - b_2 \left(U_i^{(1)} U_j^{(1)} G_{ij} + U_i^{20} g_i \right) \\ & + b_1^2 \left(\xi_L - U_i^{(1)} U_j^{(1)} G_{ij} - U_i^{11} g_i \right) + \frac{1}{2} b_2^2 \xi_L^2 - 2 b_1 b_2 \xi_L U_i^{(1)} g_i \\ & + 2\,(1+b_1)\, b_{\nabla^2\delta} \nabla^2 \xi_L + b_{\nabla^2\delta}^2 \nabla^4 \xi_L \Bigg), \end{aligned} \tag{5.24}$$

with

$$\begin{aligned} g_i &\equiv (A_L^{-1})_{ij}(q_j - r_j), \\ G_{ij} &\equiv (A_L^{-1})_{ij} - g_i g_j, \\ \Gamma_{ijk} &\equiv (A_L^{-1})_{ij} g_k + (A_L^{-1})_{ki} g_j + (A_L^{-1})_{jk} g_i - g_i g_j g_k, \end{aligned} \tag{5.25}$$

and where we defined

$$\begin{aligned} \sigma_R^2 &= \langle \delta^2 \rangle_c \\ \xi_L(\vec{q}) &= \langle \delta_1 \delta_2 \rangle_c, \\ A_{ij}^{mn}(\vec{q}) &= \langle \delta_i^m \delta_j^n \Delta_i \Delta_j \rangle_c, \\ W_{ijk}^{mn}(\vec{q}) &= \langle \delta_i^m \delta_j^n \Delta_i \Delta_j \Delta_k \rangle_c, \\ U_i^{mn}(\vec{q}) &= \langle \delta_1^m \delta_2^n \Delta_i \rangle_c. \end{aligned} \tag{5.26}$$

The Lagrangian correlators (5.26), as first defined in [46], are the elementary ingredients of the LPT correlation function (5.24) and contain cumulants of the differential LPT displacement field, $\mathbf{\Delta} = \mathbf{\Psi}_2 - \mathbf{\Psi}_1$, where we adopted the shorthand notation $\mathbf{\Psi}(\mathbf{q}_1) = \mathbf{\Psi}_1$, etc. In (5.24) we also defined $A_{ij}^{00} \equiv A_{ij}$, $W_{ijk}^{000} \equiv W_{ijk}$ and

$U_i^{10} \equiv U_i$. These correlators (5.26) differ in GR [46] and MG [17, 191], because the LPT displacement fields they contain follow a different time-evolution in each of these two cases, as explained in the previous Section 5.3.1 (this difference manifests itself in the "k-functions" in [46] and [17, 191]). Finally, we note that in (5.24) only the linear part of A_{ij} is kept exponentiated following [196, 193], a variant of the Convolution Lagrangian Perturbation Theory (CLPT) resummation scheme [46] that maintains also the loop components in the exponential.

In expression (5.24), we identify the local-in-matter-density bias parameters [119, 121]

$$b_n \equiv \int \frac{d\lambda}{2\pi} \tilde{F} e^{-\frac{1}{2}\lambda^2\sigma_R^2} (i\lambda)^n \,, \tag{5.27}$$

where $\tilde{F}$ is the Fourier-space representation of the Lagrangian function F. The extension of (5.27) to include the higher-order bias $b_{\nabla^2\delta}$ can be found in [17, 14].

One approach to evaluate biases is the excursion set approach [33]. This does not, however, have an analytical solution for generic MG models, due to the fact that the critical overdensity for gravitational collapse is not a constant at a given cosmological time, as it is in GR. One can then perform brownian-walk simulations in that case, as was done in [17].

In our analysis here, we will evaluate predictions from (5.24) *only* with a local-in-matter density Lagrangian bias, which simply corresponds to the limit $b_{\nabla^2} = 0$ of this relationship. In the total absence of an analytical method to evaluate the bias parameters b_n, they can be treated as free parameters to be fitted over the N-body simulations, a method followed by [46, 145, 193], for instance. In [191], an analytical model was developed, for the calculation of the bias parameters in MG models, which is the one we adopt in this work. Based on the PBS formalism [86], the Lagrangian bias factors of order n are given by

[125, 124, 164]:

$$b_n^L(M) = \frac{1}{\bar{n}_h(M,0)} \frac{d^n \bar{n}_h(M,\Delta)}{d\Delta^n}\bigg|_{\Delta=0}, \tag{5.28}$$

where $\bar{n}_h(M,0)$ is the halo mass function of halos with mass M and $\bar{n}_h(M,\Delta)$ is its response, in the presence of a long-wavelength density perturbation Δ. By suitably modeling $\bar{n}_h(M,0)$ and its response in MG, using the Sheth-Tormen (ST) model [166] with an environment-dependent gravitational collapse, [191] derived the PBS biases in MG models (relationships (78)-(80) in that work). This approach was shown to agree very well with simulations and thus we adopt it in this work as well; readers interested in more details about this implementation, are referred to [191]. The halo bias values b_1 and b_2, used in this chapter, are the ones shown in Table I of [191], predicted for each gravity model, halo mass range and cosmological time.

5.3.3 Direct Lagrangian Approach to RSD in Modified Gravity

In the previous section 5.3.2, we discussed how LPT can be used to robustly model the two-point statistics of halos in both the cases of GR and MG. However, the peculiar velocities of the observed galaxies, sourced by the perturbations in the underlying density field, contribute to the line-of-sight component of the observed recession velocity, contaminating thus the information extracted from spectroscopic means. These "Redshift-Space Distortions", in particular, introduce an anisotropy in the observed clustering pattern [88, 70, 71]. To model their impact on the clustering statistics, and following standard practice, we fix the line-of-sight in the Cartesian $\hat{z}$ direction for all objects, adopting the plane-parallel approximation. This approximation has been shown to work well in the context of modern surveys of the LSS [151, 210]. Having adopted this ap-

proach, if $\mathbf{x}$ is the real-space position of a tracer with peculiar velocity $\mathbf{v}(\mathbf{x})$, then its observed, "redshift-space" position $\mathbf{s}$ will be:

$$\mathbf{s} = \mathbf{x} + \frac{\hat{z} \cdot \mathbf{v}(\mathbf{x})}{aH(a)}\hat{z}, \tag{5.29}$$

with $H(a)$ the Hubble factor at a given scale-factor a. As a consequence, the redshift-space 2-point correlation function for halos

$$\xi_X^s(\mathbf{r}) = \langle \delta_X(\mathbf{s})\delta_X(\mathbf{s}+\mathbf{r})\rangle, \tag{5.30}$$

becomes directionally dependent, unlike the real-space expression given by (5.23).

With the advent of precision cosmology, a great deal of theoretical effort has been put into analytically modeling (5.30), with the various different approaches summarized in [195]. Within the framework of LPT, the most straightforward approach, called "Direct Lagrangian" in [195] and considered in [46, 203, 196], takes advantage of the fact that, in LPT, the displacement field simply transforms as:

$$\mathbf{\Psi}^s = \mathbf{\Psi} + \frac{\hat{z} \cdot \dot{\mathbf{\Psi}}(\mathbf{x})}{H(a)}\hat{z}. \tag{5.31}$$

This can be easily seen if ones combines (5.29) and (5.7) with the fact that the peculiar velocity in LPT is given by $\mathbf{v} = a\dot{\mathbf{\Psi}}$. (5.31) can then be further simplified if one notices that, up to order n, the LPT field evolves as $\mathbf{\Psi}^{(n)} \propto D^n(a)$, giving $\dot{\mathbf{\Psi}}^{(n)} = nf_0 H\mathbf{\Psi}^{(n)}$, with $f_0(a) = \frac{d\ln D}{d\ln a}$ the GR growth rate, thus giving

$$\Psi_i^{s(n)} = \left(\delta_{ij} + nf_0\hat{z}_i\hat{z}_j\right)\Psi_j^{(n)}. \tag{5.32}$$

Then it quickly follows that the Lagrangian correlators (5.26) will also transform accordingly, e.g.

$$U_i^{s(n)} = \left(\delta_{ij} + nf_0\hat{z}_i\hat{z}_j\right)U_j^{(n)}. \tag{5.33}$$

In the Direct Lagrangian approach, the RSD correlation function is calculated through directly mapping the Lagrangian correlators (5.26) to redshift-space, as in (5.32)-(5.33), and then using (5.24) with the shifted correlators.

In MG, however, the situation is a little more complicated, because, as we saw in (5.17), the MG growth factor is scale-dependent. As a result, $\dot{\mathbf{\Psi}}$ cannot be simplified as in GR and (5.32) does not apply. Instead, the LPT displacement field will now transform as

$$\Psi_i^{s(n)} = \Psi_i^{(n)} + \hat{z}_i \hat{z}_j \frac{d\Psi_j^{(n)}}{d\ln a}, \tag{5.34}$$

where the added shift has to be evaluated numerically. In the Appendix E, we present the details on how the Direct Lagrangian approach is implemented in MG theories with scale-dependence. It is worth emphasizing, at this point, that the fact that the RSD shift depends so sensitively on the underlying gravity model, is exactly what makes it such a powerful cosmological probe.

5.3.4 The Gaussian Streaming Model In Modified Gravity

In the previous section, we saw that, despite their success at accurately capturing the real-space clustering statistics for a wide range of models, Lagrangian methods prove to be inadequate at *directly* predicting the velocity-induced redshift-space anisotropies. This problem can be overcome by employing the Gaussian Streaming Model (GSM), first proposed in [145], inspired by the the work of [67]. In order to address the discrepancy between the traditional phenomenological "streaming" (or dispersion) models [56, 131] and the linear Kaiser limit [88], [67] adopted a probabilistic approach to relate the distributions of tracers in the real and redshift space. In particular, if $\mathcal{P}$ is the pairwise veloc-

ity Probability Density Function (PDF), then the real-space correlation function of tracers, $\xi_X^r(r)$, will be mapped to the redshift-space one as [67, 160]:

$$1 + \xi_X^s(s_\perp, s_\parallel) = \int dy [1 + \xi_X^r(r)] \mathcal{P}(y = s_\parallel - r_\parallel | \mathbf{r}), \tag{5.35}$$

where $s_\perp, s_\parallel$ are the perpendicular and parallel to the line-of-sight components of the redshift-space separation s, with $s = \sqrt{s_\perp^2 + s_\parallel^2}$ and $r = \sqrt{s_\perp^2 + y^2}$. By taking the linear limit of (5.35), and allowing for the scale-dependence of the pairwise velocity moments, [67] showed that line-of-sight variations of the pairwise velocity and its dispersion drive the correlation function away from isotropy in redshift space. The pairwise velocity PDF $\mathcal{P}$ is in principle not Gaussian, even in the case of a Gaussian density field, but can be well approximated by a Gaussian near its peak [160]. Using a non-perturbative resummation of the linearized limit of (5.35) in [67], [145] proposed the GSM expression:

$$1 + \xi_X^s(s_\perp, s_\parallel) = \int_{-\infty}^{\infty} \frac{dy}{\sqrt{2\pi\sigma_{12}^2(r,\mu)}} [1 + \xi_X^r(r)] \exp\left[-\frac{\Big(s_\parallel - y - \mu v_{12}(r)\Big)^2}{2\sigma_{12}^2(r,\mu)} \right], \tag{5.36}$$

where $\mu = \hat{r} \cdot \hat{z} = \frac{y}{r}$, $\mu v_{12}(r)$ the pairwise velocity and $\sigma_{12}^2(r,\mu)$ the pairwise velocity dispersion along the line-of-sight. Using CLPT to model the ingredients of the GSM, the accuracy of the initial approach was improved in [198], which was able to match the redshift-space halo clustering statistics extracted from N-body simulations at the few % level. Further improvements included adding tidal bias and EFT corrections [193], as well as higher moments in the cumulant expansion [186, 31, 32], while the GSM was also applied to observational data [144, 152, 153, 8, 211]. In [35], the GSM was employed to model the anisotropic correlation function for dark matter in MG, using RegPT and the SPT approach in [145], but not LPT.

Building upon the formalism presented in [198] and having already laid the foundation in Section 5.3.2, we proceed to expand the GSM (5.36) to predict the

anisotropic redshift-space correlation function for biased tracers in MG, modeling its ingredients with CLPT. To do so, we need to express the two velocity moments in CLPT, as we have already done with $\xi(r)$, which is performed below.

5.3.5 Velocity Moments in Modified Gravity

With regards to the calculation of the velocity moments in MG, the main point of divergence from the corresponding approach in GR employed in [198, 193], lies in the fact that the LPT growth factors are also scale-dependent in this case, as we saw in section 5.3.1. Keeping this in mind, below we present the main results and summarize how they differ from their GR counterparts, with the details shown in the Appendix D. The relative peculiar velocity between two tracers at Eulerian positions $\mathbf{x}_2$ and $\mathbf{x}_1$, is

$$\frac{\mathbf{v}_n(\mathbf{x}_2) - \mathbf{v}_n(\mathbf{x}_1)}{aH} = \frac{\dot{\mathbf{\Psi}}_{2n} - \dot{\mathbf{\Psi}}_{1n}}{H} = \frac{\dot{\mathbf{\Delta}}_n}{H}, \tag{5.37}$$

where we made use of the fact that $\mathbf{v} = a\dot{\mathbf{\Psi}}$. In GR, one typically uses, as we also saw in section 5.3.3, the fact that $\mathbf{\Psi}^{(n)} \propto D^n(a)$ in the EDS approximation, which gives $\dot{\mathbf{\Psi}}^{(n)} = n f_0 H \mathbf{\Psi}^{(n)}$, so as to simplify (5.37), which is *not* the case in MG; here $\dot{\mathbf{\Delta}}_n$ needs to be evaluated numerically. Following standard practice, one may then define the velocity generating function [160, 198]

$$Z(\mathbf{r}, \mathbf{J}) = \langle [1 + \delta_X(\mathbf{x})][1 + \delta_X(\mathbf{x} + \mathbf{r})] e^{\mathbf{J} \cdot \frac{\dot{\mathbf{\Delta}}}{H}} \rangle, \tag{5.38}$$

with $\xi_X(r) = Z(r, 0) - 1$. In the case of a local Lagrangian bias (5.22) and after the usual Fourier transforms (as in [16, 191]), it can be expressed as:

$$Z(\mathbf{r}, \mathbf{J}) = \int d^3q \int \frac{d^3k}{(2\pi)^3} e^{i\mathbf{k}\cdot(\mathbf{q}-\mathbf{r})} \int \frac{d^2\Lambda_1}{(2\pi)^2} \frac{d^2\Lambda_2}{(2\pi)^2} \tilde{F}_1 \tilde{F}_2 \langle e^{i\left[\lambda_1\delta_1 + \lambda_2\delta_2 + \eta_1\nabla^2\delta_1 + \eta_2\nabla^2\delta_2 + \mathbf{k}\cdot\mathbf{\Delta} + \mathbf{J}\cdot\frac{\dot{\mathbf{\Delta}}}{H}\right)} \rangle, \tag{5.39}$$

where we defined $\Lambda_1 = (\lambda_1, \eta_1)$, $\tilde{F}_1 = \tilde{F}(\Lambda_1)$ and $\Lambda_2 = (\lambda_2, \eta_2)$, $\tilde{F}_2 = \tilde{F}(\Lambda_2)$, as in [17]. Given a generating functional, the velocity moments of order p can then be straightforwardly evaluated as [198]:

$$\begin{aligned}
&\langle [1+\delta_X(\mathbf{x})][1+\delta_X(\mathbf{x}+\mathbf{r})]\left(\prod_{k=1}^{p}[\mathbf{v}_{i_k}(\mathbf{x}+\mathbf{r})-\mathbf{v}_{i_k}(\mathbf{x})]\right)\rangle = \\
&= \prod_{k=1}^{p}\left(-i\frac{\partial}{\partial \mathbf{J}_{i_k}}\right) Z(\mathbf{r},\mathbf{J})\Big|_{\mathbf{J}=0} \\
&= \int d^3q \int \frac{d^3k}{(2\pi)^3} e^{i\mathbf{k}\cdot(\mathbf{q}-\mathbf{r})} \int \frac{d^2\Lambda_1}{(2\pi)^2}\frac{d^2\Lambda_2}{(2\pi)^2}\tilde{F}_1\tilde{F}_2 \times \langle \prod_{k=1}^{p}\left(\frac{\dot{\mathbf{\Delta}}_{i_k}}{H}\right) e^{i\left[\lambda_1\delta_1+\lambda_2\delta_2+\eta_1\nabla^2\delta_1+\eta_2\nabla^2\delta_2+\mathbf{k}\cdot\mathbf{\Delta}\right]}\rangle \\
&= \int d^3q M_{p,(i_1,..,i_p)}(\mathbf{r},\mathbf{q}),
\end{aligned} \tag{5.40}$$

where in the last line we defined $M_{p,(i_1,..,i_p)}$ as the integrand quantity.

The real-space mean pairwise velocity along the pair separation vector, $\hat{r}$, is defined as :

$$v_{12}(r) = v_{12,n}\hat{r}_n = \frac{\langle [1+\delta_X(\mathbf{x})][1+\delta_X(\mathbf{x}+\mathbf{r})][\mathbf{v}_n(\mathbf{x}+\mathbf{r})-\mathbf{v}_n(\mathbf{x})]\rangle}{\langle [1+\delta_X(\mathbf{x})][1+\delta_X(\mathbf{x}+\mathbf{r})]\rangle}\hat{r}_n. \tag{5.41}$$

The denominator of (5.41) is simply equal to $1+\xi_X(r)$ from (5.24), whereas the numerator represents the galaxy-number weighted average pairwise velocity. Given the definition (5.40), and using the CLPT scheme for MG discussed in Section 5.3.2, we have [198]:

$$v_{12,n} = \frac{\int d^3q M_{1,n}(\mathbf{r},\mathbf{q})}{1+\xi_X(r)}, \tag{5.42}$$

with

$$\begin{aligned}
M_{1,n}(\mathbf{r},\mathbf{q}) \;=\; & f_0 \frac{e^{-\frac{1}{2}(q_i-r_i)(A_L^{-1})_{ij}(q_j-r_j)}}{(2\pi)^{3/2}\,|A_L|^{1/2}} \times \\
& \Bigg(2b_1\dot{U}_n^{(1)} - g_i\dot{A}_{in} + b_2\dot{U}^{20} + b_1^2\dot{U}^{11} - \frac{1}{2}G_{ij}\dot{W}_{ijk} - 2b_1 g_i\dot{A}_{in}^{10} \\
& +2b_1b_2\xi_L\dot{U}_n^{(1)} - 2[b_2+b_1^2]g_iU_i^{(1)}\dot{U}_n^{(1)} - b_1^2\xi_L g_i\dot{A}_{in}^{(1)} - 2b_1G_{ij}U_i^{(1)}\dot{A}_{in}^{(1)} \\
& -2b_{\nabla^2\delta}\mathcal{B}_{2,n}\Bigg),
\end{aligned} \tag{5.43}$$

where we defined

$$\begin{aligned}
\dot{U}_i(\mathbf{q}) &\equiv \frac{1}{f_0 H}\langle\delta(\mathbf{q}_1)\dot{\Delta}\rangle, \qquad & \dot{A}_{ij}(\mathbf{q}) &\equiv \frac{1}{f_0 H}\langle\Delta_i\dot{\Delta}_j\rangle \\
\dot{U}_i^{20} &\equiv \frac{\langle\delta^2(\mathbf{q}_1)\dot{\Delta}_i\rangle}{H f_0}, \qquad & \dot{U}_i^{11} &\equiv \frac{\langle\delta(\mathbf{q}_1)\delta(\mathbf{q}_2)\dot{\Delta}_i\rangle}{H f_0}, \\
\dot{A}_{ij}^{10} &= \frac{\langle\delta(\mathbf{q}_1)\Delta_i\dot{\Delta}_j\rangle}{f_0 H}, \qquad & \dot{W}_{ijk} &= \frac{\langle\Delta_i\Delta_j\dot{\Delta}_k\rangle}{f_0 H}, \\
\mathcal{B}_{2,n} &= -\nabla_n\xi_L(q).
\end{aligned} \tag{5.44}$$

The expressions for the new correlators (5.44) are presented in the Appendix D. Here we briefly stress that, even though these definitions are the same as in the GR case [198, 193], the functions (5.44) take different values in MG, because of the different evolution of the LPT displacement field (manifesting itself in the Δ and $\dot{\Delta}$ functions). Similarly, this is also the case for the $M_{1,n}$ function in (5.43), that depends on these functions. The quantity entering (5.36) is actually the pairwise velocity along the line-of-sight, rather than the separation vector, which simply accounts to multiplying v_{12} from (5.41) by μ.

The pairwise velocity dispersion along the line-of-sight is defined as

$$\hat{\sigma}_{12}^2(r,\mu) = \frac{\langle[1+\delta_X(\mathbf{x})][1+\delta_X(\mathbf{x}+\mathbf{r})][v_z(\mathbf{x}+\mathbf{r})-v_z(\mathbf{x})]^2\rangle}{\langle[1+\delta_X(\mathbf{x})][1+\delta_X(\mathbf{x}+\mathbf{r})]\rangle}, \tag{5.45}$$

which is commonly decomposed into components parallel $\hat{\sigma}_\parallel^2$ and perpendicular $\hat{\sigma}_\perp^2$ to the pair separation vector, r, in which case

$$\hat{\sigma}_{12}^2(r,\mu) = \mu^2\hat{\sigma}_\parallel^2 + (1-\mu^2)\hat{\sigma}_\perp^2. \tag{5.46}$$

The two components can be calculated after taking projections of the second velocity moment, the pairwise velocity dispersion tensor, given by [198]:

$$\hat{\sigma}_{12,nm}^2 = \frac{\int d^3q M_{2,nm}(\mathbf{r},\mathbf{q})}{1+\xi_X(r)}, \tag{5.47}$$

with

$$M_{2,nm}(\mathbf{r},\mathbf{q}) = f_0^2 \frac{e^{-\frac{1}{2}(q_i-r_i)(A_L^{-1})_{ij}(q_j-r_j)}}{(2\pi)^{3/2}\,|A_L|^{1/2}} \times \Bigg(2\left[b_1^2+b_2\right]\left(\dot{U}_n^{(1)}\dot{U}_m^{(1)}\right) - 2b_1\left(\dot{A}_{in}^{(1)}g_i\dot{U}_m^{(1)} + \dot{A}_{im}^{(1)}g_i\dot{U}_n^{(1)}\right) - \dot{A}_{im}^{(1)}\dot{A}_{jn}^{(1)}G_{ij} + \ddot{A}_{nm} + b_1^2\xi_L\ddot{A}_{nm}^{(1)} - 2b_1U_i^{(1)}g_i\ddot{A}_{nm}^{(1)} + 2b_1\ddot{A}_{nm}^{10} - \ddot{W}_{inm}g_i \Bigg), \tag{5.48}$$

and where we additionally defined

$$\ddot{A}_{ij} = \frac{\langle\dot{\Delta}_i\dot{\Delta}_j\rangle}{f_0^2H^2}, \qquad \ddot{A}_{ij}^{10} = \frac{\langle\delta(\mathbf{q}_1)\dot{\Delta}_i\dot{\Delta}_j\rangle}{f_0^2H^2}, \qquad \ddot{W}_{ijk} = \frac{\langle\Delta_i\dot{\Delta}_j\dot{\Delta}_k\rangle}{f_0^2H^2}. \tag{5.49}$$

The expressions for the functions (5.49) are presented in the Appendix D. It is worth adding here, that all $b_{\nabla^2\delta}$ terms identified in $\sigma^2_{12,nm}$, are multiplications of U functions and terms that although are order P_L, have a size similar to 1-loop terms [193], which is why they are dropped and thus absent in (5.48). More importantly, even though we do not generally include EFT corrections in our biasing scheme, we emphasize on the fact that one of the leading EFT counterterms in (5.48) is of the form $\alpha_\sigma\delta_{nm}$ [193], which corresdonds to the correction:

$$\hat{\sigma}^2_{12,nm} \to \hat{\sigma}^2_{12,nm} + \alpha_\sigma\frac{1+\xi^{0-loop}_{matter}}{1+\xi_X^{1-loop}}\delta_{nm}, \tag{5.50}$$

that leads to a constant shift, α_σ, at large scales. This naturally accommodates the need to add a constant shift to the PT prediction for $\sigma^2_{12,nm}$ so as to match the values extracted from N-body simulations, as was found in [145, 198, 193] for GR and as we will also show to be the case for MG, in the next section.

Having obtained $\hat{\sigma}^2_{12}$, we get the cumulant version $\sigma^2_{12,nm} = \hat{\sigma}^2_{12,nm} - v_{12,n}v_{12,m}$ [193], which is then projected as:

$$\sigma^2_\parallel(r) = \hat{r}_n\hat{r}_m\sigma^2_{12,nm}(\mathbf{r}), \qquad \sigma^2_\perp(r) = \frac{1}{2}(\delta_{nm}+\hat{r}_n\hat{r}_m)\sigma^2_{12,nm}(\mathbf{r}). \tag{5.51}$$

The combination of (5.46)-(5.51) gives us $\sigma^2_{12}(r,\mu)$ that is the final necessary ingredient to enter eqn (5.36). Finally, as was the case for $\xi_X(r)$ in (5.24), we eventually consider the velocity moments v_{12} and σ^2_{12} with a local in matter density

Lagrangian bias (meaning $b_{\nabla^2\delta} = 0$), the bias factors b_1 and b_2 of which are evaluated using the analytical model discussed in section 5.3.2.

5.4 Results

The objective in this work is to assess and compare configuration-space (redshift-space) predictions coming from our analytical model, against those extracted from the Group I and Group II N-body simulations, that we introduced in section 5.2.2.

In section 5.4.1, we first confirm that the velocity information entering the GSM (5.36), the real-space pairwise velocity and the pairwise velocity dispersion for halos, in (5.42) and (5.47), are accurately captured by our CLPT implementation in MG.

In section 5.4.2, we assess the predictions for the redshift-space 2-point correlation function for halos using both the Direct Langrangian and GSM approaches. Using the PBS formalism for the bias values, the 3 ingredients used as input in the GSM expression (5.36), are calculated through (5.24), (5.42) and (5.47). The real-space 2-point correlation function for halos in MG has already been cross-checked and confirmed in [191], using the same CLPT and bias schemes against the same set of simulations.

To perform the various integrations, we use a suitably modified version of the public C++ code released by [193], to incorporate the modifications to allow deviations from GR. This extends our previous work in [191], made publicly available in `https://github.com/CornellCosmology/bias_MG_`

`LPT_products`. The code accepts as input the linear power spectrum and the LPT growth factors up to 3^{rd} order, evaluated for each MG model and cosmology. The linear power spectra are calculated using the publicly available code `CAMB` [107], while the growth factors are extracted from the `MATHEMATICA` notebooks released in the above GitHub repository.

5.4.1 Halo Pairwise Velocity Statistics

We begin this section by comparing the CLPT predictions for the real-space pairwise velocity of halos in MG, obtained through (5.41)-(5.43), against the results from the N-body simulations.

In Fig. 5.1 we compare the analytical CLPT predictions for the real-space pairwise velocity of halos in MG, obtained through (5.41)-(5.43), against the results from the N-body simulations. In the top panels we show comparisons for GR and the F5 MG model for the 3 mass bins in the $z = 1$ snapshot of the Group II simulations. The F5 CLPT curves are found to trace the shape of the pairwise velocity well, across a wide range of halo masses, achieving the same level of agreement as in the known GR case, down to scales of $r \sim 10$ Mpc/h. The 1-loop CLPT result significantly improves upon the accuracy of the linear-theory prediction. These results are consistent with what was observed in the corresponding GR case in [198].

Performing the same comparison against the F6 and N1 & N5 models of the Group I snapshots at $z = 0.5$, shown in the bottom panel of Fig. 5.1, we again find that CLPT has the same level of agreement as previously, but down to scales of $r \sim 17$ Mpc/h for the F6 & N5 models and for $r \sim 20$ Mpc/h for the N1 case.

Given that this comparison is now performed at a lower redshift than in the Group II case, where the expected scale where nonlinearities become significant (and PT fails) is larger, this result is expected.

The bias parameters we use here, derived by fitting the ST parameters to the simulated halo mass function, are a key factor in achieving accurate predictions for the pairwise velocity, which is a necessary requirement for accurate predictions using the GSM approach. An alternative option is to treat the biases as free parameters, that give the best-fit to the simulations, as for example done in [46, 198, 193].

We next investigate how well our CLPT framework performs in capturing the halo pairwise velocity dispersion from the simulations, for all MG models we consider. When performing this comparison, in terms of the dispersion components parallel ($\hat{\sigma}^2_{\parallel}$) and perpendicular ($\hat{\sigma}^2_{\perp}$) to the pair separation vector, we uncover the existence of a persistent offset between the theoretical curves and the simulated values, manifesting itself in all cases we study. This phenomenon has been observed in the context of GR, both when using Eulerian [145] and Lagrangian [198, 193] PT to model σ^2 and in MG [35], which we also find to be the case in our CLPT implementation for MG models. This mismatch is attributed to small-scale contributions to the halo velocity dispersion, that are impossible to capture analytically [145, 198]. It was observed that simply adding a constant offset so as to match the two predictions at large scales suffices to get an accurate perturbative representation of σ^2. We should also note, at this point, that this feature was also discussed by [160], who noted that nonlinear contributions to the velocity dispersion contribute a constant in the large-scale limit, that cannot be captured by linear theory. In [193], that considered EFT corrections in the

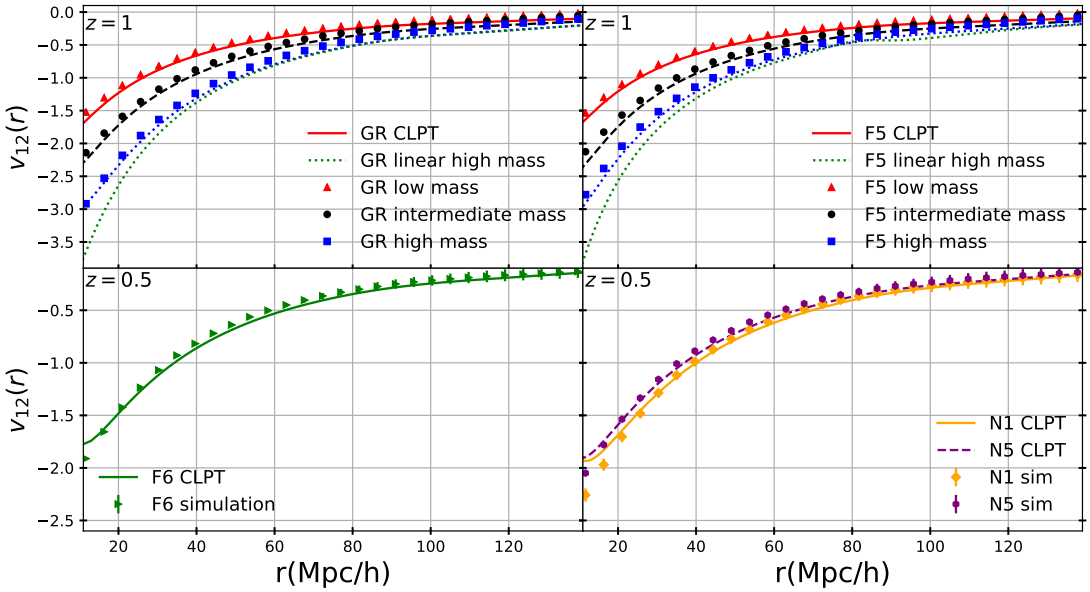

Figure 5.1: Real-space pairwise velocity for GR [top left] and the F5 model [top right] at $z = 1$, obtained by the Group II simulations in the low mass [blue square], intermediate mass [black circle] and high mass [red triangle] bins, and for F6 [bottom left] and the N1 & N5 models [bottom right, orange diamond and purple hexagon respectively] at $z = 0.5$ from the Group I simulations. Lines denote the theoretical predictions from 1-loop CLPT, through (5.41)-(5.43), for each corresponding model. The green dotted lines in the upper panels represent the linear prediction for the high mass bin.

context of the GSM, it was shown that one of the EFT counter-terms contributing to the velocity dispersion is of the form (5.50), which reduces to a constant at large scales and naturally accommodates for the need to correct this offset with a constant free parameter. In our work, and in agreement with the above results, we find the CLPT prediction from (5.47) & (5.48), combined with a constant offset to match the largest simulation bin at $r = 137.8$ Mpc/h, to be able to capture the shape of $\hat{\sigma}^2_{\parallel}$ and $\hat{\sigma}^2_{\perp}$ very well for all the modified gravity models, as well as GR. The values of the constants added for each model are reported in

Table 5.1.

When looking at Table 5.1, one notices that the Zel'dovich result for σ^2 always falls a little short of the simulated value at the largest spatial bin and needs to be corrected by a small positive constant. Trying to correct for this deficit by including the 1-loop contributions, however, always results at a relatively larger overestimate of the large-scale value of the dispersion, which then needs to corrected by adding a large negative constant, contrary to the Zel'dovich results that need only a small positive offset. This behavior has been observed before for ΛCDM in [145, 198, 186, 193] (see in particular fig.4 and the discussion after eq. 44 in [186]), with the authors of [186] arguing that the better performance of linear theory, relatively over CLPT, should be considered an accident because one expects large corrections to σ^2 due to the presence of zero-lag correlators. Furthermore, [193] also reported large values for the offset (see table 1 of that chapter), while the same method was applied to fit real data in [144, 82]. We further find parallels with what was observed in [194, 191] for predictions of the dispersion of the LPT displacement field. There, it was shown that 1-loop LPT tends to over-predict the LPT displacement-field dispersion, compared to the simulations, because this quantity depends on zero-lag correlators, that are hard to model perturbatively. Linear theory, on the other hand, was found to give a closer estimate, a little short of the simulated value, as we also see to be the case when modeling the pairwise velocity dispersion. If we take the large-scale limit of the CLPT expression for the pairwise velocity dispersion (5.47) & (5.48), we find that

$$\hat{\sigma}^2_{\parallel}, \hat{\sigma}^2_{\perp} \longrightarrow f_0^2(\ddot{X}^L_{\infty} + \ddot{X}^{\rm loop}_{\infty} + 2b_1\ddot{X}^{10}_{\infty}), \tag{5.52}$$

with $\ddot{X}_{\infty}$ and $\ddot{X}^{10}_{\infty}$ the constant limits of functions $\ddot{X}(q)$ and $\ddot{X}^{10}(q)$, defined in (D.36,D.38), as $q \to \infty$. As a result of (5.52), we see that the two pairwise

velocity dispersion components $\hat{\sigma}^2_{\parallel}$ and $\hat{\sigma}^2_{\perp}$ also involve zero-lag quantities in their large-scale limit, which explains the connection that can be drawn between these two cases. As in [191], we find this overestimation to be more pronounced in MG, compared to the GR case, getting progressively more pronounced with higher deviations from GR, which explains why the degree of analytical overestimation in the LPT predictions becomes more severe, as one considers models that are less screened. We also notice that the degree of analytical overestimation increases with halo mass in the Group II snapshots. This is also explained from (5.52) where we see that the 1-loop correction of the large-scale limit of the velocity dispersion depends on the the linear halo bias, through the third term. Higher halo masses correspond to a larger value for the linear bias b_1, which in turn makes the third term larger, relative to the lower mass cases, resulting in an overall even larger overestimation in this case. The fact that the bias dependence appears beyond the linear level, explains why the shifts required for the Zel'dovich predictions are very similar across the different mass bins for both the GR and the F5 snapshots of the Group II simulations. Also, this bias dependence implies that, for a fixed halo mass range, and given that the bias b_1 increases with redshift, this overestimation can become relatively more pronounced at higher z. [2] Finally, in Table 5.1 we notice that 1-loop LPT predicts increasing values for the large-scale limit of the pairwise velocity dispersion, as we move towards higher halo masses, whereas the opposite trend is reflected in the Group II simulations. Even though this is interesting, we cannot certainly say whether this trend is statistically significant, as there is only one available realization and thus we defer this investigation to future work, when more simulations become available.

[2] At this point, however, we should be careful *not* to directly compare the results reported for the two redshifts of Table 5.1, as they refer to two snapshots with different mass ranges, which also correspond to different cosmologies.

Model	$\hat{\sigma}^2_{\parallel}(r$ =100Mpc/h)[(Mpc/h)^2]			Shift (r=137.8Mpc/h)	
	LPT	Zel.	Sim.	LPT	Zel.
Group I: GR	36.2	23.8	27.9	−7.7	4.0
Group I: F6	43.3	25.0	27.8	−15.5	2.5
Group I: N1	44.6	29.5	36.2	−8.6	6.5
Group I: N5	37.6	25.1	29.7	−7.5	4.3
Group II: GR low-mass	28.6	19.9	20.9	−8.3	1.4
Group II: GR mid-mass	32.4	19.8	20.7	−11.8	1.0
Group II: GR hi-mass	37.6	19.8	20.5	−17.3	0.5
Group II: F5 low-mass	33.2	21.8	22.5	−10.5	0.5
Group II: F5 mid-mass	38.5	21.8	21.8	−16.5	0.0
Group II: F5 hi-mass	43.4	21.8	20.9	−22.5	−1.0

Table 5.1: The left-hand columns compare the values for $\hat{\sigma}^2_{\parallel}$, the pairwise velocity dispersion parallel to the separation vector, predicted by 1-loop LPT [1^{st} column] and the Zel'dovich approximations [2^{nd} col.] of (5.48) with those obtained from the N-body simulations [3^{rd} col.], at $r = 100Mpc/h$ for all the gravity models. The right-hand columns present the values of the constant shifts, added to theoretical predictions to give large scale agreement with simulations (at the largest bin center r =137.8 Mpc/h), for the 1-loop & Zel'dovich LPT results from (5.47) & (5.48).

In the left panel of Fig. 5.2, the $\hat{\sigma}^2_{\parallel}$ and $\hat{\sigma}^2_{\perp}$ CLPT predictions from (5.47) & (5.48) are compared against the simulations for the F6 model at $z = 0.5$. It is found that the 1-loop result, shifted by a constant, significantly improves upon the (also shifted) Zel'dovich approximation and remains consistent (within 1-σ errorbars) with the simulations down to $r \sim 30$ Mpc/h for $\hat{\sigma}^2_{\parallel}$ and $r \sim 20$ Mpc/h for $\hat{\sigma}^2_{\perp}$. When we shift the 1-loop CLPT result by the EFT counter-term (5.50), the accuracy is further improved and the results remain consistent down to smaller r. If we perform the same comparison for the F5 Group II snapshot at $z = 1$, however, as done for the high mass bin in the right panel of Fig. 5.2, we find that the constant that needs to be added to the 1-loop curve is very large and negative, comparable to the large-scale amplitude of σ^2. This leads to negative

and unphysical values for the dispersion components at low r . In particular, the perpendicular component of the pairwise velocity dispersion, $\sigma_\perp^2$, becomes negative at $r = 11.2, 6.1, 2.5$ Mpc/h for the high mass, intermediate mass and low mass bins of the F5 snapshot, respectively. The behavior is qualitatively similar for $\sigma_\parallel^2$, but the values remain physical (positive) down to slightly smaller scales. The reason this happened at $z = 1$ is that, since it is an earlier cosmological time, the velocity dispersion is smaller compared to the $z = 0.5$ case and comparable to the negative constant that needs to be added in order to adjust the CLPT prediction. To overcome this issue, which manifests itself for all three $z = 1$ halo mass bins and for both MG and GR scenarios, we can model the dispersion components using the other two approximations, the (shifted by a positive constant) Zel'dovich curve and/or the EFT-shifted 1-loop result, which are both better behaved at all scales of interest, as can be seen in Fig. 5.2. In [193] another approach to avoid the issues associated with $\sigma^2 < 0$ was proposed, namely to keep the linear part of the dispersion in the exponent and determinant of (5.36) and expand out the higher orders. As we discuss below, we did not find it to be necessary to adopt this approach in order to get accurate quadrupole predictions for the models we considered. Thus we do not consider this approach in our work.

In Fig. 5.3, we perform the same comparison between theory and simulations, with respect to $\hat{\sigma}_\parallel^2$ and $\hat{\sigma}_\perp^2$, for the N5 Group I snapshot at $z = 0.5$ and also for all 3 mass bins of the F5 Group II case at $z = 1$, finding very similar results as in Fig. 5.2. We note that the reason that we only show the shifted Zel'dovich results in the F5 Group II case of the right panel, is because it is this choice that will give the best match with the simulations, with respect to the values of the quadrupole of the redshift-space correlation function, as we will see below. In

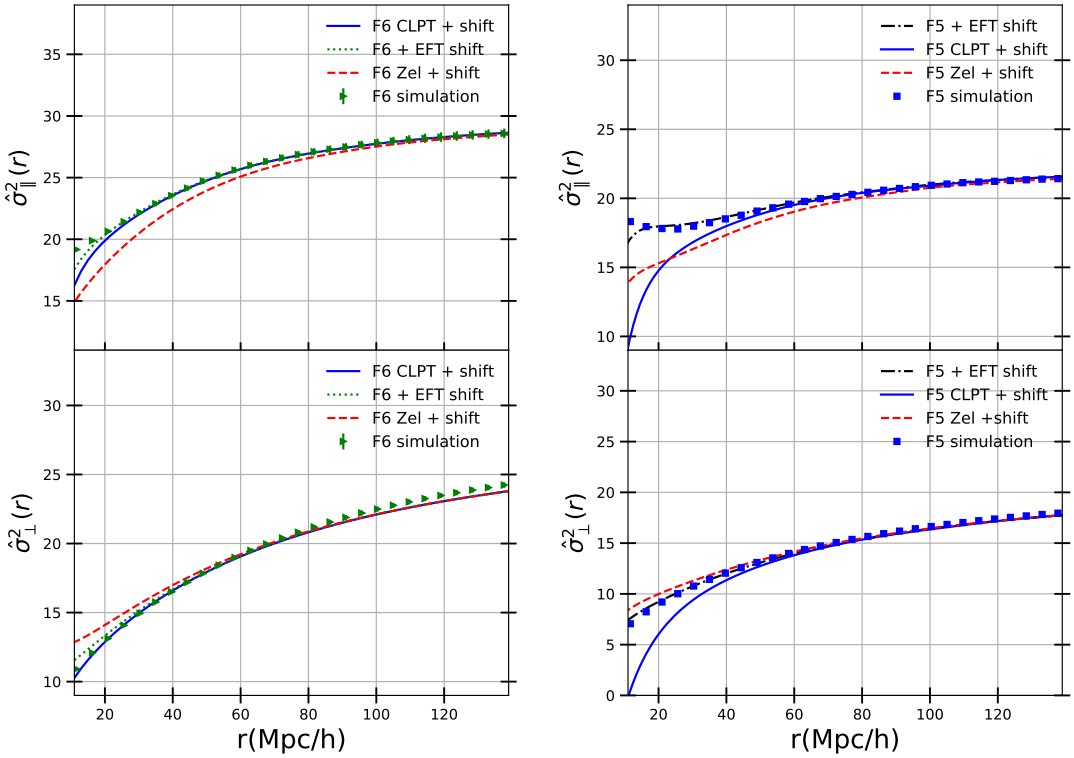

Figure 5.2: The pairwise velocity dispersion parallel [top] and perpendicular [bottom] to the pair separation vector for the F6 model at $z = 0.5$ from the Group I simulations [left panels, green right triangles]] and the F5 model at $z = 1$ from the high mass bin of the Group II simulations [right panels, blue squares]. In all panels the comparison to the theory predictions is shown for the 1-loop [solid blue line] and the Zel'dovich [red dashed line] CLPT predictions from (5.47) & (5.48), shifted by a constant, as well as from the 1-loop CLPT prediction shifted by a correction term given by EFT [green dotted line], as in (5.50). The values of the applied constant shifts are reported in Table 5.1.

this work we choose a shift constant value to match $\hat{\sigma}^2_{\parallel}$ at large scales. This gives very good agreement for both components, with only a small mismatch between the large-scale trends of the theory and simulation-derived values of $\hat{\sigma}^2_{\perp}$ in Figs 5.2 & 5.3 as was also noted in [145, 198, 193].

In the following analysis of the correlations functions, we use 1-loop CLPT to model the 3 ingredients entering the GSM expression (5.36), with the pairwise velocity dispersion shifted by a constant to match the simulations at the largest r bin. For the Group I simulations the LPT predicted value is shifted down by a constant. To compare to the Group II simulations, at higher redshift, since the constant shift to the predicted velocity dispersion leads to negative dispersion measurements at small separations, we use the (shifted) Zel'dovich result for the velocity dispersion, together with the 1-loop expressions for $\xi(r)$ and $v_{12}(r)$, as inputs into the GSM expressions.

5.4.2 Halo Redshift-Space 2-point Correlation Function

In this section, we present our predictions for the anisotropic redshift-space 2-point correlation function for halos, as obtained from the various analytical approaches considered and compare how well they capture the results from the MG N-body simulations. Given the directional dependence induced by RSD, the correlation function will now not only depend on the redshift-space separation $s = \sqrt{s^2_{\perp} + s^2_{\parallel}}$, but also on the cosine $\mu_s = \hat{z} \cdot \hat{s} = \frac{s_{\parallel}}{s}$ (not to be confused with $\mu = \frac{v}{r}$). Following common practice, the 2D anisotropic correlation function can then be expanded in a basis of Legendre polynomials, $P_l(\mu_s)$, as

$$\xi(s, \mu_s) = \sum_l \xi_l(s) P_l(\mu_s), \tag{5.53}$$

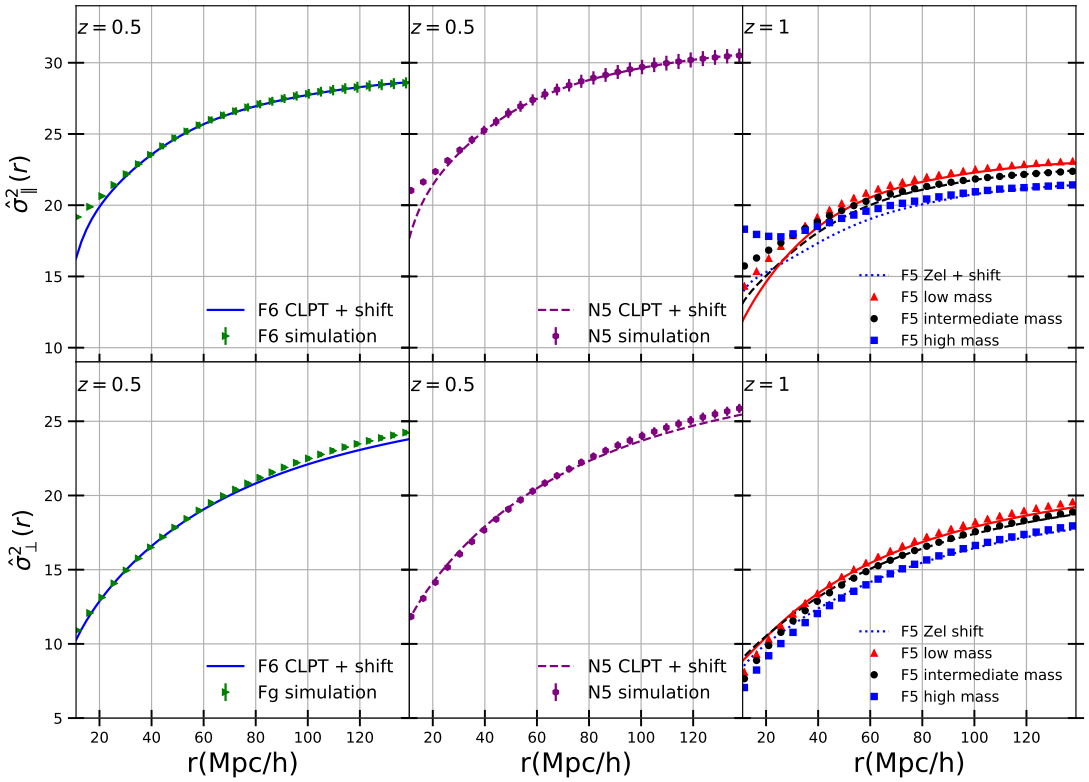

Figure 5.3: The pairwise velocity dispersion parallel [top] and perpendicular [bottom] to the pair separation vector for the F6 model at $z = 0.5$ [green right triagnles] in the left panel, for the N5 model at $z = 0.5$ [purple hexagons] in the middle panel and for the F5 model at $z = 1$ in the right panel. In the right panel, the results are shown in the low mass [blue squares], intermediate mass [black circles] and the high mass [red triangles] bins identified in the Group II simulations. For the $z = 0.5$ case, the lines represent the 1-loop CLPT prediction from (5.47) & (5.48) for each model, shifted by a constant, whereas in the $z = 1$ case, the lines show the prediction given by the Zel'dovich approximation in each bin, shifted by a constant. The values of the constant shifts are reported in Table 5.1.

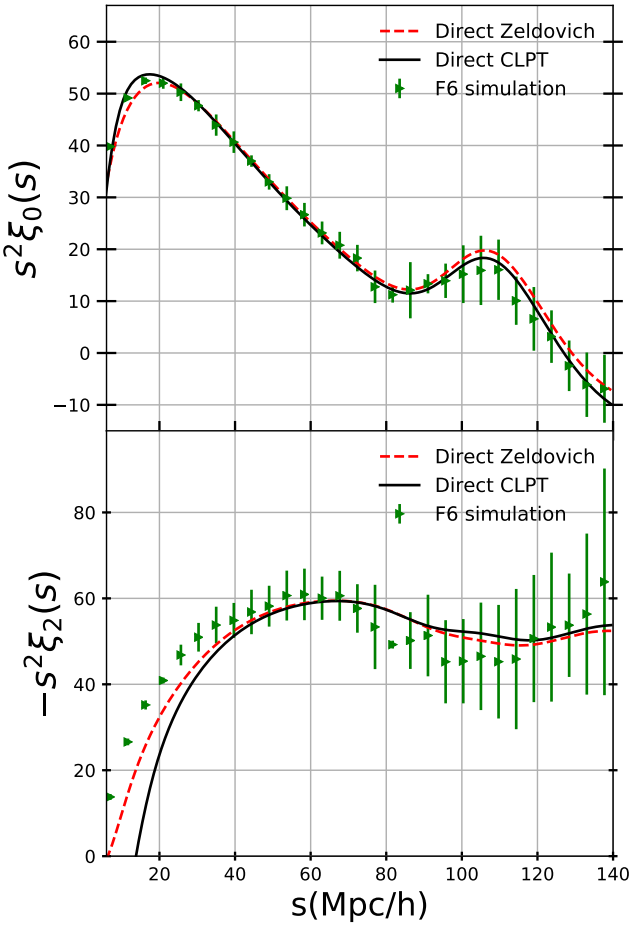

Figure 5.4: The monopole [Top] and quadrupole [Bottom] of the redshift-space correlation function for the F6 model at $z = 0.5$, as obtained by the Group I simulations [green right triangles] and by the direct Lagrangian approach using 1-loop CLPT [solid black line] and the Zel'dovich approximation [red dashed line].

where the multiples of order l can then be obtained from

$$\xi_l(s) = \frac{2l+1}{2} \int_{-1}^{1} d\mu_s \xi(s, \mu_s) P_l(\mu_s). \tag{5.54}$$

Our comparison will focus on the first three non-vanishing multipoles, the monopole, the quadrupole and the hexadecapole, for which $l = \{0, 2, 4\}$ and $P_l(\mu_s) = \{1, (3\mu_s^2 - 1)/2, (35\mu_s^4 - 30\mu_s^2 + 3)/8\}$, respectively.

Having obtained $\xi(s, \mu_s)$, either from an analytical model or the simulations,

we integrate (5.54) to get the multipoles. In the case of the Direct LPT and the GSM approaches, we perform a Gauss-Legendre integration scheme for the angular part, and trapezoidal quadrature for the radial part, whereas to extract this information from the simulations we use Simpson's rule.

In section 5.3.3, we described the Direct Lagrangian approach to the redshift-space correlation function for halos in MG. As is shown in the upper panel of Fig. 5.4, we see that this approach, both at the Zel'dovich level and including 1-loop corrections, can capture the monopole reasonably well, down to at least scales of $r \sim 20$ Mpc/h for the Group I F6 sample at $z = 0.5$. When performing the same comparison with respect to the quadrupole, however, and as shown in the bottom panel of Fig. 5.4, we find that the Direct approach performs very poorly, failing to follow the simulation trend at scales lower than $r < 50$ Mpc/h. Moreover, we notice that adding loop contributions to the linear, Zel'dovich approximation, does not improve the quadrupole analytical result, instead it performs even worse. This counterintuitive outcome is not new in the literature, but has been observed in [203] for GR (see Figs. 2 and 3 of that work), and here shown to also be the case in MG cosmologies, which motivates pursuing another avenue towards a precise modeling of redshift-space anisotropies, by means of the scale-dependent GSM approach.

We proceed to evaluate the performance of the GSM approach in MG, given by (5.36). For the comparison, the "GSM" curves are obtained following a constant shift to the LPT-predicted velocity dispersion for the lower redshift, Group I, simulations, and a shift to the Zel'dovich-predicted velocity dispersion for the higher redshift, Group II sims. When the 1-loop result for the velocity dispersion is shifted by the EFT term (5.50), the theoretical curve is labeled as "GSM

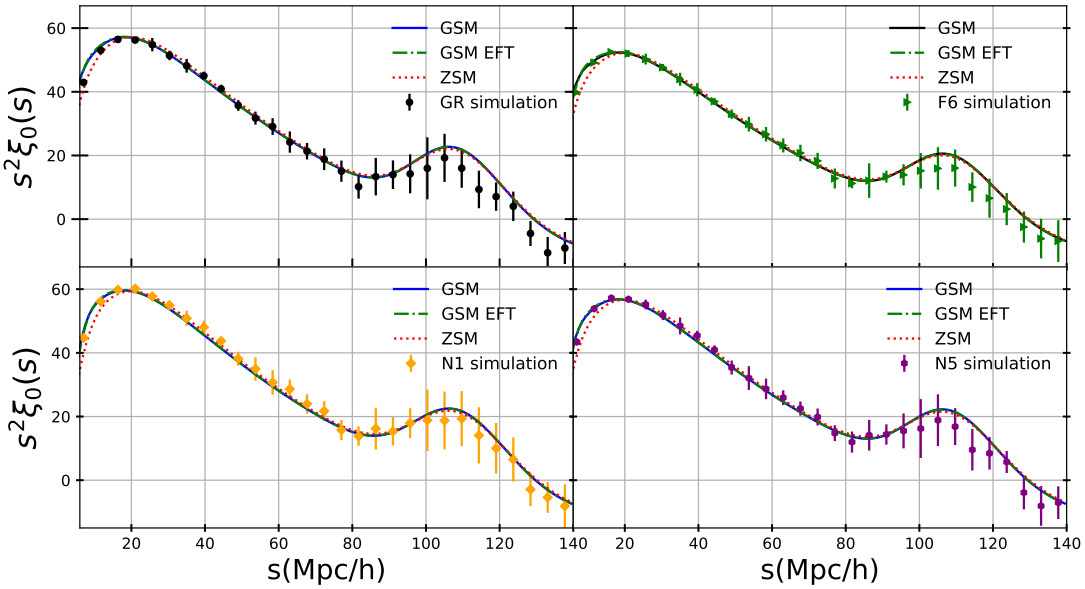

Figure 5.5: The monopole of the redshift-space two-point correlation function for GR [black circles] in the top left panel, for the F6 model [green right triangles] in the top right panel, for the N1 model [orange diamonds] in bottom left panel and for N5 model [purple hexagons] in the bottom right panel, as obtained from the Group I simulations at $z = 0.5$. Furthermore, for each model we plot the theoretical predictions given by the Gaussian Streaming Model (GSM) up to 1-loop order [black solid lines], by the Zel'dovich Streaming Model (ZSM) [magenta dotted lines] and by the GSM with the 1-loop velocity dispersion shifted by the EFT counter-term (5.50) [green dot-dash line].

EFT" in all figures. Finally, we consider the GSM predictions when simply using the Zel'dovich linear (LPT) theory to approximate all 3 ingredients of the model, the Zel'dovich Streaming Model (ZSM) [203].

In Fig. 5.5, the GSM prediction is shown to perform very well, across the spectrum of MG models probed in the Group I simulations, in capturing the monopole of the correlation function, down to scales of $r \sim 15$ Mpc/h. This is consistent with findings for the real-space monopole in [191]. The differences

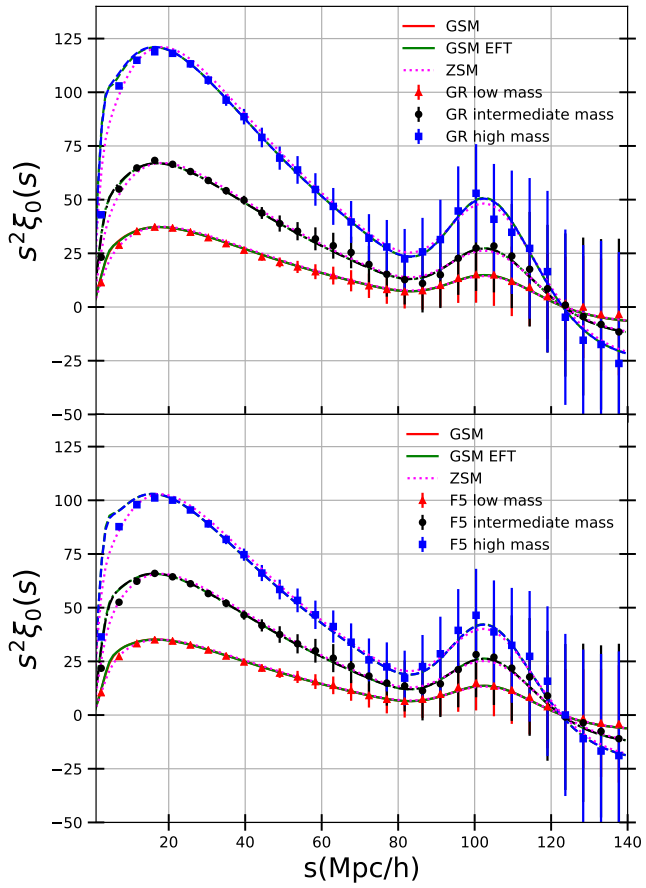

Figure 5.6: The monopole of the redshift-space two-point correlation function for GR [top] and for the F5 model [bottom], as obtained in the low mass [red triangles], the intermediate mass [black circles] and the high mass [blue squares] halo bins identified in the Group II simulations at $z = 1$. Furthermore, for each model and mass bin we plot the theoretical predictions given by the Gaussian Streaming Model (GSM) up to 1-loop order with the shifted Zel'dovich dispersion [solid red (low mass), black dot-dash (intermediate mass) and blue dash (high mass) lines], by the Zel'dovich Streaming Model (ZSM) [magenta dotted lines] and by the GSM with the 1-loop velocity dispersion shifted by the EFT counter-term (5.50) [green solid, dot-dash and dash lines].

between the results using the EFT shift and the Zel'dovich approximation are rather small, and for larger scales well within the $1-\sigma$ error bars, demonstrating consistency between the monopole predictions from the different approaches.

The same level of consistency is observed when comparing against the $z = 1$ snapshot of the Group II simulations, as apparent in Fig. 5.6, this time across all 3 mass halo bins identified in the sample. The GSM result with the shifted Zel'dovich dispersion remains consistent with the simulated monopole for a wide range of scales, including both the BAO region and also the power-law regime, down to $r \sim 20$ Mpc/h. Adding the EFT shift to the 1-loop velocity dispersion causes an almost indistinguishable change to the theoretical prediction, but the Zel'dovich approximation performs considerably better at scales $r < 20$ Mpc/h. The latter has also been observed when studying the real-space counterpart in [191].

Moving on to the redshift-space quadrupole and starting with the Group I simulations, as shown in Fig. 5.7, we determine that the GSM achieves a significant improvement compared to the Direct Lagrangian approach of the previous section, with the theoretical prediction remaining consistent with the N-body simulations, down to scales of at least $r \sim 17$ Mpc/h, for all cases. Adding the EFT shift to the velocity dispersion further improves the accuracy at small scales, with the difference being practically indistinguishable at scales $r > 40$ Mpc/h. The ZSM result, however, performs much more poorly in this case, for all models, demonstrating the need to include the 1-loop corrections for an accurate prediction of the quadrupole.

As in the monopole case, the same level of consistency is observed when comparing against the Group II simulations, which is done in Fig. 5.8, where we

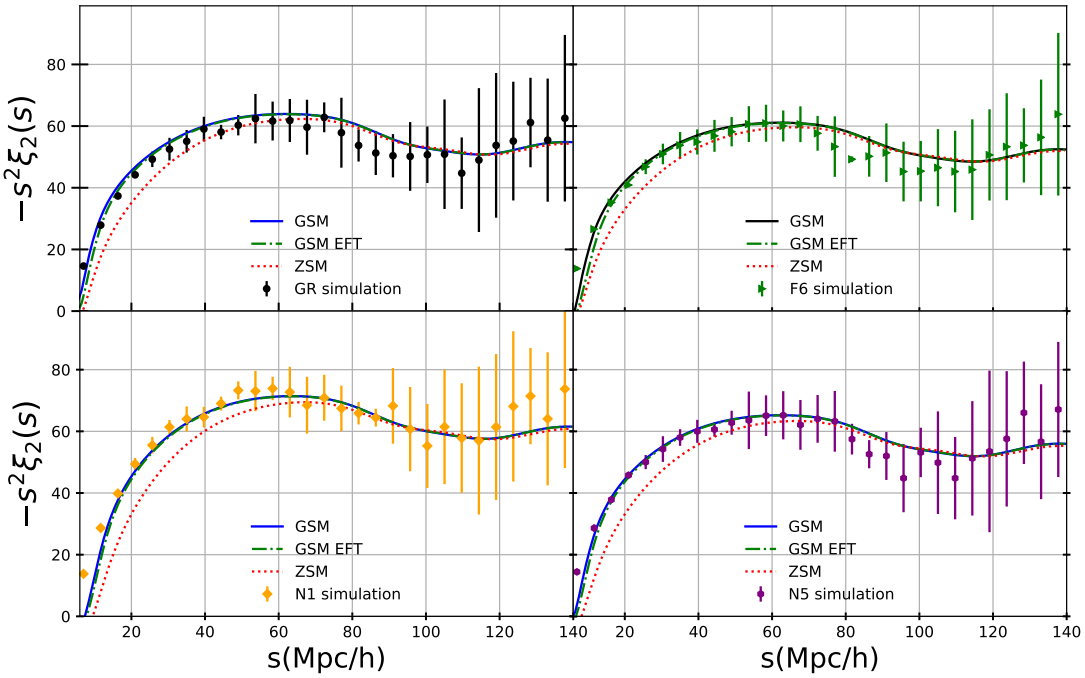

Figure 5.7: The quadrupole of the redshift-space two-point correlation function for GR [black circles] in the top left panel, for the F6 model [green right triangles] in the top right panel, for the N1 model [orange diamonds] in bottom left panel and for N5 model [purple hexagons] in the bottom right panel, as obtained from the Group I simulations at $z = 0.5$. Furthermore, for each model we plot the theoretical predictions given by the Gaussian Streaming Model (GSM) up to 1-loop order [black solid lines], by the Zel'dovich Streaming Model (ZSM) [magenta dotted lines] and by the GSM with the 1-loop velocity dispersion shifted by the EFT counter-term (5.50) [green dot-dash line].

see that the 1-loop GSM result with the shifted Zel'dovich dispersion accurately captures the simulated quadrupole, for all mass bins and both in GR and the F5 MG model. Even for the high mass bin, that contains much less halos, and is inevitably noisier, the trend of the simulation data points is clearly traced by our GSM prediction. The GSM prediction obtained using the EFT shift to the velocity dispersion seems to perform noticeably worse, in this snapshot, for

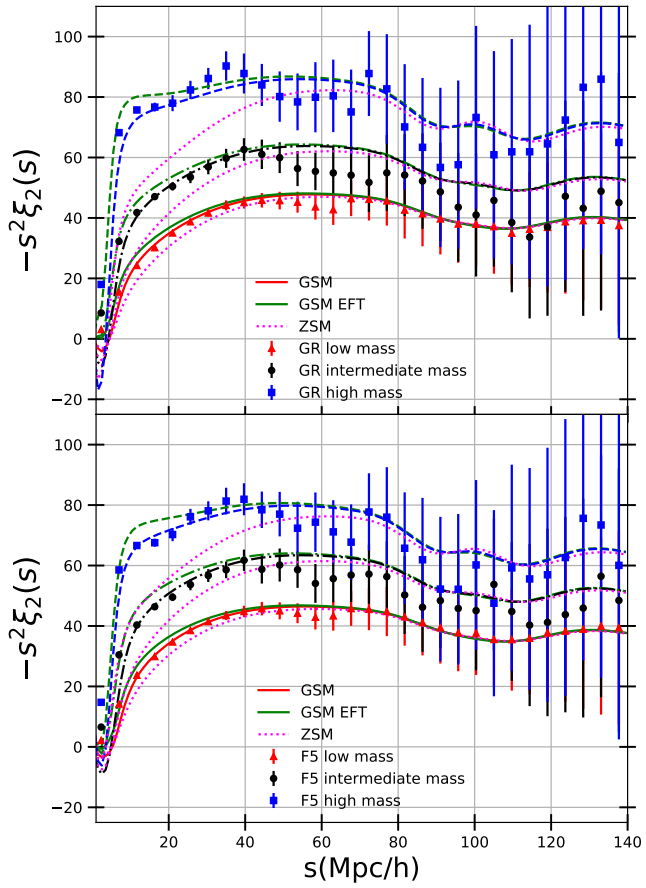

Figure 5.8: The quadrupole of the redshift-space two-point correlation function for GR [top] and for the F5 model [bottom], as obtained in the low mass [red triangles], the intermediate mass [black circles] and the high mass [blue squares] bins identified in the Group II simulations at $z = 1$. Furthermore, for each model and mass bin we plot the theoretical predictions given by the Gaussian Streaming Model (GSM) up to 1-loop order with the shifted Zel'dovich dispersion [solid red (low mass), black dot-dash (intermediate mass) and blue dash (high mass) lines], by the Zel'dovich Streaming Model (ZSM) [magenta dotted lines] and by the GSM with the 1-loop velocity dispersion shifted by the EFT counter-term (5.50) [green solid, dot-dash and dash lines].

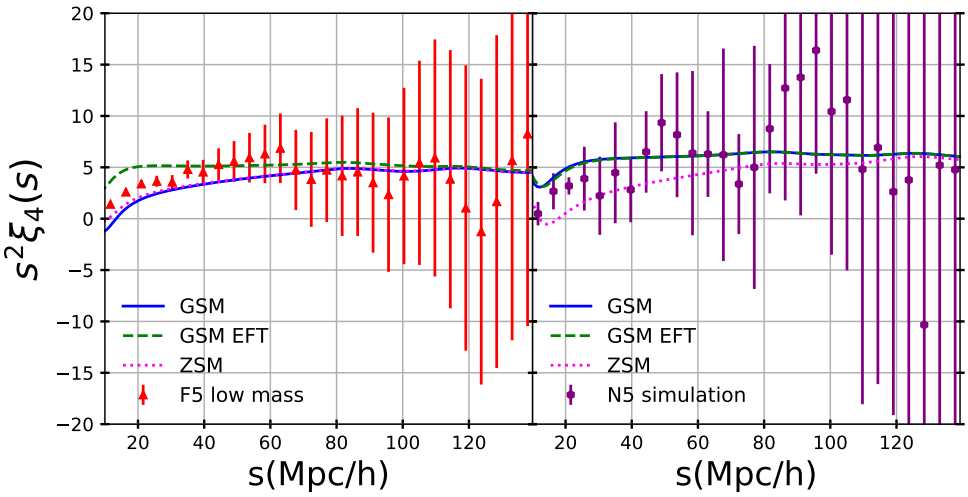

Figure 5.9: The hexadecapole of the redshift-space two-point correlation function as obtained in the F5 low mass bin identified in the Group II simulations [left], as well as in the N5 model of the Group I snapshot [right]. Furthermore, for each case we plot the theoretical predictions given by the Gaussian Streaming Model (GSM) up to 1-loop order [solid blue line], by the Zel'dovich Streaming Model (ZSM) [magenta dotted lines] and by the GSM with the 1-loop velocity dispersion shifted by the EFT counter-term (5.50) [green dashed].

all mass bins. Just like in the Group I case of Fig. 5.7, the ZSM seems to be inadequate at accurately capturing the quadrupole at quasi-linear scales.

Finally, we compare our analytical predictions with respect to the hexadecapole of the anisotropic correlation function for two cases: the F5 low mass bin in the Group II simulations, as well as the N5 model in the Group I snapshot, both of which are shown in Fig. 5.9. While the noise increases significantly between the quadrupole and the hexadecapole, so we should take these results only as indicative, we find that the GSM prediction traces the simulated hexadecapole well down to scales of at least $r \sim 17$ Mpc/h, but with an offset of a few percent. This offset is for theoretical predictions with bias values obtained with the PBS formalism; an alternative might be to allow biases to vary and fit

to the data.

These results overall demonstrate that the GSM can serve as an invaluable tool to model the anisotropic correlation function of halos in MG models, extending the success of this approach beyond the previously explored domain of GR cosmologies. It is worth emphasizing, also, that since the Lagrangian bias factors are calculated through our analytical model, the only free parameter needed to get accurate quadrupole predictions has been the constant offset added to the components of the pairwise velocity dispersion of halos, a value that can be easily determined through a single large-scale measurement of σ^2 (either from N-body simulations or observations).

5.5 Conclusions

In this work, we expanded the Gaussian Streaming Model to predict the redshift-space anisotropic correlation function for biased tracers in Modified Gravity models. This is the first time, to our knowledge, that the effects of both redshift-space distortions and halo bias have been jointly studied analytically for scenarios that go beyond GR.

We build upon our previous work on the study of biased tracers in MG using LPT [17, 191], and employ the Convolution LPT resummation scheme, with a local Lagrangian bias, to analytically describe the necessary missing ingredients that enter the GSM for such models: the real-space halo pairwise velocity and its scale-dependent dispersion. The approach includes analytic determination of the bias parameters using the PBS formalism with fitted Sheth-Tormen parameters. Through cross-checking our analytical predictions across a large suite

of state-of-the-art N-body simulations for the f(R) Hu-Sawicki and the nDGP MG models, we find that the 1-loop CLPT prediction for the real-space halo pairwise velocity remains consistent with the simulated data for the scales of interest, a fact that is crucial for the accuracy of the GSM prediction.

When performing the same comparison with respect to the halo pairwise velocity dispersion, however, we find that the CLPT approach is able to match the simulated curve only if an offset is added to the theoretical dispersion result. In doing this, we have followed two different strategies; namely, we added a phenomenological constant shift to it, as proposed in [145], and included a leading order EFT effect that contributes as a scale dependent shift, tending to a constant large scales [193]. We have seen that although theoretically well-motivated, the EFT prescription does not necessarily work better than the constant shift, which is evident in the quadrupole of the Group II of simulations (Fig. 5.8). The pairwise dispersion is nonlinear in nature, as has been settled down since the seminal work of Scoccimarro [160], such that it would be not surprising that higher order contributions were important, which also could be the reason of why their parallel and perpendicular to the line of sight components require slightly different offsets to match simulations, as it is done in [145, 198].

In establishing that the CLPT approach can accurately predict the ingredients that enter the GSM expression, we proceed to evaluate the performance of the model against the N-body simulations, with respect to the redshift-space monopole, the quadrupole and the hexadecapole of the anisotropic correlation function of halos. Unlike direct Lagrangian approaches, which prove to be significantly inaccurate, we find that the 1-loop GSM approach can successfully capture the redshift-space quadrupole for all MG models, remaining consistent

with the corresponding results from the simulations down to scales of at least $r \sim 17$ Mpc/h and including the BAO peak. In the hexadecapole case, the GSM prediction traces the shape of simulated result down to equally small scales, but with a few percent offset.

Our analysis overall shows that our theoretical analytical predictions using the GSM implementation achieve strong agreement with the non-linear simulated data for a variety of MG models, across different levels of screening and different screening mechanisms, and across a wide range of halo masses. We emphasize the fact that this agreement occurs across all scales down into the mildly non-linear regime, through simply matching a single shift parameter in the halo pairwise velocity dispersion, that can be determined through comparing the theory with a large-scale (linear regime) observed measurement. The predictions come with bias parameters determined by the PBS formalism but an alternative is to consider the bias factors as free parameters, that could be fit with the simulations. The approach is one that has great potential for making accurate clustering predictions for upcoming spectroscopic large scale structure surveys.

In this work, we have followed the commonly used approach in GSM-PT that fits a constant or EFT shift to the pairwise velocity dispersion obtained from the simulations. On the other hand, in applications of the GSM to surveys, a constant shift is added directly into eq. (5.36) by means of a substitution $\sigma^2_{12}(r) \longrightarrow \sigma^2_{12}(r) + \sigma^2_{\rm FoG}$, and with $\sigma^2_{\rm FoG}$ considered a free parameter to be fitted with observations; see e.g., [144, 82]. In order to utilize the GSM approach for parameter inferences on real data, these works treated the offset as a nuisance parameter with a broad prior of $0 - 40$ applied. We also find, in agreement with

these results in the context in GR, that adding large offsets is an inherent part of ensuring a good fit with the data. Understanding the connection between the offset and the underlying nonlinear clustering in MG, as well as the impact of marginalizing over offsets in parameter estimation are areas of definite interest in future work.

The framework developed is flexible and could be easily applied to any scalar-tensor theory of interest. Future lines of improvement include exploring how more general bias schemes, like for example including tidal bias terms, in conjunction with corrections from EFT [193] can serve to further improve the accuracy of the analytical model. It would be also very interesting to see how including higher-order cumulants to the GSM expansion, as in [186], could yield additional predictive power. Last but not least, our perturbative treatment can be used to disentangle modifications to gravity with estimators beyond the standard 2-point statistics, such as the marked correlation function [204, 190, 74, 11, 154] and higher order statistics. We plan to address these natural extensions in future work.

In this era of precision cosmology, the next-stage cosmological surveys, such as DESI, EUCLID and the LSST, will thoroughly explore the LSS of the universe providing an opportunity to shed light on the dark sector. This highlights the need to compliment such observational endeavors with efficient analytical approaches to characterize the distinctive signatures of theoretical models of the dark sector that the observations can constrain. In this work we have shown that the GSM, previously only explored for GR-based cosmologies, can also serve as a valuable predictive tool to probe cosmic modifications to gravity in redshift-space as well as real-space, to explore modified gravity cosmologies with biased

tracers observed through spectroscopic and photometric surveys.

5.6 Acknowledgments

We wish to thank Baojiu Li for kindly providing the ELEPHANT simulations, on behalf of [50] and for numerous discussions on available simulations. We would also like to thank Wojciech Hellwing for kindly making available the *n*DGP simulations, on behalf of [73], as well as Christian Arnold, together with the other authors of [13], for kindly providing their Lightcone simulations. We are also grateful to Martin White for providing valuable insights on perturbation theory and available simulations and also to Uros Seljak, Emanuele Castorina and Steven Chen for useful discussions. Last but not least, we want to thank David Alonso for useful discussions on calculating correlation functions with CUTE.

CHAPTER 6

CONCLUSIONS

It is hard to overstate how profound the impact of the discovery of cosmic acceleration has been on the foundations of modern cosmology and physics. One of the theoretical avenues explored in order to provide a viable cosmic self-accelerative mechanism, has been the idea that Einstein's General Relativity, one of the cornerstones of modern theoretical physics, might actually break down at cosmic scales. Such Modified Gravity theories that are being considered as explanations for cosmic acceleration, make tantalizing predictions in the non-linear regime of the LSS, which will be detectable in the era of precision cosmology, but also present great computational challenges in theoretically modeling and actually detecting them. In the present thesis we discussed how we can employ a combination of analytical, semi-analytical and simulation-based techniques, so that our theoretical predictions can successfully confront the upcoming cosmological observations.

In order to speed up N-body simulations for MG theories, we implemented an adaptation of the COLA approach, a hybrid scheme that combines Lagrangian perturbation theory with an N-body approach, to model non-linear collapse in the chameleon and symmetron classes of screening. The screening effects were modeled effectively, through the attachment of a suppression factor to the linearized Klein-Gordon equations. The adapted COLA approach was then benchmarked, with respect to an N-body code both for the ΛCDM scenario and for the modified gravity theories. It was found to perform well in the estimation of the dark matter power spectra, with consistency of 1% to $k \sim 2.5$ h/Mpc. Redshift space distortions were also shown to be effectively modeled

through a Lorentzian parameterization with a velocity dispersion fit to the data. These results demonstrated that COLA, proposed to enable accurate and efficient, non-linear predictions for ΛCDM, can be effectively applied to a wider set of cosmological scenarios, with intriguing properties, for which clustering behavior needs to be understood for upcoming surveys such as LSST, DESI, Euclid and WFIRST.

The screening mechanism is a fundamental property that MG models exhibit, which is necessary for them to evade stringent Solar System constraints to gravity and remain viable. This strong suppression of the deviations, however, can make a potential detection extremely challenging, even for the future ambitious surveys of the LSS. Down-weighting the high density, screened regions in favor of the low density, unscreened ones offers the potential to expose such modifications with much greater success. To that end, we assessed the performance of a new "marked" transformation with this suppression property and performed a systematic comparison with the previously known clipping and logarithmic density transformations, in the context of ΛCDM and the symmetron and $f(R)$ modified gravity models. Performance was measured in terms of the fractional boost in the Fisher information and the signal-to-noise ratio (SNR) for these models relative to the statistics derived from the standard density distribution. We found that all three statistics provided improved Fisher boosts over the basic density statistics. Our results demonstrate how a series of simple analytical transformations could dramatically increase the predicted information extracted on deviations from GR from large-scale surveys, and make the prospect for a potential detection much more feasible.

Understanding the relationship between the distribution of halos and the

underlying cosmic dark matter density field, known as large-scale halo bias, not just in ΛCDM but also in MG theories, is a necessary step in order to successfully interpret cosmological signals. To that end, we produced analytic predictions for real and Fourier space two-point statistics for biased tracers in MG, using the framework of Lagrangian Perturbation Theory, which we then compared against those from state of the art N-body simulations in the $f(R)$ Hu-Sawicki and the nDGP braneworld theories of modified gravity. We found that the novel physics of gravitational collapse in scalar-tensor theories with the chameleon or the Vainshtein screening mechanism could be effectively factored in with bias parameters analytically predicted using the Peak-Background Split formalism, when updated to include the environmental sensitivity of modified gravity theories, as well as changes to the halo mass function. These findings demonstrated that the Convolution Lagrangian Perturbation Theory (CLPT) and Standard Perturbation Theory (SPT) approaches can provide accurate analytic methods to predict the correlation function and power spectra, respectively, for biased tracers in modified gravity models and are able to characterize both the BAO, power-law and small scale regimes needed for upcoming galaxy surveys.

Finally, we extended the scale-dependent Gaussian Streaming Model (GSM) to produce analytical predictions for the anisotropic redshift-space correlation function for biased tracers in modified gravity models. This was achieved through employing the Convolution Lagrangian Perturbation Theory (CLPT) re-summation scheme, with a local Lagrangian bias schema provided by the peak-background split formalism, so as to predict the necessary ingredients that enter the GSM, the real-space halo pairwise velocity and the pairwise velocity dispersion. We further considered effective field theory contributions to the pairwise velocity dispersion in order to model correctly its large scale behav-

ior. Our method was applied on two widely-considered modified gravity models, the chameleon-screened $f(R)$ Hu-Sawicki model and the nDGP Vainshtein model, predictions that we compared against state-of-the-art N-body simulations for the same models. This analysis demonstrated that the GSM approach can comfortably predict the monopole and the quadrupole of the redshift-space correlation function for halos, achieving a very good level of agreement with the simulation data, for a wide range of screening mechanisms, levels of screening and halo masses at $z = 0.5$ and $z = 1$. Consequently, this work highlighted the applicability of the GSM for cosmologies beyond GR, demonstrating that it can serve as a powerful predictive tool for the next stage of cosmological surveys.

The work laid out in this thesis aims to serve as the stepping stone upon which multiple exciting future lines of work can emerge. Already shown to be able to achieve results at the % level of accuracy, requiring only a tiny fraction of the standard computational cost, the COLA method is ideal to use in cases where we need to perform hundreds or thousands of simulations, in order to adequately explore the parameter space of any given viable MG model. In work that is currently underway within the Dark Energy Science Collaboration, the COLA approach is being utilized to provide the training data set for a Gaussian process emulator for summary statistics in the case of the f(R) modified gravity. Going beyond the current method, COLA's capabilities can be easily expanded in order to incorporate predictions for other observables in MG, such as weak lensing, the effects from other fundamental quantities, such as the sum of neutrino masses and finally, statistics in other classes of MG models. The fundamental principles of the COLA method will be expanded, in a research theme that has recently begun, in order to produce predictions for the most general class of scalar-tensor MG theories with second order equations of

motion, which is, as we have already seen, the Horndeski class. Furthermore, the techniques developed in the MG implementation of COLA can be used to incorporate MG predictions into the mass-Peak Patch algorithm, an efficient LPT-based method for generating realistic halo mocks.

The marked statistics we considered in this work, are simple density transformations that were shown to significantly boost the signals of MG that could be lurking in the cosmic web. However, the analysis was performed in the simplified setting of pure dark matter considerations. The next step would be to quantitatively assess the performance of such transformations in the context of realistic galaxy mocks, for a variety of MG scenarios; such an attempt has already been underway within the DESI collaboration. More importantly, as Stage-IV cosmology surveys are starting to see their first light (as DESI already has done), it will be crucial and exciting to apply the statistics we developed on these datasets. Furthermore, it would be very interesting to explore whether such statistics can enhance our ability to constrain other cosmological properties that also manifest themselves in the cosmic voids, such as the sum of the neutrino masses, the dark matter equation of state or the nature of inflation.

The perturbation theory approaches explored in this thesis, represent a quick, one-time-step approach to capture the 2-point statistics of biased tracers in MG, both in the real and the redshift space of galaxy clustering. Multiple lines of improvement can be applied in order to further enhance the accuracy of these predictions and also push them down to even smaller scales. These include, but are not necessarily restricted to, improving the accuracy of the bias modeling, adding contributions from higher orders in perturbation theory and also capturing small scale effects, which are impossible to model

from first principles, through effective field theory corrections. Furthermore, the accuracy in the prediction of the statistics in redshift-space, can be further improved by considering including higher order cumulants in the Gaussian streaming model re-summation scheme. Our work was so far focused on obtaining predictions for the 2-point statistics in the configuration space only, but an effort to obtain similar predictions for the MG halo power spectrum, by modeling the various velocity moments in the Fourier space, has recently begun. Such perturbative approaches are uniquely suitable to model the covariance matrix of the 2-point galaxy correlation function, an accurate prediction of which would actually require thousands of available simulations for a given model. Indeed, the LPT framework we developed is being currently employed to forecast constraints placed on gravity theories, when spectroscopic galaxy samples will be combined with clustering abundances identified from the thermal-Sunyaez Zeldovich effect in the CMB. Last but not least, there is a wealth of other observables that can be analytically modeled using LPT for MG, such as higher-order clustering statistics, the Lyman-α forest, multiple tracers and the Sunyaev-Zeldovich effect.

In the coming decade, the next-stage cosmological surveys, such as DESI, EUCLID, the LSST and WFIRST, will thoroughly explore the LSS of the universe, providing a unique opportunity to shed light on the true nature of the dark sector. This fact highlights the need to complement such observational endeavors with a wide range of analytical, semi-analytical and simulation-based approaches to characterize the distinctive signatures of theoretical models of the dark sector that the observations can constrain. The work performed as part of this thesis serves to complete a crucial step towards this goal.

APPENDIX A

LAGRANGIAN PERTURBATION THEORY IN MODIFIED GRAVITY

LPT [38] works perturbatively in a displacement field $\mathbf{s}(\mathbf{q}, a)$

$$\mathbf{x} = \mathbf{q} + \mathbf{s}_1(\mathbf{q}, a) + \mathbf{s}_2(\mathbf{q}, a) + ..., \tag{A.1}$$

where $\mathbf{q}$ and $\mathbf{x}$ are the initial and final comoving Eulerian particle positions. In this formulation, all the information is reflected in the mapping through the displacement field. Working up to first order gives the so-called Zel'dovich approximation in ΛCDM, for which the $\mathbf{s}(\mathbf{q}, a)$ can be decomposed into a product of temporal and spatial factors

$$\nabla_{\mathbf{q}}\mathbf{s}_1(\mathbf{q}, a) = D_1(a)\nabla_{\mathbf{q}}\mathbf{s}_1(\mathbf{q}, a_0) \tag{A.2}$$

and

$$\nabla_{\mathbf{q}}\mathbf{s}(\mathbf{q}, a_0) = -\delta(\mathbf{q}, a_0) \tag{A.3}$$

with $\delta(\mathbf{q}, a_0)$ being the Gaussian density field generated by an initial linear power spectrum and $D_1(a)$ the scale independent first order growth factor, given by

$$\ddot{D}_1 + 2H\dot{D}_1 = \frac{3}{2}\Omega_m(a)H^2 D_1 \tag{A.4}$$

In an MG scenario, the growth factor is not scale independent any more and

$$\nabla_{\mathbf{q}}\mathbf{s}_1 = D_1(\mathbf{q}, a)\nabla_{\mathbf{q}}\mathbf{s}_1(\mathbf{q}, a_0) \tag{A.5}$$

where

$$\ddot{D}_1(\mathbf{k}, a) + 2H\dot{D}_1(\mathbf{k}, a) = \frac{3}{2}\Omega_m(a)H^2 D_1(\mathbf{k}, a)\frac{G_{eff}}{G} \tag{A.6}$$

in Fourier space. This implies that particle trajectories, unlike in ΛCDM, are not straight lines [188]. (A.3) and (A.5) indeed give

$$\mathbf{s}_1 = -D_1(\mathbf{q}, a)\frac{\nabla_{\mathbf{q}}}{\nabla^2_{\mathbf{q}}}\delta(\mathbf{q}, a_0) - \delta(\mathbf{q}, a_0)\frac{\nabla_{\mathbf{q}}}{\nabla^2_{\mathbf{q}}}D_1(\mathbf{q}, a) \tag{A.7}$$

The second term, responsible for the trajectory bending, vanishes when the growing mode is scale independent, in which case one recovers the standard ΛCDM Zel'dovich approximation. When working up to second order (2LPT), we have in a similar fashion

$$\nabla_{\mathbf{q}}\mathbf{s}_2(\mathbf{q},a) = D_2(a)\nabla_{\mathbf{q}}\mathbf{s}_2(\mathbf{q},a_0), \tag{A.8}$$

where the second order growth factor is given by

$$\ddot{D}_2(a) + 2H\dot{D}_2(a) = \frac{3}{2}\Omega_m(a)H^2 D_2(a)\left(1 - D_1^2(a)\right) \tag{A.9}$$

For the early times, the spatial part is given by

$$\nabla_{\mathbf{q}}\mathbf{s}_2(\mathbf{q},a_0) = \frac{1}{2}\sum_{i\neq j}\left(\mathbf{s}_{1i,i}\mathbf{s}_{1j,j} - \mathbf{s}_{1i,j}\mathbf{s}_{1j,i}\right). \tag{A.10}$$

In the MG case, we will have again

$$\nabla_{\mathbf{q}}\mathbf{s}_2(\mathbf{q},a) = D_2(\mathbf{q},a)\nabla_{\mathbf{q}}\mathbf{s}_2(\mathbf{q},a_0), \tag{A.11}$$

with the scale dependent second order growth factor that obeys

$$\begin{aligned}\ddot{D}_2(\mathbf{k},a) + 2H\dot{D}_2(\mathbf{k},a) = \frac{3}{2}\Omega_m(a)H^2 D_2(\mathbf{k},a)\times \\ (1 - D_1^2(\mathbf{k},a))\frac{G_{eff}}{G},\end{aligned} \tag{A.12}$$

in the Fourier space. The fact that all of our models recover GR at early times, guarantees that the early time spatial part is still given by (A.10). In our implementation of the full MG COLA scheme, a suitably modified version of 2LPTic produces the LPT terms at every time step, through the Fourier space versions of (A.5) and (A.11)

$$\begin{aligned}\mathbf{s}_1(\mathbf{k},a) &= \frac{i\mathbf{k}}{k^2}D_1(\mathbf{k},a)\delta(\mathbf{k},a_0) \\ \mathbf{s}_2(\mathbf{k},a) &= -\frac{i\mathbf{k}}{k^2}D_2(\mathbf{k},a)\frac{1}{2}\sum_{i\neq j}\left(\mathbf{s}_{1i,i}\mathbf{s}_{1j,j} - \mathbf{s}_{1i,j}\mathbf{s}_{1j,i}\right),\end{aligned} \tag{A.13}$$

and also the same for the accelerations

$$
\begin{aligned}
T^2[\mathbf{s}_1(\mathbf{k},a)] &= \frac{i\mathbf{k}}{k^2}T^2[D_1(\mathbf{k},a)]\delta(\mathbf{k},a_0) \\
T^2[\mathbf{s}_2(\mathbf{k},a)] &= -\frac{i\mathbf{k}}{k^2}T^2[D_2(\mathbf{k},a)]\frac{1}{2}\sum_{i\neq j}\left(\mathbf{s}_{1i,i}\mathbf{s}_{1\,j,j} - \mathbf{s}_{1i,j}\mathbf{s}_{1\,j,i}\right).
\end{aligned}
\tag{A.14}
$$

APPENDIX B

ONE LOOP CORRECTIONS FOR BIASED STATISTICS IN MG

In section 4.3.1 of the main text, it was stated that the two point statistics for biased tracers, up to one loop in CLPT, are given by equations (5.24) and (4.40), in the configuration space and the Fourier space, respectively. The expressions are convolutional integrals over a sum of individual terms that depend on the Lagrangian correlators (4.58), which are essentially the fundamental blocks of CLPT. These expressions (4.58), however, are functions of the Lagrangian coordinates $\mathbf{q}$, while the LPT solutions for the displacement fields up to various orders are found in the Fourier space (through the growth factors (4.22), (4.25) and (B.5)). As was also stated in 4.3.1, substituting the LPT solutions (4.56) into (4.58) gives the integral expressions for the MG Lagrangian correlators (4.59), that depend on the functions (4.61), which are also the building blocks of the SPT and LRT power spectra (4.64) and (4.65). We start with the innermost layer of integration, deriving the expressions for the k-dependent functions (4.61) in section B.1, before showing how to get to the correlators (4.59) in section B.2. Finally, in section B.3, we show how the SPT and LRT expressions for the two-point statistics are derived. The notation and index structure is the one adopted in [120, 119, 46]. These results are consistent with those recently presented in

[17].

B.1 Polyspectra and k-functions in MG

In LPT, we solve for the displacement field $\mathbf{\Psi}(\mathbf{q})$ across various orders in perturbation theory, as

$$\mathbf{\Psi}(\mathbf{q},t) = \sum_{n=1}^{\infty} \mathbf{\Psi}^{(n)}(\mathbf{q},t) = \mathbf{\Psi}^{(1)}(\mathbf{q},t) + \mathbf{\Psi}^{(2)}(\mathbf{q},t) + \mathbf{\Psi}^{(3)}(\mathbf{q},t)... \tag{B.1}$$

In the Fourier space representation, $\tilde{\mathbf{\Psi}}(\mathbf{p})$, the solutions are expanded as

$$\begin{aligned}\tilde{\Psi}_j^{(n)}(\mathbf{p}) = \frac{i}{n!}\int \frac{d^3p_1}{(2\pi)^3}..\frac{d^3p_n}{(2\pi)^3}\delta_D^3\left(\sum_{j=1}^{n} p_j - p\right) \\ \times L_j^{(n)}(\mathbf{p}_1,..,\mathbf{p}_n)\tilde{\delta}_L(\mathbf{p}_1)..\tilde{\delta}_L(\mathbf{p}_n),\end{aligned} \tag{B.2}$$

where $\tilde{\delta}_L(\mathbf{p}_n)$ are the linear density fields in the Fourier space at the time of evaluation. For gravitational evolution governed by GR, the growth factors are only functions of time, and under the additional assumption of an Einstein-De Sitter evolution, the Kernels $L_j^{(n)}(\mathbf{p}_1,..,\mathbf{p}_n)$ admit simple scale-independent expressions and (B.2) can be simply evolved in time by powers of the linear growth factor [120]. This assumption gives results accurate at the sub-percent level for ΛCDM cosmologies [38].

In MG, however, the simple description presented above does not hold, in principle, because the growth factors depend on both space and time, as we saw in Section 4.2.2. Following [15], we define

$$\begin{aligned}L_j^{(1)}(\mathbf{p}) &= \frac{p^j}{p^2} \\ L_j^{(2)}(\mathbf{p}_1,\mathbf{p}_2) &= \frac{p^j}{p^2}\frac{D^{(2)}(\mathbf{p_1},\mathbf{p_2})}{D^{(1)}(\mathbf{p_1})D^{(1)}(\mathbf{p_2})} \\ (L_j^{(3)})_{sym}(\mathbf{p}_1,\mathbf{p}_2,\mathbf{p}_3) &= i\frac{p^j}{p^2}\frac{D^{(3)}_{sym}(\mathbf{p_1},\mathbf{p_2},\mathbf{p}_3)}{D^{(1)}(\mathbf{p_1})D^{(1)}(\mathbf{p_2})D^{(1)}(\mathbf{p_3})},\end{aligned} \tag{B.3}$$

where the MG growth factors are calculated through the prescription described in Section 4.2.2 and their time arguments have been dropped for notational simplicity. Furthermore, the subscript in the third order Kernel is meant to emphasize on the fact that the configuration that enters the 2-point statistics should be symmetrized [120, 15]. The symmetrized third order growth factor that enters the two-point statistics is given by [15]:

$$D^{(3)}_{sym}(\mathbf{k},-\mathbf{p},\mathbf{p}) = D^{(3)}(\mathbf{k},-\mathbf{p},\mathbf{p}) + D^{(3)}(\mathbf{k},\mathbf{p},-\mathbf{p}), \tag{B.4}$$

with $D^{(3)}(\mathbf{k},-\mathbf{p},\mathbf{p})$ given by:

$$\begin{aligned}
&\left(\hat{\mathcal{T}} - A(k)\right) D^{(3)}(\mathbf{k},-\mathbf{p},\mathbf{p}) = D^{(1)}(p)\left(A(p) + \hat{\mathcal{T}} - A(k)\right) D^{(2)}(\mathbf{p},\mathbf{k})\times \\
&\left[1 - \frac{\left(\mathbf{p}\cdot(\mathbf{k}+\mathbf{p})\right)^2}{p^2|\mathbf{p}+\mathbf{k}|^2}\right] - D^{(1)}(p)\left(A(p) + A(|\mathbf{p}+\mathbf{k}|) - 2A(k)\right) D^{(2)}(\mathbf{p},\mathbf{k}) \\
&+ \left(2A(k) - A(|\mathbf{p}+\mathbf{k}|) - A(p)\right) D^{(1)}(k)\left(D^{(1)}(p)\right)^2 \frac{(\mathbf{k}\cdot\mathbf{p})^2}{k^2p^2} \\
&- \left(A(|\mathbf{p}+\mathbf{k}|) - A(k)\right) D^{(1)}(k)\left(D^{(1)}(p)\right)^2 - D^{(1)}(k)\left(D^{(1)}(p)\right)^2 \times \Bigg[\\
&\frac{M_1(\mathbf{p}+\mathbf{k})}{3\Pi(|\mathbf{p}+\mathbf{k}|)} K^{(2)}_{FL}(\mathbf{p},\mathbf{k}) - \left(\frac{2A(0)}{3}\right)^2 \frac{M_2(\mathbf{p},\mathbf{k})|\mathbf{p}+\mathbf{k}|^2}{6a^2\Pi(|\mathbf{p}+\mathbf{k}|)\Pi(k)\Pi(p)}\Bigg] + \\
&\frac{M_1(k)}{3\Pi(k)}\Bigg[\left(2\frac{\left(\mathbf{p}\cdot(\mathbf{k}+\mathbf{p})\right)^2}{p^2|\mathbf{p}+\mathbf{k}|^2} - \frac{\mathbf{p}\cdot(\mathbf{k}+\mathbf{p})}{p^2}\right)\left(A(p) - A(0)\right) D^{(2)}(\mathbf{p},\mathbf{k}) D^{(1)}(p) \\
&+ \left(2\frac{\left(\mathbf{p}\cdot(\mathbf{k}+\mathbf{p})\right)^2}{p^2|\mathbf{p}+\mathbf{k}|^2} - \frac{\mathbf{p}\cdot(\mathbf{k}+\mathbf{p})}{|\mathbf{k}+\mathbf{p}|^2}\right)\left(A(|\mathbf{k}+\mathbf{p}|) - A(0)\right) D^{(2)}_{\phi}(\mathbf{p},\mathbf{k}) D^{(1)}(p) \\
&+ 3\frac{(\mathbf{k}\cdot\mathbf{p})^2}{k^2p^2}\left(A(p) + A(k) - 2A(0)\right) D^{(1)}(k)\left(D^{(1)}(p)\right)^2\Bigg] \\
&- \frac{1}{2}\frac{k^2}{6a^2\Pi(k)} K^{(3)}_{\delta I\, sym}(\mathbf{k},-\mathbf{p},\mathbf{p}) D^{(1)}(k)\left(D^{(1)}(p)\right)^2 .
\end{aligned} \tag{B.5}$$

In (B.5), we additionally defined

$$D^{(2)}_{\phi}(\mathbf{p},\mathbf{k}) = D^{(2)}(\mathbf{p},\mathbf{k}) + \left(1+\frac{(\mathbf{k}\cdot\mathbf{p})^2}{k^2p^2}\right)D^{(1)}(k)D^{(1)}(p) \\ -\frac{2A(0)}{3}\frac{M_2(\mathbf{p},\mathbf{k}) + 2\left(\frac{3}{2A(0)}\right)^2 K^{(2)}_{FL}(\mathbf{p},\mathbf{k})\Pi(k)\Pi(p)}{3\Pi(k)\Pi(p)}D^{(1)}(k)D^{(1)}(p) \tag{B.6}$$

and also used the kernels $K^{(2)}_{FL}$ and $K^{(3)}_{\delta\mathcal{I}sym}$, the forms of which were shown in [15]. The second and third order LPT kernels (B.3) need to be evaluated numerically, now, for each value of $\mathbf{p}_1, \mathbf{p}_2$ and z and so should (B.2), which is the main point of divergence between the MG implementation and the corresponding one in GR.

Now, following [119], we define the mixed polyspectra $C_{i_1...i_N}$, as

$$\langle\tilde{\delta}_L(\mathbf{k}_1)...\tilde{\delta}_L(\mathbf{k}_l)\tilde{\Psi}_{i_1}(\mathbf{p}_1)...\tilde{\Psi}_{i_N}(\mathbf{p}_N)\rangle_c = \\ = (2\pi)^3\delta^3_D(\mathbf{k}_1+..+\mathbf{k}_l+..\mathbf{p}_1+..+\mathbf{p}_N)(-i)^N C_{i_1...i_N}(\mathbf{p}_1,..,\mathbf{p}_N). \tag{B.7}$$

It is useful to decompose the various polyspectra into the various constituents, order by order in perturbation theory, as e.g.

$$C_{ij}(\vec{p}) = C^{(11)}_{ij}(\vec{p}) + C^{(22)}_{ij}(\vec{p}) + C^{(13)}_{ij}(\vec{p}) + C^{(31)}_{ij}(\vec{p}) + ... \\ C_{ijk}(\vec{p}_1,\vec{p}_2,\vec{p}_3) = C^{(112)}_{ijk}(\vec{p}_1,\vec{p}_2,\vec{p}_3)+ \\ C^{(121)}_{ijk}(\vec{p}_1,\vec{p}_2,\vec{p}_3) + C^{(211)}_{ijk}(\vec{p}_1,\vec{p}_2,\vec{p}_3) + ..., \tag{B.8}$$

where the additional notation has been adopted

$$\langle\tilde{\delta}_L(\mathbf{k}_1)...\tilde{\delta}_L(\mathbf{k}_l)\tilde{\Psi}^{(r)}_{i_1}(\mathbf{p}_1)...\tilde{\Psi}^{(s)}_{i_N}(\mathbf{p}_N)\rangle_c = \\ = (2\pi)^3\delta^3_D(\mathbf{k}_1+..+\mathbf{k}_l+..\mathbf{p}_1+..+\mathbf{p}_N)(-i)^N C^{(r...s)}_{i_1...i_N}(\mathbf{p}_1,..,\mathbf{p}_N) \tag{B.9}$$

and as previously, the bracketed numbers in the superscripts indicate the orders of contribution in each $\tilde{\Psi}_i(\mathbf{p})$. The various polyspectra can be expressed as functions of the Lagrangian kernels (B.3), by identifying the different contributions across each order in LPT, as in (B.8) and plugging the solutions (B.2) into

equation (B.9). The ones relevant for the two-point statistics of biased tracers are [119]:

$$
\begin{aligned}
&C_{ij}^{(11)}(\mathbf{p}) = L_i^{(1)}(\mathbf{p}) L_j^{(1)}(\mathbf{p}') P_L(p) \\
&C_{ij}^{(22)}(\mathbf{p}) = \frac{1}{2}\int \frac{d^3p'}{(2\pi)^3} L_i^{(2)}(\mathbf{p}', \mathbf{p}-\mathbf{p}') L_j^{(2)}(\mathbf{p}', \mathbf{p}-\mathbf{p}') \times \\
&\times P_L(p) P_L(|p-p'|) \\
&C_{ij}^{(13)}(\mathbf{p}) = C_{ji}^{(31)}(\mathbf{p}) = -\frac{1}{2} L_i^{(2)}(\mathbf{p}) P_L(p) \times \\
&\times \int \frac{d^3p'}{(2\pi)^3} (L_j^{(3)})_{sym}(\mathbf{p}, -\mathbf{p}', \mathbf{p}') P_L(p') \\
&C_i^{(2)}(\mathbf{p}_1, \mathbf{p}_2; \mathbf{p}_3) = -L_i^{(2)}(\mathbf{p}_1, \mathbf{p}_2) P_L(p_1) P_L(p_2) \\
&C_{ij}^{(2)}(\mathbf{p}_1; \mathbf{p}_2, \mathbf{p}_3) = C_{ji}^{(21)}(\mathbf{p}_1; \mathbf{p}_3, \mathbf{p}_2) = \\
&= -L_i^{(1)}(\mathbf{p}_2) L_j^{(2)}(\mathbf{p}_1, \mathbf{p}_2) P_L(p_1) P_L(p_2) \\
&C_{ijk}^{(112)}(\mathbf{p}_1, \mathbf{p}_2, \mathbf{p}_3) = C_{kij}^{(211)}(\mathbf{p}_3, \mathbf{p}_1, \mathbf{p}_2) = C_{jki}^{(121)}(\mathbf{p}_2, \mathbf{p}_3, \mathbf{p}_1) = \\
&= L_i^{(1)}(\mathbf{p}_1) L_j^{(1)}(\mathbf{p}_2) P_L(p_1) P_L(p_2),
\end{aligned}
\tag{B.10}
$$

where by $P_L(p)$ we denote the MG linear power spectrum.

The scalar functions $Q_n(k)$ and $R_n(k)$ that contribute to the SPT power spectrum (and as we shall see in the next section, to the Lagrangian correlators (4.58)), are expressed as functions of the polyspectra (B.9) in GR [119]. Fortunately, since in MG the above picture is only modified through the modified Kernels in (B.3), the relationships that give the various scalar functions are of the same form as the ones presented in [119] (in particular, equations (A50)-(A67) in Appendix A). However, one should be cautious at this point, because certain symmetries that are present in the GR solutions, are not preserved anymore. In particular, the integral in the l.h.s of eq. (A59) in [119] will not be equal to $R_1(k) + R_2(k)$ anymore, because of the scale and redshift dependence of the MG growth factors. In a similar manner, the functions resulting from eq. (A57) and (A61), that used to be equal to $R_1(k)$ and $Q_1(k)$, respectively, in GR, will dif-

fer for our MG models and should be additionally calculated. We denote these by $[R_1(k)+R_2(k)]_{MG}$, $[R_1(k)]_{MG}$ and $[Q_1(k)]_{MG}$ to emphasize on their GR limit. In order to illustrate how these calculations are performed, we show the derivations for $[R_1(k)+R_2(k)]_{MG}$ and $[Q_1(k)]_{MG}$, that are both new in MG and serve as a representative example of each category. For the former, we have:

$$\begin{aligned}
&[R_1(k)+R_2(k)]_{MG} = -\frac{7}{3}k_i k_j \int \frac{d^3p}{8\pi^3} C^{(21)}_{ji}(-\mathbf{p};\mathbf{p}-\mathbf{k},\mathbf{k}) = \\
&= \frac{7}{3}\int \frac{d^3p}{8\pi^3} k_i k_j L^{(1)}_j(\mathbf{k}) L^{(2)}_j(-\mathbf{p},\mathbf{k}) P_L(p) P_L(k) = \\
&= P_L(k)\frac{7}{3}\int \frac{drdx}{4\pi^2} k^2 k r^2 \frac{k^2-\mathbf{k}\cdot\mathbf{p}}{|k-p|^2} \frac{D^{(2)}(-\mathbf{p},\mathbf{k})}{D^{(1)}(p)D^{(1)}(p-k)} P_L(kr) = \\
&= \frac{k^3}{4\pi^2} P_L(k) \int_0^\infty dr P_L(kr) \int_{-1}^1 dx \frac{r^2(1-rx)}{1+r^2-2rx} \bar{D}^{(2)}(-\mathbf{p},\mathbf{k}),
\end{aligned} \tag{B.11}$$

where we defined the quantities $x = \hat{\mathbf{k}}\cdot\hat{\mathbf{p}}$, $p = kr$ and

$$\begin{aligned}
&\bar{D}^{(2)}(-\mathbf{p},\mathbf{k}) = \frac{7}{3}\frac{D^{(2)}(-\mathbf{p},\mathbf{k})}{D^{(1)}(p)D^{(1)}(k)} = \\
&= \frac{7}{3}\frac{D^{(2)}\left(k\sqrt{1+r^2-2rx},k,kr\right)}{D^{(1)}(kr)D^{(1)}(k)} = \\
&\bar{D}_a - \bar{D}_b x^2 + \bar{D}_{FL} - \bar{D}_{\delta I},
\end{aligned} \tag{B.12}$$

as was done in [15]. Similarly, for $[Q_1(k)]_{MG}$ we will have:

$$\begin{aligned}
&[Q_1(k)]_{MG} = \frac{7}{3}(k_i k_j k_l - k^2 k_i \delta_{jl}) \int \frac{d^3p}{8\pi^3} C^{(211)}_{ijl}(\mathbf{k},-\mathbf{p},\mathbf{p}-\mathbf{k}) = \\
&= \frac{7}{3}(k_i k_j k_l - k^2 k_i \delta_{jl})\times \\
&\int \frac{d^3p}{8\pi^3} L^{(1)}_l(\mathbf{p}) L^{(1)}_l(\mathbf{p}-\mathbf{k}) L^{(2)}_i(-\mathbf{p},\mathbf{p}-\mathbf{k}) P_L(p) P_L(|k-p|) = \\
&= \frac{k^3}{4\pi^2}\int drdx \frac{(\mathbf{k}\cdot\mathbf{p})(\mathbf{k}\cdot\mathbf{p}-k^2) - k^2\mathbf{p}(\mathbf{k}-\mathbf{p})}{p^2|k-p|^2}\times \\
&\bar{D}^{(2)}(\mathbf{p},\mathbf{k}-\mathbf{p}) P_L(kr) P_L(|k-p|) = \\
&\frac{k^3}{4\pi^2}\int_0^\infty dr P_L(kr) \int_{-1}^1 dx \frac{r^2(1-x^2)}{(1+r^2-2rx)} \bar{D}^{(2)}(\mathbf{p},\mathbf{k}-\mathbf{p}) P_L(|k-p|),
\end{aligned} \tag{B.13}$$

where $|k-p| = k\sqrt{1+r^2-2rx}$ is used and similarly as before, we defined

$$\begin{aligned}\bar{D}^{(2)}(\mathbf{p},\mathbf{k}-\mathbf{p}) &= \frac{7}{3}\frac{D^{(2)}(\mathbf{p},\mathbf{k}-\mathbf{p})}{D^{(1)}(p)D^{(1)}(|k-p|)} = \\ &= \frac{7}{3}\frac{D^{(2)}\left(k,kr,k\sqrt{1+r^2-2rx}\right)}{D^{(1)}(p)D^{(1)}(k\sqrt{1+r^2-2rx})} = \\ &\bar{D}_a - \bar{D}_b\frac{x^2+r^2-2rx}{1+r^2-2rx} + \bar{D}_{FL} - \bar{D}_{\delta I}.\end{aligned} \tag{B.14}$$

The above two Kernels, as well as all of the rest that we need, can be compactly written in the form [119]:

$$\begin{aligned}Q_n(k) = \frac{k^3}{4\pi^2}\int_0^\infty drP_L(kr) \\ \times\int_{-1}^1 dxP_L(k\sqrt{1+r^2-2rx})\tilde{Q}_n(r,x)\end{aligned} \tag{B.15}$$

and

$$R_n(k) = \frac{k^3}{4\pi^2}P_L(k)\int_0^\infty drP_L(kr)\int_{-1}^1 dx\tilde{R}_n(r,x). \tag{B.16}$$

Using similar methods as the one presented above we get that the various $Q_n(k)$,

and after some algebra, are given by:

$$
\begin{aligned}
\tilde{Q}_1 &= r^2\left(\bar{D}_a^{(2)} - \bar{D}_b^{(2)}\frac{x^2+r^2-2rx}{1+r^2-2rx} + \bar{D}_{FL}^{(2)} - \bar{D}_{\delta I}^{(2)}\right)^2 \\
\tilde{Q}_2 &= \frac{rx(1-rx)}{1+r^2-2rx}\left(\bar{D}_a^{(2)} - \bar{D}_b^{(2)}\frac{x^2+r^2-2rx}{1+r^2-2rx} + \bar{D}_{FL}^{(2)} - \bar{D}_{\delta I}^{(2)}\right) \\
\tilde{Q}_3 &= \frac{x^2(1-rx)^2}{(1+r^2-2rx)^2} \\
\tilde{Q}_5 &= rx\left(\bar{D}_a^{(2)} - \bar{D}_b^{(2)}\frac{x^2+r^2-2rx}{1+r^2-2rx} + \bar{D}_{FL}^{(2)} - \bar{D}_{\delta I}^{(2)}\right) \\
\tilde{Q}_7 &= \frac{x^2(1-rx)}{(1+r^2-2rx)} \\
\tilde{Q}_8 &= r^2\left(\bar{D}_a^{(2)} - \bar{D}_b^{(2)}\frac{x^2+r^2-2rx}{1+r^2-2rx} + \bar{D}_{FL}^{(2)} - \bar{D}_{\delta I}^{(2)}\right) \\
\tilde{Q}_9 &= \frac{rx(1-rx)}{1+r^2-2rx} \\
\tilde{Q}_{11} &= x^2 \\
\tilde{Q}_{12} &= rx \\
\tilde{Q}_{13} &= r^2 \\
\left[\tilde{Q}_1\right]_{MG} &= \frac{r^2(1-x^2)}{1+r^2-2rx}\left(\bar{D}_a^{(2)} - \bar{D}_b^{(2)}\frac{x^2+r^2-2rx}{1+r^2-2rx} + \bar{D}_{FL}^{(2)} - \bar{D}_{\delta I}^{(2)}\right).
\end{aligned}
\tag{B.17}
$$

Similarly, in accordance with equation (B.16), we will have the $R_n(k)$ functions:

$$
\begin{aligned}
\tilde{R}_1 &= \frac{21}{10}r^2\frac{D_{sym}^{(3)}(\mathbf{k},-\mathbf{p},\mathbf{p})}{D^{(1)}(k)\left(D^{(1)}(p)\right)^2} \\
\tilde{R}_2 &= \frac{rx(1-rx)}{1+r^2-2rx}\left(\bar{D}_a^{(2)} - \bar{D}_b^{(2)}x^2 + \bar{D}_{FL}^{(2)} - \bar{D}_{\delta I}^{(2)}\right) \\
\left[\tilde{R}_1(k)+\tilde{R}_2(k)\right]_{MG} &= \frac{r^2(1-rx)}{1+r^2-2rx}\left(\bar{D}_a^{(2)} - \bar{D}_b^{(2)}x^2 + \bar{D}_{FL}^{(2)} - \bar{D}_{\delta I}^{(2)}\right) \\
\left[\tilde{R}_1\right]_{MG} &= \frac{r^2(1-x^2)}{1+r^2-2rx}\left(\bar{D}_a^{(2)} - \bar{D}_b^{(2)}x^2 + \bar{D}_{FL}^{(2)} - \bar{D}_{\delta I}^{(2)}\right).
\end{aligned}
\tag{B.18}
$$

The functions Q_1-Q_3, R_1 and R_2 are the only ones that are necessary to calculate LPT statistics for pure dark matter considerations in MG, with the rest of them that we present here, being the additional functions needed for statistics of biased tracers in MG (in the configuration space). It should be emphasized at this point, that even the functions that have the same integral structure as in

GR (for example, Q_9-Q_{13}), do differ from their GR values, but this difference is manifested in the MG linear power spectra that appear in the integral relations (B.15) and (B.16).

Let us finish this section, by noting that in the GR limit, the above functions can be rather easily shown to recover their standard GR forms given in [119], if one keeps in mind that $\bar{D}^{(2)}_{\delta\mathcal{I}} = \bar{D}^{(2)}_{FL} = 0$ and $\bar{D}^{(2)}_{a} = \bar{D}^{(2)}_{b} = 1$ (for Einstein-De Sitter) in this limit.

B.2 Lagrangian correlators and q-functions in MG

Having derived the expressions for the scalar functions $Q_n(k)$ and $R_n(k)$ in MG cosmologies, we will now derive the integral formulas for the Lagrangian correlators (4.58), that are the building blocks of the 2-point statistics in CLPT. We will adopt the notation of [46] in this section and will show how the functions in their Appendix B will change for our MG models. To illustrate how the connection between the functions (4.58) and the ones presented in the previous section is drawn and also to show how these calculations are performed, we pick a reprsentative example of one these functions, $U^{(2)}_{11}$ and show the derivation below. Starting with the definition:

$$U^{(2)}_{11}(\mathbf{q}) = \hat{q}^i \langle \delta^{(1)}_1 \delta^{(1)}_2 \Delta^{(2)}_i \rangle_c, \tag{B.19}$$

we plug in the Fourier space representation of the field $\Delta_i = \Psi_i(\mathbf{q_2}) - \Psi_i(\mathbf{q_1})$, as well of the linear overdensities and get:

$$\begin{aligned}
&U_{11}^{(2)}(\mathbf{q}) = \hat{q}^i \times \\
&\left\langle \int \frac{d^3p}{(2\pi)^3}\frac{d^3p_1}{(2\pi)^3}\frac{d^3p_2}{(2\pi)^3} e^{i\mathbf{p}_2\cdot\mathbf{q}_2} e^{i\mathbf{p}_1\cdot\mathbf{q}_1}\left(e^{i\mathbf{p}\cdot\mathbf{q}_2} - e^{i\mathbf{p}\cdot\mathbf{q}_1}\right)\tilde{\delta}(\mathbf{p}_2)\tilde{\delta}(\mathbf{p}_1)\tilde{\Psi}^{(2)}(\mathbf{p})\right\rangle_c \\
&= \hat{q}^i \int \frac{d^3p}{(2\pi)^3}\frac{d^3p_1}{(2\pi)^3}\frac{d^3p_2}{(2\pi)^3} e^{i\mathbf{p}_1\cdot\mathbf{q}_1} e^{i(\mathbf{p}+\mathbf{p}_2)\cdot\mathbf{q}_2}\left\langle \tilde{\delta}(\mathbf{p}_2)\tilde{\delta}(\mathbf{p}_1)\tilde{\Psi}^{(2)}(\mathbf{p})\right\rangle_c \\
&- \hat{q}^i \int \frac{d^3p}{(2\pi)^3}\frac{d^3p_1}{(2\pi)^3}\frac{d^3p_2}{(2\pi)^3} e^{i\mathbf{p}_2\cdot\mathbf{q}_2} e^{i(\mathbf{p}+\mathbf{p}_1)\cdot\mathbf{q}_1}\left\langle \tilde{\delta}(\mathbf{p}_2)\tilde{\delta}(\mathbf{p}_1)\tilde{\Psi}^{(2)}(\mathbf{p})\right\rangle_c .
\end{aligned} \tag{B.20}$$

This expression contains two terms, which turn out to be equal. For this reason, we focus on the first one and notice that the cumulant can be expressed as a polyspectrum, through (B.9). The substitution gives:

$$\begin{aligned}
&\hat{q}^i \int \frac{d^3p}{(2\pi)^3}\frac{d^3p_1}{(2\pi)^3}\frac{d^3p_2}{(2\pi)^3} e^{i\mathbf{p}_1\cdot\mathbf{q}_1} e^{i(\mathbf{p}+\mathbf{p}_2)\cdot\mathbf{q}_2}\left\langle \tilde{\delta}(\mathbf{p}_2)\tilde{\delta}(\mathbf{p}_1)\tilde{\Psi}^{(2)}(\mathbf{p})\right\rangle_c = \\
&- i \int \frac{d^3p_1}{(2\pi)^3}\frac{d^3p}{(2\pi)^3} e^{i\mathbf{p}_1\cdot\mathbf{q}} \hat{q}^i C_i^{(2)}(\mathbf{p}_1, \mathbf{p}; \mathbf{p}_1 - \mathbf{p}) = \\
&- i \int \frac{d^3p_1}{(2\pi)^3} \hat{q}^i e^{i\mathbf{p}_1\cdot\mathbf{q}} \underbrace{\int \frac{d^3p}{(2\pi)^3} C_i^{(2)}(\mathbf{p}_1, \mathbf{p}; \mathbf{p}_1 - \mathbf{p})}_{I_C} .
\end{aligned} \tag{B.21}$$

In the last line, we defined the integral I_C, that can be calculated by using the definitions (B.10):

$$\begin{aligned}
I_C &= \int \frac{d^3p}{(2\pi)^3} C_i^{(2)}(\mathbf{p}_1, \mathbf{p}; \mathbf{p}_1 - \mathbf{p}) = \\
&- \int \frac{d^3p}{(2\pi)^3} L_i^{(2)}(\mathbf{p}_1 - \mathbf{p}) P_L(p_1) P_L(p) = \\
&= -\frac{3}{7}\frac{p_{1i}}{p_1^2} \int \frac{d^3p}{(2\pi)^3} p_{1i} \frac{(p_{1i} - p_i)}{|\mathbf{p}_1 - \mathbf{p}|^2} \bar{D}^{(2)} P_L(p_1) P_L(p) \\
&= -\frac{3}{7}\frac{p_{1i}}{p_1^2} \underbrace{\frac{p_1^3}{4\pi^2} P_L(p_1) \int_0^\infty dr P_L(p_1 r) \int_{-1}^1 dx \frac{r^2(1 - rx)}{1 + r^2 - 2rx} \bar{D}^{(2)}}_{[R_1(p_1) + R_2(p_1)]_{MG}} \\
&= -\frac{3}{7}\frac{p_{1i}}{p_1^2} \left[R_1(p_1) + R_2(p_1)\right]_{MG} ,
\end{aligned} \tag{B.22}$$

where we made use of the previous result (B.11). Plugging the result (B.22) into (B.21) and relabelling p_1 as k, we have

$$\begin{aligned}
&\hat{q}^i \int \frac{d^3p}{(2\pi)^3}\frac{d^3k}{(2\pi)^3}\frac{d^3p_2}{(2\pi)^3} e^{i\mathbf{k}\cdot\mathbf{q}_1} e^{i(\mathbf{p}+\mathbf{p}_2)\cdot\mathbf{q}_2} \left\langle \tilde{\delta}(\mathbf{p}_2)\tilde{\delta}(\mathbf{k})\Psi^{(2)}(\mathbf{p})\right\rangle_c = \\
&i\int \frac{dkdx}{4\pi^2} e^{ix(kq)} xk \frac{3}{7}\left[R_1(k)+R_2(k)\right]_{MG} = \\
&\frac{1}{2\pi^2}\int dkk\left(-\frac{3}{7}\right)\left[R_1(k)+R_2(k)\right]_{MG} j_1(kq),
\end{aligned} \tag{B.23}$$

where we made use of the Bessel function identity $\frac{1}{2}\int_{-1}^{1} dx x e^{ixkq} = i j_1(kq)$. In exactly the same way, the second term in (B.21) is equal to the first, which finally gives:

$$U_{11}^{(2)}(q) = \frac{1}{2\pi^2}\int dkk\left(-\frac{6}{7}\right)\left[R_1(k)+R_2(k)\right]_{MG} j_1(kq). \tag{B.24}$$

This is the MG equivalent of equation (B28) in Appendix B of [46], which is obviously recovered in the GR limit. In a similar manner, but after lengthy

calculations, we get the expressions for all the correlators:

$$
\begin{aligned}
V_1^{(112)}(q) &= \frac{1}{2\pi^2}\int \frac{dk}{k}\left(-\frac{3}{7}\right)[R_1(k)]_{MG}\, j_1(kq),\\
V_3^{(112)}(q) &= \frac{1}{2\pi^2}\int \frac{dk}{k}\left(-\frac{3}{7}\right)[Q_1(k)]_{MG}\, j_1(kq),\\
S^{(112)} &= \frac{3}{14\pi^2}\int \frac{dk}{k}\left[2\,[R_1]_{MG} + 4R_2 + [Q_1]_{MG} + 2Q_2\right]\frac{j_2(kq)}{kq},\\
T^{(112)} &= \frac{-3}{14\pi^2}\int \frac{dk}{k}\left[2\,[R_1]_{MG} + 4R_2 + [Q_1]_{MG} + 2Q_2\right] j_3(kq),\\
U^{(1)}(q) &= \frac{1}{2\pi^2}\int dkk\,(-1)\,P_L(k)\,j_1(kq),\\
U^{(3)}(q) &= \frac{1}{2\pi^2}\int dkk\left(-\frac{5}{21}\right)R_1(k)\,j_1(kq),\\
U_{20}^{(2)}(q) &= \frac{1}{2\pi^2}\int dkk\left(-\frac{6}{7}\right)Q_8(k)\,j_1(kq),\\
U_{11}^{(2)}(q) &= \frac{1}{2\pi^2}\int dkk\left(-\frac{6}{7}\right)[R_1(k)+R_2(k)]_{MG}\, j_1(kq),\\
X_{10}^{(12)}(q) &= \frac{1}{2\pi^2}\int dk\frac{1}{14}\Bigg(2\left([R_1]_{MG} - R_2(k)\right) + 3\,[R_1]_{MG}\, j_0(kq)\\
&\quad - 3\left[[R_1]_{MG} + 2R_2 + 2\,[R_1(k)+R_2(k)]_{MG} + 2Q_5\right]\frac{j_1(kq)}{kq}\Bigg),\\
Y_{10}^{(12)}(q) &= \frac{1}{2\pi^2}\int dk\left(-\frac{3}{14}\right)\Bigg([R_1]_{MG} + 2R_2\\
&\quad + 2\,[R_1(k)+R_2(k)]_{MG} + 2Q_5\Bigg)\times\left[j_0(kq) - 3\frac{j_1(kq)}{kq}\right],\\
X(q) &= \frac{1}{2\pi^2}\int dk\; a(k)\left[\frac{2}{3} - 2\frac{j_1(kq)}{kq}\right],\\
Y(q) &= \frac{1}{2\pi^2}\int dk\; a(k)\left[-2j_0(kq) + 6\frac{j_1(kq)}{kq}\right],
\end{aligned}
\tag{B.25}
$$

where we defined $a(k) = P_L(k) + \frac{9}{98}Q_1(k) + \frac{10}{21}R_1(k)$ and, following [46], we decomposed the matter terms as

$$
\begin{aligned}
A_{ij}^{mn}(q) &= X_{mn}(q)\delta_{ij} + Y_{mn}\hat{q}_i\hat{q}_j\\
W_{ijk}(q) &= V_1(q)\hat{q}_i\delta_{jk} + V_2(q)\hat{q}_j\delta_{ki} + V_3(q)\hat{q}_k\delta_{ij} + T(q)\hat{q}_i\hat{q}_j\hat{q}_k.
\end{aligned}
\tag{B.26}
$$

Now that the basic framework has been laid out, let us finish this section by

briefly summarizing the steps followed to calculate the two point statistics for a given model: after calculating the necessary MG growth factors, (4.22), (4.25) and (B.5), using our *Mathematica* notebook, we feed our modified version of the code in [1] with tabulated values of the growth factors for the various values of k, r and x needed at a given cosmological redshift z, as well as with the MG linear power spectrum given by:

$$P^L_{MG}(k,z) = \left(\frac{D^1_{MG}(k,z)}{D^1_{GR}(k,0)}\right)^2 P^L_{GR}(k,0). \tag{B.27}$$

The linear power spectrum for the background ΛCDM cosmology is calculated using the publicly available code CAMB [107]. The PYTHON module computes the various $Q_n(k)$ and $R_n(k)$ functions through equations (B.17) and (B.18), which are then used to calculate the various components of the CLPT power spectrum $P_X(k)$, through the integrations (B.25) and (4.40). To calculate (B.25), the $q-$function module is modified accordingly. The k functions can then be simply combined to give the SPT and LRT power spectra, by equations (4.64) and (4.65), respectively. Finally, the modified C++ counterpart follows a similar procedure to compute the configuration space two-point correlation function given by CLPT, through (5.24).

B.3 SPT and LRT Power spectra

In the main text, it was stated that the SPT and LRT power spectra, given by (4.64) and (4.65), correspondingly, are produced when one expands the resummed terms in the exponent of relation (4.40). Here we show how this derivation takes place, a process that once again shares a lot of similarities with

[1] https://github.com/martinjameswhite/CLEFT_GSM

the corresponding one in GR. When fully expanding the resummed Lagrangian correlator A^L_{ij} in (4.40), one gets:

$$\begin{aligned} P_X(k) = &\int d^3q e^{i\mathbf{k}\cdot\mathbf{q}} \\ &\times\Bigg[1 - \frac{1}{2}k_ik_jA_{ij} - \frac{i}{6}k_ik_jk_kW_{ijk} + b_1\left(2ik_iU_i - k_ik_jA^{10}_{ij}\right) \\ &+ b_2\left(ik_iU^{20}_i - k_ik_jU^{(1)}_iU^{(1)}_j\right) + b_1^2\left(\xi_L + ik_iU^{11}_i - k_ik_jU^{(1)}_iU^{(1)}_j\right) \\ &+ \frac{1}{2}b_2^2\xi_L^2 + 2b_1b_2\xi_Lik_iU^{(1)}_i\Bigg]. \end{aligned} \tag{B.28}$$

As done previously, we pick one of terms that is modified, that is the term $b_1^2ik_iU^{11}_i$, and perform the integration as an example. Plugging in U^{11}_i from (B.25):

$$\begin{aligned} &i\,b_1^2\int d^3qe^{i\mathbf{k}\cdot\mathbf{q}}\hat{q}^ik_iU^{11} = \\ &\frac{-i\,b_1^2}{2\pi^2}\frac{6}{7}\int d^3qdpe^{ikqx}kxp\left[R_1(p)+R_2(p)\right]_{MG}j_1(pq) = \\ &\frac{-i\,b_1^2}{\pi}\frac{6}{7}\int dqdpkpq^2\left[R_1(p)+R_2(p)\right]_{MG}j_1(pq)\int_{-1}^{1}dxe^{ikqx}x = \\ &\frac{b_1^2}{\pi}\frac{12}{7}\int dq\,dp\,kpq^2\left[R_1(p)+R_2(p)\right]_{MG}j_1(pq)j_1(kq) = \\ &\frac{b_1^2}{\pi}\frac{12}{7}\int dp\,kp\left[R_1(p)+R_2(p)\right]_{MG}\int_0^\infty dqq^2j_1(pq)j_1(kq) = \\ &b_1^2\frac{6}{7}\int dp\,\frac{kp}{k\,p}\delta_D(p-k)\left[R_1(p)+R_2(p)\right]_{MG} = \\ &b_1^2\left[R_1(k)+R_2(k)\right]_{MG}, \end{aligned} \tag{B.29}$$

where we also used the identity $\int_0^\infty dqq^2j_1(pq)j_1(kq) = \frac{\pi}{2pk}\delta_D(p-k)$. Similar computations for the rest of the terms give (4.64). In the LRT case, we expand everything but the q-independent, "zero-lag" piece of A^L_{ij}, which is equal to $2\sigma_L^2\delta_{ij}$, with $\sigma_L^2 = \frac{1}{6\pi^2}\int_0^\infty dkP_L(k)$. Since this term is scale-independent, it can be pulled out of the q integral and all the other integrations can be performed in the same manner as above, resulting in (4.65), that differs from (4.64) only in terms of the resummed exponential factor.

APPENDIX C

PBS BIASES IN MG

In this section, we will explain the derivation of the Lagrangian PBS biases (4.78) in MG models with environmentally dependent gravitational collapse. The PBS argument is commonly employed in conjunction with the halo approach [125, 124, 164], where one states that the conditional halo mass function $\bar{n}_h(M, \Delta)$, modulated by a long-wavelength density perturbation Δ, is modeled by the universal mass function prescription (4.47), with the collapse threshold shifted as $\delta_{cr} \to \delta_{cr} - \Delta$. The same result was also derived in [157], based on the rigorous definition (5.28), following a separate universe approach: with regards to galaxy clustering, a large-scale density perturbation, Δ, can be viewed as a modification of the mean physical density $\bar{\varrho}_m$ by an offset, that is [59]

$$\bar{\varrho}'_m = (1 + \Delta)\bar{\varrho}_m, \tag{C.1}$$

where $\bar{\varrho}_m$ should not be confused with the mean comoving density $\bar{\rho}_m$ and in a similar manner, the fractional overdensity at a point $\mathbf{x}$, $\delta_m(\mathbf{x})$, is shifted as:

$$\delta'_m(\mathbf{x}) = \delta_m(\mathbf{x}) + \Delta. \tag{C.2}$$

This reasoning can be employed to calculate the conditional halo mass function $\bar{n}_h(\Delta)$, by noticing that (4.47) depends solely on comoving quantities (that will not change), with the only exception of the density threshold δ_{cr}, through the peak significance

$$\nu_c = \frac{\delta_{cr}}{D^{(1)}(z)\sigma(M)} = \frac{\varrho_{cr} - \bar{\varrho}_m}{D^{(1)}(z)\sigma(M)\bar{\varrho}_m}, \tag{C.3}$$

that quantifies how rare a fluctuation above the density barrier $\varrho_{cr} = (1 + \delta_{cr})\bar{\varrho}_m$ is, given an RMS amplitute at the time of collapse z, $\delta\varrho_{RMS} = D^{(1)}(z)\sigma(M)\bar{\varrho}_m$. Now

following Birkhoff's theorem, the critical density for collapse, ϱ_{cr}, will be unaffected in the presence a density perturbation Δ, since a collapsing overdensity will not depend on the external spacetime. Combining this fact with equation (C.1), relation (C.3) gives [157]

$$\nu_c'(M) = \frac{(1+\delta_{cr})\bar{\varrho}_m - (1+\Delta)\bar{\varrho}_m}{D^{(1)}(z)\sigma(M)\bar{\varrho}_m} = \frac{\delta_{cr} - \Delta}{D^{(1)}(z)\sigma(M)}. \tag{C.4}$$

The conditional halo mass function $\bar{n}_h(M, \Delta)$ is now given by the universal prescription (4.47), but with the peak significance $\nu_c'(M)$ in (C.4). Combining this fact with the rigorous definition of the bias (5.28), gives the known PBS biases (4.53) for GR.

Let us now turn to the MG case. Following the discussion in Section 4.3.1, it is now clear how the density threshold will not be scale and redshift independent anymore, but will depend on the comoving halo mass M, as well as the environmental density δ_{env}, that is, a function $\delta_{cr}(M, \delta_{env})$. As a consequence, the peak significance in MG will now become:

$$\nu_{cMG} = \frac{\delta_{cr}(M, \delta_{env})}{D^{(1)}(z)\sigma(M)} = \frac{\varrho_{cr}(M, \delta_{env}) - \bar{\varrho}_m}{D^{(1)}(z)\sigma(M)\bar{\varrho}_m}. \tag{C.5}$$

In the presence of a long-wavelength density perturbation Δ, $\bar{\varrho}_m$ will again change according to (C.1), but also δ_{env} will now change as dictated by (C.2), and so will δ_{cr} that depends on it, which will become $\delta_{cr}'(M, \delta_{env}') = \delta_{cr}(M, \delta_{env} + \Delta)$. From the equivalent of (C.4), the MG peak significance will now become:

$$\nu_{cMG}'(M) = \frac{(1+\delta_{cr}')\bar{\varrho}_m - (1+\Delta)\bar{\varrho}_m}{D^{(1)}(z)\sigma(M)\bar{\varrho}_m} = \frac{\delta_{cr}(M, \delta_{env} + \Delta) - \Delta}{D^{(1)}(z)\sigma(M)}. \tag{C.6}$$

As in the GR case, the conditional halo mass function $\bar{n}_h(M, \Delta)$ for MG is now given by the universal prescription (4.47), but with the peak significance $\nu_{cMG}'(M)$ given by (C.6). Calculating, now, the first and second order derivatives

that we need in (5.28), we will have, starting with the linear order:

$$\begin{aligned}
&\left.\frac{d\bar{n}_h(M,\Delta)}{d\Delta}\right|_{\Delta=0} = \left.\frac{d\nu'_{cMG}}{d\Delta}\right|_{\Delta=0} \left.\frac{d\bar{n}_h(M,\Delta)}{d\nu'_{cMG}}\right|_{\Delta=0} = \\
&\frac{1}{D^{(1)}(z)\sigma(M)} \left.\frac{d\left[\delta_{cr}(M,\delta_{env}+\Delta)-\Delta\right]}{d\Delta}\right|_{\Delta=0} \frac{d\bar{n}_h(M,0)}{d\nu_{cMG}} = \\
&\frac{\left[\frac{d\delta_{cr}(M,\delta_{env})}{d\delta_{env}}-1\right]}{D^{(1)}(z)\sigma(M)} \frac{d\bar{n}_h(M,0)}{d\nu_{cMG}},
\end{aligned} \tag{C.7}$$

where we used the chain rule a few times and also the fact that $\nu'_{cMG}(M) = \nu_{cMG}(M)$ at $\Delta = 0$. The definition (5.28), combined with the result (C.7) and the universal prescription (4.47), gives:

$$b^1_{MG}(M,\delta_{env}) = \frac{\left[\frac{d\delta_{cr}(M,\delta_{env})}{d\delta_{env}}-1\right]}{D^{(1)}(z)\sigma(M)} \frac{1}{\nu_{cMG} f\left[\nu_{cMG}\right]} \frac{d\left(\nu_{cMG} f\left[\nu_{cMG}\right]\right)}{d\nu_{cMG}}, \tag{C.8}$$

Similarly, the second order derivative will be:

$$\begin{aligned}
&\left.\frac{d^2\bar{n}_h(M,\Delta)}{d\Delta^2}\right|_{\Delta=0} = \frac{d}{d\Delta}\left.\frac{d\bar{n}_h(M,\Delta)}{d\Delta}\right|_{\Delta=0} \\
&= \frac{d}{d\Delta}\left[\frac{\left[\frac{d\delta_{cr}(M,\delta_{env})}{d\delta_{env}}-1\right]}{D^{(1)}(z)\sigma(M)} \frac{d\bar{n}_h(M,0)}{d\nu_{cMG}}\right], \\
&= \frac{d^2\delta_{cr}(M,\delta_{env})}{d\delta^2_{env}} \frac{1}{D^{(1)}(z)\sigma(M)} \frac{d\bar{n}_h(M,0)}{d\nu_{cMG}} + \\
&\frac{\left[\frac{d\delta_{cr}(M,\delta_{env})}{d\delta_{env}}-1\right]^2}{\left[D^{(1)}(z)\sigma(M)\right]^2} \frac{d\bar{n}^2_h(M,0)}{d\nu^2_{cMG}},
\end{aligned} \tag{C.9}$$

which will give the expression for the second order bias factor:

$$\begin{aligned}
b^2_{MG}(M,\delta_{env}) = &\frac{\frac{d^2\delta_{cr}(M,\delta_{env})}{d\delta^2_{env}}}{D^{(1)}(z)\sigma(M)} \frac{1}{\nu_{cMG} f\left[\nu_{cMG}\right]} \frac{d\left(\nu_{cMG} f\left[\nu_{cMG}\right]\right)}{d\nu_{cMG}} + \\
&\frac{\left[\frac{d\delta_{cr}(M,\delta_{env})}{d\delta_{env}}-1\right]^2}{\left[D^{(1)}(z)\sigma(M)\right]^2} \frac{1}{\nu_{cMG} f\left[\nu_{cMG}\right]} \frac{d^2\left(\nu_{cMG} f\left[\nu_{cMG}\right]\right)}{d\nu^2_{cMG}}.
\end{aligned} \tag{C.10}$$

Equations (C.8) and (C.10) give the Lagrangian PBS biases of first and second order in MG, for any universal mass function $f\left[\nu_{cMG}\right]$. Applying these to the particular ST form (4.50), we arrive at the relationships (4.78) and (4.79) in the

main text. The derivatives of the form $\frac{d\delta_{cr}(M,\delta_{env})}{\delta_{env}}$ can be easily calculated numerically, as soon as the function $\delta_{cr}(M, \delta_{env})$ is known from integrating equation (4.68). In MG models that still possess a scale and redshift *independent* barrier, like the *n*DGP model (and possibly other models in the Vainshtein family), these derivatives will vanish and we recover the standard GR expressions for the PBS biases (4.53), but with a different δ_{cr}.

APPENDIX D

GSM FUNCTIONS IN MG

In this appendix, we give expressions for the necessary ingredients to construct the Gaussian streaming model in LPT. That is, we find 1D integral expressions for (5.44) and (5.49) in cosmologies beyond ΛCDM. Before displaying all these equations, as an example we consider the "q-function" $\dot{U}_i(\mathbf{q})$:

$$\dot{U}_i(\mathbf{q}) = \frac{1}{f_0 H}\langle \delta_L(\mathbf{q}_1)\dot{\Delta}_i\rangle = \int \frac{d^3k_1 d^3k_2}{(2\pi)^6} e^{i\mathbf{k}_1\cdot\mathbf{q}_1}\left(e^{i\mathbf{k}_2\cdot\mathbf{q}_2} - e^{i\mathbf{k}_2\cdot\mathbf{q}_1}\right)\langle \delta_L(\mathbf{k}_1)\dot{\Psi}_i(\mathbf{k}_2)\rangle_c. \quad \text{(D.1)}$$

Up to 1-loop, $\langle \delta_L(\mathbf{k}_1)\dot{\Psi}_i(\mathbf{k}_2)\rangle_c \simeq Hf(k_2)\langle \delta_L(\mathbf{k}_1)\Psi_i^{(1)}(\mathbf{k}_2)\rangle + 3Hf(k_2)\langle \delta_L(\mathbf{k}_1)\Psi_i^{(3)}(\mathbf{k}_2)\rangle$, where for illustrative purposes we approximate $\dot{\Psi}^{(n)}(\mathbf{k}) = nHf(\mathbf{k})\Psi^{(n)}(\mathbf{k})$. After some straightforward manipulations one obtains (see, e.g., [46])

$$\dot{U}_i(\mathbf{q}) = -\hat{q}_i \int \frac{dk}{2\pi^2} k \frac{f(k)}{f_0}\left[P_L(k) + \frac{7}{5}R_1(k)\right] j_1(kq) \quad \text{(D.2)}$$

where the "k-function" R_1 is [120]

$$R_1(k) = \frac{21}{10}P_L(k)\int \frac{d^3p}{(2\pi)^3}\mathbf{k}\cdot\mathbf{L}^{(3)}(\mathbf{k},-\mathbf{p},\mathbf{p})P_L(p) \quad \text{(D.3)}$$

with $\mathbf{L}^{(3)}$ the third order LPT kernel. In the rest of this appendix we will find all the functions given by (5.44) and (5.49) *without* the use of the above approximation, which is not as accurate in MG models, as it is in ΛCDM.

D.1 LPT kernels

The Lagrangian displacement field is formally expanded as $\Psi_i(\mathbf{q},t) = \sum_{n=0}^{\infty}\Psi_i^{(n)}(\mathbf{q})$. In Fourier space, the nth order Lagrangian displacement is the weighted convolution of n linear density fields,

$$\Psi_i^{(n)}(\mathbf{k},t) = \frac{i}{n!}\int \frac{d^3k_1\cdots d^3k_n}{(2\pi)^{3(n-1)}}\delta_{\rm D}(\mathbf{k}-\mathbf{k}_{1\cdots n})L_i^{(n)}(\mathbf{k}_1,\ldots,\mathbf{k}_n;t)\delta(\mathbf{k}_1,t)\cdots\delta(\mathbf{k}_n,t). \quad \text{(D.4)}$$

The first order kernel is $\mathbf{L}^{(1)}(\mathbf{k}) = \mathbf{k}/k^2$, as can be seen from (5.16). Higher perturbative orders are obtained by solving iteratively (5.14) [15]. For $\mathbf{L}^{(2)}$ we have

$$L_i^{(2)}(\mathbf{k}_1, \mathbf{k}_2, t) = \frac{3}{7}\frac{(\mathbf{k}_1 + \mathbf{k}_2)_i}{|\mathbf{k}_1 + \mathbf{k}_2|^2}\left[\mathcal{A}(\mathbf{k}_1, \mathbf{k}_2, t) - \mathcal{B}(\mathbf{k}_1, \mathbf{k}_2, t)\frac{(\mathbf{k}_1 \cdot \mathbf{k}_2)^2}{k_1^2 k_2^2}\right] \tag{D.5}$$

where the $\mathcal{A}$ and $\mathcal{B}$ functions are obtained by solving second order differential equations, and are given in (2.19) of [17]; see also [15]. In ΛCDM we have that functions $\mathcal{A}$ and $\mathcal{B}$ are equal and only time-dependent, while for EdS, or more generally for ΛCDM models with $f^2 = \Omega_m$, these functions are exactly 1, and hence the kernels become time independent. Since $\mathcal{A}|_{\Lambda\text{CDM}}(z = 0) \simeq 1.01$, this is usually approximated as 1, in what is called the static kernels approximation, yielding subpercent errors at quasilinear scales. In MG, the departure from $\mathcal{A}, \mathcal{B} \simeq 1$ is larger than the percent level; moreover, the $\mathcal{A}$ function carries the non-linear terms responsible for screening mechanisms, such that the use of the static kernels approximation in MG misses this important property of MG. By isotropy we can write $\mathcal{A}, \mathcal{B}(k_1, k_2, x = \hat{\mathbf{k}}_1 \cdot \hat{\mathbf{k}}_2)$ and perform a Legendre expansion on the angle x. Such procedure shows that the monopole of these functions is the dominant term, other multipoles give smaller contributions, and hence the decomposition in (D.5) is not as arbitrary as it may look at first sight. The case of DGP, is even simpler, because $\mathcal{B}$ is only time dependent, and $\mathcal{A}$ has only a monopole and a small quadrupole, the latter given exclusively by the screening non-linear terms in the Klein-Gordon equation [16].

The expression for the third order kernel $L_i^{(3)}$ is quite large and we do not reproduce it here, but we refer the reader to ref. [15]. All these functions are time-dependent, and for compactness we will omit to write it explicitly in the following.

In LPT-RSD models one finds the time derivative of the Lagrangian displace-

ment field. As was discussed in the main text, in ΛCDM, a good approximation is given by $\dot{\Psi}^{(n)}(\mathbf{q}) \simeq nHf\Psi(\mathbf{q})$, which is no longer possible in MG since the linear growth function $D^{(1)}$ is scale-dependent, as was discussed in the main text. A general expression is

$$\Psi_i^{(n)}(\mathbf{k}) = \frac{i}{n!} n f_0 H \int \frac{d^3k_1 \cdots d^3k_n}{(2\pi)^{3(n-1)}} \delta_{\rm D}(\mathbf{k} - \mathbf{k}_{1\cdots n}) L_i^{f(n)}(\mathbf{k}_1, \cdots, \mathbf{k}_n) \delta(\mathbf{k}_1) \cdots \delta(\mathbf{k}_n), \quad \text{(D.6)}$$

with $\mathbf{k}_{1\cdots n} = \mathbf{k}_1 + \cdots + \mathbf{k}_n$, and kernels

$$\begin{aligned} L_i^{f(n)}(\mathbf{k}_1, \cdots, \mathbf{k}_n) &= \frac{f(k_1) + \cdots + f(k_n)}{n f_0} L_i^{(n)}(\mathbf{k}_1, \cdots, \mathbf{k}_n) + \frac{1}{n f_0} L_i^{\prime(n)}(\mathbf{k}_1, \cdots, \mathbf{k}_n) \\ &\equiv \frac{\mathbf{k}^i_{1\cdots n}}{k^2_{1\cdots n}} C_n \Gamma_n^f(\mathbf{k}_1, \cdots, \mathbf{k}_n), \end{aligned} \quad \text{(D.7)}$$

where we remind that $f(k,t) = d\ln D^{(1)}(k,t)/d\ln a$ is the growth factor at a scale k, and $f_0 \equiv f(k=0,t)$ is the large-scale growth factor, usually coinciding with that of ΛCDM. The last line in the above equation serves to define the scalar kernels Γ_n^f and a set of numbers C_n; for convenience we choose $C_1 = 1$, $C_2 = 3/7$. We can use a weaker version of the static approximation and neglect the second term in the second equality of (D.7); however, we find that $\mathbf{L}'$ is about the same order as the corrections introduced by MG to the EdS kernels $\mathbf{L}|_{\rm EdS}$. Hence, to be consistent we have to keep both terms in that equation.

Analogously as we introduced Γ_n^f functions, for the Lagrangian displacements we define

$$C_n \Gamma_n(\mathbf{k}_1, \ldots, \mathbf{k}_n) = k^i_{1\cdots n} L_i^{(n)}(\mathbf{k}_1, \ldots, \mathbf{k}_n), \quad \text{(D.8)}$$

and hence these Γ_n functions are the kernels of the longitudinal component of the Lagrangian displacement, $\mathbf{k} \cdot \Psi^{(n)}(\mathbf{k})$. Since for 1-loop, 2-point statistics, the transverse components project out, one can use the scalar Γ instead of vector $\mathbf{L}$ kernels without loss of generality.

The first order scalar kernels are $\Gamma_1(\mathbf{k}) = 1$ and $\Gamma_1^f(\mathbf{k}) = f(k)/f_0$. To second order

$$\Gamma_2[\mathbf{p}_1, \mathbf{p}_2] = \left[\mathcal{A}(\mathbf{p}_1, \mathbf{p}_2) - \mathcal{B}(\mathbf{p}_1, \mathbf{p}_2)\frac{(\mathbf{p}_1 \cdot \mathbf{p}_2)^2}{p_1^2 p_2^2}\right] = \frac{7}{3}\frac{D^{(2)}(\mathbf{p}_1, \mathbf{p}_2)}{D_+(p_1)D_+(p_2)}, \tag{D.9}$$

$$\begin{aligned}\Gamma_2^f[\mathbf{p}_1, \mathbf{p}_2] &= \Gamma_2[\mathbf{p}_1, \mathbf{p}_2]\frac{f(p_1) + f(p_2)}{2f_0} + \frac{1}{2f_0 H_0}\left[\dot{\mathcal{A}}(\mathbf{p}_1, \mathbf{p}_2) - \dot{\mathcal{B}}(\mathbf{p}_1, \mathbf{p}_2)\frac{(\mathbf{p}_1 \cdot \mathbf{p}_2)^2}{p_1^2 p_2^2}\right], \\ &= \frac{1}{2f_0}\frac{7}{3}\frac{\frac{d}{d\ln a}D^{(2)}(\mathbf{p}_1, \mathbf{p}_2)}{D_+(p_1)D_+(p_2)},\end{aligned} \tag{D.10}$$

where $\mathcal{A}, \mathcal{B} = \mathcal{A}, \mathcal{B}(\mathbf{p}_1, \mathbf{p}_2)$, and $D^{(2)}$ is the second order growth function defined in [15]. The third order kernels are

$$C_3\Gamma_3[\mathbf{p}_1, \mathbf{p}_2, \mathbf{p}_3] = \frac{D_+^{(3)s}(\mathbf{p}_1, \mathbf{p}_2, \mathbf{p}_3)}{D_+(\mathbf{p}_1)D_+(\mathbf{p}_2)D_+(\mathbf{p}_3)}, \tag{D.11}$$

$$C_3\Gamma_3^f[\mathbf{p}_1, \mathbf{p}_2, \mathbf{p}_3] = \frac{1}{3f_0}\frac{\frac{d}{d\ln a}D_+^{(3)s}(\mathbf{p}_1, \mathbf{p}_2, \mathbf{p}_3)}{D_+(\mathbf{p}_1)D_+(\mathbf{p}_2)D_+(\mathbf{p}_3)}. \tag{D.12}$$

with the (symmetric) third order growth function $D_+^{(3)s}$ as given in [15]. Actually, we will not use the value of C_3 at all, so we can let it free. But by defining $C_2 = 3/7$ we make the notation simpler in the following sections.

We notice that the approximation of static kernels, usually taken in ΛCDM and exact for EdS, corresponds to

$$\Gamma_n^f \simeq \Gamma_n, \qquad (\Lambda\text{CDM}), \tag{D.13}$$

and therefore, the functions presented in the rest of this appendix can be recasted in their well-known, ΛCDM counterparts by omitting the "f" labels.

D.2 k functions

The $Q_n(k)$ and $R_n(k)$ scalar functions, introduced first in [120, 119], are the building blocks of LPT statistics. These are constructed out of N-point functions of

linear density fields, Lagrangian displacements and their derivatives, as for example $\langle \delta_L(\mathbf{k}_1)\Psi^{(n)}(\mathbf{k}_2)\dot{\Psi}^{(m)}(\mathbf{k}_3)\rangle$, with (n) and (m) denoting perturbative orders; see [120, 119]. We do not write here the definitions of these polyspectra, but we refer the reader to the above referenced works and to [191, 17] for MG. Here we extend those definitions to include time derivatives of Lagrangian displacements.

The only k-functions involving third order Lagrangian displacements are

$$R_1(k) \equiv \int \frac{d^3p}{(2\pi)^3}\frac{21}{10}C_3\Gamma_3(\mathbf{k},-\mathbf{p},\mathbf{p})P_L(p)P_L(k), \tag{D.14}$$

$$R_1^f(k) \equiv \int \frac{d^3p}{(2\pi)^3}\frac{21}{10}C_3\Gamma_3^f(\mathbf{k},-\mathbf{p},\mathbf{p})P_L(p)P_L(k). \tag{D.15}$$

Expressions involving just one time derivative, and that it is operating on one Lagrangian displacement to second order are denoted with a label "f":

$$Q_1^f(k) \equiv \int \frac{d^3p}{(2\pi)^3}\Gamma_2[\mathbf{p},\mathbf{k}-\mathbf{p}]\Gamma_2^f[\mathbf{p},\mathbf{k}-\mathbf{p}]P_L(|\mathbf{k}-\mathbf{p}|)P_L(p) \tag{D.16}$$

$$Q_2^f(k) = \int \frac{d^3p}{(2\pi)^3}\frac{(\mathbf{k}\cdot\mathbf{p})\mathbf{k}\cdot(\mathbf{k}-\mathbf{p})}{p^2|\mathbf{k}-\mathbf{p}|^2}\Gamma_2^f[\mathbf{p},\mathbf{k}-\mathbf{p}]P_L(|\mathbf{k}-\mathbf{p}|)P_L(p), \tag{D.17}$$

$$Q_5^f(k) = \int \frac{d^3p}{(2\pi)^3}\frac{\mathbf{k}\cdot\mathbf{p}}{p^2}\Gamma_2^f[\mathbf{p},\mathbf{k}-\mathbf{p}]P_L(|\mathbf{k}-\mathbf{p}|)P_L(p), \tag{D.18}$$

$$Q_8^f(k) = \int \frac{d^3p}{(2\pi)^3}\Gamma_2^f[\mathbf{p},\mathbf{k}-\mathbf{p}]P_L(|\mathbf{k}-\mathbf{p}|)P_L(p), \tag{D.19}$$

$$Q_I^f(k) = \int \frac{d^3p}{(2\pi)^3}\frac{((\mathbf{k}\cdot\mathbf{p})\mathbf{k}-k^2\mathbf{p})\cdot(\mathbf{k}-\mathbf{p})}{p^2|\mathbf{k}-\mathbf{p}|^2}\Gamma_2^f[\mathbf{p},\mathbf{k}-\mathbf{p}]P_L(|\mathbf{k}-\mathbf{p}|)P_L(p), \tag{D.20}$$

$$R_2^f(k) = \int \frac{d^3p}{(2\pi)^3}\frac{\mathbf{k}\cdot\mathbf{p}\,\mathbf{k}\cdot(\mathbf{k}-\mathbf{p})}{p^2|\mathbf{k}-\mathbf{p}|^2}\Gamma_2^f[\mathbf{k},-\mathbf{p}]P_L(k)P_L(p), \tag{D.21}$$

$$R_{1+2}^f(k) = \int \frac{d^3p}{(2\pi)^3}\frac{\mathbf{k}\cdot(\mathbf{k}-\mathbf{p})}{|\mathbf{k}-\mathbf{p}|^2}\Gamma_2^f[\mathbf{p},\mathbf{k}]P_L(k)P_L(p), \tag{D.22}$$

$$R_I^f(k) = \int \frac{d^3p}{(2\pi)^3}\frac{((\mathbf{k}\cdot\mathbf{p})\mathbf{k}-k^2\mathbf{p})\cdot(\mathbf{k}-\mathbf{p})}{p^2|\mathbf{k}-\mathbf{p}|^2}\Gamma_2^f[\mathbf{k},-\mathbf{p}]P_L(k)P_L(p), \tag{D.23}$$

The usual, "undotted", Q and R functions are obtained by replacing Γ_2^f by Γ_2 in the above equations. Functions R_I, Q_I and R_{1+2} are equal to R_1, Q_1 and $R_1 + R_2$ respectively for EdS kernels. In ref.[191] these are named as $[R_1]_{\rm MG}$, $[Q_1]_{\rm MG}$ and $[R_1 + R_2]_{\rm MG}$.

Now, the "$f*$" k-functions contain one derivative in a linear field, and no derivatives in the other fields. These are given by

$$Q_I^{f*}(k) = \int \frac{d^3p}{(2\pi)^3} \frac{((\mathbf{k}\cdot\mathbf{p})\mathbf{k} - k^2\mathbf{p})\cdot(\mathbf{k}-\mathbf{p})}{p^2|\mathbf{k}-\mathbf{p}|^2} \Gamma_2[\mathbf{p},\mathbf{k}-\mathbf{p}] \frac{f(p)}{f_0} P_L(|\mathbf{k}-\mathbf{p}|)P_L(p), \tag{D.24}$$

$$Q_2^{f*}(k) = \int \frac{d^3p}{(2\pi)^3} \frac{(\mathbf{k}\cdot\mathbf{p})\mathbf{k}\cdot(\mathbf{k}-\mathbf{p})}{p^2|\mathbf{k}-\mathbf{p}|^2} \Gamma_2[\mathbf{p},\mathbf{k}-\mathbf{p}] \frac{f(p)}{f_0} P_L(|\mathbf{k}-\mathbf{p}|)P_L(p), \tag{D.25}$$

$$Q_5^{f*}(k) = \int \frac{d^3p}{(2\pi)^3} \frac{\mathbf{k}\cdot\mathbf{p}}{p^2} \Gamma_2[\mathbf{p},\mathbf{k}-\mathbf{p}] \frac{f(p)}{f_0} P_L(|\mathbf{k}-\mathbf{p}|)P_L(p), \tag{D.26}$$

$$R_2^{f*}(k) = \int \frac{d^3p}{(2\pi)^3} \frac{\mathbf{k}\cdot\mathbf{p}\,\mathbf{k}\cdot(\mathbf{k}-\mathbf{p})}{p^2|\mathbf{k}-\mathbf{p}|^2} \Gamma_2[\mathbf{k},-\mathbf{p}] \frac{f(p)}{f_0} P_L(k)P_L(p), \tag{D.27}$$

$$R_{1+2}^{f*}(k) = \int \frac{d^3p}{(2\pi)^3} \frac{\mathbf{k}\cdot(\mathbf{k}-\mathbf{p})}{|\mathbf{k}-\mathbf{p}|^2} \Gamma_2[\mathbf{k},-\mathbf{p}] \frac{f(p)}{f_0} P_L(k)P_L(p), \tag{D.28}$$

$$R_I^{f*}(k) = \int \frac{d^3p}{(2\pi)^3} \frac{((\mathbf{k}\cdot\mathbf{p})\mathbf{k} - k^2\mathbf{p})\cdot(\mathbf{k}-\mathbf{p})}{p^2|\mathbf{k}-\mathbf{p}|^2} \Gamma_2[\mathbf{k},-\mathbf{p}] \frac{f(p)}{f_0} P_L(k)P_L(p). \tag{D.29}$$

While the "ff" k-functions —that contain two time derivatives, one in a linear field and the other in a second order field— are obtained by replacing $\Gamma_2 \to \Gamma_2^f$ in the above equations. The exception to this rule is Q_1, where a label "ff" denotes that the two second order Lagrangian displacements are differentiated,

$$Q_1^{ff}(k) = \int \frac{d^3p}{(2\pi)^3} \Gamma^f[\mathbf{p},\mathbf{k}-\mathbf{p}]\Gamma^f[\mathbf{p},\mathbf{k}-\mathbf{p}] P_L(|\mathbf{k}-\mathbf{p}|)P_L(p). \tag{D.30}$$

Also, there are functions that contain two derivatives, and both in linear displacement fields, denoted with an "$f*f*$" label, these are

$$Q_I^{f*f*}(k) = \int \frac{d^3p}{(2\pi)^3} \frac{((\mathbf{k}\cdot\mathbf{p})\mathbf{k} - k^2\mathbf{p})\cdot(\mathbf{k}-\mathbf{p})}{p^2|\mathbf{k}-\mathbf{p}|^2} \Gamma_2[\mathbf{p},\mathbf{k}-\mathbf{p}] \frac{f(|\mathbf{k}-\mathbf{p}|)}{f_0} \frac{f(p)}{f_0} P_L(|\mathbf{k}-\mathbf{p}|)P_L(p), \tag{D.31}$$

$$Q_2^{f*f*}(k) = \int \frac{d^3p}{(2\pi)^3} \frac{(\mathbf{k}\cdot\mathbf{p})\mathbf{k}\cdot(\mathbf{k}-\mathbf{p})}{p^2|\mathbf{k}-\mathbf{p}|^2} \Gamma_2[\mathbf{p},\mathbf{k}-\mathbf{p}] \frac{f(|\mathbf{k}-\mathbf{p}|)}{f_0} \frac{f(p)}{f_0} P_L(|\mathbf{k}-\mathbf{p}|)P_L(p). \tag{D.32}$$

The q-functions of (5.44) and (5.49) can be recasted as 1D integrations of the above Q and R functions, which we will do in the upcoming section. The main

differences with these functions and the corresponding in ΛCDM, are the use of the kernels Γ, differing in the percent level in MG and standard cosmologies, and more importantly, the appereance of factors $f(k)/f_0$ that can be as large as ~ 1.1.

D.3 q functions

Several q dependent functions should be calculated before computing the correlation function, the pairwise velocity and the pairwise velocity dispersion. These are the "U", "A" and "W" functions defined in (5.44) and (5.49)

The $U_i(q)$ vector functions can be written as

$$U_i(\mathbf{q}) = U(q)\hat{q}_i, \tag{D.33}$$

with

$$\begin{aligned}
\dot{U}(q) &= -\frac{1}{2\pi^2}\int dk\, k\left[\frac{f(k)}{f_0}P_L(k) + \frac{5}{7}R_1^f(k)\right] j_1(kq), \\
\dot{U}^{20}(q) &= -\frac{3}{7\pi^2}\int dk\, k Q_8^f(k) j_1(kq), \\
\dot{U}^{11}(q) &= -\frac{6}{7\pi^2}\int dk\, k R_{1+2}^f(k) j_1(kq).
\end{aligned} \tag{D.34}$$

In ΛCDM $R^f, Q^f \simeq R, Q$ and $f(k) = f_0$, hence we obtain the standard results $\dot{U} = U^{(1)} + 3U^{(3)}$, $\dot{U}^{20} = 2U^{20}$ and $\dot{U}^{11} = 2U^{11}$; see [198].

The A functions are decomposed as

$$\dot{A}_{ij}(\mathbf{q}) = \dot{X}(q)\delta_{ij} + \dot{Y}(q)\hat{q}_i\hat{q}_j, \qquad \ddot{A}_{ij}(\mathbf{q}) = \ddot{X}(q)\delta_{ij} + \ddot{Y}(q)\hat{q}_i\hat{q}_j, \tag{D.35}$$

with

$$\dot{X}(q) = \frac{1}{\pi^2}\int dk \left[\frac{f(k)}{f_0}P_L(k) + \frac{9}{49}Q_1^f(k) + \frac{5}{21}\frac{f(k)}{f_0}R_1(k) + \frac{5}{7}R_1^f(k)\right]\left[\frac{1}{3} - \frac{j_1(kq)}{kq}\right],$$
$$\dot{Y}(q) = \frac{1}{\pi^2}\int dk \left[\frac{f(k)}{f_0}P_L(k) + \frac{9}{49}Q_1^f(k) + \frac{5}{21}\frac{f(k)}{f_0}R_1(k) + \frac{5}{7}R_1^f(k)\right] j_2(kq),$$
$$\ddot{X}(q) = \frac{1}{\pi^2}\int dk \left[\left(\frac{f(k)}{f_0}\right)^2 P_L(k) + \frac{18}{49}Q_1^{ff}(k) + \frac{10}{7}\frac{f(k)}{f_0}R_1^f(k)\right]\left[\frac{1}{3} - \frac{j_1(kq)}{kq}\right],$$
$$\ddot{Y}(q) = \frac{1}{\pi^2}\int dk \left[\left(\frac{f(k)}{f_0}\right)^2 P_L(k) + \frac{18}{49}Q_1^{ff}(k) + \frac{10}{7}\frac{f(k)}{f_0}R_1^f(k)\right] j_2(kq), \tag{D.36}$$

and the A^{10} functions as

$$\dot{A}_{ij}^{10}(\mathbf{q}) = \dot{X}^{10}(q)\delta_{ij} + \dot{Y}^{10}(q)\hat{q}_i\hat{q}_j, \qquad \ddot{A}_{ij}^{10}(\mathbf{q}) = \ddot{X}^{10}(q)\delta_{ij} + \ddot{Y}^{10}(q)\hat{q}_i\hat{q}_j, \tag{D.37}$$

with

$$\begin{aligned}
\dot{X}_{10}(q) &= \frac{1}{\pi^2}\int_0^\infty dk \frac{1}{28}\Big[2(2R_I^f - 2R_2^f + R_I^{f*} - R_2^{f*}) + 3(2R_I^f + R_I^{f*})j_0(kq) \\
&\quad - 3(2R_I^f + 4R_2^f + 4R_{1+2}^f + 4Q_5^f + R_I^{f*} + 2R_2^{f*} + 2R_{1+2}^{f*} + 2Q_5^{f*})\frac{j_1(kq)}{kq}\Big], \\
\dot{Y}_{10}(q) &= \frac{1}{\pi^2}\int_0^\infty dk \frac{3}{28}\Big[2R_I^f + 4R_2^f + 4R_{1+2}^f + 4Q_5^f \\
&\quad + R_I^{f*} + 2R_2^{f*} + 2R_{1+2}^{f*} + 2Q_5^{f*}\Big] j_2(kq), \\
\ddot{X}_{10}(q) &= \frac{1}{\pi^2}\int_0^\infty dk \frac{4}{28}\Big[2(R_I^{ff} - R_2^{ff}) + 3R_I^{ff} j_0(kq) \\
&\quad - 3(R_I^{ff} + 2R_2^{ff} + 2R_{1+2}^{ff} + 2Q_5^{ff})\frac{j_1(kq)}{kq}\Big], \\
\ddot{Y}_{10}(q) &= \frac{1}{\pi^2}\int_0^\infty dk \frac{4\times 3}{28}\Big[R_I^{ff} + 2R_2^{ff} + 2R_{1+2}^{ff} + 2Q_5^{ff}\Big] j_2(kq).
\end{aligned} \tag{D.38}$$

Now, the W functions have the form

$$\dot{W}_{ijk} = W_{ijk}^{(1\dot{1}\dot{2})} + W_{ijk}^{(1\dot{2}\dot{1})} + W_{ijk}^{(2\dot{1}\dot{1})}, \quad \ddot{W}_{ijk} = W_{ijk}^{(1\dot{1}\dot{2})} + W_{ijk}^{(1\dot{2}\dot{1})} + W_{ijk}^{(2\dot{1}\dot{1})}, \tag{D.39}$$

where the dot over a number indicates that the Lagrangian displacement of that order should be differentiated. Except for the undotted case, these cannot be

decomposed as $W_{ijk} = V\hat{q}_{\{i}\delta_{jk\}} + T\hat{q}_i\hat{q}_j\hat{q}_k$, because in general $\dot{W}_{ijk} \neq \dot{W}_{(jki)}$. However, we do have $\dot{W}_{ijk} = \dot{W}_{(ij)k}$ and $\ddot{W}_{ijk} = \ddot{W}_{i(jk)}$. These symmetries allow us to decompose

$$W_{ijk} = V(q)\hat{q}_{\{i}\delta_{jk\}} + T(q)\hat{q}_i\hat{q}_j\hat{q}_k, \tag{D.40}$$

$$\dot{W}_{ijk}(\mathbf{q}) = \dot{V}_1(q)\Big(\hat{q}_i\delta_{jk} + \hat{q}_j\delta_{ki}\Big) + \dot{V}_3(q)\hat{q}_k\delta_{ij} + \dot{T}(q)\hat{q}_i\hat{q}_j\hat{q}_k, \tag{D.41}$$

$$\ddot{W}_{ijk}(\mathbf{q}) = \ddot{V}_1(q)\hat{q}_i\delta_{jk} + \dot{V}_3(q)\Big(\hat{q}_j\delta_{ki} + \hat{q}_k\delta_{ij}\Big) + \ddot{T}(q)\hat{q}_i\hat{q}_j\hat{q}_k, \tag{D.42}$$

with $V(q)$ and $T(q)$ given in refs. [191, 17] for MG, and

$$\begin{aligned}
\dot{T}(q) = &-\int \frac{dk}{\pi^2}\frac{3}{7k}\bigg[2Q_2^f + 2Q_2^{f*} + Q_I^f + Q_I^{f*} + 2\frac{f(k)}{f_0}R_2 + 4R_2^f \\
&\quad + 2R_2^{f*} + \frac{f(k)}{f_0}R_I + 2R_I^f + R_I^{f*}\bigg]j_3(kq), \\
\dot{V}_1(q) = &\int \frac{dk}{\pi^2}\frac{3}{70k}\bigg[4Q_2^f + 4Q_2^{f*} + 2Q_I^f - 3Q_I^{f*} + 4\frac{f(k)}{f_0}R_2 + 8R_2^f \\
&\quad + 4R_2^{f*} + 2\frac{f(k)}{f_0}R_I - 6R_I^f - 3R_I^{f*}\bigg]j_1(kq) - \frac{1}{5}\dot{T}(q), \\
\dot{V}_3(q) = &\dot{V}_1(q) - \int \frac{dk}{\pi^2}\frac{3}{14k}\bigg[2Q_1^f - Q_1^{f*} + \frac{f(k)}{f_0}R_I - 2R_I^f\bigg]j_1(kq),
\end{aligned} \tag{D.43}$$

and

$$\begin{aligned}
\ddot{T}(q) = &-\int \frac{dk}{\pi^2}\frac{3}{14k}\bigg[8Q_2^{ff} + 2Q_2^{f*f*} + 4Q_I^{ff} + Q_I^{f*f*} + 8\frac{f(k)}{f_0}R_2^f + 8R_2^{ff} \\
&\quad + 4\frac{f(k)}{f_0}R_2^{f*} + 4\frac{f(k)}{f_0}R_I^f + 4R_I^{ff} + 2\frac{f(k)}{f_0}R_I^{f*}\bigg]j_3(kq), \\
\ddot{V}_1(q) = &\int \frac{dk}{\pi^2}\frac{3}{35k}\bigg[4Q_2^{ff} + Q_2^{f*f*} + 2Q_I^{ff} - 2Q_I^{f*f*} + 4\frac{f(k)}{f_0}R_2^f + 4R_2^{ff} \\
&\quad + 2\frac{f(k)}{f_0}R_2^{f*} + 2\frac{f(k)}{f_0}R_I^f - 8R_I^{ff} + \frac{f(k)}{f_0}R_I^{f*}\bigg]j_1(kq) - \frac{1}{5}\ddot{T}(q), \\
\dot{V}_3(q) = &\dot{V}_1(q) - \int \frac{dk}{\pi^2}\frac{3}{14k}\bigg[2Q_1^{ff} - Q_1^{f*f*} - 4R_I^{ff} + \frac{f(k)}{f_0}(2R_I^f + R_I^{f*})\bigg]j_1(kq),
\end{aligned} \tag{D.44}$$

which complete our search for 1D integral expressions for the functions defined in (5.44) and (5.49).

We end this section by emphasizing that the ΛCDM standard results are recovered by making the substitutions $Q, R^{f,f*,f*f*,ff} = Q, R$.

D.4 Tidal bias

In this subsection we introduce tidal bias following [193]. This is achieved by adding $s^2 = s_{ij}s_{ij}$ as an argument to the Lagrangian biasing function F [see (5.21)], with the shear tensor

$$s_{ij}(\mathbf{q}) = \left(\frac{\partial_i\partial_j}{\partial^2} - \frac{1}{3}\delta_{ij}\right)\delta(\mathbf{q}). \tag{D.45}$$

Almost all expressions related to tidal bias contain only linear fields, such that in the integrals of Appendix D of [193], they only need the substitution $P_L \to (f(k)/f)P_L$ for dotted functions and $P_L \to (f(k)/f)^2 P_L$ for double-dotted functions . The only new, substantially different function, is

$$V_i^{10} = \langle s^2(\mathbf{q}_1)\Psi_i^{(2)}(\mathbf{q}_2)\rangle_c = -\frac{3}{7}\int \frac{dk}{2\pi^2} Q_{s^2}(k) j_1(kq), \tag{D.46}$$

with

$$Q_{s^2}(k) = \int \frac{d^3p}{(2\pi)^3}\Gamma_2(\mathbf{k}-\mathbf{p},\mathbf{p})\left[\frac{\big((\mathbf{k}-\mathbf{p})\cdot\mathbf{p}\big)^2}{p^2|\mathbf{k}-\mathbf{p}|^2} - \frac{1}{3}\right] P_L(|\mathbf{k}-\mathbf{p}|)P_L(p). \tag{D.47}$$

This does not reduce to the result of [193] for ΛCDM. Instead, it differs by a 1/2 factor: $V_i^{10} = \frac{1}{2}V_i^{10\,[\text{That work}]}$.

APPENDIX E

DIRECT LAGRANGIAN APPROACH IN MG

In this Appendix section, we explain how the Direct Lagrangian approach to RSD, laid out in section 5.3.3, will be implemented in MG theories and point out the differences with respect to the GR case. In particular, starting with the simpler GR case, in section 5.3.3 we explained how the LPT field evolves as $\mathbf{\Psi}^{(n)} \propto D^n(a)$, giving $\dot{\mathbf{\Psi}}^{(n)} = nf_0 H \mathbf{\Psi}^{(n)}$, which allows us to map the LPT field to redshift space, order by order, through

$$\Psi_i^{s(n)} = \left(\delta_{ij} + nf_0 \hat{z}_i \hat{z}_j\right) \Psi_j^{(n)}, \tag{E.1}$$

where we made use of (5.31). Equation (E.1) then allows us to easily "Directly" map each of the Lagrangian correlators (5.26) to redshift space. Focusing on the function $U_i(\mathbf{q}) = U(q)\hat{q}_i$, as an example, and expanding order by order as $U(q) = U^{(1)}(q) + U^{(3)}(q) + ..$, we get

$$U_i^{s(n)} = \left(\delta_{ij} + nf_0 \hat{z}_i \hat{z}_j\right) U_j^{(n)}, \tag{E.2}$$

where $U_i^{s(n)}$ denotes the redshift space version of $U^{(n)}(q)$.

The above derivation does not hold in MG theories however, because of the scale-dependent growth factors that are introduced, which means that $\dot{\mathbf{\Psi}}^{(n)} \neq nfH\mathbf{\Psi}^{(n)}$. In this case, and as explained in detail in the previous appendix section D, $\dot{\mathbf{\Psi}}^{(n)}$ is instead given by (D.6), combined with (D.7), which leads to the mapping

$$\Psi_i^{s(n)} = \Psi_i^{(n)} + \hat{z}_i \hat{z}_j \frac{d\Psi_j^{(n)}}{d\ln a} = \Psi_i^{(n)} + \hat{z}_i \hat{z}_j \frac{\dot{\Psi}_j^{(n)}}{H(a)}. \tag{E.3}$$

From the definitions (5.26), we will now get

$$U_i^{s(n)} = U_i^{(n)} + f_0 \hat{z}_i \hat{z}_j \dot{U}_j^{(n)}, \tag{E.4}$$

where $\dot{U}_j^{(n)}$ is given in (D.34). In the GR limit, $\dot{U}(q) = U^{(1)}(q) + 3U^{(3)}(q)$ and (E.4) reduces back to the GR expression (E.2). The rest of the correlators (5.26) can be similarly mapped to their redshift space expressions, following the same procedure, combined with the "dot" functions presented in appendix D.

BIBLIOGRAPHY

[1] B. P. Abbott et al. Gravitational Waves and Gamma-rays from a Binary Neutron Star Merger: GW170817 and GRB 170817A. Astrophys. J., 848(2):L13, 2017.

[2] B. P. Abbott et al. Multi-messenger Observations of a Binary Neutron Star Merger. Astrophys. J., 848(2):L12, 2017.

[3] B.P. Abbott et al. GW170817: Observation of Gravitational Waves from a Binary Neutron Star Inspiral. Phys. Rev. Lett., 119(16):161101, 2017.

[4] T. Abbott et al. The dark energy survey. 2005.

[5] Paul A. Abell et al. LSST Science Book, Version 2.0. 2009.

[6] P. A. R. Ade et al. Planck 2015 results. XIII. Cosmological parameters. Astron. Astrophys., 594:A13, 2016.

[7] P.A.R. Ade et al. Planck 2013 results. XVI. Cosmological parameters. 2013.

[8] Shadab Alam et al. The clustering of galaxies in the completed SDSS-III Baryon Oscillation Spectroscopic Survey: cosmological analysis of the DR12 galaxy sample. Mon. Not. Roy. Astron. Soc., 470(3):2617–2652, 2017.

[9] David Alonso. CUTE solutions for two-point correlation functions from large cosmological datasets. arXiv e-prints, page arXiv:1210.1833, October 2012.

[10] Raul Angulo, C. M. Baugh, C. S. Frenk, and C. G. Lacey. The detectability of baryonic acoustic oscillations in future galaxy surveys. Mon. Not. Roy. Astron. Soc., 383:755, 2008.

[11] Joaquin Armijo, Yan-Chuan Cai, Nelson Padilla, Baojiu Li, and John A. Peacock. Testing modified gravity using a marked correlation function. Mon. Not. Roy. Astron. Soc., 478(3):3627–3632, 2018.

[12] Pablo Arnalte-Mur, Wojciech A. Hellwing, and Peder Norberg. Real- and redshift-space halo clustering in f(R) cosmologies. Monthly Notices of the Royal Astronomical Society, 467(2):1569–1585, 01 2017.

[13] Christian Arnold, Pablo Fosalba, Volker Springel, Ewald Puchwein, and Linda Blot. The modified gravity lightcone simulation project I: Statistics of matter and halo distributions. 2018.

[14] Alejandro Aviles. Renormalization of Lagrangian bias via spectral parameters. Phys. Rev., D98(8):083541, 2018.

[15] Alejandro Aviles and Jorge L. Cervantes-Cota. Lagrangian perturbation theory for modified gravity. Phys. Rev., D96(12):123526, 2017.

[16] Alejandro Aviles, Jorge L. Cervantes-Cota, and David F. Mota. Screenings in Modified Gravity: a perturbative approach. Astron. Astrophys., 622:A62, 2019.

[17] Alejandro Aviles, Mario Alberto Rodriguez-Meza, Josue De-Santiago, and Jorge L. Cervantes-Cota. Nonlinear evolution of initially biased tracers in modified gravity. JCAP, 1811(11):013, 2018.

[18] Eugeny Babichev and Cdric Deffayet. An introduction to the Vainshtein mechanism. Class. Quant. Grav., 30:184001, 2013.

[19] T. Baker, E. Bellini, P. G. Ferreira, M. Lagos, J. Noller, and I. Sawicki. Strong constraints on cosmological gravity from GW170817 and GRB 170817A. Phys. Rev. Lett., 119(25):251301, 2017.

[20] J. M. Bardeen, J. R. Bond, N. Kaiser, and A. S. Szalay. The statistics of peaks of Gaussian random fields. ApJ, 304:15–61, May 1986.

[21] Alexandre Barreira, Sownak Bose, and Baojiu Li. Speeding up N-body simulations of modified gravity: Vainshtein screening models. JCAP, 1512(12):059, 2015.

[22] Alexandre Barreira, Baojiu Li, Carlton M. Baugh, and Silvia Pascoli. Spherical collapse in Galileon gravity: fifth force solutions, halo mass function and halo bias. JCAP, 1311:056, 2013.

[23] Alexandre Barreira, Baojiu Li, Wojciech A. Hellwing, Lucas Lombriser, Carlton M. Baugh, and Silvia Pascoli. Halo model and halo properties in Galileon gravity cosmologies. JCAP, 1404:029, 2014.

[24] Alexandre Barreira, Ariel G. Sánchez, and Fabian Schmidt. Validating es-

timates of the growth rate of structure with modified gravity simulations. Phys. Rev. D, 94:084022, Oct 2016.

[25] P. S. Behroozi, R. H. Wechsler, and H.-Y. Wu. The ROCKSTAR Phase-space Temporal Halo Finder and the Velocity Offsets of Cluster Cores. The Astrophysical Journal, 762:109, January 2013.

[26] C. Beisbart, M. Kerscher, and K. Mecke. Mark Correlations: Relating Physical Properties to Spatial Distributions. In K. Mecke and D. Stoyan, editors, Morphology of Condensed Matter, volume 600 of Lecture Notes in Physics, Berlin Springer Verlag, pages 358–390, 2002.

[27] Claus Beisbart and Martin Kerscher. Luminosity- and morphology-dependent clustering of galaxies. Astrophys. J., 545:6, 2000.

[28] Emilio Bellini and Miguel Zumalacárregui. Nonlinear evolution of the baryon acoustic oscillation scale in alternative theories of gravity. Phys. Rev. D, 92:063522, Sep 2015.

[29] Andreas A. Berlind and David H. Weinberg. The halo occupation distribution: Toward an empirical determination of the relation between galaxies and mass. The Astrophysical Journal, 575(2):587, 2002.

[30] F. Bernardeau, S. Colombi, E. Gaztanaga, and R. Scoccimarro. Large scale structure of the universe and cosmological perturbation theory. Phys. Rept., 367:1–248, 2002.

[31] Davide Bianchi, Matteo Chiesa, and Luigi Guzzo. Improving the modelling of redshift-space distortions ? I. A bivariate Gaussian description for the galaxy pairwise velocity... Mon. Not. Roy. Astron. Soc., 446:75–84, 2015.

[32] Davide Bianchi, Will Percival, and Julien Bel. Improving the modelling of redshift-space distortions? II. A pairwise velocity model covering large and small scales. Mon. Not. Roy. Astron. Soc., 463(4):3783–3798, 2016.

[33] J. R. Bond, S. Cole, G. Efstathiou, and N. Kaiser. Excursion set mass functions for hierarchical Gaussian fluctuations. The Astrophysical Journal, 379:440–460, October 1991.

[34] Benjamin Bose and Kazuya Koyama. A Perturbative Approach to the

Redshift Space Power Spectrum: Beyond the Standard Model. JCAP, 1608(08):032, 2016.

[35] Benjamin Bose and Kazuya Koyama. A Perturbative Approach to the Redshift Space Correlation Function: Beyond the Standard Model. JCAP, 1708(08):029, 2017.

[36] Benjamin Bose and Atsushi Taruya. The one-loop matter bispectrum as a probe of gravity and dark energy. JCAP, 1810(10):019, 2018.

[37] Sownak Bose, Baojiu Li, Alexandre Barreira, Jian-hua He, Wojciech A. Hellwing, Kazuya Koyama, Claudio Llinares, and Gong-Bo Zhao. Speeding up *N*-body simulations of modified gravity: Chameleon screening models. JCAP, 1702(02):050, 2017.

[38] F. R. Bouchet, S. Colombi, E. Hivon, and R. Juszkiewicz. Perturbative Lagrangian approach to gravitational instability. Astron. Astrophys., 296:575, 1995.

[39] P. Brax, A.-C. Davis, B. Li, H. A. Winther, and G.-B. Zhao. Systematic simulations of modified gravity: symmetron and dilaton models. JCAP, 10:002, October 2012.

[40] Philippe Brax, Anne-C. Davis, Baojiu Li, Hans A. Winther, and Gong-Bo Zhao. Systematic simulations of modified gravity: chameleon models. JCAP, 1304:029, 2013.

[41] Philippe Brax, Anne-Christine Davis, Baojiu Li, and Hans A. Winther. A Unified Description of Screened Modified Gravity. Phys. Rev., D86:044015, 2012.

[42] Philippe Brax and Patrick Valageas. Impact on the power spectrum of screening in modified gravity scenarios. Phys. Rev. D, 88:023527, Jul 2013.

[43] Philippe Brax, Carsten van de Bruck, Anne-Christine Davis, and Douglas J. Shaw. f(R) Gravity and Chameleon Theories. Phys. Rev., D78:104021, 2008.

[44] T. Buchert. A class of solutions in Newtonian cosmology and the pancake theory. Astron. Astrophys., 223:9–24, October 1989.

[45] Clare Burrage and Jeremy Sakstein. Tests of Chameleon Gravity. Living Rev. Rel., 21(1):1, 2018.

[46] J. Carlson, B. Reid, and M. White. Convolution Lagrangian perturbation theory for biased tracers. MNRAS, 429:1674–1685, February 2013.

[47] J. Carlson, M. White, and N. Padmanabhan. Critical look at cosmological perturbation theory techniques. Phys. Rev. D, 80(4):043531, August 2009.

[48] Sean M. Carroll, Vikram Duvvuri, Mark Trodden, and Michael S. Turner. Is cosmic speed - up due to new gravitational physics? Phys. Rev., D70:043528, 2004.

[49] J. Carron. Information Escaping the Correlation Hierarchy of the Convergence Field in the Study of Cosmological Parameters. Physical Review Letters, 108(7):071301, February 2012.

[50] Marius Cautun, Enrique Paillas, Yan-Chuan Cai, Sownak Bose, Joaquin Armijo, Baojiu Li, and Nelson Padilla. The SantiagoHarvardEdinburgh-Durham void comparison I. SHEDding light on chameleon gravity tests. Mon. Not. Roy. Astron. Soc., 476(3):3195–3217, 2018.

[51] Asantha Cooray and Ravi K. Sheth. Halo models of large scale structure. Phys. Rept., 372:1–129, 2002.

[52] Edmund J. Copeland, M. Sami, and Shinji Tsujikawa. Dynamics of dark energy. Int. J. Mod. Phys., D15:1753–1936, 2006.

[53] J. Coupon, M. Kilbinger, H. J. McCracken, O. Ilbert, S. Arnouts, Y. Mellier, U. Abbas, S. de la Torre, Y. Goranova, P. Hudelot, J.-P. Kneib, and O. Le Fèvre. Galaxy clustering in the CFHTLS-Wide: the changing relationship between galaxies and haloes since z ˜ 1.2*. Astronomy and Astrophysics, 542:A5, June 2012.

[54] Paolo Creminelli and Filippo Vernizzi. Dark Energy after GW170817 and GRB170817A. Phys. Rev. Lett., 119(25):251302, 2017.

[55] Anne-Christine Davis, Baojiu Li, David F. Mota, and Hans A. Winther. Structure Formation in the Symmetron Model. Astrophys. J., 748:61, 2012.

[56] M. Davis and P. J. E. Peebles. A survey of galaxy redshifts. V - The

two-point position and velocity correlations. The Astrophysical Journal, 267:465–482, April 1983.

[57] Antonio De Felice and Shinji Tsujikawa. f(R) theories. Living Rev. Rel., 13:3, 2010.

[58] C. Deffayet, Xian Gao, D. A. Steer, and G. Zahariade. From *k*-essence to generalized galileons. Phys. Rev. D, 84:064039, Sep 2011.

[59] Vincent Desjacques, Donghui Jeong, and Fabian Schmidt. Large-Scale Galaxy Bias. Phys. Rept., 733:1–193, 2018.

[60] G. R. Dvali, Gregory Gabadadze, and Massimo Porrati. 4-D gravity on a brane in 5-D Minkowski space. Phys. Lett., B485:208–214, 2000.

[61] Gia Dvali, Gian F. Giudice, Cesar Gomez, and Alex Kehagias. UV-Completion by Classicalization. JHEP, 08:108, 2011.

[62] G. Efstathiou, C. S. Frenk, S. D. M. White, and M. Davis. Gravitational clustering from scale-free initial conditions. MNRAS, 235:715–748, December 1988.

[63] Daniel J. Eisenstein et al. Detection of the baryon acoustic peak in the large-scale correlation function of SDSS luminous red galaxies. Astrophys.J., 633:560–574, 2005.

[64] R. C. Elandt-Johnson and N. L. Johnson. Survival Distributions, in Survival Models and Data Analysis (p.72). John Wiley & Sons, Inc., Hoboken, NJ, USA., 1999.

[65] Jose Mara Ezquiaga and Miguel Zumalacrregui. Dark Energy After GW170817: Dead Ends and the Road Ahead. Phys. Rev. Lett., 119(25):251304, 2017.

[66] Matteo Fasiello and Zvonimir Vlah. Screening in perturbative approaches to LSS. Phys. Lett., B773:236–241, 2017.

[67] K. B. Fisher. On the Validity of the Streaming Model for the Redshift-Space Correlation Function in the Linear Regime. The Astrophysical Journal, eprint = astro-ph/9412081, keywords = COSMOLOGY: LARGE-SCALE STRUCTURE OF UNIVERSE, COSMOLOGY: THEORY, year = 1995, month = aug, volume = 448,

pages = 494, doi = 10.1086/175980, adsurl = https://ui.adsabs.harvard.edu/abs/1995ApJ...448..494F, adsnote = Provided by the SAO/NASA Astrophysics Data System.

[68] A. Goldstein et al. An Ordinary Short Gamma-Ray Burst with Extraordinary Implications: Fermi-GBM Detection of GRB 170817A. Astrophys. J., 848(2):L14, 2017.

[69] Stefan Gottloeber, Martin Kerscher, Andrey V. Kravtsov, Andreas Faltenbacher, Anatoly Klypin, and Volker Mueller. Spatial distribution of galactic halos and their merger histories. Astron. Astrophys., 387:778, 2002.

[70] A. J. S. Hamilton. Measuring Omega and the real correlation function from the redshift correlation function.

[71] A. J. S. Hamilton. Linear redshift distortions: A Review. In Ringberg Workshop on Large Scale Structure Ringberg, Germany, September 23-28, 1996 1997.

[72] A. J. S. Hamilton, C. D. Rimes, and R. Scoccimarro. On measuring the covariance matrix of the non-linear power spectrum from simulations. Mon. Not. Roy. Astron. Soc., 371:1188–1204, September 2006.

[73] Wojciech A. Hellwing, Kazuya Koyama, Benjamin Bose, and Gong-Bo Zhao. Revealing modified gravity signals in matter and halo hierarchical clustering. Phys. Rev., D96(2):023515, 2017.

[74] Csar Hernandez-Aguayo, Carlton M. Baugh, and Baojiu Li. Marked clustering statistics in $f(R)$ gravity cosmologies. Mon. Not. Roy. Astron. Soc., 479(4):4824–4835, 2018.

[75] Csar Hernandez-Aguayo, Jiamin Hou, Baojiu Li, Carlton M. Baugh, and Ariel G. Sanchez. Large-scale redshift space distortions in modified gravity theories. Mon. Not. Roy. Astron. Soc., 485(2):2194–2213, 2019.

[76] G. Hinshaw, D. Larson, E. Komatsu, D. N. Spergel, C. L. Bennett, J. Dunkley, M. R. Nolta, M. Halpern, R. S. Hill, N. Odegard, L. Page, K. M. Smith, J. L. Weiland, B. Gold, N. Jarosik, A. Kogut, M. Limon, S. S. Meyer, G. S. Tucker, E. Wollack, and E. L. Wright. Nine-year wilkinson microwave anisotropy probe (wmap) observations: Cosmological parameter results. The Astrophysical Journal Supplement Series, 208(2):19, 2013.

[77] Kurt Hinterbichler and Justin Khoury. Screening long-range forces through local symmetry restoration. Phys. Rev. Lett., 104:231301, Jun 2010.

[78] E. Hivon, F. R. Bouchet, S. Colombi, and R. Juszkiewicz. Redshift distortions of clustering: A Lagrangian approach. Astron. Astrophys., 298:643–660, 1995.

[79] Kai Hoffmann, Julien Bel, and Enrique Gaztanaga. Comparing halo bias from abundance and clustering. Mon. Not. Roy. Astron. Soc., 450(2):1674–1692, 2015.

[80] Gregory Walter Horndeski. Second-order scalar-tensor field equations in a four-dimensional space. International Journal of Theoretical Physics, 10(6):363–384, 1974.

[81] Wayne Hu and Ignacy Sawicki. Models of f(R) Cosmic Acceleration that Evade Solar-System Tests. Phys. Rev., D76:064004, 2007.

[82] M. Icaza-Lizaola et al. The clustering of the SDSS-IV extended Baryon Oscillation Spectroscopic Survey DR14 LRG sample: structure growth rate measurement from the anisotropic LRG correlation function in the redshift range 0.6 ¡ z ¡ 1.0. 2019.

[83] Wolfram Research, Inc. Mathematica, Version 11.3. Champaign, IL, 2018.

[84] Mustapha Ishak. Testing General Relativity in Cosmology. 2018.

[85] E. Jennings, C. M. Baugh, B. Li, G.-B. Zhao, and K. Koyama. Redshift-space distortions in f(R) gravity. MNRAS, 425:2128–2143, September 2012.

[86] N. Kaiser. On the spatial correlations of Abell clusters. The Astrophysical Journal, 284:L9–L12, September 1984.

[87] Nick Kaiser. Clustering in real space and in redshift space. Monthly Notices of the Royal Astronomical Society, 227(1):1–21, 1987.

[88] Nick Kaiser. Clustering in real space and in redshift space. Monthly Notices of the Royal Astronomical Society, 227(1):1–21, 07 1987.

[89] Eyal A. Kazin, Jun Koda, Chris Blake, and Nikhil Padmanabhan. Improved WiggleZ Dark Energy Survey Distance Measurements to z = 1 with Reconstruction of the Baryonic Acoustic Feature. 2014.

[90] Justin Khoury. Theories of Dark Energy with Screening Mechanisms. 2010.

[91] Justin Khoury. Les Houches Lectures on Physics Beyond the Standard Model of Cosmology. 2013.

[92] Justin Khoury and Amanda Weltman. Chameleon cosmology. Phys. Rev. D, 69:044026, Feb 2004.

[93] Justin Khoury and Amanda Weltman. Chameleon fields: Awaiting surprises for tests of gravity in space. Phys. Rev. Lett., 93:171104, Oct 2004.

[94] Justin Khoury and Mark Wyman. N-Body Simulations of DGP and Degravitation Theories. Phys. Rev., D80:064023, 2009.

[95] Anatoly Klypin and Jon Holtzman. Particle mesh code for cosmological simulations. 1997.

[96] Kazuya Koyama. Ghosts in the self-accelerating universe. Class. Quant. Grav., 24(24):R231–R253, 2007.

[97] Kazuya Koyama. Cosmological Tests of Modified Gravity. Rept. Prog. Phys., 79(4):046902, 2016.

[98] Kazuya Koyama, Atsushi Taruya, and Takashi Hiramatsu. Nonlinear evolution of the matter power spectrum in modified theories of gravity. Phys. Rev. D, 79:123512, Jun 2009.

[99] Andrey V. Kravtsov, Andreas A. Berlind, Risa H. Wechsler, Anatoly A. Klypin, Stefan Gottlber, Brandon Allgood, and Joel R. Primack. The dark side of the halo occupation distribution. The Astrophysical Journal, 609(1):35, 2004.

[100] J. Kwan, G. F. Lewis, and E. V. Linder. Mapping Growth and Gravity with Robust Redshift Space Distortions. The Astrophysical Journal, 748:78, April 2012.

[101] T. Y. Lam and R. K. Sheth. Perturbation theory and excursion set estimates of the probability distribution function of dark matter, and a method for reconstructing the initial distribution function. Mon. Not. Roy. Astron. Soc., 386:407, 2008.

[102] Tsz Yan Lam and Baojiu Li. Excursion set theory for modified gravity: correlated steps, mass functions and halo bias. Monthly Notices of the Royal Astronomical Society, 426(4):3260–3270, 2012.

[103] Stephen D. Landy and Alexander S. Szalay. An inversion method for measuring beta in large redshift surveys. Astrophys. J., 579:76–82, 2002.

[104] Istvan Laszlo and Rachel Bean. Nonlinear growth in modified gravity theories of dark energy. Phys. Rev., D77:024048, 2008.

[105] R. Laureijs et al. Euclid Definition Study Report. 2011.

[106] Michael Levi et al. The DESI Experiment, a whitepaper for Snowmass 2013. 2013.

[107] Antony Lewis, Anthony Challinor, and Anthony Lasenby. Efficient computation of CMB anisotropies in closed FRW models. Astrophys. J., 538:473–476, 2000.

[108] Baojiu Li and John D. Barrow. N-Body Simulations for Coupled Scalar Field Cosmology. Phys. Rev., D83:024007, 2011.

[109] Baojiu Li and George Efstathiou. An extended excursion set approach to structure formation in chameleon models. Monthly Notices of the Royal Astronomical Society, 421(2):1431–1442, 2012.

[110] Baojiu Li and Tsz Yan Lam. Excursion set theory for modified gravity: Eulerian versus lagrangian environments. Monthly Notices of the Royal Astronomical Society, 425(1):730–739, 2012.

[111] Baojiu Li, Gong-Bo Zhao, and Kazuya Koyama. Exploring Vainshtein mechanism on adaptively refined meshes. JCAP, 1305:023, 2013.

[112] Baojiu Li, Gong-Bo Zhao, Romain Teyssier, and Kazuya Koyama. Ecosmog : an efficient code for simulating modified gravity. Journal of Cosmology and Astroparticle Physics, 2012(01):051, 2012.

[113] Baojiu Li and Hongsheng Zhao. Structure formation by a fifth force: n-body versus linear simulations. Phys. Rev. D, 80:044027, Aug 2009.

[114] Claudio Llinares and Nuala McCullagh. Weighted density fields as improved probes of modified gravity models. 2017.

[115] Lucas Lombriser, Baojiu Li, Kazuya Koyama, and Gong-Bo Zhao. Modeling halo mass functions in chameleon f(R) gravity. Phys. Rev., D87(12):123511, 2013.

[116] Lucas Lombriser, Fergus Simpson, and Alexander Mead. Unscreening Modified Gravity in the Matter Power Spectrum. Phys. Rev. Lett., 114(25):251101, 2015.

[117] Chung-Pei Ma and James N. Fry. Deriving the nonlinear cosmological power spectrum and bispectrum from analytic dark matter halo profiles and mass functions. Astrophys. J., 543:503–513, 2000.

[118] M. Manera, Ravi K. Sheth, and R. Scoccimarro. Large-scale bias and the inaccuracy of the peak-background split. Monthly Notices of the Royal Astronomical Society, 402:589–602, February 2010.

[119] Takahiko Matsubara. Nonlinear perturbation theory with halo bias and redshift-space distortions via the Lagrangian picture. Phys. Rev., D78:083519, 2008. [Erratum: Phys. Rev.D78,109901(2008)].

[120] Takahiko Matsubara. Resumming Cosmological Perturbations via the Lagrangian Picture: One-loop Results in Real Space and in Redshift Space. Phys. Rev., D77:063530, 2008.

[121] Takahiko Matsubara. Nonlinear perturbation theory integrated with nonlocal bias, redshift-space distortions, and primordial non-gaussianity. Phys. Rev. D, 83:083518, Apr 2011.

[122] Takahiko Matsubara. Recursive Solutions of Lagrangian Perturbation Theory. Phys. Rev., D92(2):023534, 2015.

[123] P. McDonald and A. Roy. Clustering of dark matter tracers: generalizing bias for the coming era of precision LSS. JCAP, 8:020, August 2009.

[124] H. J. Mo, Y. P. Jing, and S. D. M. White. High-order correlations of peaks and halos: A Step toward understanding galaxy biasing. Mon. Not. Roy. Astron. Soc., 284:189, 1997.

[125] H. J. Mo and Simon D. M. White. An Analytic model for the spatial clustering of dark matter halos. Mon. Not. Roy. Astron. Soc., 282:347, 1996.

[126] Steven Murray, Chris Power, and Aaron Robotham. HMFcalc: An Online Tool for Calculating Dark Matter Halo Mass Functions. 2013.

[127] M. C. Neyrinck, I. Szapudi, N. McCullagh, A. Szalay, B. Falck, and J. Wang. Density-dependent clustering: I. Pulling back the curtains on motions of the BAO peak. ArXiv e-prints, October 2016.

[128] M. C. Neyrinck, I. Szapudi, and A. S. Szalay. Rejuvenating the Matter Power Spectrum: Restoring Information with a Logarithmic Density Mapping. Astrophysical Journal, Letters, 698:L90–L93, June 2009.

[129] Mark C. Neyrinck and Istvan Szapudi. Information content in the halo-model dark-matter power spectrum II: Multiple cosmological parameters. Mon. Not. Roy. Astron. Soc., 375:L51–L55, 2007.

[130] Keith A. Olive and Maxim Pospelov. Environmental dependence of masses and coupling constants. Phys. Rev., D77:043524, 2008.

[131] J. A. Peacock. Errors on the measurement of ? via cosmological dipoles. Monthly Notices of the Royal Astronomical Society, 258(3):581–586, 10 1992.

[132] J. A. Peacock and S. J. Dodds. Reconstructing the linear power spectrum of cosmological mass fluctuations. Mon. Not. Roy. Astron. Soc., 267:1020–1034, 1994.

[133] J. A. Peacock and R. E. Smith. Halo occupation numbers and galaxy bias. Mon. Not. Roy. Astron. Soc., 318:1144, 2000.

[134] J. A. Peacock and M. J. West. The power spectrum of Abell cluster correlations. MNRAS, 259:494–504, December 1992.

[135] P. J. E. Peebles. The large-scale structure of the universe. 1980.

[136] Will J. Percival et al. Measuring the Baryon Acoustic Oscillation scale using the SDSS and 2dFGRS. Mon. Not. Roy. Astron. Soc., 381:1053–1066, 2007.

[137] Will J. Percival et al. Baryon Acoustic Oscillations in the Sloan Digital Sky Survey Data Release 7 Galaxy Sample. 2009.

[138] S. Perlmutter et al. Measurements of Omega and Lambda from 42 high redshift supernovae. Astrophys. J., 517:565–586, 1999.

[139] Planck Collaboration, P. A. R. Ade, N. Aghanim, M. Arnaud, M. Ashdown, J. Aumont, C. Baccigalupi, A. J. Banday, R. B. Barreiro, J. G. Bartlett, and et al. Planck 2015 results. XIII. Cosmological parameters. Astronomy and Astrophysics, 594:A13, September 2016.

[140] W. H. Press and P. Schechter. Formation of Galaxies and Clusters of Galaxies by Self-Similar Gravitational Condensation. The Astrophysical Journal, 187:425–438, February 1974.

[141] Ewald Puchwein, Marco Baldi, and Volker Springel. Modified-gravity-gadget: a new code for cosmological hydrodynamical simulations of modified gravity models. Monthly Notices of the Royal Astronomical Society, 436(1):348–360, 2013.

[142] Thomas R. Quinn, Neal Katz, Joachim Stadel, and George Lake. Time stepping N body simulations. Submitted to: Astrophys. J., 1997.

[143] Bharat Ratra and P. J. E. Peebles. Cosmological consequences of a rolling homogeneous scalar field. Phys. Rev. D, 37:3406–3427, Jun 1988.

[144] Beth A. Reid, Lado Samushia, Martin White, Will J. Percival, Marc Manera, Nikhil Padmanabhan, Ashley J. Ross, Ariel G. Sánchez, Stephen Bailey, Dmitry Bizyaev, Adam S. Bolton, Howard Brewington, J. Brinkmann, Joel R. Brownstein, Antonio J. Cuesta, Daniel J. Eisenstein, James E. Gunn, Klaus Honscheid, Elena Malanushenko, Viktor Malanushenko, Claudia Maraston, Cameron K. McBride, Demitri Muna, Robert C. Nichol, Daniel Oravetz, Kaike Pan, Roland de Putter, N. A. Roe, Nicholas P. Ross, David J. Schlegel, Donald P. Schneider, Hee-Jong Seo, Alaina Shelden, Erin S. Sheldon, Audrey Simmons, Ramin A. Skibba, Stephanie Snedden, Molly E. C. Swanson, Daniel Thomas, Jeremy Tinker, Rita Tojeiro, Licia Verde, David A. Wake, Benjamin A. Weaver, David H. Weinberg, Idit Zehavi, and Gong-Bo Zhao. The clustering of galaxies in the SDSS-III Baryon Oscillation Spectroscopic Survey: measurements of the growth of structure and expansion rate at z = 0.57 from anisotropic clustering. MNRAS, 426(4):2719–2737, Nov 2012.

[145] Beth A. Reid and Martin White. Towards an accurate model of the redshift-space clustering of haloes in the quasi-linear regime. Monthly Notices of the Royal Astronomical Society, 417(3):1913–1927, 2011.

[146] A. Repp and I. Szapudi. Precision prediction of the log power spectrum. Mon. Not. Roy. Astron. Soc., 464:L21–L25, January 2017.

[147] Adam G. Riess et al. Type Ia supernova discoveries at z ¿ 1 from the Hubble Space Telescope: Evidence for past deceleration and constraints on dark energy evolution. Astrophys. J., 607:665–687, 2004.

[148] Christopher D. Rimes and Andrew J. S. Hamilton. Information content of the non-linear matter power spectrum. Mon. Not. Roy. Astron. Soc., 360:L82–L86, 2005.

[149] Christopher D. Rimes and Andrew J. S. Hamilton. Information content of the non-linear power spectrum: the effect of beat-coupling to large scales. Mon. Not. Roy. Astron. Soc., 371:1205–1215, 2006.

[150] Jeremy Sakstein and Bhuvnesh Jain. Implications of the Neutron Star Merger GW170817 for Cosmological Scalar-Tensor Theories. Phys. Rev. Lett., 119(25):251303, 2017.

[151] L. Samushia, W. J. Percival, and A. Raccanelli. Interpreting large-scale redshift-space distortion measurements. Monthly Notices of the Royal Astronomical Society, 420(3):2102–2119, 02 2012.

[152] Lado Samushia, Beth A. Reid, Martin White, Will J. Percival, Antonio J. Cuesta, Lucas Lombriser, Marc Manera, Robert C. Nichol, Donald P. Schneider, Dmitry Bizyaev, Howard Brewington, Elena Malanushenko, Viktor Malanushenko, Daniel Oravetz, Kaike Pan, Audrey Simmons, Alaina Shelden, Stephanie Snedden, Jeremy L. Tinker, Benjamin A. Weaver, Donald G. York, and Gong-Bo Zhao. The clustering of galaxies in the SDSS-III DR9 Baryon Oscillation Spectroscopic Survey: testing deviations from Λ and general relativity using anisotropic clustering of galaxies. MNRAS, 429(2):1514–1528, Feb 2013.

[153] Lado Samushia, Beth A. Reid, Martin White, Will J. Percival, Antonio J. Cuesta, Gong-Bo Zhao, Ashley J. Ross, Marc Manera, Éric Aubourg, Florian Beutler, Jon Brinkmann, Joel R. Brownstein, Kyle S. Dawson, Daniel J. Eisenstein, Shirley Ho, Klaus Honscheid, Claudia Maraston, Francesco Montesano, Robert C. Nichol, Natalie A. Roe, Nicholas P. Ross, Ariel G. Sánchez, David J. Schlegel, Donald P. Schneider, Alina Streblyanska, Daniel Thomas, Jeremy L. Tinker, David A. Wake, Benjamin A. Weaver, and Idit Zehavi. The clustering of galaxies in the SDSS-III Baryon Oscillation Spectroscopic Survey: measuring growth rate and geometry with anisotropic clustering. MNRAS, 439(4):3504–3519, Apr 2014.

[154] Siddharth Satpathy, Rupert A. C. Croft, Shirley Ho, and Baojiu Li. Measurement of marked correlation functions in SDSS-III Baryon Oscillation Spectroscopic Survey using LOWZ galaxies in Data Release 12. Mon. Not. Roy. Astron. Soc., 484(2):2148–2165, 2019.

[155] V. Savchenko et al. INTEGRAL Detection of the First Prompt Gamma-Ray Signal Coincident with the Gravitational-wave Event GW170817. Astrophys. J., 848(2):L15, 2017.

[156] F. Schmidt, W. Hu, and M. Lima. Spherical collapse and the halo model in braneworld gravity. Phys. Rev. D, 81(6):063005, March 2010.

[157] Fabian Schmidt, Donghui Jeong, and Vincent Desjacques. Peak-background split, renormalization, and galaxy clustering. Phys. Rev. D, 88:023515, Jul 2013.

[158] Roman Scoccimarro. Transients from initial conditions: a perturbative analysis. Mon. Not. Roy. Astron. Soc., 299:1097, 1998.

[159] Roman Scoccimarro. Redshift-space distortions, pairwise velocities and nonlinearities. Phys. Rev., D70:083007, 2004.

[160] Román Scoccimarro. Redshift-space distortions, pairwise velocities, and nonlinearities. Phys. Rev. D, 70:083007, Oct 2004.

[161] Roman Scoccimarro, Ravi K. Sheth, Lam Hui, and Bhuvnesh Jain. How many galaxies fit in a halo? Constraints on galaxy formation efficiency from spatial clustering. Astrophys. J., 546:20–34, 2001.

[162] Uroš Seljak, Nico Hamaus, and Vincent Desjacques. How to suppress the shot noise in galaxy surveys. Phys. Rev. Lett., 103:091303, Aug 2009.

[163] Ravi K. Sheth, Andrew J. Connolly, and Ramin Skibba. Marked correlations in galaxy formation models. Submitted to: Mon. Not. Roy. Astron. Soc., 2005.

[164] Ravi K. Sheth and Gerard Lemson. Biasing and the distribution of dark matter haloes. Mon. Not. Roy. Astron. Soc., 304:767, 1999.

[165] Ravi K. Sheth, H. J. Mo, and Giuseppe Tormen. Ellipsoidal collapse and an improved model for the number and spatial distribution of dark matter haloes. Mon. Not. Roy. Astron. Soc., 323:1, 2001.

[166] Ravi K. Sheth and Giuseppe Tormen. Large scale bias and the peak background split. Mon. Not. Roy. Astron. Soc., 308:119, 1999.

[167] Ravi K. Sheth and Giuseppe Tormen. On the environmental dependence of halo formation. Mon. Not. Roy. Astron. Soc., 350:1385, 2004.

[168] F. Simpson, J. B. James, A. F. Heavens, and C. Heymans. Clipping the Cosmos: The Bias and Bispectrum of Large Scale Structure. Physical Review Letters, 107(27):271301, December 2011.

[169] Fergus Simpson, Alan F. Heavens, and Catherine Heymans. Clipping the cosmos. II. Cosmological information from nonlinear scales. Phys. Rev., D88(8):083510, 2013.

[170] Ramin Skibba, Ravi K. Sheth, Andrew J. Connolly, and Ryan Scranton. The luminosity-weighted or 'marked' correlation function. Mon. Not. Roy. Astron. Soc., 369:68–76, 2006.

[171] R. E. Smith, J. A. Peacock, A. Jenkins, S. D. M. White, C. S. Frenk, F. R. Pearce, P. A. Thomas, G. Efstathiou, and H. M. P. Couchmann. Stable clustering, the halo model and nonlinear cosmological power spectra. Mon. Not. Roy. Astron. Soc., 341:1311, 2003.

[172] D. Spergel, N. Gehrels, J. Breckinridge, M. Donahue, A. Dressler, et al. Wide-Field InfraRed Survey Telescope-Astrophysics Focused Telescope Assets WFIRST-AFTA Final Report. 2013.

[173] D. N. Spergel et al. First year Wilkinson Microwave Anisotropy Probe (WMAP) observations: Determination of cosmological parameters. Astrophys. J. Suppl., 148:175–194, 2003.

[174] V. Springel. The cosmological simulation code GADGET-2. MNRAS, 364:1105–1134, December 2005.

[175] V. Springel, S. D. M. White, G. Tormen, and G. Kauffmann. Populating a cluster of galaxies - I. Results at [formmu2]z=0. Monthly Notices of the Royal Astronomical Society, 328:726–750, December 2001.

[176] Hans F. Stabenau and Bhuvnesh Jain. N-Body Simulations of Alternate Gravity Models. Phys. Rev., D74:084007, 2006.

[177] Ryuichi Takahashi, Naoki Yoshida, Masahiro Takada, Takahiko Matsubara, Naoshi Sugiyama, Issha Kayo, Atsushi J. Nishizawa, Takahiro Nishimichi, Shun Saito, and Atsushi Taruya. Simulations of Baryon Acoustic Oscillations II: Covariance matrix of the matter power spectrum. Astrophys. J., 700:479–490, 2009.

[178] Atsushi Taruya and Takashi Hiramatsu. A Closure Theory for Non-linear Evolution of Cosmological Power Spectra. Astrophys. J., 674:617, 2008.

[179] Atsushi Taruya, Kazuya Koyama, Takashi Hiramatsu, and Akira Oka. Beyond consistency test of gravity with redshift-space distortions at quasi-linear scales. Phys. Rev., D89(4):043509, 2014.

[180] Atsushi Taruya, Takahiro Nishimichi, Francis Bernardeau, Takashi Hiramatsu, and Kazuya Koyama. Regularized cosmological power spectrum and correlation function in modified gravity models. Phys. Rev. D, 90:123515, Dec 2014.

[181] Svetlin Tassev. Lagrangian or Eulerian; Real or Fourier? Not All Approaches to Large-Scale Structure Are Created Equal. JCAP, 1406:008, 2014.

[182] Svetlin Tassev, Matias Zaldarriaga, and Daniel Eisenstein. Solving Large Scale Structure in Ten Easy Steps with COLA. JCAP, 1306:036, 2013.

[183] A. N. Taylor and A. J. S. Hamilton. Nonlinear cosmological power spectra in real and redshift space. Mon. Not. Roy. Astron. Soc., 282:767, 1996.

[184] Max Tegmark, Andy Taylor, and Alan Heavens. Karhunen-Loeve eigenvalue problems in cosmology: How should we tackle large data sets? Astrophys. J., 480:22, 1997.

[185] Romain Teyssier. Cosmological hydrodynamics with adaptive mesh refinement: a new high resolution code called ramses. Astron. Astrophys., 385:337–364, 2002.

[186] Cora Uhlemann, Michael Kopp, and Thomas Haugg. Edgeworth streaming model for redshift space distortions. Phys. Rev., D92(6):063004, 2015.

[187] A.I. Vainshtein. To the problem of nonvanishing gravitation mass. Physics Letters B, 39(3):393 – 394, 1972.

[188] Wessel Valkenburg and Bin Hu. Initial conditions for cosmological N-body simulations of the scalar sector of theories of Newtonian, Relativistic and Modified Gravity. JCAP, 1509(09):054, 2015.

[189] Georgios Valogiannis and Rachel Bean. Efficient simulations of large scale structure in modified gravity cosmologies with comoving Lagrangian acceleration. Phys. Rev., D95(10):103515, 2017.

[190] Georgios Valogiannis and Rachel Bean. Beyond δ: Tailoring marked statistics to reveal modified gravity. Phys. Rev., D97(2):023535, 2018.

[191] Georgios Valogiannis and Rachel Bean. Convolution Lagrangian perturbation theory for biased tracers beyond general relativity. Phys. Rev., D99(6):063526, 2019.

[192] Georgios Valogiannis, Rachel Bean, and Alejandro Aviles. An accurate perturbative approach to redshift space clustering of biased tracers in modified gravity. JCAP, 2001(01):055, 2020.

[193] Zvonimir Vlah, Emanuele Castorina, and Martin White. The Gaussian streaming model and convolution Lagrangian effective field theory. JCAP, 1612(12):007, 2016.

[194] Zvonimir Vlah, Uro Seljak, and Tobias Baldauf. Lagrangian perturbation theory at one loop order: successes, failures, and improvements. Phys. Rev., D91:023508, 2015.

[195] Zvonimir Vlah and Martin White. Exploring redshift-space distortions in large-scale structure. JCAP, 1903(03):007, 2019.

[196] Zvonimir Vlah, Martin White, and Alejandro Aviles. A Lagrangian effective field theory. JCAP, 1509(09):014, 2015.

[197] Junpu Wang, Lam Hui, and Justin Khoury. No-Go Theorems for Generalized Chameleon Field Theories. Phys. Rev. Lett., 109:241301, 2012.

[198] Lile Wang, Beth Reid, and Martin White. An analytic model for redshift-space distortions. Mon. Not. Roy. Astron. Soc., 437(1):588–599, 2014.

[199] Xin Wang, Mark Neyrinck, Istvan Szapudi, Alex Szalay, Xuelei Chen, Julien Lesgourgues, Antonio Riotto, and Martin Sloth. Perturbation Theory of the Cosmological Log-Density Field. Astrophys. J., 735:32, 2011.

[200] Y. Wang, C.-H. Chuang, and C. M. Hirata. Towards more realistic forecasting of dark energy constraints from galaxy redshift surveys. MNRAS, 430:2446–2453, April 2013.

[201] Steven Weinberg. The Cosmological Constant Problem. Rev. Mod. Phys., 61:1–23, 1989.

[202] Christof Wetterich. Cosmology and the fate of dilatation symmetry. Nuclear Physics B, 302(4):668–696, 1988.

[203] Martin White. The Zel'dovich approximation. Mon. Not. Roy. Astron. Soc., 439(4):3630–3640, 2014.

[204] Martin White. A marked correlation function for constraining modified gravity models. JCAP, 1611(11):057, 2016.

[205] Martin White and Nikhil Padmanabhan. Breaking Halo Occupation Degeneracies with Marked Statistics. Mon. Not. Roy. Astron. Soc., 395:2381, 2009.

[206] Clifford M. Will. The Confrontation between general relativity and experiment. Living Rev. Rel., 9:3, 2006.

[207] Hans A. Winther and Pedro G. Ferreira. Fast route to nonlinear clustering statistics in modified gravity theories. Phys. Rev., D91(12):123507, 2015.

[208] Hans A. Winther, Kazuya Koyama, Marc Manera, Bill S. Wright, and Gong-Bo Zhao. COLA with scale-dependent growth: applications to screened modified gravity models. 2017.

[209] M. Wolk, J. Carron, and I. Szapudi. On the total cosmological information in galaxy clustering: an analytical approach. Mon. Not. Roy. Astron. Soc., 454(1):560–568, 2015.

[210] Jaiyul Yoo and Uro Seljak. Wide Angle Effects in Future Galaxy Surveys. Mon. Not. Roy. Astron. Soc., 447(2):1789–1805, 2015.

[211] Pauline Zarrouk et al. The clustering of the SDSS-IV extended Baryon Oscillation Spectroscopic Survey DR14 quasar sample: measurement of the growth rate of structure from the anisotropic correlation function between redshift 0.8 and 2.2. Mon. Not. Roy. Astron. Soc., 477(2):1639–1663, 2018.

[212] Ya. B. Zeldovich. Gravitational instability: An Approximate theory for large density perturbations. Astron. Astrophys., 5:84–89, 1970.

[213] Gong-Bo Zhao, Baojiu Li, and Kazuya Koyama. N-body Simulations for f(R) Gravity using a Self-adaptive Particle-Mesh Code. Phys. Rev., D83:044007, 2011.

[214] Zheng Zheng, Andreas A. Berlind, David H. Weinberg, Andrew J. Benson, Carlton M. Baugh, Shaun Cole, Romeel Dav, Carlos S. Frenk, Neal Katz, and Cedric G. Lacey. Theoretical models of the halo occupation distribution: Separating central and satellite galaxies. The Astrophysical Journal, 633(2):791, 2005.